

CONTENTS

Adam Adamowicz, Piotr Grześ <i>Convective Cooling of a Disc Brake During Single Braking</i>	5
Jacek Bałchanowski, Antoni Gronowicz <i>Design and Simulations of Wheel-Legged Mobile Robot</i>	11
Paweł Baranowski, Paweł Bogusz, Paweł Gotowicki, Jerzy Małachowski <i>Assessment of Mechanical Properties of Offroad Vehicle Tire: Coupons Testing and FE Model Development</i>	17
Leszek Cedro <i>Identification of an Electrically Driven Manipulator Using the Differential Filters – Input Error Method</i>	23
Adam Czaplicki, Krzysztof Dziewiecki, Tomasz Sacewicz <i>Identification of Internal Loads at the Selected Joints and Validation of a Biomechanical Model During Performance of the Handspring Front Somersault</i>	28
Marek Dźwiarek <i>Practical Examples of Determination of Frequency of Periodical Inspection of Machinery Safety Systems</i>	33
Marcin Graba <i>Numerical Verification of the Relationship Between The “In-Plane Geometric Con-Straints” used in Fracture Mechanics Problems</i>	38
Antoni Gronowicz, Jarosław Szrek, Sławomir Wudarczyk <i>A Rig for Testing the Leg of a Wheel-Legged Robot</i>	48
Jerzy Jaroszewicz, Krzysztof K. Żur <i>Limitation of Cauchy Function Method in Analysis of Estimators of Frequency and Form of Natural Vibrations of Circular Plate with Variable Thickness and Clamped Edges</i>	53
Tadeusz Kaczorek <i>Positive Realizations for Descriptor Discrete-Time Linear Systems</i>	58
Józef Knapczyk, Mateusz Ryska <i>Stiffness Matrix Analysis of Six-Revolute Serial Manipulator</i>	62
Igor Maciejewski <i>Load-Dependent Controller of the Active Seat Suspension with Adaptive Mass Recognizing</i>	66
Adam Niesłony, Michał Böhm <i>Mean Stress Value in Spectral Method for the Determination of Fatigue Life</i>	71
Grzegorz Orzechowski, Janusz Frączek <i>Integration of the Equations of Motion of Multibody Systems Using Absolute Nodal Coordinate Formulation</i>	75
Andrzej A. Stępniewski <i>Loads of Lower Limb Joints During Bicycle Ride</i>	84
Andrzej Zbrowski, Wojciech Jóźwik <i>Impact Process Identification for Impact Cylinder Piston</i>	88

CONVECTIVE COOLING OF A DISC BRAKE DURING SINGLE BRAKING

Adam ADAMOWICZ*, Piotr GRZEŚ*

*Faculty of Mechanical Engineering, Białystok University of Technology, ul. Wiejska 45C, 15-351 Białystok, Poland

a.adamowicz@pb.edu.pl, p.grzes@doktoranci.pb.edu.pl

Abstract: This study is primarily focused on the investigation of an impact of heat transfer coefficient on heat dissipation from the solid disc using the finite element method (FEM). The analysis was carried out within four individual cases of braking of the passenger vehicle simulating mountain descent with different velocities and the following release periods, where the convective terms of cooling were dependent on the angular velocity of the disc. For the purpose of confronting contrasting conditions of the braking action, apart from heating region, the whole surface of the disc was insulated. The process was performed under the operation conditions of a real front disc brake, whose dimensions and thermophysical properties of materials were adopted and applied to the FE model. It was concluded that the influence of cooling of the exposed surfaces of the disc during relatively short braking is insignificant. However the period after brake release results in considerable decrease in temperature of the disc.

Key words: Braking, Pad/disc System, Finite Element Method, Convective Cooling

1. INTRODUCTION

While considering the mechanical problem of a braking system, the force of friction is the most advisable quantity during the action. The magnitude of total force that opposes motion is influenced by the coefficient of friction, the surface area of a disc remaining in contact with the pad during slipping process and the contact pressure. However, the large amount of heat generated at the pad/disc interface undeniably participates in restriction of the operation range of a brake system. The conditions of friction, in which the critical value of temperature is exceeded, may cause a brake fade, premature wear, thermal cracks, brake fluid vaporization, thermal judder (Gao and Lin, 2002; Gao et al., 2007; Talati and Jalalifar, 2008, 2009). The variety of mechanical, physical and chemical phenomena in the immediate vicinity of contact surface causes difficulties in formulating frictional heating model which would include their sophisticated interactions (Scieszka, 1998).

For the contact temperature evaluation, the amount of kinetic energy is assumed to be entirely converted into thermal energy (Zagrodzki, 1985; Wawrzonek and Bialecki 2008; Grzes, 2009; Grzes, 2010; Adamowicz and Grzes, 2011a, 2011b). For this to happen, the total friction power expressed by the product of friction coefficient, relative linear velocity of the bodies and the contact pressure is applied as the intensity of thermal flux to the surfaces of contact of the friction pair. This approach was implemented by Zagrodzki (1985) to determine the temperature fields and thermal stresses of a multidisc wet clutch after engagement. Two-dimensional model of discs with distributed heat source was used. Thereby the uniform thermal load in the circumference after its separation, set a priori by the heat partition ratio, was applied to the model. In other cases special coefficient determining the energy generated during frictional heating was employed (Scieszka and Zolnier, 2007a, 2007b).

Analytical models of heating process during braking were proposed in monograph by Awrejcewicz and Pyr'yev (2009). Bauzin

and Laraqi (2004) carried out numerical simulation for a problem of sliding contact to calculate the heat flux generated due to friction, the thermal contact conductance and the intrinsic heat partition coefficient. Some analytical models to determine three-dimensional temperature field and the thermal constriction resistance for the problem of moving heat source on semi-infinite bodies were proposed in article by Laraqi et al. (2004).

The heat exchange during the braking process is accomplished by conduction through brake assembly and hub, convection to surrounding air and radiation to adjacent elements. Although conduction is an efficient mode of heat transfer, it may have negative effects, such as brake fluid vaporization or bearing damage (Talati and Jalalifar, 2008, 2009), whereas radiation affects the beading of a tyre.

The finite element analysis of a ventilated disc brake rotor with straight rounded radial vanes, which included macroscopic and microscopic model of frictional heat generation, was developed in article by Talati and Jalalifar (2008). The uniform pressure, as well as the uniform wear conditions, were studied separately for calculation of a boundary heat flux. Empirical correlations were used in order to obtain the heat transfer coefficient. The disc and pad temperature fields versus braking time in axial and radial directions were presented. The convective terms of cooling were concluded to be the most important factors preventing overheating of components of the brake assembly and causing the decrease in friction coefficient.

Adamowicz and Grzes (2011b) studied an influence of convective cooling on three-dimensional temperature fields in a solid disc brake generated during repetitive braking process. The calculations were carried out employing wide range of established a priori values of the heat transfer coefficient of the exposed surfaces of the disc.

The rotational motion of a disc during braking process in relation to stationary pads is a problem of a moving heat source. Non-axisymmetric thermal load of a brake rotor, for the selected spot on the friction surface, causes periodic heating during pad transition and the following cooling phase for each rotation of a wheel

of a vehicle. In order to overcome the difficulties of geometrical scheme of the disc brake system, where the pad is treated as the heat source and is intrinsically a portion of rubbing path in the subsequent moments of time, three-dimensional representation is required. The problem of a moving heat source in relation to disc brake system was studied in a number of articles (Gao and Lin, 2002; Gao et al., 2007; Wawrzonek and Bialecki, 2008; Adamowicz and Grzes, 2011; Scieszka and Zolnierz 2007a, 2007b). The solution of iterative process of disc heating was developed with an assumption of exponential pressure increase and non-linear angular velocity descent, in order to simulate real conditions after the brake engagement, as proposed in study of Gao and Lin (2002). The review of FE modelling techniques of frictional heat generation in disc brakes and clutches was developed in article by Yevtushenko and Grzes (2010).

Belhocine and Bouchetara (2012) analysed three-dimensional temperature field of both solid and ventilated type of a brake disc incorporating three different cast iron materials. The heat transfer coefficient was calculated separately for specified locations on the free surfaces of the disc and implemented to FE element model.

This paper aims to study the influence of convective heat transfer on the transient temperature distributions of a real disc brake. The process of braking was conducted for the braking with constant velocity of the vehicle. The problem of pad transition based code as a moving heat source was developed and transferred into FE model. The determined temperature distributions of a disc during braking were confronted and compared for the cooling influence assessment.

2. HEAT TRANSFER PROBLEM

The disc brake system consists of a rotating disc and fixed pads. When the braking process occurs, the forces that act on pads, oppose the motion of the system. The accumulated amount of kinetic energy is converted into thermal energy at the interface of the connecting parts according to the first law of thermodynamics. The generated heat is dissipated by forced convection due to enlarged airflow and the natural convection after the full stop, whereas conduction absorbs energy from the interface of the friction pair. However the third mode of heat transfer which takes place has an insignificant influence on the temperature distributions, and therefore has been neglected in this study.

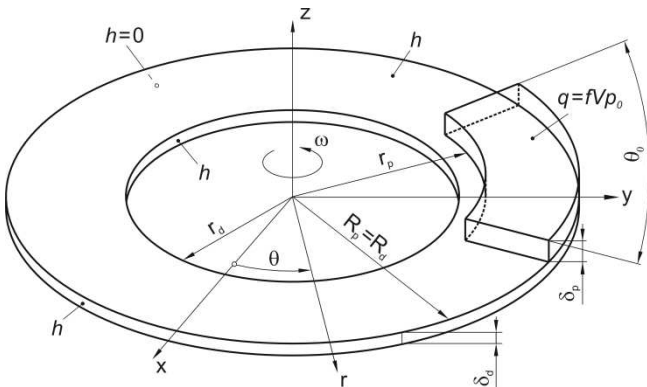


Fig. 1. A schematic diagram of a pad/disc brake system

As for the symmetry of the problem, the analysed region was limited to the half of the entire disc of thickness δ_d and one pad

(Fig. 1). However only disc temperature distributions were analysed. For the purpose of estimating the influence of convective heat exchange mode on the transient temperatures of a disc, two individual cases of braking process were investigated. The first is related to the problem of non-axisymmetric disc heating with the convective terms of cooling and velocity dependent heat transfer coefficient, whereas in the second, exclusively thermal load without convective boundary conditions was applied to the three-dimensional FE model of a disc. It was assumed that the thermo-physical properties of materials are isotropic and independent of temperature (Grzes, 2011b). Such an assumption stems from the fact of relatively low temperature attained in the process. The nominal surface of contact of a disc equals the real surface of contact thereby the contact pressure is uniform at every time t of braking process.

Assuming that the total friction energy is converted into heat, the total intensity of heat flux generated between the pad and the disc is given by $q = fVp_0$, where f is the friction coefficient, V is the sliding velocity, p_0 is the contact pressure. The separation of heat entering the disc and the pad was adjusted by the heat partition ratio calculated as $\gamma = 1/(1+\varepsilon)$ (Charron, 1943, Grzes 2011a), where $\varepsilon = K_d k_p^{1/2} / (K_p k_d^{1/2})$ is the thermal activity coefficient (Luikov, 1968), K is the thermal conductivity, k is the thermal diffusivity, the subscripts p and d denote the pad and the disc, respectively.

The amount of the intensity of heat flux that enters the disc is calculated from the formula:

$$q_d(r, \theta, t) \Big|_{z=0} = (1-\gamma) f p_0 r \omega_0, \quad r_p \leq r \leq R_p, \quad 0 \leq \theta \leq 2\pi, \quad 0 \leq t \leq t_s, \quad (1)$$

and into pad:

$$q_p(r, \theta, t) \Big|_{z=\delta_p} = \gamma f p_0 r \omega_0, \quad r_p \leq r \leq R_p, \quad 0 \leq \theta \leq \theta_0, \quad 0 \leq t \leq t_s, \quad (2)$$

where δ is the thickness, θ_0 is the cover angle of pad, ω_0 is the angular velocity, t is the time, t_s is the braking time, r and R are the internal and external radii, respectively.

Both, the contact pressure p_0 and angular velocity ω_0 are constant during the analysis.

3. MATHEMATICAL PROBLEM

The transient heat conduction equation of the rotating disc for non-axisymmetric problem described in cylindrical coordinate system (r, θ, z) is given as follows (Nowacki, 1962):

$$\frac{\partial^2 T}{\partial r^2} + \frac{1}{r} \frac{\partial T}{\partial r} + \frac{1}{r^2} \frac{\partial^2 T}{\partial \theta^2} + \frac{\partial^2 T}{\partial z^2} = \frac{1}{k_d} \left(\frac{\partial T}{\partial t} + \omega \frac{\partial T}{\partial \theta} \right), \quad (3)$$

$$r_d \leq r \leq R_d, \quad 0 \leq \theta \leq 2\pi, \quad -\delta_d < z < 0, \quad t > 0$$

where T is the temperature, r is the radial coordinate, z is the axial coordinate.

Two separate cases were studied. The first simulated the process of real braking with constant velocity, therefore the following boundary conditions including convective mode of heat transfer were established:

- the surface placed in the disc's mid-plane of symmetry – adiabatic condition;

- the internal cylindrical surface, the contact surface free from frictional heating (out of pad contact area), and the external cylindrical surface of a disc – convective cooling terms;
- the contact surface under relative transition of a pad – portion of the total intensity of the heat flux calculated from the known quantity of heat rate, applied as the plane heat source acting with calculated value for the respective elements of the mesh (equation (1)).

$$K_d \frac{\partial T}{\partial z} \Big|_{z=0} = q_d(r, \theta, t), \quad r_p \leq r \leq R_p, \quad 0 \leq \theta \leq 2\pi, \quad 0 \leq t \leq t_s, \quad (4)$$

$$K_d \frac{\partial T}{\partial z} \Big|_{z=0} = h[T_a - T(r, \theta, t)], \quad r_d \leq r \leq r_p, \quad 0 \leq \theta \leq 2\pi, \quad z = 0, \quad t \geq 0, \quad (5)$$

$$K_d \frac{\partial T}{\partial r} \Big|_{r=R_d} = h[T_a - T(\theta, z, t)], \quad r = R_d, \quad 0 \leq \theta \leq 2\pi, \quad -\delta_d \leq z \leq 0, \quad t \geq 0, \quad (6)$$

$$K_d \frac{\partial T}{\partial r} \Big|_{r=r_d} = h[T(\theta, z, t) - T_a], \quad r = r_d, \quad 0 \leq \theta \leq 2\pi, \quad -\delta_d \leq z \leq 0, \quad t \geq 0, \quad (7)$$

$$\frac{\partial T}{\partial z} \Big|_{z=-\delta_d} = 0, \quad (r, \theta, z), \quad r_d \leq r \leq R_d, \quad 0 \leq \theta \leq 2\pi, \quad z = -\delta_d, \quad t \geq 0, \quad (8)$$

$$T(r, \theta, z, 0) = T_0, \quad r_d \leq r \leq R_d, \quad 0 \leq \theta \leq 2\pi, \quad -\delta_d \leq z \leq 0, \quad (9)$$

where T_a is the ambient temperature, h is the heat transfer coefficient.

For the second case, unlike the previous case, the thermal insulation was applied on every surface of convective heat exchange. However such an assumption does not correspond with the real conditions of braking process, in this study it is used primarily to confront contrasting terms and to answer whether the average constant heat transfer coefficient is sufficiently precise assumption for single braking.

In order to formulate the following matrix form of the equation (3) the Galerkin method was employed:

$$[C] \frac{d\{T\}}{dt} + [K]\{T\} = \{R\} \quad (10)$$

where $[C]$ is the matrix of heat capacitance, $\{T\}$ is the matrix of temperature at grid points, $[K]$ is the matrix of thermal conductance, $\{R\}$ is the matrix of applied thermal loads.

In order to solve equation (10) Crank-Nicolson method was used. Based on the assumption that temperature $\{T\}_t$ and $\{T\}_{t+\Delta t}$ at time t and $t + \Delta t$ respectively, the following relation is specified:

$$\frac{1}{\Delta t} [\{T\}_{t+\Delta t} - \{T\}_t] = (1 - \beta) \left\{ \frac{dT}{dt} \right\}_t + \beta \left\{ \frac{dT}{dt} \right\}_{t+\Delta t} \quad (11)$$

Substituting equation (11) to equation (10) we get the following implicit algebraic equation:

$$([C] + \beta \Delta t [K]) \{T\}_{t+\Delta t} = ([C] - (1 - \beta) [K] \Delta t) \{T\}_t + (1 - \beta) \Delta t \{R\}_t + \beta \Delta t \{R\}_{t+\Delta t} \quad (12)$$

where β is the factor which ranges from 0.5 to 1 and is given to determine an integration accuracy and stable scheme.

4. CONVECTIVE HEAT TRANSFER

Since the forced convection takes place on the contact surface during every rotation of a disc (out of pad area on the rubbing path) as well as on the cylindrical external and internal surface (Fig. 2), the convective heat transfer coefficient h is of the form $h = K \text{Nu} / r$, where r is the radial location, which denotes mean radius of the friction surface, Nu is the Nusselt number, K is the thermal conductivity of surrounding air.

Furthermore the Nusselt number is related to dimensionless Reynolds number Re and Prandtl number Pr evaluated from the expression (MSC NASTRAN THERMAL, MSC Software Corporation) $\text{Nu} = 0.0267 \text{Re}^{0.8} \text{Pr}^{0.6}$ where Reynolds number is given by $\text{Re} = \rho \omega r^2 / \mu$ where ρ is the density, μ is the dynamic viscosity, and Prandtl number is given as $\text{Pr} = c \mu / K$, where c is the specific heat capacity.

The natural convection may affect the convective heat transfer coefficient when the forced convection is relatively weak. The influence of mixed convection was neglected according to the condition given by Mills A. F. (1995):

$$\text{Re}_D < 4.7 \left(\frac{\text{Gr}_D^3}{\text{Pr}} \right)^{0.137} \quad (13)$$

where Re_D and Gr_D are Reynolds and Grashof number for linear element with dimension D , respectively.

5. NUMERICAL ALGORITHM TO EVALUATE TEMPERATURE ON THE CONTACT SURFACE OF THE DISC

During mutual slipping process of the rotational rotor over the immovable pads, the inboard and outboard surface of a disc is subjected to non-axisymmetric thermal load. In case of braking with constant velocity (such as mountain descent), time of every rotation of the disc is equal in relation to a specific spot on the circumference within the contact region. Two phases – heating and cooling – may be distinguished. The heating time equals $\theta_0/360^\circ$ of time of one rotation of the wheel, whereas cooling phase equals $1 - \theta_0/360^\circ$ of time of one rotation.

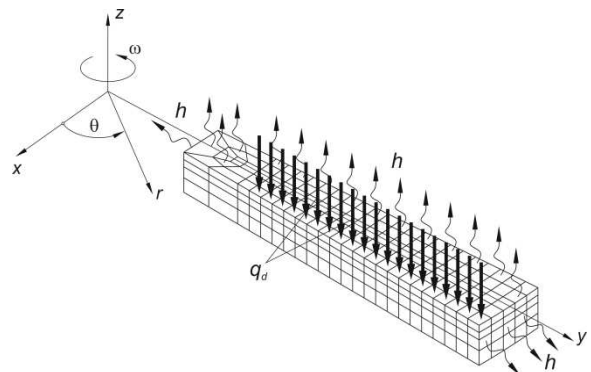


Fig. 2. A 1/72 section of FE model of disc with boundary conditions

In the present thermal finite element analysis, the boundary intensity of heat flux, as well as cooling terms, are calculated individually for every element mesh (regarding radial location) for the specific time t . For the convenience purposes the heat exchange through forced convection was assumed to be independent of the radius within the range of maximal and minimal radius of the pad (mean radius of friction surface r_m was considered).

The numerical algorithm was accomplished by the boundary conditions formulation. The segment of final mesh with moving heat source, accomplished by the thermal flux (pad) entering the disc is shown in Fig. 2. The intensity of heat flux as well as the convective terms are interchangeably calculated within the region of contact surface. Furthermore, to obtain the effect of gradual covering of every element of the mesh on the disc contact surface, specific evolution of the intensity of heat flux was applied by the use of specific boundary conditions. For the second case, in which the adiabatic boundary conditions replace the convective heat transfer, the same algorithm was implemented.

6. FE DISCRETIZATION

In order to calculate the temperature distributions of the disc brake, appropriate mesh division regarding respective coordinates of the model is essential. High temperature gradients require very fine mesh, therefore in the area adjacent to the contact surface, lower dimension of the elements was employed. Nonetheless, for the purpose of validation of the final mesh use, tests of different grids of elements for every direction, with the speed of the vehicle of 25 km/h, were developed. The final mesh consists of 43 200 eight-node hexagonal elements and 33 693 nodes (360 elements in the circumference, 4 in the axial direction, and 20 in the radial direction – Fig. 2). As the temperature gradients in region beneath friction surface were relatively low, the mesh division was of “paver” type (irregular).

7. RESULTS AND DISCUSSION

The 3D finite element analysis of the transient temperature field of the disc for heat conduction problem was conducted. The computations were carried out comprising two different phases. The first is the continuous braking process with the constant velocity lasting $t = 3.96$ s, whereas the second concerns the cooling of the brake system after brake release ($t = 296.04$ s) which is shown in Fig. 3. The thermophysical material properties, dimensions, and parameters of the operation including different values of convective heat transfer coefficient are given in Tab. 1. Because of the magnitude of the obtained differences of temperatures in the model where the convective heat exchange was applied as well as the case with thermally insulated surface out of pad domain, the presentation of the results is restricted exclusively to the friction surface of a disc.

Fig. 4 shows the variations of temperature on the contact surface of a disc at the mean radius of 95 mm during braking with constant velocity, until the moment of brake release. Obviously higher velocity with the same rate thermal load results in higher temperature at every moment of braking. It may be observed that the differences of the temperatures between subsequent velocities for both definite types of heat transfer at the end of braking are of the same range, which indicate their linear dependence.

However, as the cooling impact on the temperature of pad/disc interface appeared insignificant, the areas comprising the moment before the last entire pad transition was enlarged for the purpose of clarity. The highest obtained temperature difference regarding the model with and without convective cooling appeared for the velocity of 100 km/h and equals 1.48°C.

Tab. 1. Thermophysical properties of materials, operation parameters and dimensions of the disc and the pad (Talati and Jalalifar, 2009)

Items	Disc		Pad	
thermal conductivity, K [W/(mK)]		43		12
specific heat capacity, c [J/(kgK)]		445		900
density, ρ [kg/m ³]		7850		2500
inner radius, r [mm]		66		76.5
outer radius, R [mm]		113.5		
cover angle of pad, θ_0 [deg]				64.5
thickness, δ [mm]		5.5		10
radius of the wheel, R_w [mm]		314		
velocity of the vehicle, V_0 [km/h]	100	75	50	25
heat transfer coefficient, h [W/(m ² K)]	35.5	28.2	20.4	11.7
pressure, p_0 [MPa]		3.17		
coefficient of friction, f		0.5		
initial temperature, T_0 [°C]		20		
ambient temperature, T_a [°C]		20		

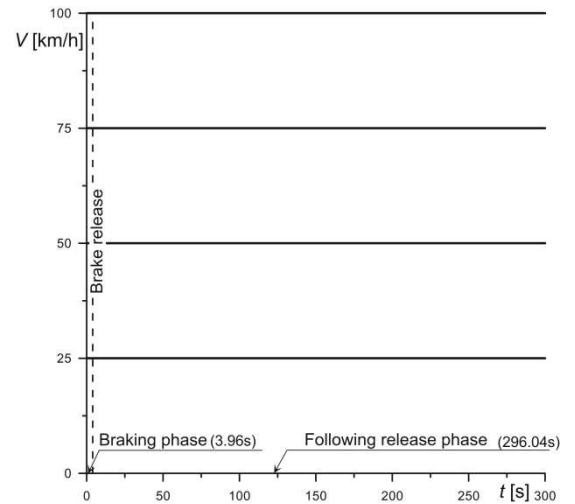


Fig. 3. Scheme of four cases of braking and the following release phases

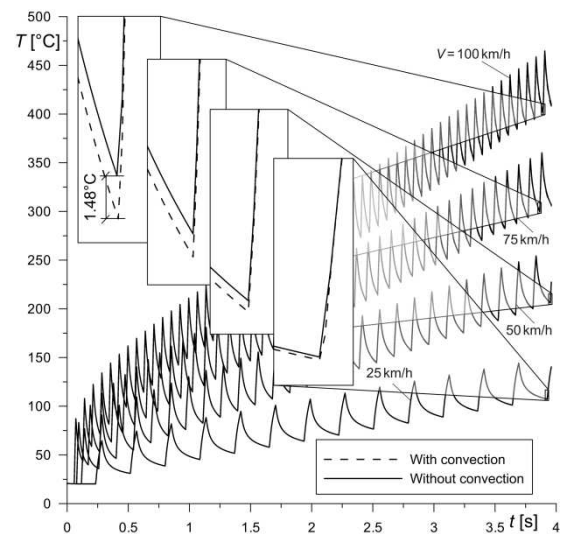


Fig. 4. Evolutions of temperature on the contact surface of a disc at the mean radius of the rubbing path

The comparison of temperature evolutions extended to the succeeding cooling periods after the brake release is shown in Fig. 5. It may be observed that the time significantly affects the temperature values after the phase of heating. As the adiabatic conditions (solid lines) on the friction surfaces were established, the temperature of the entire model equalize after the time of about 50 s. This phenomenon is observable for each of the presented velocities. Furthermore, the same order of temperatures at the end of simulated process ($t = 300$ s) regarding subsequent velocities of 25, 50, 75 and 100 km/h presented in Fig. 4, is evident. Nonetheless, convective terms on all of the surfaces of disc, apart from inner cylindrical surface, result in irregular decrease in the temperatures.

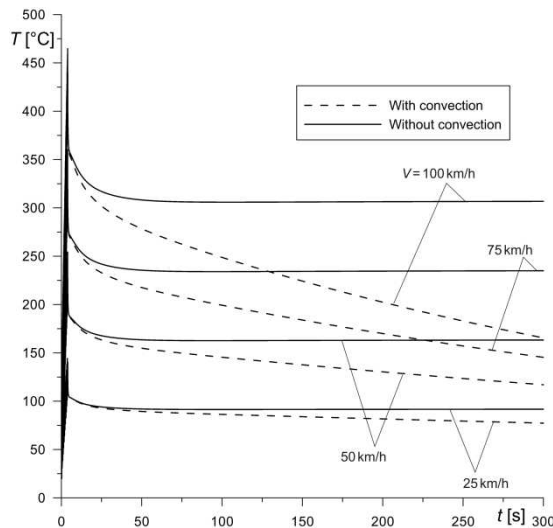


Fig. 5. Evolutions of temperature on the contact surface of a disc for the mean radius

It may be explained by the influence of convective boundary condition which includes the temperature difference multiplied by convective heat transfer coefficient h . Both of the factors correspond to the velocity of the vehicle. Obviously, if the temperature difference is greater, more intense cooling takes place.

The relationship between the braking time and the temperature on the chosen circumferential location $\theta = 0^\circ$ on the contact surface of a disc brake for the velocity of 100 km/h is shown in Fig. 6. Both, temperature of the case with established convective terms dependent on the velocity (dashed lines) and fully adiabatic conditions (solid lines) are confronted for corresponding radial locations. The obtained results for the operation conditions simulating real process of braking during mountain descent reveal that the influence of convective heat transfer is very low. The corresponding temperatures for the maximal radius of the contact surface $r = 113.5$ mm at the end of operation results in difference of 3.97°C . However, the decrease in temperature difference with the decrease in a radius (enlarged area of the radial position of 113.5 and 95 mm) is observable, which is accounted directly by the expression of the convective heat flux. The even increase in temperature without phases of heating and cooling is observable at the radial location of 66 mm, which indicate insignificant influence of pad transition on the surface out of the rubbing path.

Fig. 7 depicts the temperature evolutions on the contact surface for circumferential position $\theta = 0^\circ$ during braking and after brake release. Four specific radial locations present correspond-

ing values of transient temperature in two cases of three-dimensional FE model. The first, where the convection is taken into account, and the second without influence of cooling. It may be observed that after a certain time – about $t = 100$ s, the temperatures for every radius on friction surface of the case with adiabatic condition on the surfaces free from cooling, equalize ($T = 306.7^\circ\text{C}$) and remain on the same level until time of end of the process $t = 300$ s, whereas the case with convective heat exchange reveals their gradual decrease, however equal on each radial position. As can be seen the temperature at the end of cooling phase equals approximately $T = 165^\circ\text{C}$.

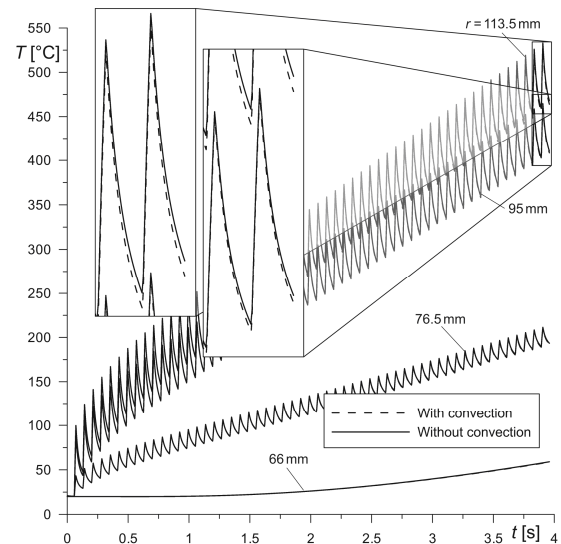


Fig. 6. Evolution of temperature on the contact surface of a disc during braking with the velocity of 100 km/h

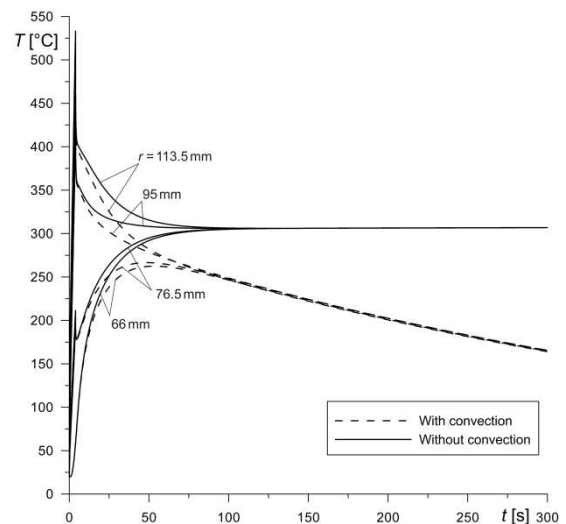


Fig. 7. Evolution of temperature on the contact surface of a disc during braking with the velocity of 100 km/h and after brake release

8. CONCLUSIONS

The aim of this paper was to investigate the temperature distributions caused by the process of braking of a common passenger vehicle with a special emphasis placed on the influence of convective heat exchange from surfaces free from heating.

The obtained results support the claim that in terms of single braking process for the specified dimensions and thermophysical properties of materials the convective heat transfer mode doesn't allow to significantly lower the temperatures of the rotor. The temperature of two studied types of disc brakes almost coincide at every instant of time during short braking period. However the following release period after the braking action when the velocity of the vehicle remains on the same level, results in considerable decrease in temperature. The temperature difference between the case with established convective terms dependent on the velocity and fully adiabatic conditions lowers with the decrease in the velocity.

REFERENCES

1. Adamowicz A., Grzes P. (2011a), Analysis of disc brake temperature distribution during single braking under non-axisymmetric load, *Applied Thermal Engineering*, Vol. 31, No. 6–7, 1003–1012.
2. Adamowicz A., Grzes P. (2011b), Influence of convective cooling on a disc brake temperature distribution during repetitive braking, *Applied Thermal Engineering*, Vol. 31, No. 14–15, 2177–2185.
3. Awrejcewicz J., Pyr'yev Yu. (2009), *Nonsmooth dynamics of contacting thermoelastic bodies*, Springer-Verlag, New York.
4. Bauzin J.-G., Laraqi N. (2004), Simultaneous estimation of frictional heat flux and two thermal contact parameters for sliding contacts, *Numerical Heat Transfer, Part A: Applications*, Vol. 45, No. 4, 313–328.
5. Belhocine A., Bouchetara M. (2012), Thermal analysis of a solid brake disc, *Applied Thermal Engineering*, Vol. 32, 59–67.
6. Charron F. (1943), Partage de la chaleur entre deux corps frottants, *Publ. scient. et techn. Ministère air.*, No. 182.
7. Gao C. H., Huang J. M., Lin X. Z., Tang X. S. (2007), Stress analysis of thermal fatigue fracture of brake disks based on thermomechanical coupling, *ASME Journal of Tribology*, Vol. 129, No. 3, 536–543.
8. Gao C. H., Lin X. Z. (2002), Transient temperature field analysis of a brake in a non-axisymmetric three-dimensional model, *Journal of Materials Processing Technology*, Vol. 129, No. 1-3, 513–517.
9. Grzes P. (2009), Finite element analysis of disc temperature during braking process, *Acta Mechanica et Automatica*, Vol. 3, No. 4, 36–42.
10. Grzes P. (2010), Finite element analysis of temperature distribution in axisymmetric model of disc brake, *Acta Mechanica et Automatica*, Vol. 4, No. 4, 23–28.
11. Grzes P. (2011a), Partition of heat in 2D finite element model of a disc brake, *Acta Mechanica et Automatica*, Vol. 5, No. 2, 35–41.
12. Grzes P. (2011b), Influence of thermosensitivity of materials on the temperature of a pad/disc system, *Acta Mechanica et Automatica*, Vol. 5, No. 4, 46–53.
13. Holman J. P. (1990), *Heat Transfer*, McGraw-Hill, Inc.
14. Laraqi N., Bairi A., Ségui L. (2004), Temperature and thermal resistance in frictional devices, *Applied Thermal Engineering*, Vol. 24, No. 17–18, 2567–2581.
15. Luikov A. V. (1968), *Analytical heat diffusion theory*, Academic Press, New York.
16. Mills A. F. (1995), *Heat and Mass Transfer*, Richard D. Irwin Inc, Chicago.
17. Nowacki W. (1962), *Thermoelasticity*, Pergamon Press, Oxford.
18. Scieszka S. F. (1998), *Hamulce cieme. Zagadnienia konstrukcyjne, materiałowe i tribologiczne*, WZP – IteE, Radom.
19. Scieszka S., Zolnierz M. (2007a) The effect of the mine winder disc brake's design feature on its thermoelastic instability. Part I. Set-up for finite element modelling and numerical model verification, *Problems of Machines Operation and Maintenance* Vol. 42, No. 3, 111–124.
20. Scieszka S., Zolnierz M. (2007b), The effect of the mine winder disc brake's design feature on its thermoelastic instability. Part II. Finite element simulation, *Problems of Machines Operation and Maintenance* Vol. 42, No. 4, 183–193.
21. Talati F., Jalalifar S. (2008), Investigation of heat transfer phenomena in a ventilated disk brake rotor with straight radial rounded vanes, *Journal of Applied Sciences*, Vol. 8, No. 20, 3583–3592.
22. Talati F., Jalalifar S. (2009), Analysis of heat conduction in a disk brake system, *Heat Mass Transfer*, Vol. 45, No. 8, 1047–1059.
23. Wawrzonek L., Bialecki R. A. (2008), Temperature in a disk brake, simulation and experimental verification, *International Journal of Numerical Methods for Heat & Fluid Flow*, Vol. 18, No. 3–4, 387–400.
24. Yevtushenko A., Grzes P. (2010), FEM-modeling of the frictional heating phenomenon in the pad/disc tribosystem (a review), *Numerical Heat Transfer Part A*, Vol. 58, No. 3, 207–226.
25. Zagrodzki P. (1985), Numerical analysis of temperature fields and thermal stresses in the friction discs of a multidisc wet clutch, *Wear*, Vol. 101, No. 3, 255–271.

The work is based on the calculations presented at the 19th International Conference on Computer Methods in Mechanics, CMM 2011, May 9-12, 2011, Warsaw, Poland and is supported by the Białystok University of Technology under the research project No. WWM/11/2011.

DESIGN AND SIMULATIONS OF WHEEL-LEGGED MOBILE ROBOT

Jacek BAŁCHANOWSKI*, Antoni GRONOWICZ*

*Institute of Machine Design and Operation, Mechanical Department, Wrocław University of Technology,
ul. Łukasiewicza 7/9, 50-371 Wrocław, Poland

jacek.balchanowski@pwr.wroc.pl, antoni.gronowicz@pwr.wroc.pl

Abstract: The problems of determining dynamic and kinematic parameters of wheel-legged mobile robot were considered in the paper. The numerical computer model of robot was worked out and simulation researches of suspension were completed. The motion of wheel on road with obstacles and walking motion of wheel were analyzed for determining kinematic and dynamic parameters.

Key words: Mobile Robots, Wheel-Legged Robots, Computer Simulation

1. INTRODUCTION

The demands of today's world, the need for automating transport processes and the necessity of inspecting explosion hazard areas or chemically or biologically contaminated areas necessitate the use of automatic vehicles, i.e. mobile robots (Trojnecki et al., 2008).

Mobile robots have been the subject of research at many (university, military and industrial) research centres. The research covers wheeled robots, walking robots, tracked robots, crawling robots, flying robots, floating robots, and their hybrids. As a result of the research many varieties of such vehicles, differing in their way of travel: wheeled systems (WalkPartner (Halme 2003)), tracked systems (INSPECTOR Robot (Holdanowicz 2008)), walking systems (PetMan (Boston Dynamics)), floating systems and flying systems (Hermes® 900 (Elbit Systems)), have been created.

The problems investigated in the research centres relate to the design of the particular mechanical assemblies, the control systems and the sensor systems, the modelling of kinematics and dynamics and the potential application of the proposed solutions (Tchoń et al., 2000, Zielińska 2003).

Today vehicles mainly move on wheels. Wheeled solutions are most effective on smooth surfaces in urbanized areas, but their drawback is that they are unable to negotiate obstacles in the form of base discontinuities, such as curbs, stairs and sharp dips.

The commonest form of locomotion of living organism on the surface of the earth is walking. This kind of locomotion is especially effective for moving in unurbanized terrain with an irregular ground with obstacles.

One of the trends in mobile robot design are hybrid wheel-legged robots. Such robots combine efficient travel on wheels in flat terrain with the capability of surmounting obstacles by walking. Owing to its hybrid structure the robot is capable of higher speeds on a suitable base and when it encounters an obstacle which cannot be driven over, the robot moves by walking.

A robot of this kind is being designed and built as part of a research project funded from the financial resources for science (Bałchanowski and Gronowicz 2009). This paper presents the structure of the computational models used and the results of the

simulations run. A special focus is on developing an algorithm for robot walking and on simulation studies of robot travel in terrain with obstacles.

2. DESIGN OF WHEEL-LEGGED ROBOT

As part of the project a wheeled-walking robot design, shown schematically in Fig. 1, has been created. When designing the robot a major challenge was to design a wheel suspension system enabling the robot to both move on wheels and walk. The wheel suspension is a complex mechanism with four degrees of freedom relative to the robot's chassis. The mechanism, shown schematically in Fig. 2, must steer the wheel in such a way that it can run (roll and turn – 2 DOF) and walk (be lifted and protruded – 2 DOF) (Bałchanowski 2012, Sperzyński 2010).

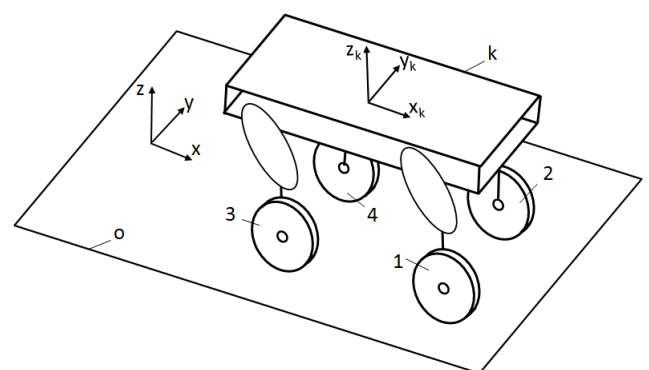


Fig. 1. The general scheme of wheel-legged robot (1 ÷ 4 – wheel suspensions, o – ground, k – robot's chassis)

As a result of the studies a suspension structure was designed and then its basic dimensions were matched through geometric synthesis (Sperzyński et al., 2010). The fundamental assumption in the design of the suspension structure was that a single drive would effect the particular wheel movements (the lifting, protruding, turning and rolling of the wheel), which would

simplify the steering system design and facilitate steering.

The next step was to design the wheel-legged robot structure. It was assumed that the wheels would be symmetrically arranged relative to both the axis of travel and the chassis's lateral axis. This arrangement of the wheels ensures identical travel conditions for going forward and backward. Fig. 3 shows the right side of the robot and a kinematic scheme of suspensions of wheels 1 and 3.

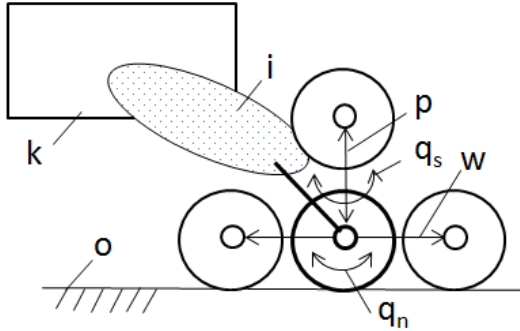


Fig. 2. Schematic diagram of suspension of robot's wheel i (p – lifting, w – protruding, q_n – rolling, q_s – turning)

The robot is designed for inspection work both outdoors and indoors (e.g. in buildings, production halls, etc.). Since it is to move inside rooms, pass through typical doorways (less than 0.9 m wide) and be able to surmount an obstacle with a height equal to that of a typical stair step (the wheel lifting height greater than 0.2 m) its overall dimensions had to be limited.

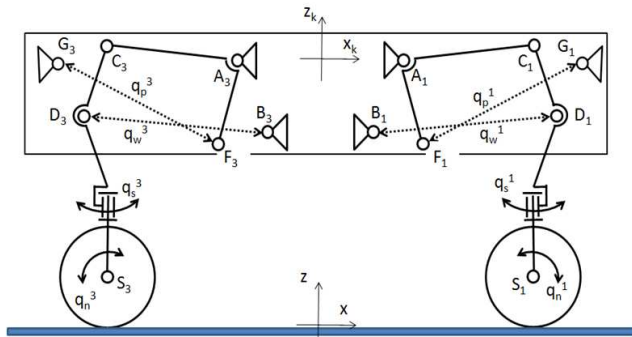


Fig. 3. The kinematic scheme of right side wheel-legged robot (view of suspensions of wheels 1 and 3)

Tab. 1. Main geometrical parameters of wheel 1 suspension

Name	Value	Name	Value	Name	Value
x_{A1}	0.11 m	y_{A1}	-0.65 m	z_{A1}	0 m
x_{B1}	-0.04 m	y_{B1}	-0.65 m	z_{B1}	-0.152 m
x_{G1}	0.518 m	y_{G1}	-0.65 m	z_{G1}	0.005 m
D_1S_1	0.353 m	A_1F_1	0.17 m	A_1C_1	0.303 m
C_1S_1	0.5 m	C_1D_1	0.162 m		



The suspension system's design and basic dimensions are such that the lift and protrusion (walking) motions can be effected by linear drives, i.e. electric actuators LINAK LA36. Solid rubber-steel wheels with a motor and a gear integrated with the hub (GOLDENMOTOR HUB24E) were chosen for the travelling drive. Tab. 1 shows the main geometrical parameters of the suspension

of wheel 1. The main specifications of the wheel drives and the lift and protrusion actuators are shown in Tab. 2.

3. COMPUTATIONAL MODEL OF WHEEL-LEGGED ROBOT

In order to carry out simulation studies, a computational model of the robot (Fig. 4) was created in the LMS DADS (Haug1989) system for dynamic analysis. The robot has 22 DOF, each wheel suspension having 4 DOF relative to the body and the latter having 6 DOF relative to the ground.

Tab. 2. Main specifications of drives

Actuator LINAK LA36		
	q_w, q_p (stroke length)	0.35-0.5 m
	v_w, v_p (speed)	0.068 m/s
	F_w, F_p (Force)	1700 N
	m_s (mass)	4.9 kg
Wheel GOLDENMOTOR HUB24		
	dq_n/dt (angular velocity)	13.08 rad/s (125 rpm)
	M_n (nominal Torque)	13.5 Nm
	k_r (radial stiffness)	$9.5 \times 10^5 \text{ N/m}$
	m_k (mass)	5 kg
	r_k (radius of wheel)	0.105 m

Sixteen kinematic excitations: 8 rotational excitations q_n^i and q_s^i (wheel rolling and turning) and 8 linear excitations q_p^i and q_w^i (wheel lifting and protruding), for each suspension i ($i = 1 \div 4$) were defined in the robot.

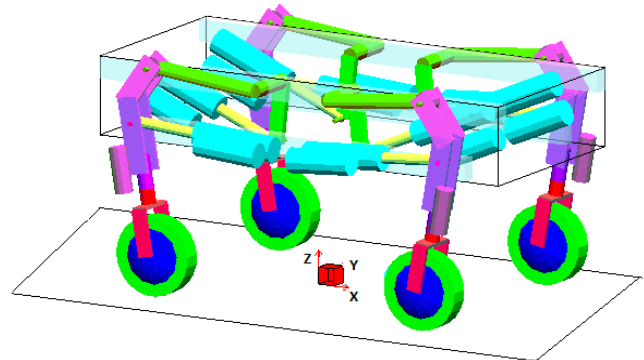


Fig. 4. General view of wheel-legged robot computer model

The wheel/base interactions were modelled using a tyre / ground interaction force model (TIRE). The mass of the wheels is quite large due to the fact that a motor and a gear are incorporated into the hub, and because of their high radial and longitudinal stiffness (Tab. 2).

The total weight (the deadweight + the payload) of the wheeled-legged robot was estimated at 100 kg. The mass and geometry of the suspension, wheel and actuator members were assumed as in the design. The body's weight (comprising the deadweight of the frame bearer, the steering system, the batteries and the current generator, and the payload) was appropriately matched to obtain the robot's assumed total weight of 100 kg, with the centre of gravity located in the body's centre.

4. SIMULATIONS OF WHEEL-LEGGED ROBOT

Computer simulations are run in order to study the behaviour of a system while it performs the working motions and to determine the main kinematic and dynamic parameters. Through computer simulations one can determine the validity of the structure being created when the latter is at a virtual prototype stage.

As part of this research the travelling of the robot on a ground with an obstacle was studied. The dimensions of the obstacle placed on the track are such that the obstacle has to be surmounted by walking. Walking becomes necessary when the obstacle's height h_p is larger than the wheel's radius r_k .

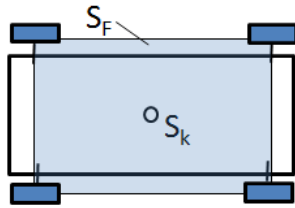


Fig. 5a. Robot stability field S_F for four-wheel support

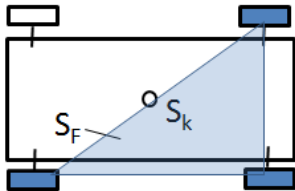


Fig. 5b. Robot stability field S_F for three-wheel support

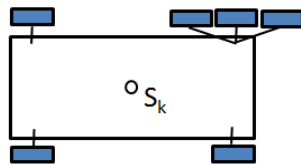


Fig. 5c. Examples of wheel position change effected by changing settings of protrusion actuator q_p

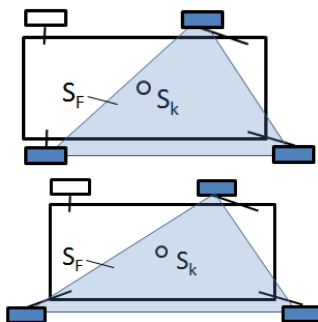


Fig. 5d. Robot stability field S_F for three-wheel support for two wheel protrusion

When performing the walking motion the wheel is lifted by lift actuator q_p and moved into a position above the obstacle by protrusion actuator q_w . During this motion the wheel loses contact with the base, as a result of which the number of the robot's points

of support changes from four to three whereby the shape of the system's stability field S_F changes.

When robot rests on its four wheels the system's stability field S_F is quadrangular with gravity centre S_k (Fig. 5a) lying in the centre of the quadrangle. When one of the wheels is lifted, the robot's stability field S_F is triangular with gravity centre S_k situated on the stability boundary (Fig. 5b). This position does not ensure the system's stability during walking and the robot may overturn. In order to ensure the operation of the system is stable one should change the locations of the robot's points of support to enlarge stability zone S_F . This can be achieved through protrusion motions q_p^i of individual wheels i (Fig. 5c). The possibilities of changing the area of stability zone S_F when wheel 4 is lifted are shown in Fig. 5d.

The fundamental problem in negotiating an obstacle by walking is to program the walking in such a way that when the successive wheels are lifted in the course of surmounting the obstacle the stability of the robot is always ensured.

The lifting of the chassis relative to the ground is used to adjust the body's working elevation h_k relative to the ground during robot travel, i.e. to adjust the clearance under the robot. The clearance is usually set before travel. For travelling at the maximum speed the robot's clearance is set to minimum ($h_k^{\min} = 0.3$ m) whereby the system's centre of gravity is situated low (as shown in Fig. 6). For travelling in terrain with obstacles the chassis is maximally lifted ($h_k^{\max} = 0.52$ m). The nominal working chassis elevation setting is $h_k = 0.41$ m. Lifting height h_k is effected by lift actuator q_p .

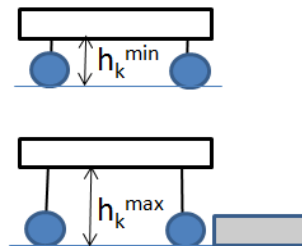


Fig. 6. View of robot for two variants of body position above base

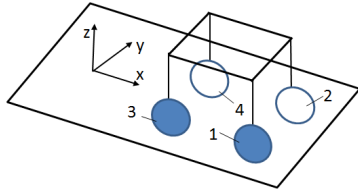
Wheel separation from the ground is effected by lift actuator q_p^i which lifts one of the wheels while the position of the other three wheels remains fixed. The robot can lift the wheel to height $h_s = 0.25$ m. This height can be achieved only at the maximum body elevation. The obstacle to be negotiated by the robot cannot be higher than 0.25 m.

The obstacle negotiation procedure consists of many stages which can be summarized in the form of the following algorithm:

1. the robot's front wheels move up to the obstacle.
2. the robot's chassis is maximally lifted.
3. the stability field is set for wheel 1 to be lifted.
4. wheel 1 is lifted and moved into a position above the obstacle.
5. the stability field is set for wheel 2 to be lifted.
6. wheel 2 is lifted and moved into a position above the obstacle.
7. the robot's rear wheels move up to the obstacle.
8. the stability field is set for wheel 3 to be lifted.
9. wheel 3 is lifted and moved into a position above the obstacle.
10. the stability field is set for wheel 4 to be lifted.
11. wheel 4 is lifted and moved into a position above the obstacle.
12. the stability field is set for the four-wheel support.
13. the body is set to the working elevation.

The particular stages in walking over an obstacle are shown in Figs 7a and 7b.

The following were simulated: the approach of the robot to an obstacle with height $h_p = 0.15$ m and length $l_p = 2$ m, its ascent of the obstacle by walking, its drive on the obstacle and rapid descend (without walking) from it. A schematic of the simulation is shown in Fig. 8. The total motion time is $t = 24$ s. The robot approaches the obstacle and drives on it at body speed $v_k = 1$ m/s.



Rys. 7a. Schematic diagram of wheel-legged robot
 (blue wheels right side, white wheels left side)

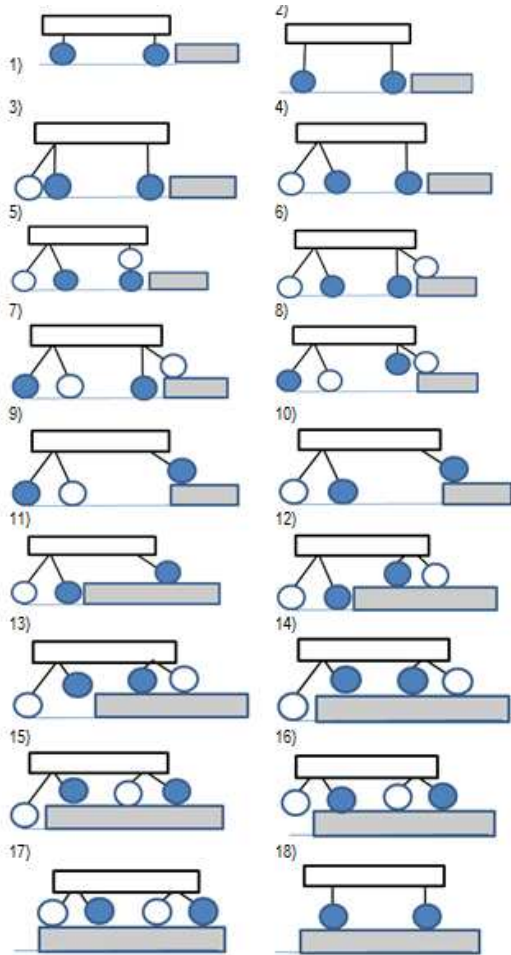


Fig. 7b. Procedure for obstacle negotiation by wheel-legged robot

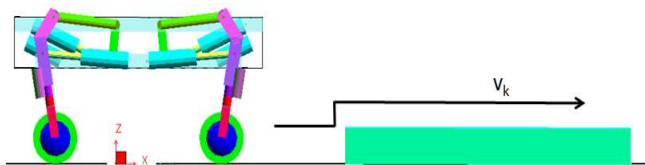


Fig. 8. Schematic of simulation of robot travel on base with obstacles

Figs. 9-16 show the results of the computations. Fig. 9 shows the changes in the location of robot's chassis centre S_k (coordinates x, z). The diagrams in Fig. 10 show the changes in the height of the centres of the robot's (the left side) wheels 1 and 3 during its motion. One can clearly distinguish the particular stages in robot travel: $t = 0-2.0$ s – the approach to the obstacle. $t = 3.0$ s – the beginning of walking. $t = 16.0$ s – the end of walking (the robot is on the obstacle). $t = 16.0-18.9$ s – the drive on the obstacle. $t = 18.9$ s – the front wheels begin to fall from the obstacle. $t = 22.12$ s – the rear wheels begin to fall from the obstacle.

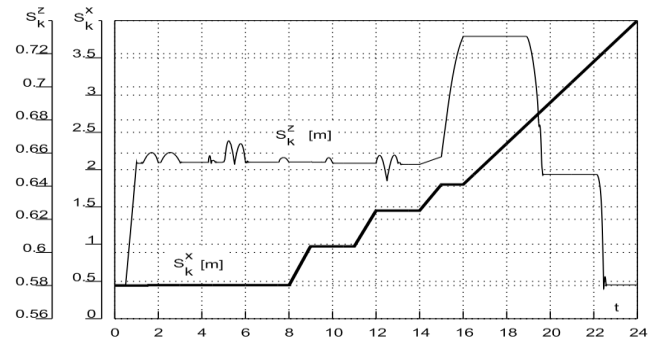


Fig. 9. Changes in location S_k^x, S_k^z of robot's chassis centre during robot travel

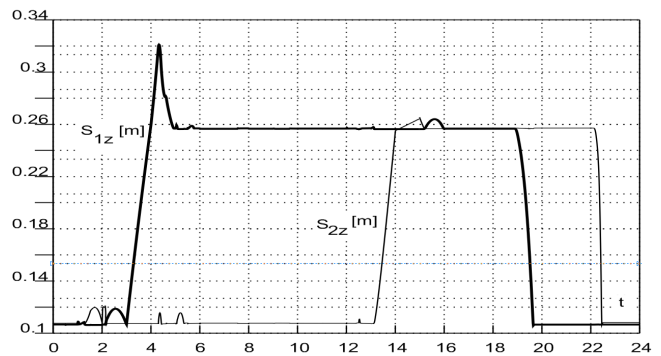


Fig. 10. Changes in height S_1^z, S_3^z of centres of wheels 1 and 3

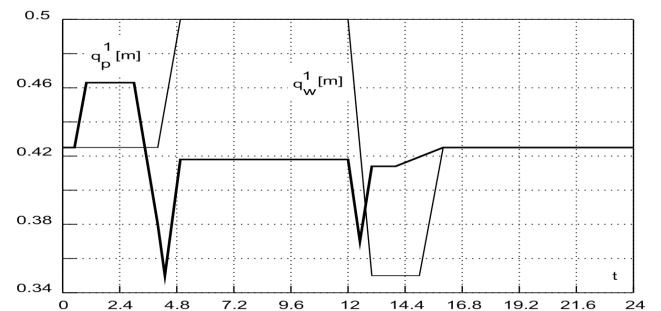


Fig. 11. Diagrams of lift q_p^1 and protrusion q_w^1 excitations for (front right) suspension 1

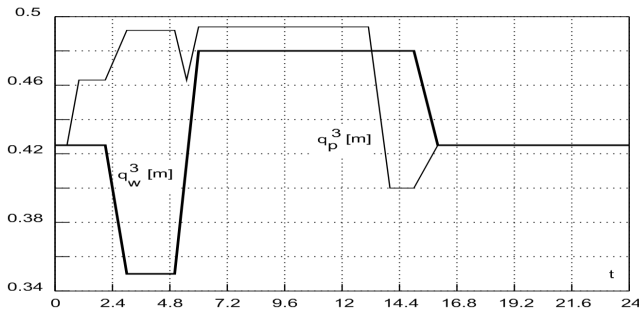


Fig. 12. Diagrams of lift q_p^3 and protrusion q_w^3 excitations for (rear right) suspension 3

The changes in lift excitations q_p and protrusion excitations q_w for suspensions 1 and 3 (the robot's right side) are shown in Figs. 11 and 12. The excitations are responsible for the performance of the particular walking stages according to the algorithm shown in Fig. 7. Active lifting forces F_p and active protrusion forces F_w for (front left) suspension 2 are shown in Figs. 13 and 14.

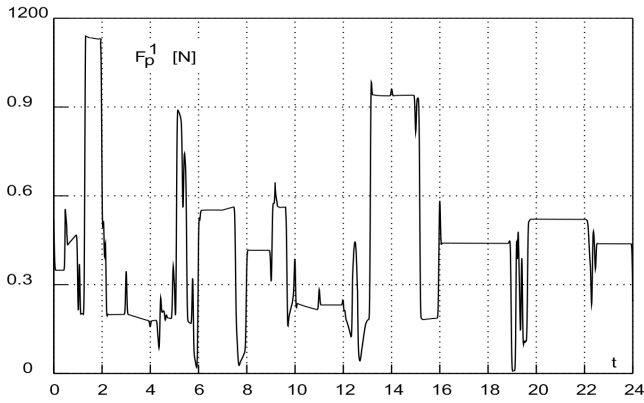


Fig. 13. Diagram of active force F_p^1 in lift actuator in (front right) suspension 1

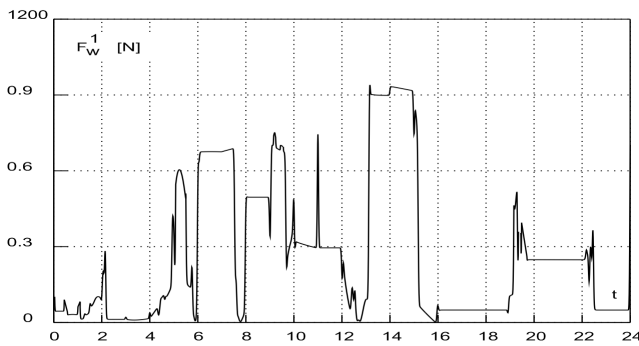


Fig. 14. Diagram of active force F_w^1 in protrusion actuator in (front right) suspension 1

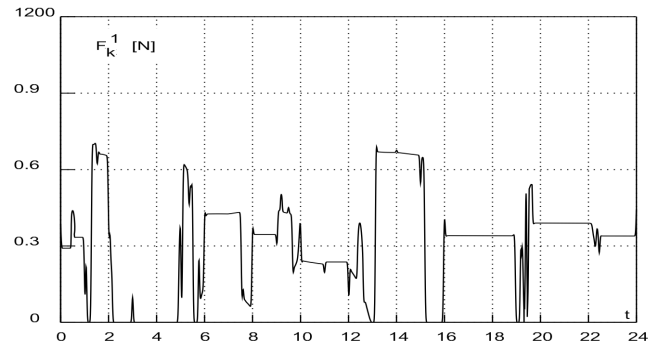


Fig. 15. Diagram of (front left) wheel 1 and base interaction forces F_k^1

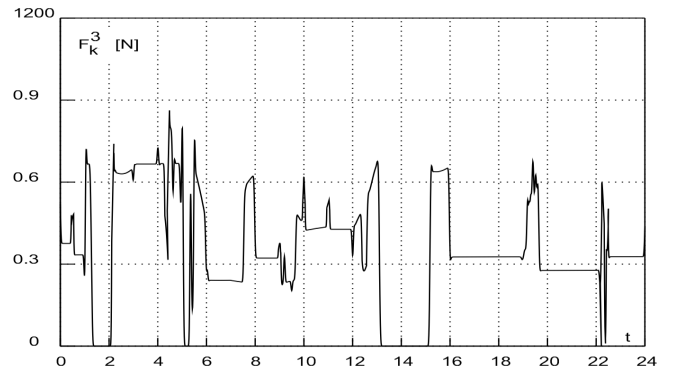


Fig. 16. Diagram of (rear right) wheel 3 and base interaction forces F_k^3

Figs. 15 and 16 show the diagrams of interaction forces F_k in the contact of wheels 1 and 3 with the base. Also in these diagrams the character of the changes in the wheel travel phases is clearly visible. In the force diagrams (for time $t = 2.0-16.0$ s) when examining the wheel/base contact loss instants one can distinguish the particular walking stages.

The last stage of motion (for $t > 18.9$ s) illustrates the results of a numerical experiment simulating the travel of the robot on a ground with a sharp dip negotiated without walking. The moment when the front wheels (shortly followed by the rear wheels) fall from the obstacle is particularly distinct (Fig. 10). The lift and protrusion actuators are particularly heavily loaded in this phase (Figs. 13 and 14).

The simulation results presented here are only a sample selected from the results of the numerous studies which have been carried out. A detailed analysis of the robot loads needs to be made in order to select proper drives and to do structural calculations. As it appears from Tab. 2. the electric drives LINAK LA36 adopted for lifting and protruding meet the dynamic requirements since driving forces F_w and F_p (Figs. 13 and 14) do not exceed the nominal forces specified by the manufacturer. even during the negotiation of extreme obstacles.

5. CONCLUSIONS

The creation of a computational model and simulation studies of a wheeled-walking robot have been described. Robots of this kind are complex mechanisms subjected to considerable variable loads resulting from travel on a ground with obstacles. The identification of the state of load in the robot is an essential step

in building an efficient and reliable robot system.

For the robot considered here a computational model was created using a computer system for dynamic analysis. A procedure for robot walking aimed to overcome an obstacle appearing on the track was developed. The walking procedure takes into account a change in the stability field, resulting from a change in the way the robot is supported while the wheels are being lifted and from the adjustment of the field to ensure the stability of the system.

The robot structure was evaluated and its performance verified through simulations of driving and walking and an analysis of the obtained results for one chosen procedure for obstacle negotiation. The adopted design can be the basis for the construction of a wheeled-walking robot.

REFERENCES

1. **Bałchanowski J., Gronowicz A.** (2009). *Designing, building and dynamic researches of wheel-legged robot* (in Polish). Project no. N N502 271037 funded from the resources for science in the years 2009-2012 in Poland.
2. **Bałchanowski J., Gronowicz A.** (2012b). Design and simulation researches of wheel-legged robot suspension (in Polish). *Systems. Journal of Transdisciplinary Systems Science*. Vol. 16. Issue no 2.
3. **Halme A., I. Leppänen, J. Suomela, S. Ylönen** (2003). WorkPartner: Interactive Human-like Service Robot for Outdoor Applications. *The International Journal of Robotics Research*. Vol. 22. No. 7–8.
4. **Haug E. J.** (1989). *Computer Aided Kinematics and Dynamics of Mechanical Systems*. Allyn and Bacon. Boston 1989.
5. **Holtdanowicz G.** (2008). *PIAP Robots eyes combat role*. Jane's International Defence Review. July 2008
6. **Sperzyński P., Szrek J., Gronowicz A.** (2010). Synthesis of a mechanism for generating straight line indexing trajectory (in Polish). *Acta Mechanica et Automatica*. Vol. 4. No 2.
7. **Tchoń K., A. Mazur, I. Dulęba, R. Hossa, R. Muszyński** (2000). *Manipulators and mobile robots* (in Polish). Akademicka Oficyna Wydawnicza. Warszawa.
8. **Trojnacki M., Szynkarczyk P., Andrzejuk A.** (2008). Trends in land-based robots (in Polish). *Pomiary Automatyka Robotyka*. 6/2008.
9. **Zielińska T.** (2003). *Walking machines* (in Polish). PWN. Warszawa.
10. http://www.bostondynamics.com/robot_petman.html
11. <http://www.elbitsystems.com/elbitmain/areain2.asp?parent=3&num=31&num2=31>

This research, under project no. N N502 271037, was funded from the resources for science in the years 2009-2012.

ASSESSMENT OF MECHANICAL PROPERTIES OF OFFROAD VEHICLE TIRE: COUPONS TESTING AND FE MODEL DEVELOPMENT

Paweł BARANOWSKI*, Paweł BOGUSZ*, Paweł GOTOWICKI*, Jerzy MALACHOWSKI*

*Faculty of Mechanical Engineering, Department of Mechanics and Applied Computer Science, Military University of Technology,
ul. Kaliskiego 2, 00-908 Warsaw, Poland

pbaranowski@wat.edu.pl, pbogusz@wat.edu.pl, pgotowicki@wat.edu.pl, jerzy.malachowski@wat.edu.pl

Abstract: In this paper the subsequent stages of tire rubber coupons mechanical properties experimental assessment are presented. Experimental uniaxial tension and compression tests were carried out on the strength testing machine with the assistance of high-speed camera and special software for strain measurements. Obtained stress-strain curves were applied into the chosen Mooney-Rivlin constitutive rubber material model in order to estimate necessary material constants. Simultaneously, the numerical off-road vehicle tire model was developed. Geometry of the tire and rim was achieved using a 3D scanning method. Moreover, with the assistance of microscope and X-ray device the tire cords pattern was verified, which in the next stages was implemented into the FE model. Consequently, tire radial deflection test was simulated in order to validate evaluated material constants and proposed concept of the numerical tire modelling. Obtained results were compared with the actual deflection test data included in technical documentation of the tire.

Key words: Tire, Rubber, Mechanical Properties, Finite Element Analysis

1. INTRODUCTION

Development of a pneumatic tire structure with a high operating standard is associated with carrying out the series of experimental studies to determine the stability and reliability of its implementation. It also involves large financial outlays and time constraints. An alternative to experimental testing is numerical modelling using Finite Element Method (FEM), thank to which it is possible to estimate deformation and stress states occurring in the tire structure and perform necessary design modifications even before the production stage. Thus for effective and correct analyses a numerical model of the complicated tire structure should be developed with particular attention and care. The authors of the papers (Helnwein et al., 1993; Cho et al., 2004; Reid et al., 2006; Neves et al., 2010; Baranowski, 2011) present a conception of discrete tire modelling and validating process. The final form and characteristics of the numerical tire model are affected by many factors, including knowledge and availability of information on modelled wheels (tires), or correct material data, which turns out to have a significant impact on the results (Malachowski et al., 2007).

In this paper the results of experimental uniaxial tension and compression tests of rubber coupons are presented. Object of investigation is a terrain vehicle Michelin 255/100/R16 tire (Michelin, 2003), from which rubber slices were cut out in order to prepare the coupons for testing. Experimental uniaxial tension and compression tests were carried out on the fatigue machine INSTRON 8802 with the assistance of high-speed PHANTOM V12 camera and special software for strain measurements TEMA 3.3. Obtained stress-strain curves were applied into to chosen constitutive rubber material model of the tire. Consequently, tire radial deflection test was simulated in order to validate evaluated material constants and proposed concept of the numerical tire modelling. Obtained results were compared with the actual deflection test data included in technical documentation of the tire.

2. EXPERIMENTAL TESTS

2.1. Rubber coupons preparation process

In order to carry out experimental tests the coupons with geometry complied with standards PN-54/C-04253 and PN-ISO 37:2007 had to be prepared. Firstly, it was necessary to cut out, with water jet cutting technique, slices of rubber with thickness of 3-4 mm, from which tension coupons were obtained. Due to the complexity of the tire tread structure (cords inside) from this area it was possible to make only cylindrical coupons for the compression tests with the 17.8 mm height and 35 mm diameter. Instead from sidewall of the tire only tension coupons were obtained with 2 mm thickness, measuring length size of 40 mm and measuring length width of 6 mm. Rubber slices needed to be cut out without cords. Otherwise, obtained results from the experimental tests would give unreliable results. Thus, for cords pattern verifying a microscope and X-ray device were used, which gave the possibility to investigate their structure and geometrical arrangement. As can be seen in Fig. 1 below, steel cords are arranged radially inside tire sidewall, whereas within tread area they are placed circumferentially.



Fig. 1. Steel cords microscopic photo

Also, what can be noticed from Fig. 2, a single cord consists of 9 smaller wires, with their average total measured diameter of ~1.2 mm. Moreover, the rubber-steel cords volumetric ratio was verified, which was taken into account in numerical tire modelling.

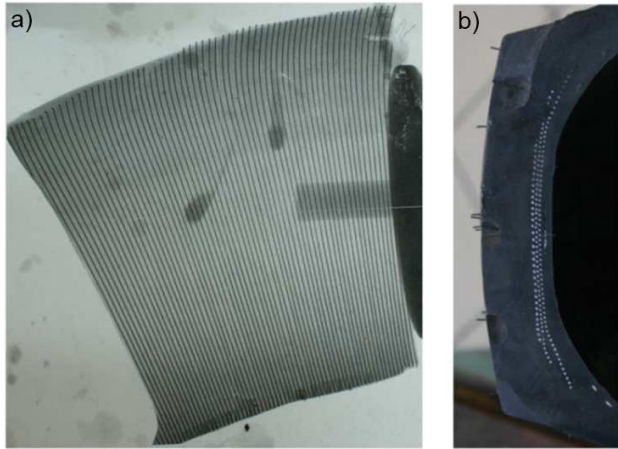


Fig. 2. X-ray photography of cords pattern in tire sidewall (a), Tread cords pattern in microscale (b) (Baranowski, 2011)

2.2. Mechanical characteristics assessment of rubber coupons in compression and tension tests

For experimental testing six tensile and eight compression coupons were prepared (Fig. 3).

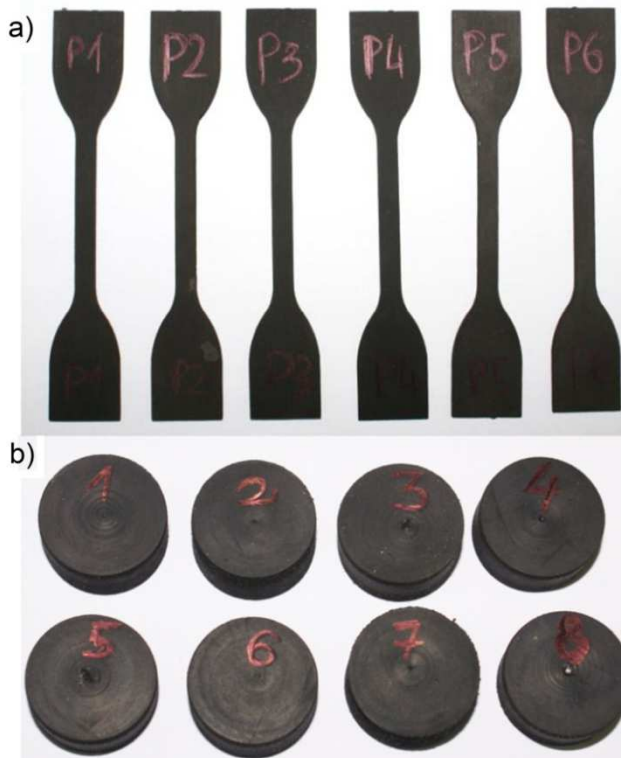


Fig. 3. Rubber tension coupons (a), Rubber compression coupons (b)

As stated before mechanical characteristics of rubber were assessed in static experimental uniaxial tension and compression tests which were carried out on the strength testing machine

INSTRON 8802 with the assistance of high-speed PHANTOM V12 camera and special software for strain measurements TEMA 3.3 (Fig. 4).



Fig. 4. High-speed camera Phantom V12 and strength testing machine Instron 8802 (Baranowski P., 2011)

Tensile rubber coupons experimental testing

With software Tema 3.3 it was possible to perform measurements of deformation in tensile tests. Computed strain values were synchronous recorded with the force values from Instron machine. In this method displacement of points is recorded with high frequency at each frame, followed by strain calculation using a correlation method. In order to perform measurements two positioning points need to be placed on the coupon surface: in the bottom and upper area of coupon measurement length (Fig. 5).



Fig. 5. An example of measurement points placing on a coupon with adopted coordinate system

For the measurements points in TEMA software the following values were defined:

- X_1 component (x position) and Y_1 component (y position) for point 1,
- X_2 (x position) and Y_2 (y position) components for point 2,
- X_{12} and Y_{12} distance between points components.

Distance and position components in TEMA software have 0.1 pixel size. Thus, strain value is calculated with 0.1 pixel / 0.1 pixel accuracy using the following formula:

$$\varepsilon_{12} = \frac{X_{12} - X_{12}^0}{X_{12}^0} \quad (1)$$

where: X_{12}^0 – initial distance between points, X_{12} – distance between points in the specific time t .

Calculated strain values were synchronized with the registered values of force and calculated values of engineering stress. The point corresponded to maximum force and the distance value X_{12} obtained from the image taken just before a failure of the coupon were used to determine the value of failure stress and strain. In conducted experimental tests camera recording and strength testing machine sampling frequency was identical (50 Hz). In Fig. 6 selected frames showing the rubber coupon from the start to an end of the tests are presented.

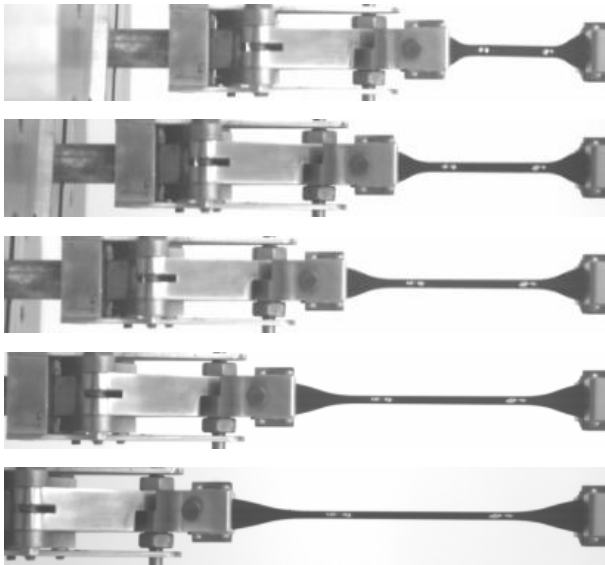


Fig. 6. Rubber coupon in tensile tests – selected frames

Compression rubber coupons experimental testing

In compression tests only force values and displacements were recorded on the strength testing machine without simultaneously using the high-speed camera. This was due to limitations of TEMA software, i.e. problem with measuring point recognizing at the time of maximum coupon compression. In Fig. 7 selected photos of rubber cylindrical compression test are presented.

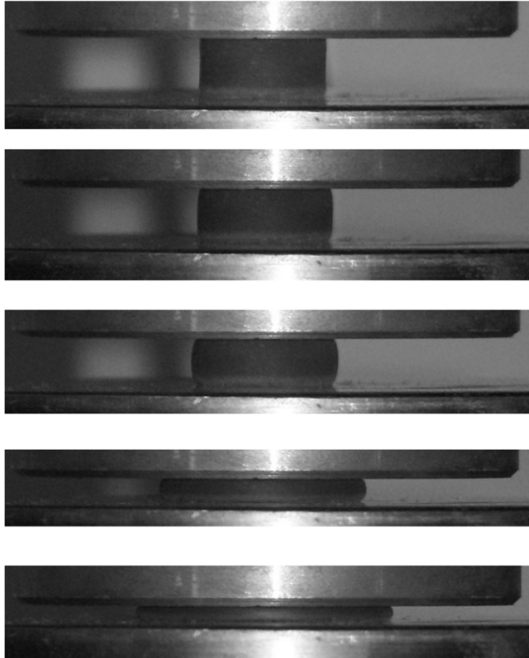


Fig. 7. Rubber coupon in compression tests – selected photos

2.3. Experimental tests results

As the results of carried out tests mechanical characteristics of tire rubber (from tread and sidewall) were obtained. In Fig. 8 stress-strain curve from tension coupons are presented, whereas

curves from compression coupons are presented in Fig. 9. It should be also pointed out that due to the static characteristic of loading no strain effects were taken into consideration.

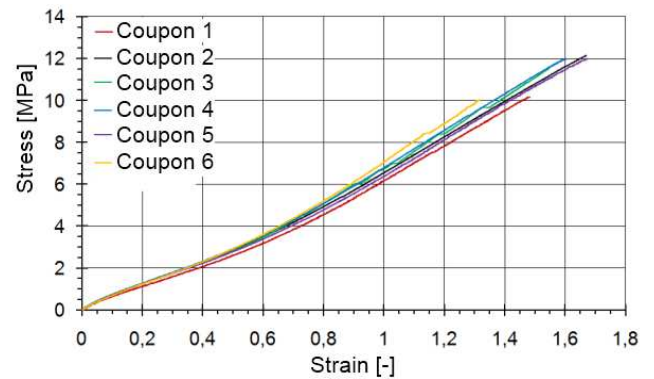


Fig. 8. Stress-strain curves obtained from experimental tensile tests (Baranowski, 2011)

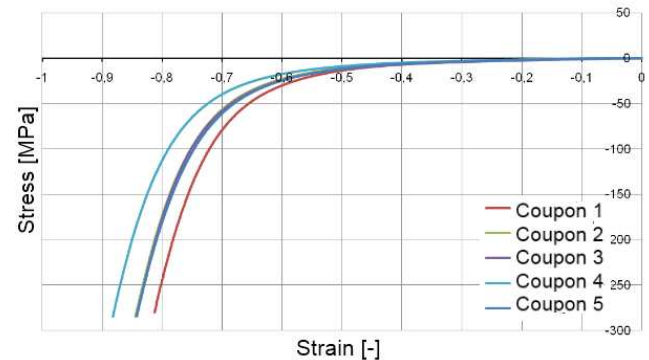


Fig. 9. Stress-strain curves obtained from experimental compression tests (Baranowski, 2011)

3. NUMERICAL TIRE MODELLING

The tire is a very complex structure consisting of several strengthening layers made of parallel fibers. These fibers, depending on the tire application are made of polyester, nylon and steel. Immersed in the rubber with different orientation they form a special ring-like laminate. Generally it consists of several interconnected elementary parts with different material parameters, i.e. sidewall, tread, bead core etc. (Helwein et al., 1993; Cho et al., 2004; Reid et al., 2006; Pondel et al., 2006; Sokolov, 2007; Neves et al., 2010; Baranowski and Małachowski, 2011; Baranowski et al., 2011).

In the first stage of tire numerical model development process the tire geometry was achieved thanks to the reverse engineering technology. Subsequently, from obtained cross-section curves and other geometry datums, CAD model was developed which was the basis for numerical model of the wheel. Due to the fact that a tire is such a complex structure to be represented with numerical methods, it was important to develop a discrete model of tire as much similar to the real one as possible. Hence the tire was divided into six different parts, with corresponding material properties (with experimental data added) and with steel cords arranged radially and circumferentially (Tönük et al., 2001; Bolarinwa et al., 2004; Reid et al., 2006; Neves et al., 2010; Baranowski and Małachowski, 2011). Selected slice of the analysed

discrete model is presented in Fig. 10. Numerical model of the tire was developed using solid hexagonal elements and beam elements for steel cords modelling. Tab. 1 presents the statistic data of the tire.

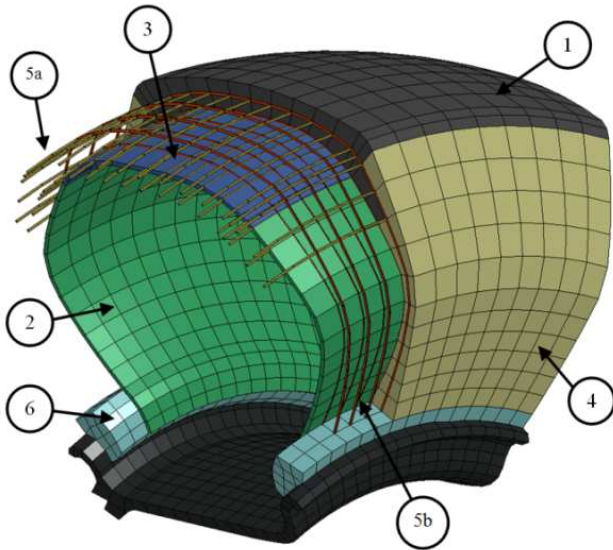


Fig. 10. FE model of tire with constituent components:
 1. Tread, 2. Inner fabric, 3. Carcass, 4. Sidewall,
 5a, b. Circumferential and radial cords, 6. Bead core with cords
 (Baranowski, 2011, 2012)

Tab. 1. Statistic data of discrete tire model

Hexagonal elements		
Part	No. of elements	No. of nodes
Tread	3840	6360
Inner fabric	3600	7680
Carcass	1680	3600
Sidewall	4800	8160
Bead core	2400	3840
Rim	7192	12164
SUM	23512	41804
Beam elements		
Circumferential cords	4560	4561
Radial cords	8639	8881
Bead core cords	968	962
SUM	14167	14404

3.1. Tire material description

FEM modelling, besides finite element meshing is associated with defining the characteristics of materials for components of a simulated structure. In presented case steel cords and rim were developed using elastic-plastic material description. Also, for carcass and inner fabric an orthotropic material was implemented. Finally, rubber-based components were modelled using non-linear material, which behaves differently during compression and tension (Fig. 11). This kind of behaviour is typical for rubber (e.g. tire) which is an elastomer with high filler content, mainly in the form of soot and silica. Due to the extremely small fillers particle size this kind of composite can be treated as homogene-

ous and isotropic material.

Rubber constitutive relations which are essential in modelling tires, i.e. the relationship between stress and strain, are formulated within the nonlinear elasticity theory, called hyperelasticity.

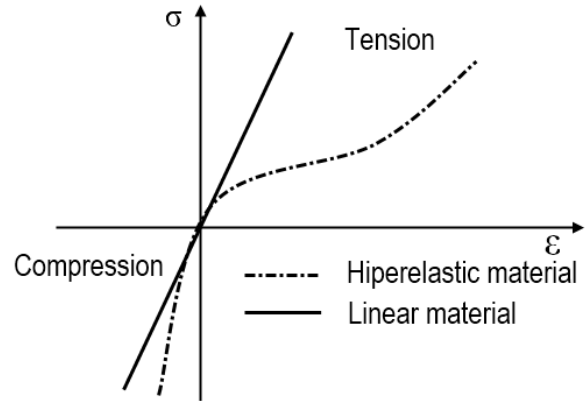


Fig. 11. Stress-strain curve for (non-linear) hyperelastic material
 (Ansys, 1999)

Tab. 2. Material description for tire components

Mooney-Rivlin components (with experimental data)							
Part	E [Pa] (10e+6)	ρ [kg/m³]	ν	A [Pa] (10e+3)	B [Pa] (10e+6)		
Tread	14.00	1173.00	0.450	806.00	1.80		
Sidewall	5.05	1132.00	0.450	171.00	0.83		
Bead core	5.05	1132.00	0.450	171.00	0.83		
Elastic-plastic components							
Part	E [Pa] (10e+11)	ρ [kg/m³]	ν	Yield strength[Pa] (10e+8)			
Rim	2.11	7860.00	0.300	3.50			
Cords	2.11	7860.00	0.300	3.50			
Orthotropic components							
Part	E [Pa] (10e+8)			ρ [kg/m³]	ν		
	E ₁	E ₂	E ₃		ν ₁₂	ν ₁₃	ν ₂₃
Carcass	1.07	1.27	1.07	1351.00	0.451	0.0038	0.0038
Inner fabric	31.81	0.83	0.83	2497.00	0.00011	0.00011	0.454

One of the most popular material model, which is widely used in numerical computations is Mooney – Rivlin constitutive material model (Mooney, 1940; Rivlin, 1948; Shiraishi et al., 2000; Tönük et al., 2001; Bolarinwa et al., 2004; Reid et al., 2006; Małachowski et al., 2007; Neves et al., 2010; Baranowski and Małachowski, 2011). According to this theory the unitary strain energy function exists, which is an analytic function of the strain tensor, which plays the role of the stress potential:

$$W = A(I_1 - 3) + B(I_2 - 3) + C \left(\frac{1}{I_3} - 1 \right) + D(I_3 - 1)^2, \quad (2)$$

$$C = 0.5A + B, \quad (3)$$

$$D = \frac{A(5\nu - 2) + B(11\nu - 5)}{2(1 - 2\nu)}, \quad (4)$$

where: ν – Poisson ratio, $G = 2(A + B)$ – modulus of rigidity,

I_1, I_2, I_3 – three invariants of deformation tensor.

Material description for all tire components including A and B constants for Mooney-Rivlin rubber are presented in Tab. 2 (Tönük et al., 2001; Pondel et al., 2006; ; Neves et al., 2010)

3.2. Radial deflection numerical test description

In order to validate the proposed discrete model of the tire it was necessary to perform a test which would verify used material properties and the conception of tire structure modelling. Thus, based on the technical documentation (obtained by courtesy of Michelin company employees) (Michelin, 2003) the numerical radial deflection test was carried out. Implicit analysis was performed using LS-Dyna code. For numerical verification tests three chosen values of force (taken from real tests) were implemented: 30000, 40000 and 50000 N applied on centre axis of the rim. Also, 400000 and 500000 Pa pressure inside the tire was represented with the airbag model (Green function closed volume integration) (Hallquist, 1998). Contacting surface was modelled as rigid body, which significantly reduced simulation time. Numerical model of the tire along with applied initial-boundary conditions for one case is presented in Fig. 12.



Fig. 12. Numerical model of the tire with applied force

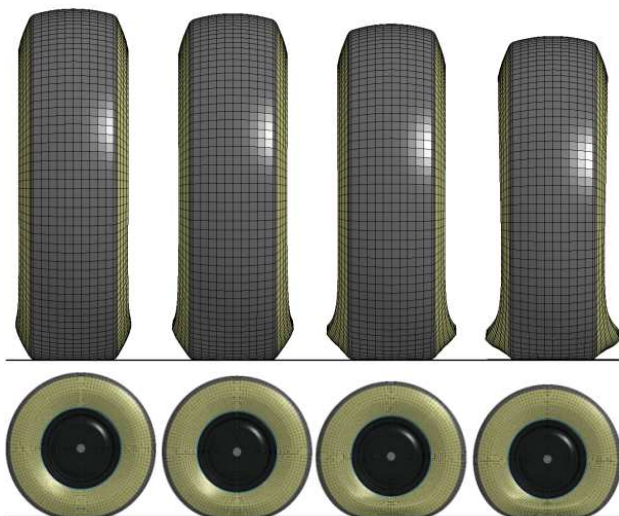


Fig. 13. Tire deflection from the beginning of the test to maximum deformation presented in two views: one from the side of the tire and second from the rim surface side

From the carried out analysis (50000N force and 5 bar pressure) the tire deformation was obtained (Fig. 13). It can be noticed that the deformation shape of tire caused by the subjected loading is characteristic and its behaviour is typical in this type of tests investigating real tires (Michelin, 2003; Cho et al., 2004; Małachowski et al., 2007; Pelc, 2007).

In the figures above only the tire deformation from one test with chosen force and pressure inside the tire values were presented. In Table 3 the results from all three cases compared with actual experimental tests are listed. It can be noticed that numerical model of the tire is less stiff than the real one, which is caused by the absence of tread in FE model and accuracy in determination of the materials coefficients.

Tab. 3. Numerical and experimental tests comparison for all simulated force and pressure values (Michelin, 2003)

Force [N]	Tire pressure [Pa]	Numerical deflection [m]	Experimental deflection [m]	Error [%]
30000	400000	0.069	0.063	8.696
	500000	0.059	0.054	8.475
40000	400000	0.088	0.080	9.091
	500000	0.074	0.068	8.108
50000	400000	0.112	0.097	13.393
	500000	0.094	0.083	11.702

4. CONCLUSIONS

This paper is an example of effective coupling experimental tests with numerical analyses. By using special fatigue machines with the assistance of modern optical methods for strain measuring it is possible to obtain indispensable material characteristics which are essential for proper numerical modelling. By implementing them into the discrete model of the investigated object a high accuracy of numerical solution is provided, which is confirmed in the presented paper. In the next stages numerical analyses of a suspension system response subjected dynamic impact loading will be carried out. With experimentally obtained mechanical characteristics and proper validation process of tire discrete model obtained results will correspond to reality even more.

REFERENCES

1. **ANSYS** (1999), *Hyperelasticity, Structural Nonlinearities*, Chapter 6, Second Edition Release 5.5 (001156).
2. **Baranowski P., Małachowski J. (2011)**, Blast wave and suspension system interaction- numerical approach, *Journal of KONES*, 18, 1, 23-30.
3. **Baranowski P., Małachowski J., Niezgoda T. (2011)**, Numerical analysis of vehicle suspension system response subjected to blast wave, *Applied Mechanics and Materials*, 82, 728-733.
4. **Bolarinwa E.O., Olatunbosun O.A. (2004)**, Finite element simulation of the tyre burst test, *Proceedings of the Institution of Mechanical Engineers*, 218, 1251.
5. **Cho J.R., Kim K.W., Jeong H.S. (2004)**, Mesh generation considering detailed tread blocks for reliable 3D tire analysis, *Advance in Engineering Software*, 35, 105-113.
6. **Hallquist J.O. (2003)**, *LS-Dyna: Theoretical manual*, California Livermore Software Technology Corporation.

7. **Heinwein P., Liu C.H., Meschke G., Mang H.A.** (1993) A new 3-D finite element model for cord-reinforced rubber composites-application to analysis of automobile tyres, *Finite Elements in Analysis and Design*, 4, 1-16.
8. **Małachowski J., M. Wesołowski, W. Krasoń** (2007), Computational study of transport aircraft landing gear during touchdown, *Journal of KONES*, 13, 4, 187-195.
9. **Michelin** (2003), *Technical characteristics 255/100 R 16 XZL TL 126/124 K*, Michelin, 2003.
10. **Mooney M.** (1940), A theorie of elastic deformations, *Journal of Application Physics*, 11, 582-592.
11. **Neves R.V. Micheli G.B., Alves M.** (2010), An experimental and numerical investigation on tyre impact, *Internation Journal of Impact EGINEERING*, 10, 685-693.
12. **Pelc J.** (2007), Modelling of finite deformations of pneumatic tires (in Polish), UWM, Olsztyn.
13. **Pondel B., Małachowski J.** (2006), Numerical analysis of automobile tire (in Polish), WAT, Warszawa.
14. **Reid J.D., Boesch D.A., Bielenberg R.W.** (2006), Detailed Tire Modeling for Crash Applications, *ICrash 2006*, Athens, Greece.
15. **Rivlin R.S.** (1948), Large elastic deformations of isotropic materials, Fundamental Concepts, *Philos Trans R Soc Land Ser A*, 240, 459-490.
16. **Shiraishi M. et al.** (2000), Making FEM tire model and applying it for durability simulation, *6th International LS-Dyna Users conference*, Detroit.
17. **Sokolov S.L.** (2007), Calculation of the Stress- Strain State of Pneumatic Tires by the Finite Element Method, *Journal of Machinery Manufacture and Reliability*, 36, 1, 45-49.
18. **Tönük E., Unlüsoy Y.S.** (2001), Prediction of automobile tire cornering force characteristics by finite element modeling and analysis, *Computer and Structures*, 79, 1219-1232.

IDENTIFICATION OF AN ELECTRICALLY DRIVEN MANIPULATOR USING THE DIFFERENTIAL FILTERS – INPUT ERROR METHOD

Leszek CEDRO*

*Kielce University of Technology, Faculty of Mechatronics and Machinery Design, Al. Tysiąclecia PP 7, 25-314 Kielce, Poland

lcetro@tu.kielce.pl

Abstract: The paper presents an example of solving the parameter identification problem in case of robot with three degrees of freedom has been presented. The identification has been performed with the use of elaborated differential filters. The applied identification method does not require differential equations solving but only determining the appropriate derivatives. Identification method and its generalizations using the object inverse model require information on time derivatives of the input and output signals. The required derivative order depends on the order of differential equations describing the object.

Key words: Differential Filters, Identification, Input Error Method

1. INTRODUCTION

The rapid developments in computer hardware and software and, consequently, the common use of computers to control processes have aroused wide interest in mathematical modeling, control processes and, accordingly, control system identification.

The method of identification applied in the analysis involves fine-tuning of the inverse model. The method can be used only for such values of the input signals that are determined from the measurement data. Identifying a dynamic system by means of the input error method (Fig. 1) requires looking for a model that generates the same input as the object. Only in the case of model reversibility is such a procedure possible. This reversibility is true for linear minimum-phase models and a certain class of non-linear models where the input is determined basing on the output data (Cedro and Janecki 2009; Cedro and Janecki 2011).

Let us assume, for instance, that the object is described by means of a differential equation:

$$f(\varphi^{(n)}, \varphi^{(n-1)}, \dots, \varphi, \theta) = \tau \quad (1)$$

where f is a certain known function, θ unknown parameters and τ input signal. Thus, the identification error is defined as:

$$e = \tau - \hat{\tau},$$

$$\hat{\tau} = f(\varphi^{(n)}, \varphi^{(n-1)}, \dots, \varphi, \hat{\theta}) \quad (2)$$

where $\hat{\tau}$ estimate input signal and $\hat{\theta}$ estimate unknown parameters.

A drawback of this method is that derivative estimates need to be determined. An advantage, on the other hand, is that it is not necessary to solve the differential equations describing the model at each step of iteration.

The fundamental problem related to the implementation of the input error method and its generalization is the necessity to determine the estimates of signal derivatives. This is achieved by applying differential filters (Janecki and Cedro 2007).

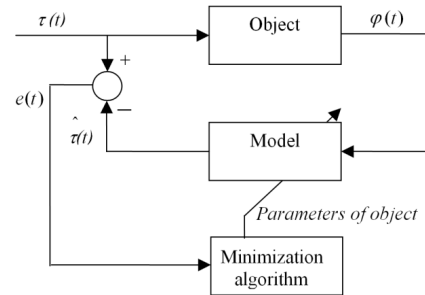


Fig. 1. Schematic diagram of the identification process

2. DIFFERENTIAL FILTERS

Let us assume that the differential filter of the k -th order is a series connection of a low-pass filter with boundary frequency Ω_g and a difference quotient of the k -th order (Fig. 2).



Fig. 2. Block diagram of the differential filter

The low-pass filter will be responsible firstly for reducing the signal spectrum and secondly for correcting the characteristics of the difference quotient in the range of low frequencies. Thus, the filter will be called a low-pass correction filter. The desired transfer function of the low-pass filter is:

$$H_{\text{kor}k}(\Omega) = \begin{cases} H_k(\Omega)/H_{\nabla k}(\Omega) & \text{for } \Omega \leq \Omega_g \\ 0 & \text{for } \Omega > \Omega_g. \end{cases} \quad (3)$$

As a result, the transfer function of the series connection of the difference quotient and the low-pass filter in the range of low frequencies will be equal to the transfer function of an ideal differential filter.

The transfer function of the low-pass filter for $\Omega \leq \Omega_g$ is equal

to:

$$H_{\text{kor}k}(\Omega) = H_k(\Omega) / H_{\nabla k}(\Omega) = \begin{cases} \Omega / \sin \Omega & k = 1 \\ \Omega^2 / 2(1 - \cos \Omega) & k = 2 \\ \Omega^3 / (-2 \sin \Omega + \sin(2\Omega)) & k = 3. \end{cases} \quad (4)$$

The filter impulse response is the inverse Fourier transform of its frequency characteristic, thus:

$$h_{\text{kor}k}(n) = \frac{1}{2\pi} \int_{-\Omega_g}^{\Omega_g} H_{\text{kor}k}(\Omega) e^{j\Omega n} d\Omega. \quad (5)$$

Unfortunately, integral (5) cannot be expressed by means of the analytic functions. It needs to be determined using some approximation. By expanding function $H_{\text{kor}k}(\Omega)$ into a Taylor series around the value $\Omega = 0$, we obtain:

$$H_{\text{kor}k}(\Omega) = \begin{cases} 1 + \frac{\Omega^2}{6} + O(\Omega^4) & k = 1 \\ 1 + \frac{\Omega^2}{12} + O(\Omega^4) & k = 2 \\ 1 + \frac{\Omega^2}{4} + O(\Omega^4) & k = 3. \end{cases} \quad (6)$$

The four-term approximation of the expansion appears to be fairly sufficient. The inverse Fourier transform of the function obtained by rejecting the terms of the higher orders is equal to:

$$h_{\text{kor}k}(n) = \begin{cases} \frac{12}{6n^3\pi} n\Omega_g \cos(n\Omega_g) + \\ + (6n^2 + \Omega_g^2 n^2 - 2) \sin(n\Omega_g) & k = 1 \\ \frac{1}{12n^3\pi} (2n\Omega_g \cos(n\Omega_g) + \\ + (12n^2 + n^2\Omega_g^2 - 2) \sin(n\Omega_g)) & k = 2 \\ \frac{1}{4n^3\pi} (2n\Omega_g \cos(n\Omega_g) + \\ + (4n^2 + n^2\Omega_g^2 - 2) \sin(n\Omega_g)) & k = 3. \end{cases} \quad (7)$$

Assume that the impulse response of the low-pass differential filter is:

$$h_{dk}(n) = \frac{1}{\chi_k} h_{\text{kor}k}(n) W_{\text{Harris}}(n), \quad (8)$$

Where $W_{\text{Harris}}(n)$ is Harris window described by the following equation:

$$W_{\text{Harris}}(n) = 0.36 + 0.49 \cos(\pi n / M) + 0.14 \cos(2\pi n / M) + 0.01 \cos(3\pi n / M). \quad (9)$$

The parameter χ_k should be selected in such a way that the slope of the characteristic of the filter being designed at point $\Omega = 0$ be the same as that of the ideal differential equation, thus:

$$\frac{\partial^k}{\partial \Omega^k} H_{dk}(\Omega) H_{\nabla k}(\Omega) |_{\Omega=0} = \frac{k! j^k}{\Delta^k}. \quad (10)$$

3. A MATHEMATICAL MODEL OF A ROBOT MANIPULATOR

In the next sections, the following problems will be solved: first, we will derive the equations for the DC motors, then, we will define the kinetic and potential energy of the system, and finally, we will symbolically derive the robot dynamic equations, using the second order Lagrange equations.

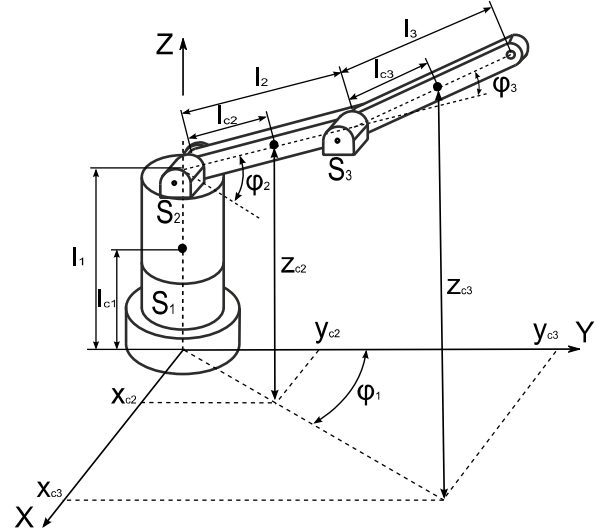


Fig. 3. An electrically-driven manipulator

Let $\varphi = [\varphi_1 \varphi_2 \varphi_3]$ denote the vector of joint variables acting as generalized coordinates, m_j – the mass, l_j – the arm length, l_{c_j} – the distance from the centre of gravity and S_j – the motor of the link j .

Using typical equivalent diagrams of DC motors available in the literature, e.g. (Kowal, 2004), and the second Kirchoff law, we can write the following electrical equation of the DC motor:

$$U_{z_j} = U_{R_j} + U_{L_j} + E_{e_j}, \text{ for } j = 1, 2, 3 \quad (11)$$

where U_{z_j} is the voltage supplied to the rotor.

Since an open-loop system may be difficult to control, it is essential that the identification be performed for a closed-loop system with properly selected PD controllers. Let us assume that the equations of the controllers have the following form:

$$U_{z_j} = K_{p_j} (\varphi_{z_j}(t) - \varphi_j(t)) - K_{d_j} \dot{\varphi}_j(t), \quad (12)$$

where: K_{p_j} , K_{d_j} – the parameters of the controllers, $\varphi_{z_j}(t)$ – the control signals, $\varphi_j(t)$ – the variables describing the position of the manipulator arms.

The voltage drops across the rotor winding resistance and inductance are:

$$U_{R_j} = R_{w_j} i_{w_j}(t), \text{ and} \quad (13)$$

$$U_{L_j} = L_j \frac{di_{w_j}(t)}{dt}, \quad (14)$$

where R_{w_j} is the equivalent rotor winding resistance, L_j is the equivalent rotor winding inductance, and i_{w_j} is the current flowing through the rotor windings.

The electromotive inductance force is:

$$E_{e_j} = k_{e_j} \dot{\varphi}_j(t), \quad (15)$$

where k_{e_j} is an electromotive constant.

Substituting the subsequent components to Eq. (11), we obtain:

$$L_j \frac{di_{w_j}(t)}{dt} + R_{w_j} i_{w_j}(t) + k_{e_j} \dot{\varphi}_j(t) = , \text{ for } j = 1, 2, 3. \quad (16)$$

$$= K_{p_j} [\varphi_{z_j}(t) - \varphi_j(t)] - K_{d_j} \dot{\varphi}_j(t)$$

The rotor torque is:

$$M_{s_j} = k_{m_j} i_{w_j}(t), \quad (17)$$

where k_{m_j} is a mechanical constant.

Let us define the manipulator kinetic and potential energy. The following geometrical relations take place:

$$\begin{aligned} x_{c2} &= l_{c2} \cos(\varphi_2(t)) \cos(\varphi_1(t)), \\ x_{c3} &= l_2 \cos(\varphi_2(t)) \cos(\varphi_1(t)) + l_{c3} \cos(\varphi_2(t) + \\ &+ \varphi_3(t)) \cos(\varphi_1(t)), \\ y_{c2} &= l_{c2} \cos(\varphi_2(t)) \sin(\varphi_1(t)), \\ y_{c3} &= l_2 \cos(\varphi_2(t)) \sin(\varphi_1(t)) + l_{c3} \cos(\varphi_2(t) + \\ &+ \varphi_3(t)) \sin(\varphi_1(t)), \\ z_{c2} &= l_1 + l_{c2} \sin(\varphi_2(t)), \\ z_{c3} &= l_1 + l_2 \sin(\varphi_2(t)) + l_{c3} \sin(\varphi_2(t) + \varphi_3(t)). \end{aligned} \quad (18)$$

The velocity of the centre of gravity of the second arm of the manipulator is:

$$\begin{aligned} v_2 &= \sqrt{\dot{x}_{c2}^2 + \dot{y}_{c2}^2 + \dot{z}_{c2}^2}, \\ v_3 &= \sqrt{\dot{x}_{c3}^2 + \dot{y}_{c3}^2 + \dot{z}_{c3}^2}. \end{aligned} \quad (19)$$

Thus, the kinetic energy of the system is:

$$E = E_1 + E_2 + E_3, \quad (20)$$

$$\begin{aligned} E_1 &= \frac{J_{c1} \dot{\varphi}_1^2(t)}{2}, \quad E_2 = \frac{m_2 v_2^2}{2} + \frac{J_{c2} \dot{\varphi}_2^2(t)}{2}, \\ E_3 &= \frac{m_3 v_3^2}{2} + \frac{J_{c3} \dot{\varphi}_3^2(t)}{2}, \quad J_{c_j} = \frac{m_j l_j^2}{12}, \quad l_{c_j} = \frac{l_j}{2}, \end{aligned}$$

where J_{c_j} are moments of inertia of the robot arms assumed for a uniform beam.

The potential energy of the system is:

$$U = U_1 + U_2 + U_3, \quad (21)$$

$$U_1 = m_1 g l_{c1}, \quad U_2 = m_2 g (l_1 + l_{c2} \sin(\varphi_2(t))),$$

$$U_3 = m_3 g (l_1 + l_2 \sin(\varphi_2(t)) + l_{c3} \sin(\varphi_2(t) + \varphi_3(t)))$$

where g is the acceleration of gravity.

Using the expressions for the kinetic and potential energy, we obtain two second-order Lagrange equations:

$$\frac{d}{dt} \frac{\partial E}{\partial \dot{\varphi}_j} - \frac{\partial E}{\partial \varphi_j} + \frac{\partial U}{\partial \varphi_j} = M_{s_j}, \text{ for } j = 1, 2, 3. \quad (22)$$

After substitution and simplification of all the variables, we have a system of three equations (where: $\varphi_j = \varphi_j(t)$, $\dot{\varphi}_j = \dot{\varphi}_j(t)$, $\ddot{\varphi}_j = \ddot{\varphi}_j(t)$):

$$\begin{aligned} &\frac{1}{k_{m_1}} ((R_1 (2l_1^2 m_1 + 3(l_3^2 m_3 + l_2^2 (m_2 + 4m_3))) + 3l_2^2 (m_2 + \\ &+ 4m_3) \cos(2\varphi_2) + 3l_3 m_3 (8l_2 \cos(\varphi_2) \cos(\varphi_2 + \varphi_3) + \\ &+ l_3 \cos(2(\varphi_2 + \varphi_3)))) - 12L_1 (l_2^2 (m_2 + 4m_3) \sin(2\varphi_2) + \\ &+ l_3 m_3 (l_3 \sin(2(\varphi_2 + \varphi_3)) + 4l_2 \sin(2\varphi_2 + \varphi_3))) \dot{\varphi}_2 + \\ &- 24L_1 l_3 m_3 (2l_2 \cos(\varphi_2) + l_3 \cos(\varphi_2 + \varphi_3)) \sin(\varphi_2 + \\ &+ \varphi_3) \dot{\varphi}_3) \ddot{\varphi}_1 + 6\dot{\varphi}_1 (4k_{e_1} k_{m_1} - 2L_1 (l_2^2 (m_2 + \\ &+ 4m_3) \cos(2\varphi_2) + l_3 m_3 (l_3 \cos(2(\varphi_2 + \varphi_3)) + 4l_2 \cos(2\varphi_2 + \\ &+ \varphi_3))) \dot{\varphi}_2^2 - 2l_3 m_3 R_1 (2l_2 \cos(\varphi_2) + l_3 \cos(\varphi_2 + \\ &+ \varphi_3)) \sin(\varphi_2 + \varphi_3) \dot{\varphi}_3 - 2L_1 l_3 m_3 (2l_2 \cos(\varphi_2) \cos(\varphi_2 + \\ &+ \varphi_3) + l_3 \cos(2(\varphi_2 + \varphi_3))) \dot{\varphi}_3^2 + \dot{\varphi}_2 (-R_1 (l_2^2 (m_2 + \\ &+ 4m_3) \sin(2\varphi_2) + l_3 m_3 (l_3 \sin(2(\varphi_2 + \varphi_3)) + 4l_2 \sin(2\varphi_2 + \\ &+ \varphi_3))) - 4L_1 l_3 m_3 (l_3 \cos(2(\varphi_2 + \varphi_3)) + 2l_2 \cos(2\varphi_2 + \\ &+ \varphi_3)) \dot{\varphi}_3) - L_1 (l_2^2 (m_2 + 4m_3) \sin(2\varphi_2) + \\ &+ l_3 m_3 (l_3 \sin(2(\varphi_2 + \varphi_3)) + 4l_2 \sin(2\varphi_2 + \varphi_3))) \ddot{\varphi}_2 + \\ &- 2L_1 l_3 m_3 (2l_2 \cos(\varphi_2) + l_3 \cos(\varphi_2 + \varphi_3)) \sin(\varphi_2 + \\ &+ \varphi_3) \ddot{\varphi}_3) + 2L_1 (l_1^2 m_1 + 3l_2^2 (m_2 + 4m_3) \cos(\varphi_2)^2 + \\ &+ 12l_2 l_3 m_3 \cos(\varphi_2) \cos(\varphi_2 + \varphi_3) + 3l_3^2 m_3 \cos(\varphi_2 + \\ &+ \varphi_3)^2) \ddot{\varphi}_1) = U_{z_1} \\ &\frac{1}{k_{m_2}} (3\dot{\varphi}_1^2 (R_2 (l_2^2 (m_2 + 4m_3) \sin(2\varphi_2) + l_3 m_3 (l_3 \sin(2(\varphi_2 + \\ &+ \varphi_3)) + 4l_2 \sin(2\varphi_2 + \varphi_3))) + 2L_2 (l_2^2 (m_2 + 4m_3) \cos(2\varphi_2) + \\ &+ l_3 m_3 (l_3 \cos(2(\varphi_2 + \varphi_3)) + 4l_2 \cos(2\varphi_2 + \varphi_3))) \dot{\varphi}_2 + \\ &+ 2L_2 l_3 m_3 (l_3 \cos(2(\varphi_2 + \varphi_3)) + 2l_2 \cos(2\varphi_2 + \varphi_3)) \dot{\varphi}_3 + \\ &+ 6L_2 (l_2^2 (m_2 + 4m_3) \sin(2\varphi_2) + l_3 m_3 (l_3 \sin(2(\varphi_2 + \\ &+ \varphi_3)) + 4l_2 \sin(2\varphi_2 + \varphi_3))) \dot{\varphi}_1 \dot{\varphi}_1 + 2(6gR_2 (l_2 (m_2 + \\ &+ 2m_3) \cos(\varphi_2) + l_3 m_3 \cos(\varphi_2 + \varphi_3)) + 4l_2^2 m_2 R_2 \ddot{\varphi}_2 + \\ &+ 12l_2^2 m_3 R_2 \ddot{\varphi}_2 + 3l_3^2 m_3 R_2 \ddot{\varphi}_2 + 3l_3^2 m_3 R_2 \ddot{\varphi}_3 - \\ &+ 6l_3 m_3 \sin(\varphi_3) \dot{\varphi}_3 (l_2 R_2 \dot{\varphi}_3 + L_2 (g \cos(\varphi_2) + 4l_2 \ddot{\varphi}_2 + \\ &+ 3l_2 \ddot{\varphi}_3)) + 6\dot{\varphi}_2 (2k_{e_2} k_{m_2} + gL_2 (-l_2 (m_2 + 2m_3) \sin(\varphi_2) + \\ &- l_3 m_3 \sin(\varphi_2 + \varphi_3) - 2l_2 l_3 m_3 (L_2 \cos(\varphi_3) \dot{\varphi}_3^2 + \\ &+ \sin(\varphi_3) (R_2 \dot{\varphi}_3 + L_2 \ddot{\varphi}_3))) + 4l_2^2 L_2 m_2 \ddot{\varphi}_2 + 12l_2^2 L_2 m_3 \ddot{\varphi}_2 + \\ &+ 3L_2 l_3^2 m_3 \ddot{\varphi}_2 + 3L_2 l_3^2 m_3 \ddot{\varphi}_3 + \\ &+ 6l_3 m_3 \cos(\varphi_3) (-gL_2 \sin(\varphi_2) \dot{\varphi}_3 - l_2 L_2 \dot{\varphi}_3^3 + l_2 (2R_2 \ddot{\varphi}_2 + \\ &+ R_2 \ddot{\varphi}_3 + 2L_2 \ddot{\varphi}_2 + L_2 \ddot{\varphi}_3))) = U_{z_2} \\ &\frac{1}{k_{m_3}} (6(gl_3 m_3 R_3 \cos(\varphi_2 + \varphi_3) + k_{e_3} k_{m_3} \dot{\varphi}_3) + \\ &+ l_3 m_3 (6l_2 \dot{\varphi}_2^2 (R_3 \sin(\varphi_3) + L_3 \cos(\varphi_3) \dot{\varphi}_3) + \\ &+ 3\dot{\varphi}_1^2 (R_3 (2l_2 \cos(\varphi_2) + l_3 \cos(\varphi_2 + \varphi_3)) \sin(\varphi_2 + \varphi_3) + \\ &+ L_3 (l_3 \cos(2(\varphi_2 + \varphi_3)) + 2l_2 \cos(2\varphi_2 + \varphi_3)) \dot{\varphi}_2 + \\ &+ L_3 (2l_2 \cos(\varphi_2) \cos(\varphi_2 + \varphi_3) + l_3 \cos(2(\varphi_2 + \varphi_3))) \dot{\varphi}_3) + (23) \\ &+ 6L_3 (2l_2 \cos(\varphi_2) + l_3 \cos(\varphi_2 + \varphi_3)) \sin(\varphi_2 + \varphi_3) \dot{\varphi}_1 \dot{\varphi}_1 + \\ &+ 3R_3 (l_3 + 2l_2 \cos(\varphi_3)) \ddot{\varphi}_2 - 6L_3 \dot{\varphi}_2 (g \sin(\varphi_2 + \varphi_3) - \\ &+ 2l_2 \sin(\varphi_3) \ddot{\varphi}_2) + 4l_3 R_3 \ddot{\varphi}_3 + L_3 (-6\dot{\varphi}_3 (g \sin(\varphi_2 + \varphi_3) + \\ &+ l_2 \sin(\varphi_3) \ddot{\varphi}_2) + 3(l_3 + 2l_2 \cos(\varphi_3)) \ddot{\varphi}_2 + 4l_3 \ddot{\varphi}_3))) = U_{z_3} \end{aligned}$$

4. SIMULATION

This section discusses the results of a simulation of closed-loop equations including a robot model with PD controllers (Fig. 4). The collected data will then be used in the identification algorithm.

First, the pre-determined signal was defined: $[\varphi_{z1} \varphi_{z2} \varphi_{z3}]$. The signal was assumed to be a properly delayed step function (each arm with a different delay) passing through an additional low-pass filter with a boundary frequency $\Omega_g = 0.025$ [rad/s]. The filtering was responsible for limiting the signal spectrum.

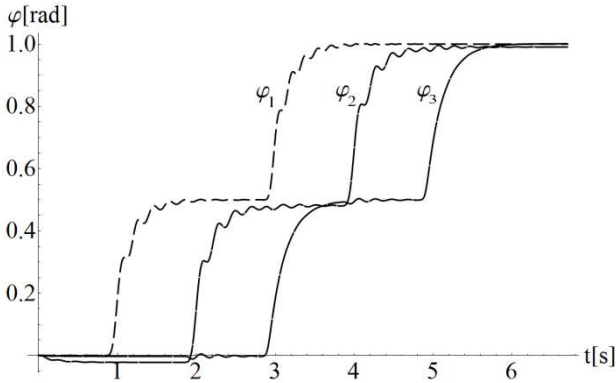


Fig. 4. Responses of $\varphi_1, \varphi_2, \varphi_3$

The responses are not satisfactory from the point of view of regulation. The aim of the study was to generate signals to be used in the identification process. It is advisable that the pre-determined signals and the controller parameters be carefully selected so that the signals provide sufficient information about the object dynamics.

5. IDENTIFICATION WITHOUT MEASUREMENT NOISE

Let us recall that the robot mass and arm length are the unknown parameters denoted as $\theta = [m_1, m_2, m_3, l_1, l_2, l_3, k_{e1}, k_{e2}, k_{e3}]$. The method used for the parameter identification is represented graphically in Fig. 1. It is assumed that the measurement data concerning the trajectories of the generalized variables and the necessary input signals are available. The estimate of the input signals, $\hat{\tau}^f$, is determined basing on the current estimates of the object parameters $\hat{\theta} = [\hat{m}_1, \hat{m}_2, \hat{m}_3, \hat{l}_1, \hat{l}_2, \hat{l}_3, \hat{k}_{e1}, \hat{k}_{e2}, \hat{k}_{e3}]$. These equations have the same structure as Eq. (23); yet, the unknown parameters θ , are replaced by the estimates $\hat{\theta}$, the generalized variables are replaced by variables filtered through a low-pass filter, and their derivatives (which are not measured) are replaced by their estimates obtained by using relevant differentiating filters. Let us assume that the boundary frequency of the differentiating filters is: $\Omega_g = 0.2$ [rad/s]. The identification requires determining the estimates of the parameters responsible for the quality factor minimization.

$$J(\hat{\theta}) = \frac{1}{T} \int_0^T (\hat{\tau}^f - \tau^f)^2 dt, \quad (24)$$

where τ^f is an input signal filtered with a low-pass filter.

The identification procedure is commenced for the following initial values: $\hat{\theta} = [99.8, 151.7, 49.9, 0.49, 1.01, 0.75, 22.95, 22.95, 23.05]$. The final values of the parameters are determined after 52 iterations of the minimization algorithm. The estimates $\hat{\theta} = [76.616, 150.133, 49.9456, 0.57938, 1.0003, 0.700715, 23.0012, 22.9996, 23.0002]$ slightly depart from the real values of the parameters, $\theta = [100, 150, 50, 0.5, 1, 0.7, 23, 23, 23]$.

6. IDENTIFICATION AND MEASUREMENT NOISE

In this point we will examine how far the elaborated filters eliminate the measurement and quantization noise (Mocak and other 2007; Rabiner and Gold 1975). We will also examine the influence of the measurement and quantization noise on the result of identification process with the use of finite elements differentiation method and elaborated filters.

The signal processing theory comprises activities aimed on selection of substantial information on the examined phenomena and elimination of redundant information. It is commonly known that the measured signals contain components resulting from the disturbances. In our case the quantization noise value is connected directly with the number of bits of the n-bit A/D converter (Lyons 1999; Pintelon and Schoukens 1990).

Using the same identification method and elaborated filters following parameters have been obtained for the noisy signal ($n=16$) $\hat{\theta} = [91.7605, 149.478, 50.8972, 0.516604, 0.9963, 0.691788, 23.0015, 22.9962, 23.0002]$, ($n=14$) $\hat{\theta} = [11.4876, 153.601, 48.2456, -1.66054, 1.00276, 0.715608, 22.9934, 22.9787, 23.0018]$.

Using the finite elements method following parameters have been obtained for the noisy signal ($n=16$) $\hat{\theta} = [-2.62172 \cdot 10^{-7}, -2.31916 \cdot 10^{-6}, 530190.0, -0.0000152889, -0.000337396, 0.000112932, 15.3375, 14.4677, 22.5499]$.

Comparing the obtained results we can state that the differential filters eliminate the measurement noise in a major degree and the parameters determined in the identification process are close to the actual ones. Traditional differentiation does not ensure noise elimination and the identified parameters differ significantly from the actual ones.

Using the elaborated filters in identification methods we obtain well determined parameters in case of quantization on the level of 16-bit cards.

7. CONCLUSIONS

In contrast to the conventional output error method, which involves comparing and estimating input signals, the input error method is considerably faster. The identification procedure does not require solving a series of differential equations in each iteration of the algorithm minimizing the quality factor.

It should be noted that the spectrum of the pre-determined signals is limited. In spite of the fact that the robot system is a non-linear system, the following relationship is obtained for the filtered signals: $\hat{\tau}^f \cong \tau^f$ if $\hat{\theta} = \theta$. As the slight differences are due to the system non-linearity and quantization errors, the equation can be solved approximately.

Elaborated differential filters have low-pass character. This feature enables removing of high-frequency components of the

signal, for example the noise. Differential filters ensure determining of appropriate derivatives of signal with errors far more less than simple differentiation methods, what plays particularly important role in the identification process. In various calculations which have been performed, proper operation of the method for more complicated mechanical systems and for systems of greater number of identified parameters has been stated.

REFERENCES

1. **Cedro L., Janecki D.** (2009), Differential filters and the identification of a manipulator using Mathematica software, *XXXIV. Seminar ASR '2009 Instruments and Control*, Ostrava, ISBN 978-80-248-1953-2.
2. **Cedro L., Janecki D.** (2011), Model parameter identification with nonlinear parameterization applied to a manipulator model, *Monographic series of publications-Computer science in the age of XXI century*, ISBN 978-83-7789-006-6, ISBN 978-83-7351-324-2.
3. **Janecki D., Cedro L.** (2007), Differential Filters With Application To System Identification, *7th European Conference of Young Research and Science Workers in Transport and Telecommunications TRANSCOM 2007*, Žilina, Slovakia, p. 115.
4. **Kowal J.** (2004), *Fundamentals of control engineering*. Vol. II, UWND, Kraków.
5. **Lyons R. G.** (1999), *An introduction to digital signal processing* (in Polish), WKiŁ, Warsaw.
6. **Mocak J., Janiga I. I., Rievaj M., Bustin D.** (2007), The Use of Fractional Differentiation or Integration for Signal Improvement, *Measurement Science Review*, Volume 7, Section 1, No. 5.
7. **Pintelon R., Schoukens J.** (1990), Real-Time Integration and Differentiation of Analog Signals by Means of Digital Filtering, *IEEE Transactions on Instrumentation and Measurement*. Vol. 39. No. 6.
8. **Rabiner L. R. and Gold B.** (1975), *Theory and Application of Digital Signal Processing*, Prentice-Hall, Inc.: Englewood Cliffs, NJ.

IDENTIFICATION OF INTERNAL LOADS AT THE SELECTED JOINTS AND VALIDATION OF A BIOMECHANICAL MODEL DURING PERFORMANCE OF THE HANDSPRING FRONT SOMERSAULT

Adam CZAPLICKI*, Krzysztof DZIEWIECKI**, Tomasz SACEWICZ*

*Faculty of Physical Education and Sport, Academy of Physical Education in Warsaw, ul. Akademicka 2, 21-500 Białą Podlaską, Poland

**Institute of Applied Mechanics and Power Engineering, Technical University of Radom, ul. Krasickiego 54, 26-600 Radom, Poland

adam.czaplicki@awf-bp.edu.pl, krzysztof.dziewiecki@pr.radom.pl, tomasz.sacewicz@awf-bp.edu.pl

Abstract: The handspring front somersault in pike position is analyzed in this paper. The computations have been based on a three-dimensional model of the human body defined in natural coordinates. The time histories of net muscle torques and internal reactions at the ankle, knee, hip and upper trunk-neck joints have been obtained after the solution of the inverse dynamics problem. The sagittal, frontal and transverse plane components of selected net muscle torques and internal reactions are presented and discussed in the paper. It has also been demonstrated that natural coordinates provide a useful framework for modelling spatial biomechanical structures.

Key words: Biomechanics, Modelling, Natural Coordinates, Internal Loads, Somersault

1. INTRODUCTION

There are several hundred classified bounds in men's artistic gymnastics. Blank jump is the only one among them associated with the name of a Polish athlete. It is reasonable then that this jump deserves biomechanical identification by domestic researchers. Since none of Polish gymnasts is currently able to perform Blank jump effectively, numerical simulations remain the basic tool to investigate this jump. The valuable input data for such simulations can be obtained through a dynamic analysis of the handspring front somersault, which differs from Blank jump for one revolution only in the airborne phase.

The first aim of this paper is thus to identify internal and external loads when performing the handspring front somersault.

The second aim is to validate a 3D biomechanical model of the human body, defined in natural coordinates, used earlier in the biomechanical analyses of a long jump (Czaplicki et al., 2006), and a backward somersault from the standing position (Czaplicki, 2009). The handspring front somersault gives an opportunity to verify this model in a movement with two support phases and external loads acting on lower and upper extremities, respectively.

2. BIOMECHANICAL MODEL

The kinematic structure of the biomechanical model is defined in natural coordinates. It is composed of 33 rigid bodies originating from the pelvis in open chain linkages (Fig. 1). The rigid bodies that form the neck, arms, forearms, thighs, shanks, upper torso (numbers in circles from 19 to 25) and the lower torso (numbers 6, 7, 8) are defined by the Cartesian coordinates of two points and one unit vector each. The hands, feet and the head are defined by the coordinates of three points and one unit vector. The complete set of rigid bodies is described by means of 25 points and 22 unit vectors, accounting for a total number of 141 natural coordinates.

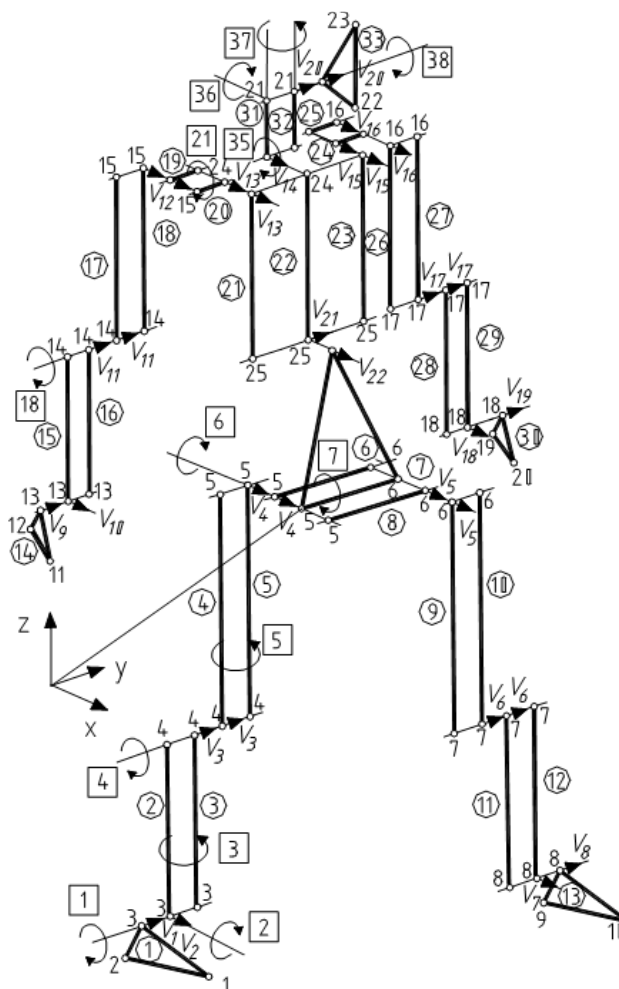


Fig. 1. Biomechanical model of the human body

The biomechanical model comprises revolute and universal joints only. The latter ones are situated in the ankle, the radioulnar

articulations, between the 12th thoracic and 1st lumbar vertebrae (the lower-upper torso joint), and between the 7th cervical and 1st thoracic vertebrae (the upper torso-neck joint).

The model has 44 degrees-of-freedom. Thirty eight of them are attributed to rotations about the revolute and universal joints (Czaplicki et. al, 2006; Czaplicki, 2009a,b). The remaining 6 degrees-of-freedom are from the translational and rotational motion of the pelvis (Fig. 1), which is treated as the base body. The degrees-of-freedom discussed in the paper are shown in Fig. 1 (numbers in squares) demonstrating the way they have been defined.

In order to solve the inverse dynamics problem each degree-of-freedom of the biomechanical model has been associated with appended driving constraints of the dot product type (Nikravesh, 1988). An example of these constraints, coupled to 18th degree-of-freedom, is illustrated in Fig. 2.

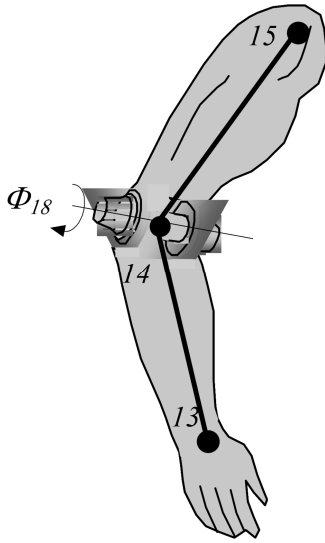


Fig. 2. Driving constraints associated with the right elbow joint

The driving constraints for the right elbow joint are defined as follows:

$$\Phi_{18} = \mathbf{r}_{14,13}^T \mathbf{r}_{14,15} - |\mathbf{r}_{14,13}| |\mathbf{r}_{14,15}| \cos(\psi_{18}(t)) = 0, \quad (1)$$

where $\psi_{18}(t)$ is the angle between vectors $\mathbf{r}_{14,13}$ and $\mathbf{r}_{14,15}$, and its time characteristic is known from kinematic measurements. The complete set of driving constraints is presented in the work of Czaplicki (2009a).

It is necessary to underline that only the key features of the biomechanical model have been discussed. The explanation of double rigid bodies arrangement of most anatomical segments, their inertial properties, and rigid body constraints are described in (Czaplicki et. al, 2006; Czaplicki, 2009a,b), and Garcia de Jalón and Bayo's textbook (1993).

3. INVERSE DYNAMICS

All the constraints, including the appended ones (Fig. 2), can be written in the generic form:

$$\Phi(\mathbf{q}) = 0, \quad (2)$$

where vector \mathbf{q} contains the coordinates of the basic points, the components of the unit vectors, and the angles associated with

degrees-of-freedom of the biomechanical model.

The set of nonlinear equations (2) can be solved iteratively by means of Newton-Raphson method:

$$(\Phi_q^T \Phi_q)_i (\mathbf{q}_{i+1} - \mathbf{q}_i) = -(\Phi_q^T)_i (\Phi)_i, \quad (3)$$

where $(\Phi_q^T)_i$ denotes the Jacobian matrix of the constraints at iteration i . The least square approach is needed since the number of the constraints exceeds the number of natural coordinates.

After computing the coordinates of basic points and unit vectors, the velocities and accelerations of natural coordinates are obtained by differentiating Eq. (2) with respect to the time:

$$\Phi_q \dot{\mathbf{q}} = 0 \Rightarrow \Phi_q \ddot{\mathbf{q}} = -\dot{\Phi}_q \dot{\mathbf{q}}. \quad (4)$$

The dynamic equations of the motion for the biomechanical model can be expressed as:

$$\mathbf{M} \ddot{\mathbf{q}} = \mathbf{Q} - \Phi_q^T \boldsymbol{\lambda}, \quad (5)$$

where \mathbf{M} denotes the mass matrix of the system, the vector of accelerations, \mathbf{Q} the vector of external loads containing the gravitational forces and reactions from the ground, and $\boldsymbol{\lambda}$ is the vector of Lagrange multipliers associated with the constraints forces and net driving torques at the joints.

Having known the accelerations from (4), equation (5) can be solved for the Lagrange multipliers.

4. DATA ACQUISITION

A twenty-three-year-old member of Polish women's olympic gymnastics team, with the height of 163 cm and a body mass of 53 kg, performed several handspring vaults with a front somersault in pike position. One of the trials was chosen as the most representative and subjected to the identification. The key phases of the investigated jump have been depicted in Fig. 3. The upper pictures show the configuration of the athlete's body at the beginning and at the end of the first support phase, whereas the lower ones indicate the body position at the moment of touching the gymnastic table and after one revolution in the air.



Fig. 3. Handspring front somersault in pike position

The body motion kinematic data were simultaneously recorded by 4 synchronized cameras (Fig. 3) working at the sampling

frequency of 100 Hz. The positions of the 23 anatomical points required to reconstruct the motion of the biomechanical model were digitized in APAS package environment. The remaining stages of data acquisition process as well as handling the raw kinematic data were similar to those described elsewhere (Czaplicki, 2009a,b).

The external reactions acting on the athlete's body during support phases were not measured directly. Instead, they were obtained using Newton-Euler iterative scheme starting from the top-most segment. This procedure in natural coordinates can only be applied if Lagrange multipliers have been known earlier. A planar model of the human body (Blajer et al., 2010) was therefore used to calculate the vertical and horizontal ground reaction forces in the sagittal plane during the contact of the feet with the springboard and the hands with the gymnastic table. The medial-lateral component of the ground reaction force was calculated through optimization designed for minimizing the difference between recorded and computed trajectory of the jumper's centre of mass in the frontal plane.

The centre of pressure path during the support phases was determined using a Kistler force plate (Fig. 4), which measured two coordinates of the path while the athlete imitated the positions recorded when performing the jump.

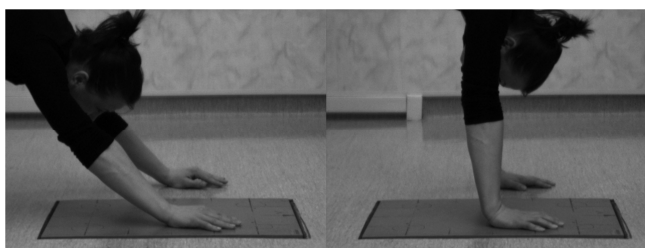


Fig. 4. Measuring the centre of pressure path for the hands

5. RESULTS AND DISCUSSION

The time histories of the component moments associated with the first, fourth and seventh degrees-of-freedom are depicted in Fig. 5. They represent the flexion or extension action of the muscles at ankle, knee, and hip joint. All the characteristics possess a clearly recognized contact phase with the springboard between 0.17 and 0.28 s. The component moment at a hip joint reaches the highest values and its negative sign indicates the action of hip extensors. The sudden change of the value of this moment to the level of -600 Nm, and other moments to the level of 200 Nm reflects the impact of the ground. The impact must be absorbed through the tendons and passive joint structures (ligaments), since the muscles are not able to generate large moments in such short periods of time (Bobbert and Zandwijk, 1999). A double peak shape of most characteristics is due to the drift of the centre of pressure as well as to large friction force at the initial contact, which is also induced by a slight slope of the springboard towards the feet. The remarkable values of the component moments about the medial-lateral and vertical axis suggest that the planar analysis of the investigated vault can produce a systematic error. It would be particularly evident for the torques at the knee and ankle joints.

The characteristics of horizontal, medial-lateral, and vertical reactions in the right leg joints are presented in Fig. 6. The damping effect of the vertical reaction between the ankle joint and the

hip joint is evident. The highest value of this reaction during contact with the springboard reaches 2400 N in the ankle joint whereas about 1500 N in the hip joint. Since small inertia effects originating from the foot can be neglected, the shape of the internal reactions in the ankle joint reflects explicitly (with the opposite sign) the profiles of the ground reaction components.

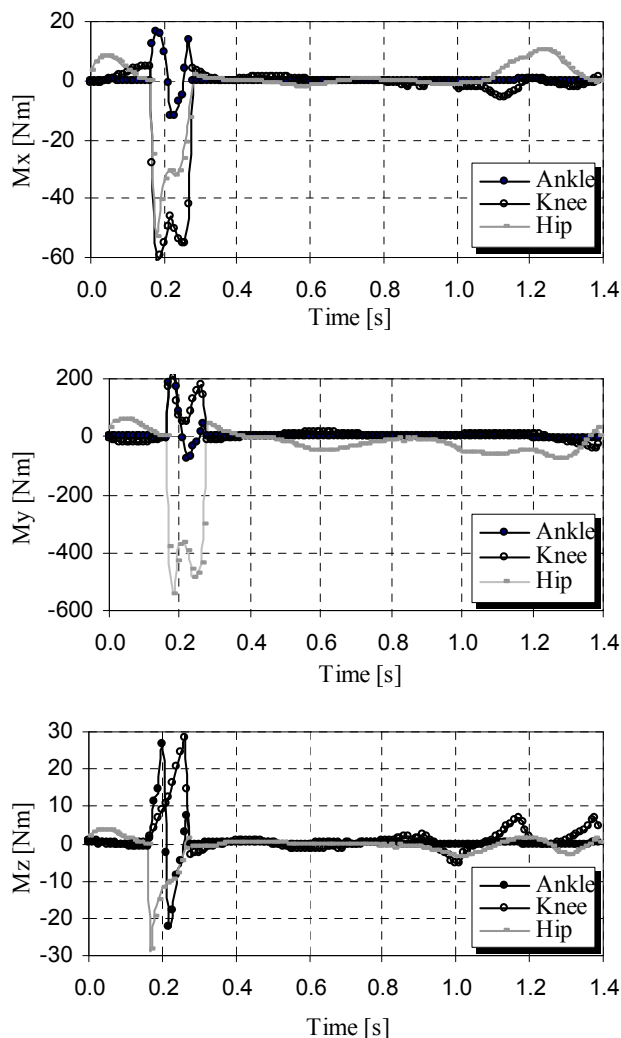


Fig. 5. Component moments associated with the 1st, 4th and 7th degrees-of-freedom

The time courses of the component moments attributed to the 21st degree-of-freedom are presented in Fig. 7. They can be identified with the movement of the arm in the sagittal plane. The highest values of the component moment (M_y) about medial-lateral axis reach the level of 60 Nm pointing out the second support phase when the hands get in touch with the gymnastic table. Low values of the other components during the jump show that the arm movement takes place firmly in the sagittal plane.

Fig. 8 presents the time histories of component moments associated with the 35th degree-of-freedom, which reflect the neck movements with respect to the trunk in the sagittal plane. The significant domination of the medial-lateral component moment is clearly visible. The peak values of this parameter occur just before the first support phase to ensure the proper orientation of the body with respect to the springboard, and after body grouping in the airborne phase to keep the head aligned with the trunk.

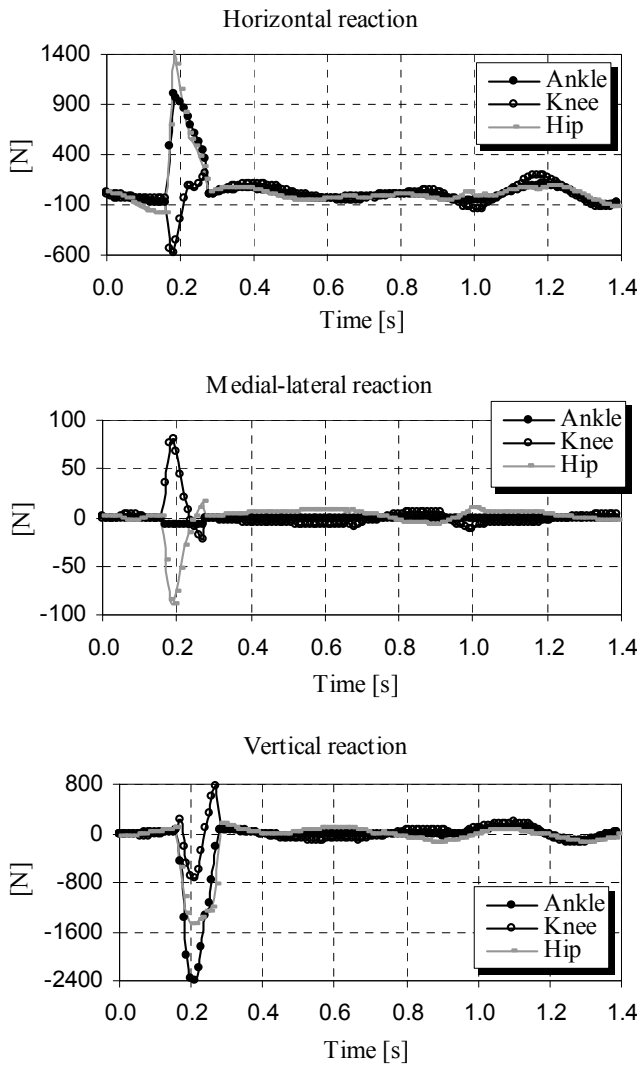


Fig. 6. Internal reactions in the joints of the right leg

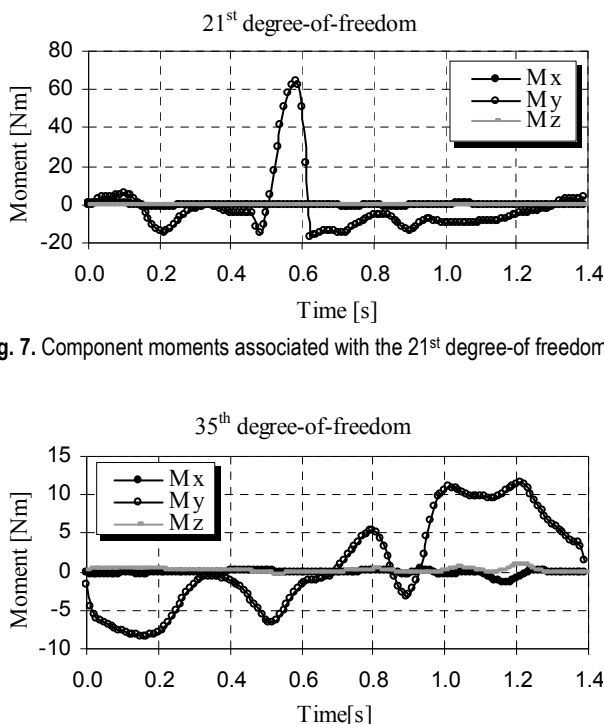


Fig. 7. Component moments associated with the 21st degree-of-freedom

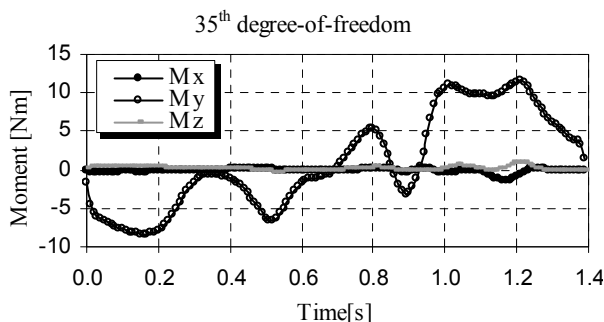


Fig. 8. Component moments associated with the 35th degree-of-freedom

A 3D state of loads at the neck-head joint, rarely described in the biomechanics literature, is shown in Fig. 9.

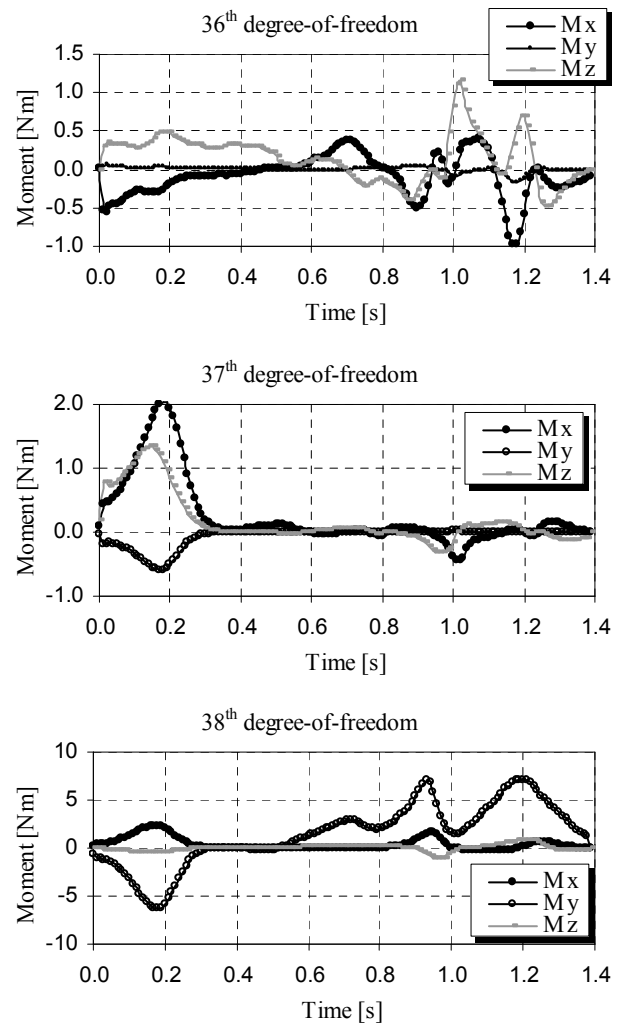


Fig. 9. Component moments associated with the 36th, 37th and 38th degrees-of-freedom

The time characteristics of component moments related to the 36th, 37th and 38th degrees-of-freedom represent side bending of the head in the frontal plane, rotation of the head with respect to the neck in the transversal plane, and flexion/extension of the head in the sagittal plane, respectively. The largest values are achieved in the sagittal plane by the component moment connected with the 38th degree-of-freedom. The time course of this component is similar to the already discussed characteristics of the upper trunk-neck joint and again, its significant domination over the other components can be easily recognized. The component moments associated with the 36th and the 37th degrees-of-freedom reach low values not exceeding the level of 2 Nm.

6. CONCLUSIONS

The work has been focused on the loads' identification in the leg, shoulder and other joints when performing the handspring front somersault in the pike position. The obtained time courses of torques and internal reactions in the joints have, apart from cognitive reasons, a clear interpretation, reflecting a distinctly impulsive character of movement during the contact with the

springboard and gymnastic table, and the nature of the other phases of the vault.

The highest values of the internal loads are in the first support phase. The net muscle torque at the hip joint reach then the level of -600 Nm whereas the internal vertical reaction in the ankle joint is about 2400 N. The maximum value of the net muscle torque at the shoulder joint is one order of magnitude lower reaching the level of 60 Nm in the second support phase.

The knowledge of load characteristics in the joints during the analyzed vault can be of interest to both athletes and gymnastics coaches.

A three-dimensional model of the human body defined in natural coordinates turned out to be effective in full rotations of individual parts of the body, and during the contact of the upper extremities with the ground. The latter aspect of the model has been checked for the first time.

Inverse simulations with different body positions just before the contact with the springboard and gymnastic table seem to be necessary in order to answer the question if a proper body configuration during both support phases influences the loads' reduction in the joints. If so, the research will gain another practical quality, since its results can help to reduce the risk of injuries.

Forward simulations with changing initial conditions, as those described by Wilson et al. (2011), are also needed to check how such perturbations can influence the quality of the vault. There is a place within these simulations to analyze Blaznik vault. The authors of this work are convinced that the presented results will be helpful to complete this task. However, knowing the specificity of integration in natural coordinates (Czaplicki, 2007) a 2D approach ought to be recommended for starting the simulations.

REFERENCES

1. **Blajer W., Dziewiecki K., Mazur Z.** (2010), Remarks on human body movement modeling for the inverse dynamics analysis, *Acta Mechanica et Automatica*, Vol. 4, No. 2, 17-24.
2. **Bobbett M., van Zandwijk J.** (1999), Dynamics of force and muscle stimulation in human vertical jumping, *Medicine and Science in Sports and Exercise*, Vol. 31, No. 2, 303-310.
3. **Czaplicki A.** (2007), Are natural coordinates a useful tool in modeling planar biomechanical linkages, *Journal of Biomechanics*, Vol. 40, No. 10, 2307-2312.
4. **Czaplicki A.**, (2009a), *Modelling in natural coordinates in biomechanics*, ZWWF, Biala Podlaska, (in Polish).
5. **Czaplicki A.**, (2009b), Identification of the internal loads at the selected joints during performance of a backward somersault, *Archive of Mechanical Engineering*, Vol. LVI, No. 3, 303-313.
6. **Czaplicki A., Silva M., Ambrósio J., Jesus O., Abrantes J.** (2006), Estimation of the muscle force distribution in ballistic motion based on multibody approach, *Computer Methods in Biomechanics and Biomedical Engineering*, Vol. 9, No. 1, 45-54.
7. **Garcia de Jalón J., Bayo E.** (1993), *Kinematic and dynamic simulations of multibody systems: the real-time challenge*, Springer Verlag, New York.
8. **Kellis E., Arabatzis F., Papadopoulos C.** (2003), Muscle co-activation around the knee in drop jumping using the cocontraction index, *Journal of Electromyography and Kinesiology*, Vol. 13, No. 3, 229-238.
9. **McNitt-Grey J., Hester D., Mathiyokom W., Munkasy B.** (2001), Mechanical demand and multijoint control during landing depend on orientation of the body segments relative to the reaction force, *Journal of Biomechanics*, Vol. 34, No. 11, 1471-1482.
10. **Nikravesh P. E.**, (1988), *Computer-aided analysis of mechanical systems*, Prentice Hall, Englewood Cliffs.
11. **Wilson C., King M., Yeadon M.** (2011), The effects of initial conditions and takeoff technique on running jumps for height and distance, *Journal of Biomechanics*, Vol. 44, No. 12, 2207-2212.
12. **Yeadon M., King M., Forrester S., Caldwell G., Pain M.**, (2010), The need for muscle co-contraction prior to landing, *Journal of Biomechanics*, Vol. 43, No. 2, 364-369.

This work was financed in part from the government support of scientific research for years 2010-2012, under grant N N501156438.

PRACTICAL EXAMPLES OF THE DETERMINATION OF PERIODICAL INSPECTION FREQUENCY IN MACHINERY SAFETY SYSTEMS

Marek DŹWIAREK*

*Central Institute for Labour Protection – National Research Institute, ul. Czerniakowska 16, 00-701 Warsaw, Poland

madzw@ciop.pl

Abstract: The paper deals with the problem of choosing an appropriate inspection interval for monitoring of safety related control systems in machinery. According to international standards the safety related systems are categorized according to their Safety Integrity Levels or Performance Levels, depending on their reliability parameters. Extremely simple, approximate models have been proposed in order to provide practitioners without reliability training with useful tools for the determination of inspection policies. The method(s) based on the required availability of the system. The paper presents some practical examples of systems of categories B, 1 and 3, respectively. The frequencies of periodical inspection are calculated for: system monitoring closure of the door, behind which a dangerous element moves slowly, system of monitoring the access door on the automated production line and system, in which a light curtain is employed to monitor the access to the dangerous zone of an automatic assembly machine.

Key words: Safety of Machinery, Safety Related Parts of Control System, Functional Safety, Periodical Inspection

1. INTRODUCTION

In the course of electronic technology development it can be observed that machine control systems despite their operational functions perform also more and more safety functions. More and more complex electronic systems, for example vision systems (Grabowski et al., (2011)), are applied as protective systems for machinery. General roles for application of such systems are well known and it is described, for example by Dźwiarek (2010). But the most important problem is ensuring proper functioning of the system on demand. The analyses of accidents happened in the course of machine operation presented in Dźwiarek (2004) showed that 36% of them were caused by improper functioning of the machine control systems. Additionally, in the group of accidents caused by improper functioning of machine control systems serious accidents happened much more frequently (41%) as compared to the group of accidents with no relation to the control system (7%). Most common cause of such accidents consisted in the lack of safety functions (58%). Most often, functions like monitoring of guard position or presence in the dangerous zone were missing. Other group of accidents comprises those caused by failure of a safety-related element of the control system due to insufficient resistance to fault (26% of all accidents). Other reported causes, i.e., mistakes in definitions of safety functions (4%), errors in control system software (6%) too low resistance to environmental effects (climatic agents, power supply distortion – 6%) affected much lower number of the accidents happened. Those results proved that machine control systems are very important in view of the safety of machine operators. Therefore, designers of the safety related control systems should apply the structures that improve their resistance to fault, which most frequently means the application of reliable elements and redundant architecture of the systems. But, in preventing the accidents due to improper operation of the control system periodical inspection of its functioning is also of crucial importance. Therefore, the

control system designer should specify how often the system should undergo the periodical inspection. Unfortunately, in the binding standards, there are no suggestions on how to determine the frequency of periodical inspection of the control system. The aforementioned problem has been discussed many times at meetings of the working group VG11 "Safety components" of the European Co-ordination of Notified Bodies for Machinery and Safety Components (Machinery Directive 2006/42/WE), however, no satisfactory solution has been found yet, thus the Recommendation for Use could not be developed. The research aimed at formulation of the rules for determination of periodical inspection frequency of safety related parts of control systems in machinery, as simple as possible so as to ensure that their possible defect would be detected early enough. The results of these studies have been presented in Dźwiarek and Hryniewicz (2011). The paper shows sample practical applications of those methods.

2. SAFETY FUNCTIONS PERFORMED BY THE MACHINERY CONTROL SYSTEM

Most often, a machinery control system performs both the safety functions and those irrelevant to safety. A safety function is a function, a failure of which can increase risk(s). Generally, the safety function can be implemented for the reduction of risk associated with the following three groups of hazards (Dźwiarek, 2007):

- resulting from improper machine operation,
 - resulting from the application of technological processes the physical parameters of which differ significantly from standard environmental conditions,
 - mechanical hazards.
- The following safety functions are most common:
- safety-related stop function initiated by a safeguard,
 - manual reset function,

- start/restart function,
- local control function,
- muting function,
- monitoring of parameterization of the safety-related input values,
- response time,
- monitoring of safety-related parameters such as speed, temperature or pressure,
- reaction to fluctuations, loss and restoration of power sources.

Since failure of those functions can increase the risk, therefore the designers of safety related control systems should apply the structures that improve their resistance to fault. Basic rules for improving the machinery control system resistance to fault were formulated in the following standards (Dźwiarek 2006, Dźwiarek 2007):

- IEC 62061:2005 „Safety of machinery - functional safety of safety-related electrical, electronic and programmable electronic control systems”,
- ISO 13849-1:2006 „Safety of machinery. Safety-related parts of control systems - Part 1: General principles for design”, where, depending on their behaviour under fault conditions the devices were classified into 5 categories.

In standard IEC 62061:2005 the functional safety methodology formulated in IEC 61508:2001 “Functional safety of electrical/electronic/ programmable electronic safety-related systems” was adapted so as to be applicable to machinery control systems. For each safety-related control system performing the defined safety-related function the probabilistic criteria for assessing their resistance to fault (named the Safety Integrity Level) are defined in IEC 62061.

Standard ISO 13849-1 formulates a simplified method for the assessment of machinery control systems. The following parameters are characteristic of each system: *Structure (Category)*, *Mean time to failure (MTTF)*, *Diagnostic coverage (DC)* and *Common cause failure factor (CCF)*. Those parameters are divided into the following qualitative groups: high, medium, low. The expected safety performance level is determined from a graph into which the assessed parameters and the system architecture (single channel, redundancy, monitoring, etc.) have been included. It allows for assessment of the designed system in a relatively simple way. The performance level (PL) represents the system resistance to faults. The relationship between the performance level (PL) and SIL is given in Tab. 1.

Tab. 1. Relationship between the Performance Level and SIL (ISO 13849-1)

Performance level (PL)	Probability of a dangerous failure per hour (PFH_D)	Safety integrity level (SIL)
a	$[10^{-5}, 10^{-4})$	No correspondence
b	$[3 \times 10^{-6}, 10^{-5})$	1
c	$[10^{-6}, 3 \times 10^{-6})$	1
d	$[10^{-7}, 10^{-6})$	2
e	$[10^{-8}, 10^{-7})$	3

According to both the aforementioned standards the designer of machinery control system should determine, taking into account the results of risk assessment, the required SIL or PL for each safety function performed by the control system. The required SIL or PL should be achieved by applying the design solutions appropriate for the considered control system.

The required SIL or PL should be also maintained during the whole life time of machinery. The long-term results of using a machine usually involve consistent degradation of its sub-assemblies, due to both material deterioration and mechanical wear. The aforementioned phenomena can lead to decrease of the achieved SIL or PL. It means that all safety functions should be periodically inspected for identification of any changes in their parameters, which can reduce the ability of control system to perform its functions.

3. SIMPLIFIED ALGORITHMS FOR THE DETERMINATION OF INSPECTION INTERVALS FOR THE SAFETY RELATED CONTROL SYSTEMS

The determination issues of periodical inspection frequency of safety related systems were analyzed mainly in view of the critical infrastructure in processing industry (Taghipour et al., (2010). That resulted mainly from both the hazard levels arising there as well as high costs of stopping the process to make the inspection including its performance costs. As a result, very complicated procedures were developed for the determination of periodical inspection frequency of such systems. The procedures are far too much complicated and expensive to be applied to periodical inspection of safety devices in machinery. Mainly, due to their mathematical complexity. Therefore, the simplified procedures presented by Dźwiarek and Hryniewicz (2011) and Dźwiarek and Hryniewicz (2012) are much more suitable in such cases.

Let us consider the simplest case when the inspection allows for immediate checking if a system is ready to perform its safety function or not. The assumption that the “probability of a dangerous failure per hour” remains constant over the whole life cycle of the machine accepted in standards ISO 13849-1 and IEC 62061 means that also the availability of the system should remain unchanged in every year of its exploitation. The availability of the system, when its time to failure is represented by the exponential distribution, is given by the following simple formula:

$$A(T) = \frac{1}{PFH_D T} (1 - e^{-PFH_D T}) \quad (1)$$

If $PFH_D T \ll 1$, then the following approximation can be applied:

$$A(T) \approx 1 - \frac{1}{2} PFH_D T + \frac{1}{6} (PFH_D T)^2 \quad (2)$$

Taking into consideration the values of PFH_D given in Tab. 1 we can determine the required availability of the system per year A_r (see Tab. 2).

Tab. 2. Required availability of the system per year for particular values of SIL and PL (Dźwiarek and Hryniewicz, 2011)

Performance level (PL)	A_r	Safety integrity level (SIL)
a	0.957	No correspondence
b	0.987	1
c	0.997	1
d	0.99956	2
e	0.999956	3

It should be noted, that for the purposes of risk assessment from among the variety of possible faults one should select the

dangerous ones; i.e., those causing the safety function loss, to be considered in the process. For example, in a redundant system a failure of one channel may not necessary result in safety function loss for the whole system, since it the function is performed by the second channel. Therefore, the periodical inspections aim at detecting the faults that however do not cause the safety function loss but still result in reducing the values of SIL or PL.

According to Hryniewicz (2008), if we set the required value of the availability A_r we can find the inspection interval T_0 by solving the equation $A(T_0)=A_r$. Thus, that value can be found from the expression:

$$A_r = 1 - \frac{1}{2} \lambda T + \frac{1}{6} (\lambda T)^6 \quad (3)$$

where λ stands for the probability of any failure, not only the dangerous one.

Hence, the required inspection interval should be calculated from the following equation:

$$T_0 = \frac{3-6\sqrt{0.25-\frac{2}{3}(1-A_r)}}{2\lambda} \approx \frac{2(1-A_r)}{\lambda} \quad (4)$$

When the safety related control system has a parallel structure with two channels represented by the exponentially distributed random variables characterized by the failure rates λ_1 and λ_2 , respectively, we can use the procedure proposed in international standard ISO 13849-1, Annex D that allows one to approximate this system using an equivalent one having two identical channels characterized by the failure rate calculated from the following equation:

$$MTTF_m = \frac{2}{3} (MTTF_1 + MTTF_2 - \frac{1}{MTTF_1 + MTTF_2}) \quad (5)$$

Then, we can use:

$$T_0 = \frac{1}{\lambda} \sqrt{2(1-A_r)} \quad (6)$$

in calculation of the inspection interval.

When the inspection and repair times cannot be neglected, Hryniewicz (2008) proposed the following formula for calculation of the optimal values of inspection intervals:

$$T_0 = \sqrt{\frac{2\mu_0}{\lambda}} \quad (7)$$

where μ_0 means the time required for inspection and repair.

4. CASE STUDIES

The method presented above for determination of periodical inspection frequency of safety-related control systems in machinery was put into practice in systems of different complexity and different requirements for their fault resistance. Usually, periodical inspections of machines are carried out during their idle times and the duration of such inspection is negligible as compared to the machine working time. There are, however, cases in which the inspection time cannot be neglected, therefore both the cases have been considered.

4.1. A system of category B

The simplest systems of category B according ISO 13849-1 are applied in the case when risk from the hazard being reduced

is very small. A typical case consists in monitoring the closure of the door, behind which a dangerous element moves slowly. In such a case the risk assessment carried out following the A1 graph shown in standard ISO 13849-1 leads to the required performance level PL_r of b and $3 \times 10^{-6} \leq PFH_{Dr} < 10^{-5}$.

A proximity switch is usually applied to monitor the door closure state. A sample system of that type is shown in Fig.1. When the guard opens the power supply to motor M is cut off by relay Q1, controlled by proximity switch C1. C1 is a classical proximity switch of MTTF_D equal to 30 years. According to the manufacturer's declaration the electrical switching capacity of Q1 is $B_{10}Q1 = 10\,000$.

Since in the considered case the access door to the dangerous zone is to be opened every hour and the fraction of dangerous failure is 50% we can determine:

$$\begin{aligned} MTTF_{Q1} &= 10000 / 0.1 * 8 * 365 = 34 \text{ years} \\ MTTF_{DQ1} &= 2 * MTTF_{Q1} = 68 \text{ years} \end{aligned} \quad (8)$$

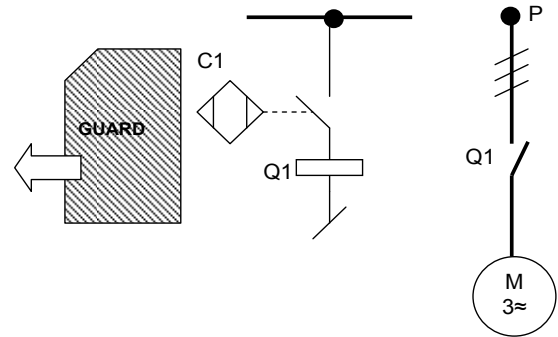


Fig. 1. Sample control system of category B

Finally, for the safety function we have:

$$\begin{aligned} MTTF_D &= \frac{1}{\frac{1}{30} + \frac{1}{68}} = 20 \text{ years} \\ PFH_D &= \frac{1}{24 * 365 * 20} = 5.71 * 10^{-6} \\ \lambda &= 2 * PFH_D = 1.14 * 10^{-5} \end{aligned} \quad (8)$$

In the case of systems of category B with no embedded mechanisms of fault detection, in which a single fault causes the loss of safety function, it is necessary to make periodical inspections. In that case the inspection consists in actuation of safety functions and verifying that the dangerous motion has been stopped. Therefore, the inspection is simple and of short duration.

In that case we apply formula (6). According to Table 2 we have:

$$T_0 = \frac{2(1-0.987)}{1.14 * 10^{-5}} = 2280h \approx 3 \text{ month} \quad (9)$$

4.2. A system of category 1

If the access door is situated by the automated production line it is opened very rarely, while the hazards created are much greater. In such a case the protection level ensured by a system of cat B is not high enough. The results of risk assessment lead to the required performance level PL_r of c and $10^{-6} \leq PFH_{Dr} < 3 \times 10^{-6}$.

It can be achieved by means of using a device monitoring the door closing that satisfies the requirements of category 1 accord-

ing ISO 13849-1. In such a case one should employ a limit switch manufactured in accordance with standard IEC 60947-5-1. Annex K. Also to stop the motor a contactor should be applied that satisfies the requirements specified for "well-tried elements" in Tab. D3 given in standard ISO 13849-2. For controlling the dangerous movement directional control valve 1V1 have been used.

In the manufacturer's declaration of the limit switch it is $B_{10} K1 = 10^6$, while in that of the contactor the durability is $B_{10} Q1 = 1.3 \times 10^6$ and $f B_{10} 1V1 = 40 \times 10^6$.

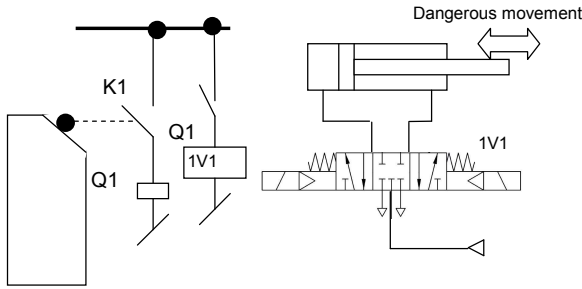


Fig. 2. Sample control system of category 1

Let us assume that the production line works twenty-four hours a day and the access to the dangerous zone should be provided once a week, and the valves 1V1 are activated every 2 minutes:

$$\begin{aligned} MTTF_{1V1} &= 40 \times 10^6 / 0.1(30 \times 24 \times 365) = 1530 \text{ years} \\ MTTF_{K1} &= 10^6 / 0.1 \times 52 = 192300 \text{ years} \\ MTTF_{Q1} &= 1.3 \times 10^6 / 0.1 \times 52 = 250000 \text{ years} \end{aligned} \quad (10)$$

and for the safety function, taking into consideration the fact that only half of faults are dangerous we have:

$$\begin{aligned} MTTF &= \frac{1}{\frac{1}{1530} + \frac{1}{192300} + \frac{1}{250000}} = 1510 \text{ years} \\ MTTF_D &= 2 \times MTTF = 3020 \text{ years} \end{aligned} \quad (11)$$

According to standard ISO 13849-1 the maximal value of $MTTF_D$ for the system of category 1 is 100 years and:

$$\lambda = PFH_D = 1.14 \times 10^{-6} \quad (12)$$

To carry out the inspection of automated production line it is necessary to stop it over the whole length. Stopping the whole production line and then restarting it is rather time-consuming and creates the need for engaging a special supervising crew, which may take a few hours. Upon the application of formula (7) we have:

$$\begin{aligned} \mu_0 &= 4h \\ T_0 &= \sqrt{\frac{2\mu_0}{\lambda}} = 2650 \approx 4 \text{ month} \end{aligned} \quad (13)$$

Which means that the safety function should be checked at least once every three months.

4.3. A system of category 3

Another example consists in the system in which a light curtain is employed to monitor the access to the dangerous zone

of an automatic assembly machine. In such a system there arises a hazard of amputation, the access to the dangerous zone is required every 1 minute and the hazard can be easily avoided. In that case the risk assessment leads to the required performance level PL_r of d and $10^{-7} \leq \lambda_r < 10^{-6}$.

In view of high frequency of its activation the system of category 3 according ISO 13849-1, the scheme of which is shown in Fig. 3, was chosen to perform the safety function. Light curtain LC has been certified as to be applied in systems up to category 4, SIL CL 3, $PFH_D LC = 5 \times 10^{-8}$, as an input sensor with two line signalling interruption of detection zone. The signal from the curtain is transmitted to a standard PLC, therefore one should assume $MTTF_{PLC} = 25$ years. The PLC switches contactor Q2, which disconnects the motor. Safety relay SR makes the redundant channel for PLC and it satisfies the requirements of category 4. In the manufacturer's declaration is specified that $PFH_D SR = 3 \times 10^{-8}$. The controller switches contactor Q1, which also disconnects the motor. In the manufacturer's declaration of contactors Q1 and Q2 it is specified that the value of parameter $B_{10} Q1, Q2 = 10^6$. The PLC also monitored supplementary contact of Q1 and Q2. According ISO 13849-1, Annex E in this case the diagnostic coverage is $DC=90\%$.

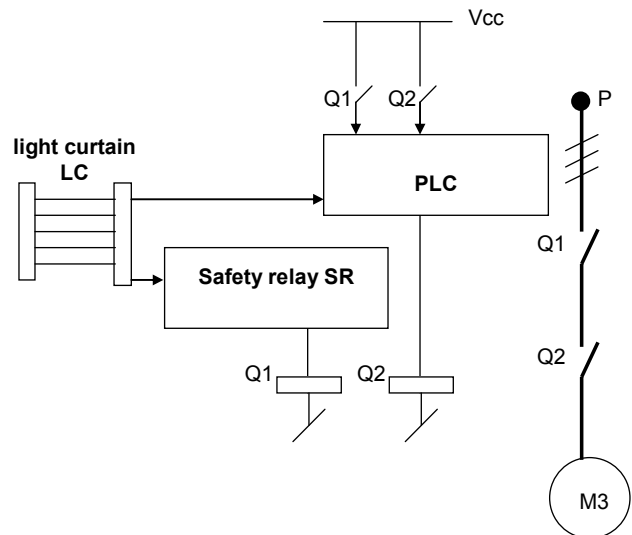


Fig. 3. Sample control system of category 3

The Reliability Block Diagram of the safety function is shown in Fig. 4.

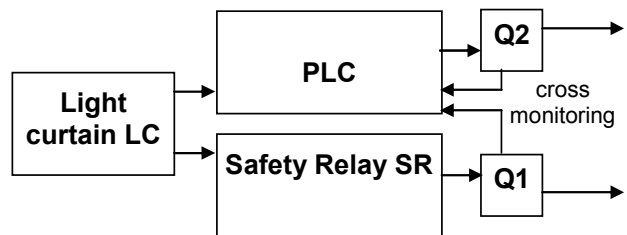


Fig. 4. Sample control system of category 3

Upon the assumption that the automatic machine works double shifts for 220 days per year and taking into consideration

the demand frequency of the safety function we arrive at:

$$\begin{aligned}MTTF_{Q1,Q2} &= 47.3 \text{ years} \\ MTTF_{D,Q1,Q2} &= 94.6 \text{ years}\end{aligned}\quad (14)$$

Now, we can determine the value of MTTF for each channel:

$$\begin{aligned}MTTF_{D,LC,PLC,Q2} &= 19.77 \text{ years} \\ MTTF_{D,LS,SR,Q1} &= 94.5 \text{ years}\end{aligned}\quad (15)$$

and:

$$\begin{aligned}MTTF_{LC,PLC,Q2} &= 16.36 \text{ years} \\ MTTF_{LC,SR,Q1} &= 47.2 \text{ years}\end{aligned}\quad (16)$$

Upon application of the symmetrization formula (5) we have:

$$\begin{aligned}MTTF_D &= 65.28 \text{ years} \\ MTTF &= 34.27 \text{ years}\end{aligned}\quad (17)$$

According to ISO 13849-1, Table K1 we can assume:

$$\begin{aligned}PFH_D &= 2.13 \cdot 10^{-7} \\ \lambda &= 3.33 \cdot 10^{-6}\end{aligned}\quad (18)$$

In the aforementioned case the periodic inspection consists in actuation of the safety function and observation of light signals generated by the light curtain and controllers S1 and PLC. The frequency of periodic inspection can be determined using formula (6):

$$T_0 = \frac{1}{3.33 \cdot 10^{-6}} \sqrt{2(1 - 0.99956)} = 8906h \approx 1 \text{ year} \quad (19)$$

5. CONCLUSIONS

The discussion presented above as well as the case study results prove that the assessment problem of resistance to faults revealed by a machine control system can be solved in a relatively simple way. Finally, we have found that the calculated periods of periodical inspections agree with commonly accepted rules for their conductance. The manufacturers of machines and protective devices should make such calculations and include the results into the "User manual" according to the requirements of Machinery Directive 2006/42/WE.

REFERENCES

1. **Dźwiarek, M.** (2004), An analysis of Accident Caused by Improper Functioning of Machine Control Systems, *International Journal of Occupational Safety and Ergonomics*, Vol. 10 No. 2, 129-136.
2. **Dźwiarek, M.** (2006), Assessment of software and hardware safety of programmable control systems of machinery, In: C. Guedes Soares & E. Zio (ed.) *Safety and Reliability for Managing Risk*, 2325-2330, Taylor & Francis Group, London, ISBN 978-0-415-42315-2.
3. **Dźwiarek, M.** (2007), Functional safety of machinery control systems - general consideration. In: Kosmowski K. T. (ed.) *Functional Safety Management in Critical Systems*: 101-114, Fundacja Rozwoju Uniwersytetu Gdańskiego, ISBN 978-83-7531-006-1.
4. **Dźwiarek, M.**, (2010), Basic Principles for Protective Equipment Application, In: *Handbook of Occupational Safety and Health* Koradecka, D., (ed.) © CRC Press, Taylor & Francis Group, LCC, ISBN 978-1-4398-0684-5, p.p. 579-592.
5. **Dźwiarek, M., Hryniewicz, O.** (2011), Periodical inspection frequency of safety related control systems of machinery – practical recommendations for the determination, In: Grall & Soares (eds.) *Advances in Safety, Reliability and Risk Management*, Taylor & Francis Group, London, ISBN 978-0-415-68379-1, 495 – 502.
6. **Dźwiarek, M., Hryniewicz, O.** (2012), Practical examples of determination of periodical inspection of safety related control systems of machinery (in Polish), *Przegląd Elektrotechniczny* 5a/2012, 290-295.
7. **Grabowski A., Kosiński R., Dźwiarek M.**, (2011) Vision safety system based on cellular neural networks, *Machine Vision and Applications*, Vol. 22, Issue 3 (2011), 581-590.
8. **Hryniewicz, O. H.** (2008), Optimal inspection intervals for maintainable equipment, In: Matorell S., Guedes Soares C., Barnett J. (Eds.): *Safety, Reliability and Risk Analysis. Theory, Methods and Applications*, Vol. 1., CRC Press, Boca Raton 2008, 581-586.
9. **Taghipour, S., Banjevic, D., Jardine, A.K.S.** (2010), Periodic inspection optimization model for a complex repairable system, *Reliability Engineering and System Safety*, 95, 944-952.

This paper has been prepared basing on the results obtained from a research task carried out within the scope of two first stages of the National Programme "Improvement of safety and working conditions" partly supported in 2008-2013 – within the scope of state services – by the Ministry of Labour and Social Policy. The Central Institute for Labour Protection – National Research Institute acts as the main coordinator of the Programme.

NUMERICAL VERIFICATION OF THE RELATIONSHIP BETWEEN THE "IN-PLANE GEOMETRIC CONSTRAINTS" USED IN FRACTURE MECHANICS PROBLEMS

Marcin GRABA*

*Kielce University of Technology, Faculty of Mechatronics and Machine Design, Al. 1000-lecia PP 7, 25-314 Kielce, Poland

mgraba@tu.kielce.pl

Abstract: In the paper, numerical verification and catalogue of the numerical solutions based on Modify Boundary Layer Approach to determine the relationship between Q-stress and T-stress are presented. Based on the method proposed by Larsson and Carlsson, the Q-stress value are calculated for some elastic-plastic materials for different value of T-stress and external load expressed by J-integral. The influence of the external load, T-stress value and material properties on Q-stress value were tested. Such catalogue may be useful during solving the engineering problems, especially while is needed to determine real fracture toughness with including the geometric constraints, what was proposed in FITNET procedures.

Key words: Fracture, Crack, Stress Fields, HRR, MBLA, in-Plane Constraints, Q-Stress, T-Stress.

1. DESCRIPTION OF THE STRESS FIELD NEAR CRACK TIP – THEORETICAL BACKGROUNDS

For mode I of loading, stress field ahead of a crack tip in elastic linear isotropic material can be given by (Williams, 1957):

$$\begin{aligned}\sigma_{11} = \sigma_{xx} &= \frac{K_I}{\sqrt{2\pi r}} \left[\cos \frac{\theta}{2} \left(1 - \sin \frac{\theta}{2} \sin \frac{3\theta}{2} \right) \right], \\ \sigma_{22} = \sigma_{yy} &= \frac{K_I}{\sqrt{2\pi r}} \left[\cos \frac{\theta}{2} \left(1 + \sin \frac{\theta}{2} \sin \frac{3\theta}{2} \right) \right], \\ \sigma_{12} = \tau_{xy} &= \frac{K_I}{\sqrt{2\pi r}} \left[\cos \frac{\theta}{2} \sin \frac{\theta}{2} \cos \frac{3\theta}{2} \right], \\ \sigma_{33} = \sigma_{zz} &= 0 \quad \text{for plane stress,} \\ \sigma_{33} = \sigma_{zz} &= \nu(\sigma_{xx} + \sigma_{yy}) \quad \text{for plane strain,}\end{aligned}\tag{1}$$

where σ_{ij} is the stress tensor, r and θ are as defined in Fig. 1, ν is Poisson's ratio, K_I is the Stress Intensity Factor (SIF).

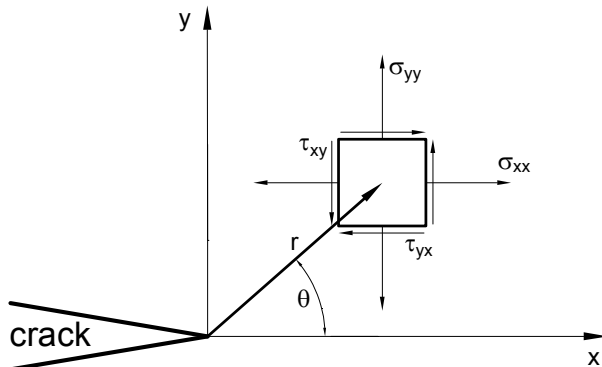


Fig. 1. Definition of the coordinate axis ahead of a crack tip
The z direction is normal to the page
(own Fig. based on (Williams, 1957))

The SIF defines the amplitude of the crack tip singularity. That is, stresses near the crack tip increase in proportion to K . Moreover, the stress intensity factor completely defines the crack tip conditions; if K is known, it is possible to solve for all components of stress, strain, and displacement as a function of r and θ .

This single-parameter description of crack tip conditions turns out to be one of the most important concepts in fracture mechanics (Williams, 1957).

In 1968, Hutchinson (1968) and Rice and Rosengren (1968) derived the singular stress-strain fields at a crack tip in a power-law hardening material (which called the HRR-field). The hardening law used by Hutchinson and Rice and Rosengren is given by:

$$\frac{\varepsilon}{\varepsilon_0} = \alpha \left(\frac{\sigma}{\sigma_0} \right)^n, \tag{2}$$

where σ_0 is a reference stress value that is usually equal to the yield strength, $\varepsilon_0 = \sigma_0/E$, α is a dimensionless constant, and n is the strain hardening exponent.

Assuming the Ramberg-Osgood material, the results obtained by Hutchinson and Rice and Rosengren for plane strain and for plane stress may be expressed in the following form:

$$\sigma_{ij} = \sigma_0 \left(\frac{J}{\alpha \sigma_0 \varepsilon_0 I_n r} \right)^{\frac{1}{1+n}} \tilde{\sigma}_{ij}(\theta, n), \tag{3}$$

$$\varepsilon_{ij} = \alpha \varepsilon_0 \left(\frac{J}{\alpha \sigma_0 \varepsilon_0 I_n r} \right)^{\frac{n}{1+n}} \tilde{\varepsilon}_{ij}(\theta, n), \tag{4}$$

where J is the J-integral, I_n is an integration constant that depends on n , $\tilde{\sigma}_{ij}(\theta, n)$ and $\tilde{\varepsilon}_{ij}(\theta, n)$ are dimensionless functions of n and θ . These parameters also depend on the stress state (i.e. plane stress or plane strain). All this function may be determined using the algorithm and computer program presented by Galkiewicz and Graba (2006).

The J -integral defines the amplitude of the HRR singularity, just as the stress intensity factor characterizes the amplitude of the linear elastic singularity. Thus, J -integral completely describes the conditions within the plastic zone. A structure in small-scale yielding has two singularity-dominated zones: one in the elastic region, where stress varies as $1/\sqrt{r}$ and one in the plastic zone where stress varies as $(1/r)^{1/(1+n)}$. The latter often persists long after the linear elastic singularity zone has been destroyed by crack tip plasticity.

The HRR singularity contains the same apparent anomaly as the linear elastic fracture mechanics singularity; namely, both predict infinite stresses as $r \rightarrow 0$. The singular field does not persist all the way to the crack tip, however. The large strains at the crack tip cause the crack to blunt, which reduces the stress triaxiality locally. The blunted crack tip is a free surface; thus σ_{xx} must vanish at $r = 0$.

The analysis that leads to the HRR singularity doesn't consider the effect of the blunted crack tip on the stress fields, nor does it take account of the large strains that are present near the crack tip. This analysis is based on small strain theory, which is the multi-axial equivalent of engineering strain in a tensile test. Small strain theory breaks down when strains are greater than about 10%.

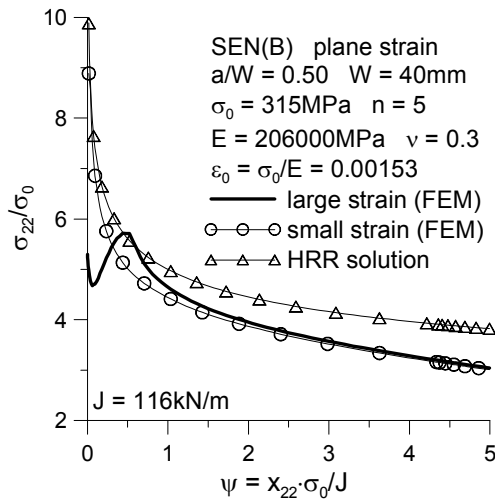


Fig. 2. The stress distribution near a crack tip (curves were obtained using the FEM for small and finite strain and HRR formula)

McMeeking and Parks (1979) performed crack tip finite element analyses that incorporated large strain theory and finite geometry changes. Some of their results are shown in Fig. 2, which is a plot of stress normal to the crack plane versus distance. The HRR singularity is also shown on this plot. Note that both axes are dimensionless in such a way that both curves are invariant, as long as the plastic zone is small compared to specimen dimensions. The solid curve in Fig. 2 reaches a peak when the ratio $x \cdot \sigma_0 / J$ is approximately unity, and decreases as $x \rightarrow 0$. This distance corresponds approximately to twice the Crack Tip Opening Displacement (CTOD). The HRR singularity is invalid within this region, where the stresses are influenced by large strains and crack blunting.

Presented above solutions for stress (Eq. (1) for linear fracture mechanics and Eq. (3) for nonlinear fracture mechanics) only describe the near tip field and consider only the first term of Taylor expansion. In the linear case, the second term in the Taylor expansion corresponds to the so called T -stress which acts in the

direction parallel to the crack advance direction. The mode I stress field becomes:

$$\sigma_{ij} = \frac{K_I}{\sqrt{2\pi r}} f_{ij}(\theta) + \begin{bmatrix} T & 0 & 0 \\ 0 & 0 & 0 \\ 0 & 0 & \nu T \end{bmatrix}, \quad (5)$$

here T is a uniform stress in the x direction (which induces a stress νT in the z direction in plane strain).

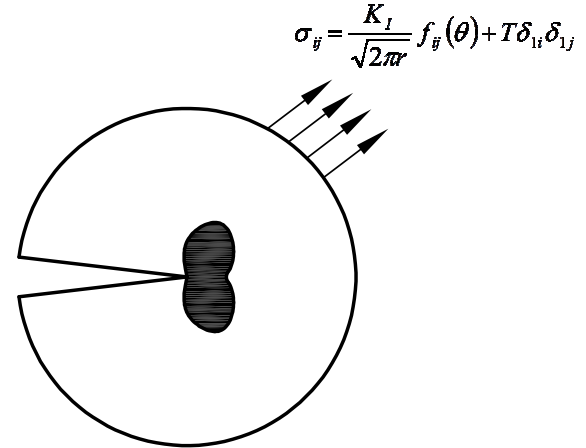


Fig. 3. Modified boundary layer analysis. The first two terms of the Williams series are applied as boundary conditions (own Fig. based on Anderson, (1995))

The more common form of Eq. (9) is the following entry:

$$\sigma_{ij} = \frac{K_I}{\sqrt{2\pi r}} f_{ij}(\theta) + T\delta_{ij}\delta_{1j}, \quad (6)$$

where δ_{ij} is the Kronecker delta.

We can assess the influence of the T stress by constructing a circular model that contains a crack, as illustrated in Fig. 3. On the boundary of this model, let us apply in-plane tractions that correspond to Eq. (5). A plastic zone develops at the crack tip, but its size must be small relative to the size of the model in order to ensure the validity of the boundary conditions, which are inferred from an elastic solution. This configuration, often referred to as a modified boundary layer analysis, simulates the near tip conditions in an arbitrary geometry, provided the plasticity is well contained within the body.

Fig. 4 is a plot of finite element results from a modified boundary layer analysis (Neimitz et al., 2007) that show the effect of the T stress on stresses deep inside the plastic zone, obtained for large strain assumption. The special case of $T=0$ corresponds to the small-scale yielding limit, where the plastic zone is a negligible fraction of the crack length and size of the body, and the singular term uniquely defines the near-tip fields. The single-parameter description is rigorously correct only for $T=0$. Note that negative T values cause a significant downward shift in the stress fields. Positive T values shift the stresses to above the small-scale yielding limit, but the effect is much less pronounced than it is for negative T stress.

Note that the HRR solution does not match the $T=0$ case. The stresses deep inside the plastic zone can be represented by a power series, where the HRR solution is the leading term. Fig. 4 indicates that the higher order plastic terms are not negligible when $T=0$.

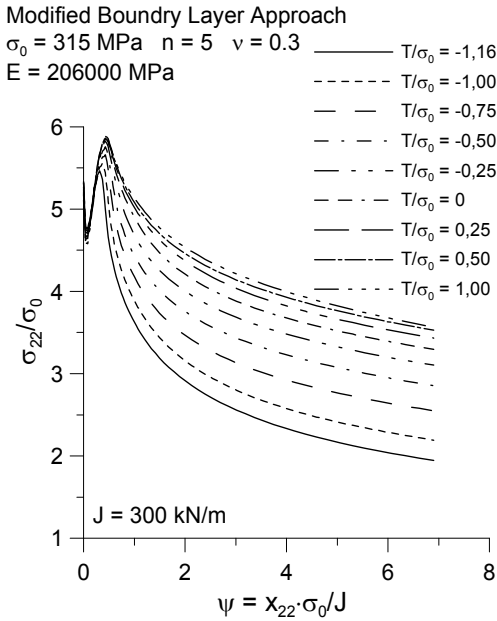


Fig. 4. The stress distribution in front of the crack, computed using modified boundary layer approach for constant SIF, K_I , and changing T -stress. Properties of material like in the Sumpter and Forbes paper (Sumpter and Forbes, 1992)

In a cracked body subject to Mode I loading, the T stress, like K_I , scales with the applied load. The biaxiality ratio relates T to stress intensity:

$$\beta = \frac{T\sqrt{\pi a}}{K_I}, \quad (7)$$

where a is the crack length.

For a through-thickness crack in an infinite plate subject to a remote normal stress $\beta = -1$. Thus a remote stress induces a T stress of $-\sigma$ in the x direction.

In the nonlinear fracture mechanics, the Q factor was introduced by O'Dowd and Shih (1991, 1992) to account for difference between the HRR field and finite element results. The Q factor (also called Q -stress) corresponds to an additional hydrostatic pressure. The modified by O'Dowd and Shih stress field is obtained as:

$$\sigma_{ij} = (\sigma_{ij})_{HRR} + Q\sigma_0\delta_{ij}, \quad (8)$$

where $(\sigma_{ij})_{HRR}$ is given by Eq. (3).

For small scale yielding, Eq. (8) can be written in the following form:

$$\sigma_{ij} = (\sigma_{ij})_{T=0} + Q\sigma_0\delta_{ij}. \quad (9)$$

The Q parameter can be inferred by subtracting the stress field for the $T=0$ reference state from the stress field of interest. O'Dowd and Shih and most subsequent researchers defined Q as follows:

$$Q = \frac{(\sigma_{yy}) - (\sigma_{yy})_{T=0}}{\sigma_0} \text{ for } \theta=0 \text{ and } \frac{r\sigma_0}{J} = 2. \quad (10)$$

Referring to Fig. 4, we see that Q is negative when T is negative. For the modified boundary layer solution, T and Q are uniquely related.

Fig. 5 is a plot of Q versus T for a two work hardening exponents. A relation between Q and T stress, based on numerical calculations, using large strain theory and incremental strain plasticity is given by O'Dowd and Shih (1991) as:

$$Q \approx a_0 + a_1(T/\sigma_0) + a_2(T/\sigma_0)^2 + a_3(T/\sigma_0)^3, \quad (11)$$

where coefficients a_0 , a_1 , a_2 and a_3 were given only for two work hardening exponents: for $n=5$: $a_0=-0.10$, $a_1=0.76$, $a_2=-0.32$, $a_3=-0.01$ and for $n=10$: $a_0=-0.10$; $a_1=0.76$, $a_2=-0.52$, $a_3=0$. Proposed by Eq. (11) relationship is the result of the matching mathematical formula to numerical results.

In 1995 O'Dowd (O'Dowd, 1995) was proposed, to describe the relationship between Q and T stress by linear formula, as

$$Q = \begin{cases} T/\sigma_0 & \text{for } T/\sigma_0 < 0 \\ 0.5 \cdot T/\sigma_0 & \text{for } T/\sigma_0 > 0 \end{cases}. \quad (12)$$

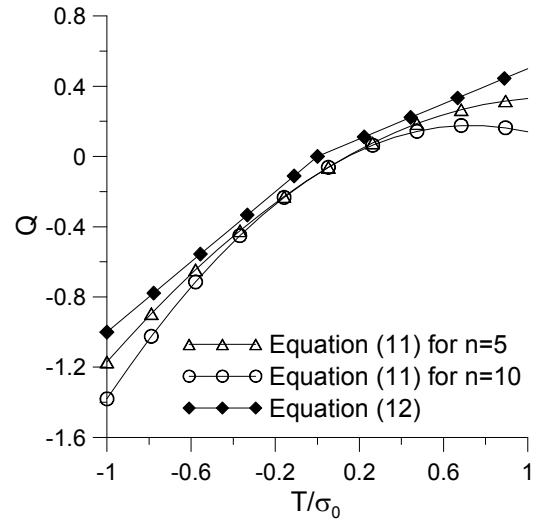


Fig. 5. Relationship between Q and T stress, based on Equations (11) and (12) (based on O'Dowd and Shih (1991))

Fig. 5 shows graphically the mutual relationship between the Q and T stress, based on formulas (11) and (12). The use of both dependencies is relatively simple. In the case of formula (11) must know the values of the coefficients a_0 , a_1 , a_2 and a_3 . Seems to be easier to use formula (12), because it is required only knowledge level of T stress, which for various geometries can be found in the literature (Sherry et al., 1991), (Leevers and Radon, 1983).

When Equation (12) will be used in analysis of the real structural element, as can be observed, this formula did not take into account the geometry characterization, for example material properties, external load, kind of specimen. Formula (12), takes into account only crack length, because, T stress depend on relative crack length (Leevers and Radon, 1983).

However, thanks to its simplicity, Equation (12) has found use in the solving engineering problems and it was recommended by FITNET procedures (FITNET, 2006). It should be noted that both Equations - (11) and (12) were based on analysis of small scale yielding, based on Modify Boundary Layer Approach (MBLA).

It should be noted also that both Equations generally do not include external load, which in the case of plane strain strongly affects the Q stress level.

2. UTILIZATION OF THE CONSTRAINT PARAMETERS IN THE EVALUATION OF FRACTURE TOUGHNESS

Both constraint parameters, the Q and T stress were found application in European Engineering Programs, like SINTAP (SINTAP, 1999) and FITNET (FITNET, 2006). The Q -stress or T -stress is applied under construction of the fracture criterion and to assessment the fracture toughness of the structural component. Real fracture toughness K_{mat}^C , may be evaluated using the formula proposed by Ainsworth and O'Dowd (1994). Ainsworth and O'Dowd have shown that the increase in fracture in both the brittle and ductile regimes may be represented by an expression of the form:

$$K_{mat}^C = \begin{cases} K_{mat} & \beta L_r > 0 \\ K_{mat} [1 + \alpha(-\beta L_r)^k] & \beta L_r < 0 \end{cases} \quad (13)$$

where K_{mat} is the fracture toughness for plane strain condition obtained using FITNET procedures, and β is the parameter calculated using following formula:

$$\beta = \begin{cases} T/(L_r \sigma_0), & \text{for elastic materials,} \\ Q/L_r, & \text{for elastic-plastic materials,} \end{cases} \quad (14)$$

where L_r is the ratio of the actual external load P and the limit load P_0 (or the reference stress), which may be calculated using FITNET procedures (FITNET, 2006).

The constants α and k which are occurring in Eq. (13), are material and temperature dependent (Tab. 1). Sherry and et al., (2005a, b) proposed the designation procedures to calculate the constants α and k . Thus J - Q and K - T theories have practical application in engineering issues.

Tab 1. Some values of the α and k parameters, which are occurring in Eq. (13) (SINTAP, 1999; FITNET, 2006)

material	temperature	fracture mode	α	k
A533B (steel)	-75°C	cleavage	1.0	1.0
A533B (steel)	-90°C	cleavage	1.1	1.0
A533B (steel)	-45°C	cleavage	1.3	1.0
Low Carbon Steel	-50°C	cleavage	1.3	2.0
A515 (steel)	+20°C	cleavage	1.5	1.0
ASTM 710 Grade A	+20°C	ductile	0.0	1.0
			0.6	1.0
			1.0	2.0

The reciprocal relationship between "in-plane constraint" parameters, for what can be considered the Q -stress and T -stress may be very useful in practical engineering problems, to determination of the real fracture toughness or in failure assessment diagrams (FAD) analysis when correction of the FAD curve using constraint parameter is done (SINTAP, 1999), (FITNET, 2006).

Thus, in this paper, catalogue of the Q - T trajectories obtained using MBLA analysis will be presented. The influence of the material properties will be tested.

3. DETAILS OF THE NUMERICAL ANALYSIS

In the numerical analysis, ADINA System 8.5.4 (ADINA, 2008a, b) was used. Computations were performed for plane strain using small strain option and the Modify Boundary Layer Approach (MBLA) model. The MBLA model consists of big circle, which radius around the crack tip where the boundary conditions are modeled is 10 meters long. Due to the symmetry, only a half of the circle was modeled (see Fig. 6). The boundary conditions are modeled using the following relationship:

$$\begin{cases} u_1 = \frac{K}{E} (1+\nu) \sqrt{\frac{r}{2\pi}} \cos\left(\frac{\theta}{2}\right) \left[\kappa - 1 + 2 \sin^2\left(\frac{\theta}{2}\right) \right] + \\ + (1-\nu^2) \frac{T}{E} r \cos(\theta) \\ u_2 = \frac{K}{E} (1+\nu) \sqrt{\frac{r}{2\pi}} \sin\left(\frac{\theta}{2}\right) \left[\kappa + 1 - 2 \cos^2\left(\frac{\theta}{2}\right) \right] + \\ - \nu(1+\nu) \frac{T}{E} r \sin(\theta) \end{cases}, \quad (15)$$

where K is the stress intensity factor (SIF) calculated from J -integral value using formula $K = \sqrt{JE/(1-\nu^2)}$ – in presented in the paper numerical program the following values of the J -integral were tested: $J=\{10, 25, 50, 100, 250, 500\}$ kN/m; r and θ are polar coordinates; ν is the Poisson's ratio; E is Young's modulus; T is the T stress expressed in stress unit ($T \cdot \sigma_0$) – in presented in the paper numerical program, the following values of the T parameter were tested: $T=\{0.5, 0.25, 0, -0.25, -0.5, -1\}$; $\kappa=3-4\nu$ for plane strain; $\kappa=(3-\nu)/(1+\nu)$ for plane stress.

The radius of the crack front was equal to $r_w=5 \cdot 10^{-6}$ m. The crack tip was modeled as half of arc. The crack tip region about to $5 \cdot 10^{-4}$ m was divide into 50 semicircles. The first of them, was at least 20 times smaller then the last one. The finite element mesh was filled with the 9-node plane strain elements. The size of the finite elements in the radial direction was decreasing towards the crack tip, while in the angular direction the size of each element was kept constant. It varied from $\Delta\theta=\pi/19$ to $\Delta\theta=\pi/30$ for various cases tested.

The whole MBLA model was modeled using 2584 finite elements and 10647 nodes. The example finite element model for MBLA analysis is presented in Fig. 6.

In the FEM simulation, the deformation theory of plasticity and the von Misses yield criterion were adopted. In the model the stress-strain curve was approximated by the relation:

$$\frac{\varepsilon}{\varepsilon_0} = \begin{cases} \sigma/\sigma_0 & \text{for } \sigma \leq \sigma_0 \\ \alpha(\sigma/\sigma_0)^n & \text{for } \sigma > \sigma_0 \end{cases}, \quad \text{where } \alpha \neq 1. \quad (16)$$

The tensile properties for the materials which were used in the numerical analysis are presented below in Tab. 2. In the FEM analysis, calculations were done for sixteen material configurations, which were differed by yield stress and the work hardening exponent.

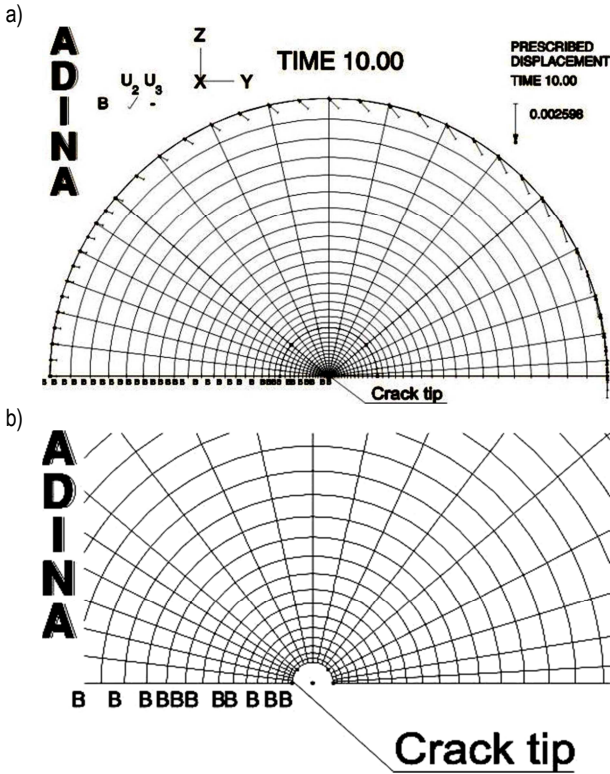


Fig. 6. The MBLA model which was used in the numerical program a); Crack tip region using in the MBLA model b)

The J -integral were calculated using two methods. The first method, called the "virtual shift method", uses concept of the virtual crack growth to compute the virtual energy change. The second method is based on the J -integral definition:

$$J = \int_C [w dx_2 - \mathbf{t}(\partial \mathbf{u} / \partial x_1) ds], \quad (17)$$

where w is the strain energy density, \mathbf{t} is the stress vector acting on the contour C drawn around the crack tip, \mathbf{u} denotes displacement vector and ds is the infinitesimal segment of contour C .

Tab. 2. The mechanical properties of the materials used in numerical analysis and the HRR parameters for plane strain

σ_0 [MPa]	E [MPa]	ν	$\varepsilon_0 = \sigma_0/E$	α	n	$\bar{\sigma}_{\theta\theta}(\theta=0)$	I_n
315	206000	0.3	0.00153	1	3	1.94	5.51
500			0.00243		5	2.22	5.02
1000			0.00485		10	2.50	4.54
1500			0.00728		20	2.68	4.21

4. RESULTS OF THE NUMERICAL ANALYSIS

Fig. 7 presents the influence of the T stress parameter value on the shape and size (denoted in Fig. as r_p) of the plastic zone near crack tip. For smaller value of the T stress parameter, the greater plastic zone is observed, if the same level of the J -integral was used to calculate the boundary conditions and the same material characteristic was established. The bigger plastic zone is observed for MBLA model characterized by smaller yield stress (see Fig. 8).

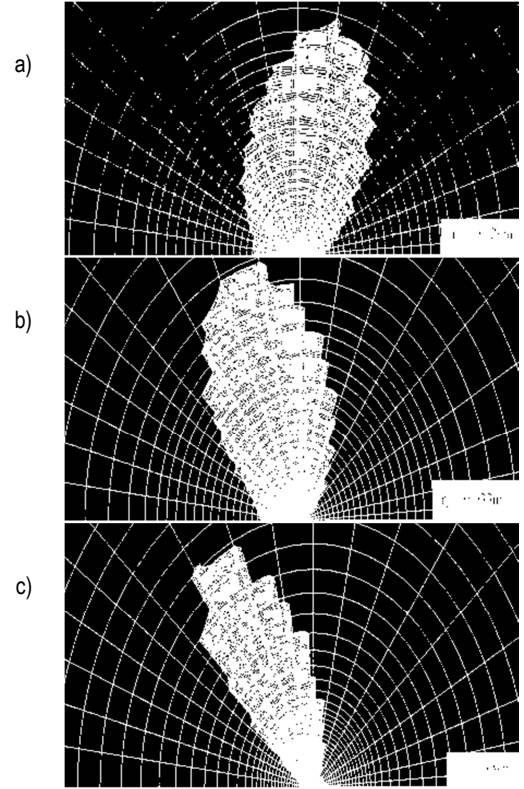


Fig. 7. Influence of the T stress parameter on shape and size of the plastic zone for MBLA model characterized by $\sigma_0=315$ MPa, $n=10$, $J=100$ kN/m: a) $T=0.5$, $r_p=0.029$ m; b) $T=0$, $r_p=0.033$ m; c) $T=-0.5$, $r_p=0.090$ m (brighter region is the plastic zone)

For smaller values of the T stress parameter the, smaller value of the Q stress are observed. The influence of the work hardening exponent on $Q=Q(T)$ trajectories should be considered for a number of configurations. For the cases characterized by yield stress $\sigma_0 \geq 500$ MPa and for J -integral values between 10 and 25kN/m (which are used to determine the boundary conditions), the lower values of the Q stress are observed for weakly strengthen materials (see Fig. 9). For theses cases almost parallel arrangement of the $Q=Q(T)$ trajectories is observed. The highest on the chart are situated curves for strongly strengthen material ($n=3$).

In other cases, when the J -integral value is equal to or greater than 50kN/m, it can be seen the intersecting of the $Q=Q(T)$ curves for different values of the work hardening exponent (see Fig. 10). For small values of the T stress parameter (which means that we are dealing with a case of high-level of the flat geometric constraints), the lower values of Q parameter are observed for weakly hardening materials. Increase value of the T stress parameter makes cutting curves and the reversal of the trend on the chart - then a smaller values of the Q parameter are observed for the case of the strongly hardening materials.

Numerical analysis shown, that the influence of the yield stress on $Q=Q(T)$ trajectories is quite complex. For small values of the J -integral ($J=10$ kN/m or $J=25$ kN/m), it can be concluded, that $Q=Q(T)$ curves characterized by regularity of arrangement, especially for strong hardening materials ($n=3$ and $n=5$). The lowest on the charts are arranged the $Q=Q(T)$ curves, described by small value of the yield stress. This means that for the materials characterized by higher yield stress, the higher values of the Q parameter are obtained (see Fig. 11).

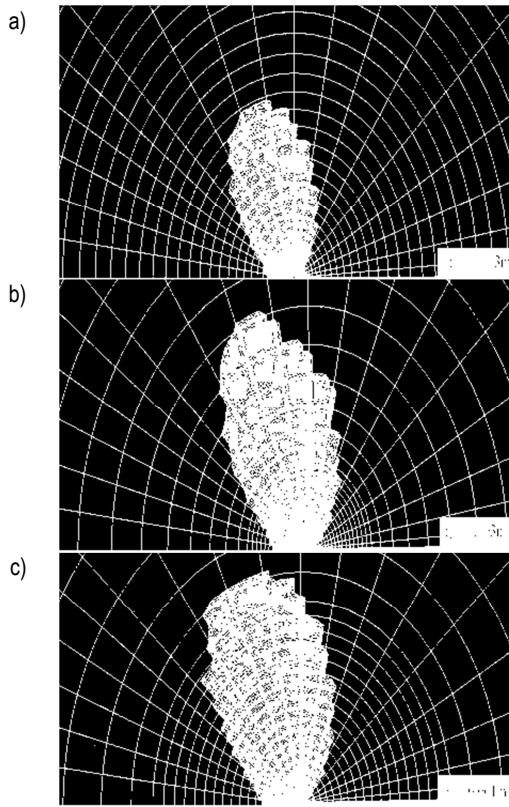


Fig. 8. Influence of the yield stress on shape and size of the plastic zone for MBLA model characterized by $T=0$, $n=10$, $J=100\text{kN/m}$:
a) $\sigma_0=500\text{MPa}$, $r_p=0.013\text{m}$; b) $\sigma_0=1000\text{MPa}$, $r_p=0.003\text{m}$;
c) $\sigma_0=1500\text{MPa}$, $r_p=0.001\text{m}$ (brighter region is the plastic zone)

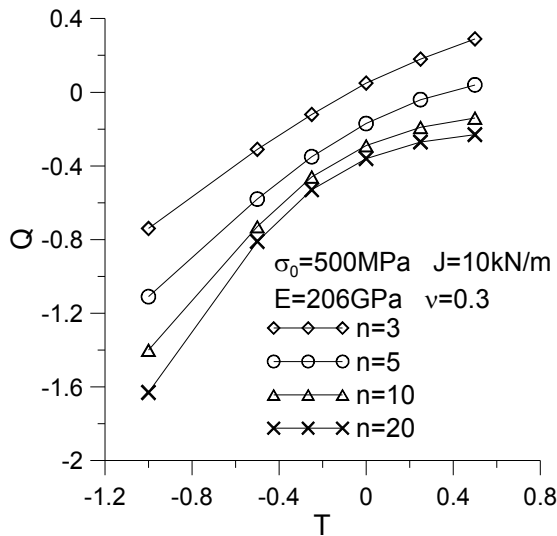


Fig. 9. The influence of the work hardening exponent on the $Q=Q(T)$ trajectories for MBLA characterized by $\sigma_0=500\text{MPa}$, $J=10\text{kN/m}$

The influence of the yield stress on $Q=Q(T)$ trajectories is significant for the low level of the J -integral which was used to determination of the boundary conditions. Sometimes the influence of the yield stress on Q stress value is negligible, when material characterized by big work hardening exponent and the level of the J -integral is quite large ($J \geq 50\text{kN/m}$). For weakly hardening materials, $Q=Q(T)$ trajectories are parallel, when J -integral characterized by very high level (for example $J=250\text{kN/m}$ or $J=500\text{kN/m}$).

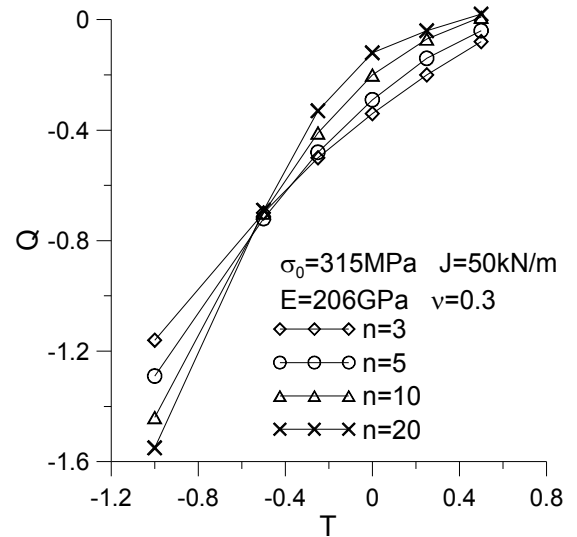


Fig. 10. The influence of the work hardening exponent on the $Q=Q(T)$ trajectories for MBLA characterized by $\sigma_0=315\text{MPa}$, $J=50\text{kN/m}$

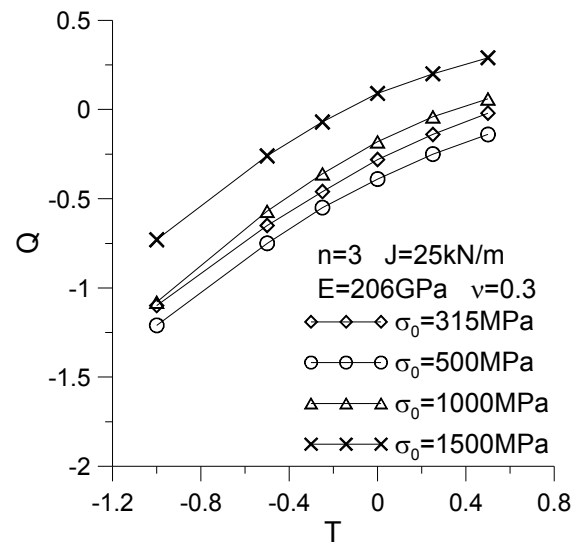


Fig. 11. The influence of the yield stress on the $Q=Q(T)$ trajectories for MBLA characterized by $n=3$, $J=25\text{kN/m}$

The most important conclusion concerns the influence of the J -integral (which is used to determination of the boundary conditions for MBLA model) on Q stress value. As shown by numerical calculations, the value of the Q parameter as a function of the T stress parameter in a very small extent depends on the J -integral value adopted to determine the boundary conditions at MBLA issue. A very little impact (hardly insignificant), or the lack of impact is characterized for MBLA models, for which the J -integral level used to determination of the boundary conditions was equal to or greater than 50kN/m (see Fig. 12).

Fig. 13 presents the influence of the work hardening exponent on Q stress value for different level of the T stress parameter, which may be considered as a measure of the "in-plane constraint" parameter. For the case of low constraints (low value of the T stress, equal to -0.5 or -1.0), Q stress value decreases when the value of the work hardening exponent increases. When the value of the T stress parameter is greater than -0.25 , it can be seen that Q stress value is constant or slightly increases if value of the work hardening exponent increases.

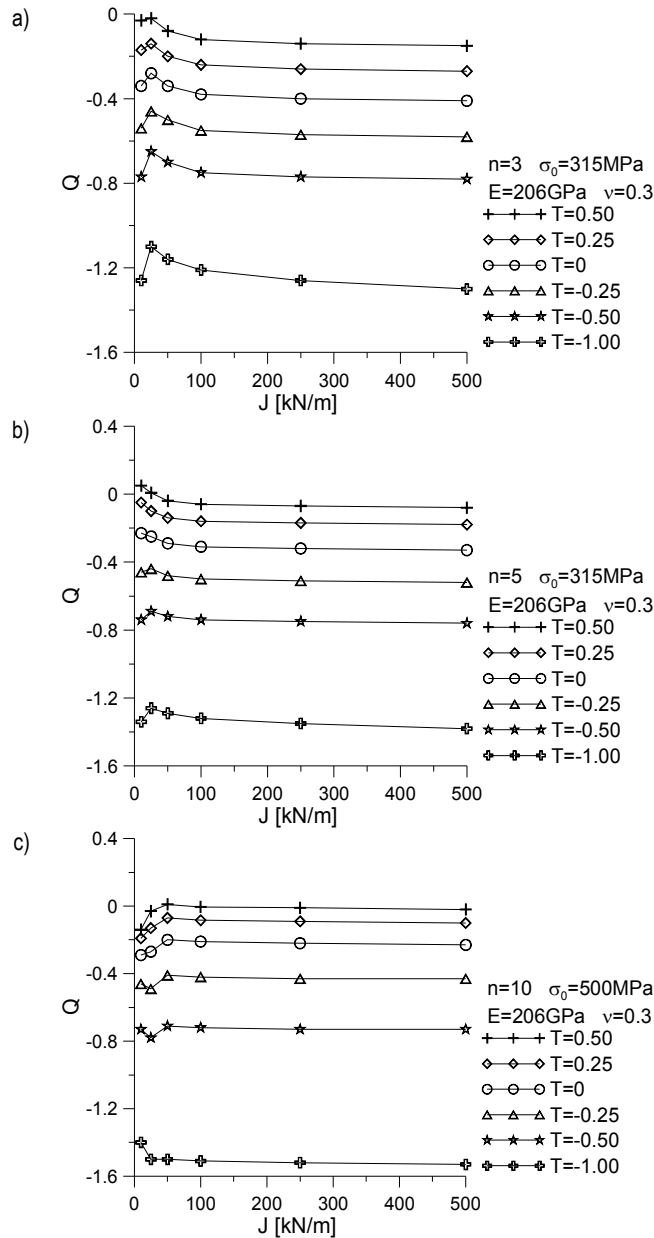


Fig. 12. The influence of the J -integral value which was used to determination of the boundary conditions, on Q stress value for different T stress parameter: a) $n=3$, $\sigma_0=315$ MPa; b) $n=5$, $\sigma_0=315$ MPa; c) $n=10$, $\sigma_0=500$ MPa

5. CONCLUSIONS

In the paper, catalogue of the numerical solutions based on Modify Boundary Layer Approach to determine the relationship between Q -stress and T -stress were presented. Based on method proposed by Larsson and Carlsson, the Q -stress value were calculated for sixteen elastic-plastic materials for different value of T -stress and external load expressed by J -integral – both parameter were used to determine the boundary conditions, which are necessary to carry out the MBLA analysis. The influence of the T -stress parameter and material properties on Q -stress value were tested.

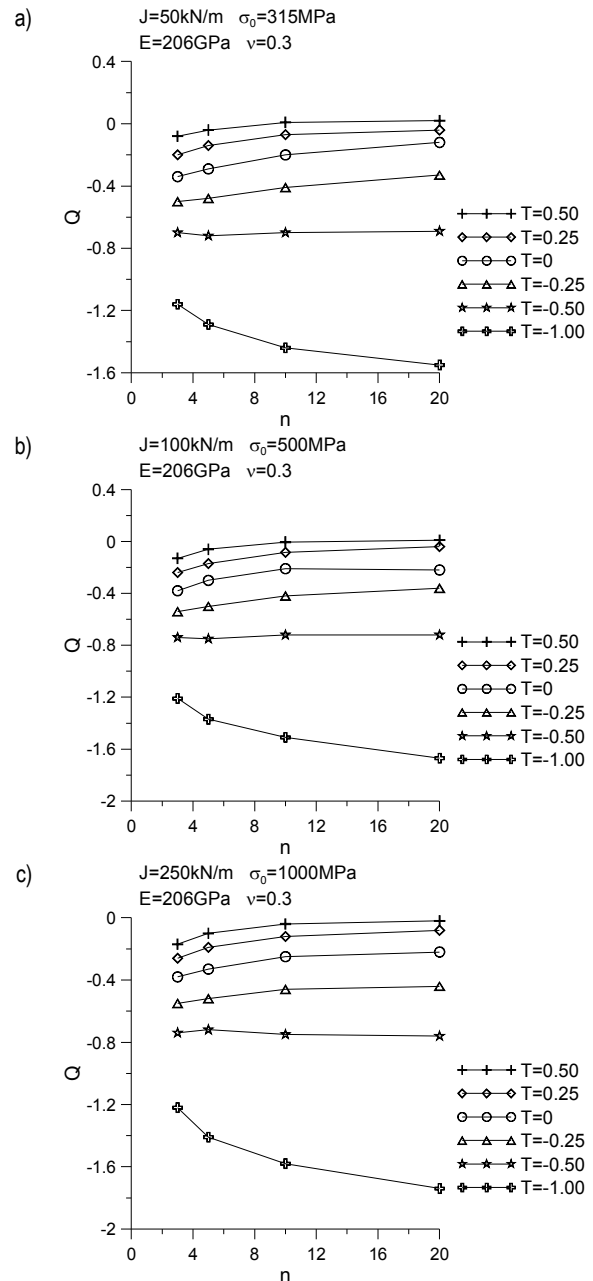


Fig. 13. The influence of the work hardening exponent on Q stress value for different level of the T stress parameter: a) $J=50$ kN/m, $\sigma_0=315$ MPa; b) $J=100$ kN/m, $\sigma_0=500$ MPa; c) $J=250$ kN/m, $\sigma_0=1000$ MPa

Obtained numerical results lead to following conclusions:

- for smaller value of the T stress parameter, the smaller value of the Q stress are observed;
- the influence of yield stress on the Q stress value is significant for the case characterized by low level of the J -integral, adopted to determine the boundary conditions at MBLA issue;
- in case of a higher level of the J -integral, it can be observed a little impact of the yield stress on the Q stress value, sometimes this effect is negligible;
- for different T stress value, Q stress value depends on work hardening exponent n ; this influence should be discussed for each MBLA models separately;
- the Q stress parameter very weak depends (or in general does not depend) on the level of the J -integral adopted

to determine the boundary conditions in MBLA issue, especially for the case when the level of the J -integral is equal to or greater than 50kN/m.

Presented in the paper such catalogue may be useful during solving the engineering problems, especially while is needed to determine real fracture toughness with including the geometric constraints, what was proposed in FITNET procedures (FITNET, 2006).

REFERENCES

1. **ADINA** (2008a), *ADINA 8.5.4: ADINA: Theory and Modeling Guide - Volume I: ADINA*, Report ARD 08-7, ADINA R&D, Inc., 2008.
2. **ADINA** (2008b), *ADINA 8.5.4: ADINA: User Interface Command Reference Manual - Volume I: ADINA Solids & Structures Model Definition*, Report ARD 08-6, ADINA R&D, Inc., 2008.
3. **Ainsworth R.A., O'Dowd N.P.** (1994), A Framework of Including Constraint Effects in the Failure Assessment Diagram Approach for Fracture Assessment, *ASME Pressure Vessels and Piping Conference*, PVP-Vol 287/MD-Vol47, ASME.
4. **Betegon, C. and Hancock, J.W.** (1991), Two Parameter Characterization of Elastic-Plastic Crack Tip Fields, *Journal of Applied Mechanics*, Vol. 58, 104-110.
5. **Bilby, B.A., Cardew, G.E., Goldthorpe, M.R., Howard, I.C.** (1986), A Finite Element Investigation of the Effects of Specimen Geometry on the Fields of Stress and Strain at the Tips of Stationary Cracks, *Size Effects in Fracture*, Institute of Mechanical Engineers, London, 37-46.
6. **FITNET Fitness for Service Procedure – Final Draft** (2006), Edited by M. Koçak, S. Webster, JJ. Janosh, RA. Ainsworth, R. Koers.
7. **Galkiewicz J., Graba M.** (2006), Algorithm for Determination of $\tilde{\sigma}_{ij}(n, \theta)$, $\tilde{\varepsilon}_{ij}(n, \theta)$, $\tilde{u}_i(n, \theta)$, $d_n(n)$ and $I_n(n)$ Functions in Hutchinson-Rice-Rosengren Solution and its 3d Generalization, *Journal of Theoretical and Applied Mechanics*, Vol. 44, No. 1, 19-30.
8. **Hutchinson J. W.** (1968), Singular Behaviour at the End of a Tensile Crack in a Hardening Material, *Journal of the Mechanics and Physics of Solids*, 16, 13-31.
9. **Irwin, G.R.** (1957), Analysis of Stresses and Strains near the End of a Crack Traversing a Plate, *Journal of Applied Mechanics*, Vol. 24, 361-364.
10. **Leevers P.S., Radon J.C.** (1983), Inherent Stress Biaxiality in Various Fracture Specimen Geometries, *International Journal of Fracture*, 19, 311-325.
11. **McMeeking, R.M. and Parks, D.M.** (1979), On Criteria for J-Dominance of Crack Tip Fields in Large-Scale Yielding, *ASTM STP 668*, American Society for Testing and Materials, Philadelphia, 175-194.
12. **Neimitz A., Graba M., Galkiewicz J.** (2007), An Alternative Formulation of the Ritchie-Knott-Rice Local Fracture Criterion, *Engineering Fracture Mechanics*, Vol. 74, 1308-1322.
13. **O'Dowd N. P.** (1995), Applications of two parameter approaches in elastic-plastic fracture mechanics, *Engineering Fracture Mechanics*, Vol. 52, No. 3, 445-46.
14. **O'Dowd N. P., Shih C. F.** (1992), Family of Crack-Tip Fields Characterized by a Triaxiality Parameter – II. Fracture Applications, *J. Mech. Phys. Solids*, Vol. 40, No. 5, 939-963.
15. **O'Dowd N. P., Shih C.F.** (1991), Family of Crack-Tip Fields Characterized by a Triaxiality Parameter – I. Structure of Fields, *J. Mech. Phys. Solids*, Vol. 39, No. 8, 989-1015.
16. **Rice J. R., Rosengren G. F.** (1968), Plane Strain Deformation Near a Crack Tip in a Power-law Hardening Material, *Journal of the Mechanics and Physics of Solids*, 16, 1-12.
17. **Rice, J.R.** (1968), A Path Independent Integral and the Approximate Analysis of Strain Concentration by Notches and Cracks, *Journal of Applied Mechanics*, Vol. 35, pp. 379-386.
18. **Sherry A.H., Hooton D.G., Beardsmore D.W., Lidbury D.P.G.** (2005), Material constraint parameters for the assessment of shallow defects in structural components – Part II: constraint – based assessment of shallow cracks, *Engineering Fracture Mechanics*, 72, 2396-2415.
19. **Sherry A.H., France C.C., Goldthorpe M.R.** (1995), Compendium of T-stress solutions for two and three dimensional cracked geometries, *Fatigue & Fracture of Engineering Materials & Structures*, Vol. 18, No. 1, 141-155.
20. **Sherry, A.H., Wilkes M.A., Beardsmore D.W., Lidbury D.P.G.** (2005), Material constraint parameters for the assessment of shallow defects in structural components – Part I: Parameter solutions, *Engineering Fracture Mechanics*, 72, 2373-2395.
21. **SINTAP** (1999), *SINTAP: Structural Integrity Assessment Procedures for European Industry. Final Procedure*, Brite-Euram Project No BE95-1426. – Rotherham: British Steel.
22. **Sneddon, I.N.** (1946), The Distribution of Stress in the Neighbourhood of a Crack in an Elastic Solid, *Proceedings*, Royal Society of London, Vol. A-187, 229-260.
23. **Sumpter J. G. D., Forbes A. T.** (1992), Constraint based analysis of shallow cracks in mild steels, *Proceedings of TWI/EWI/IS Int. Conf on Shallow Crack Fracture Mechanics, Toughness Tests and Applications*, Paper 7, Cambridge U.K.
24. **Westergaard, H.M.** (1939), Bearing Pressures and Cracks, *Journal of Applied Mechanics*, Vol. 6, 49-53.
25. **Williams, M.L.** (1957), On the Stress Distribution at the Base of a Stationary Crack, *Journal of Applied Mechanics*, Vol. 24, 109-114.

Acknowledgments: The support of the Kielce University of Technology – Faculty of Mechatronics and Machine Design through grant No 1.22/7.14 is acknowledged by the author of the paper.

ANNEX - NUMERICAL RESULTS OBTAINED FOR ALL MBLA MODELS

Tab. A.1. Results for MBLA models, characterized by $J=10\text{kN/m}$

$J=10\text{kN/m}$ $\sigma_y=315\text{MPa}$	n			
	3	5	10	20
T	Q			
0.50	-0.03	0.05	0.05	0.02
0.25	-0.17	-0.05	-0.01	-0.02
0	-0.34	-0.23	-0.16	-0.15
-0.25	-0.54	-0.46	-0.4	-0.39
-0.50	-0.77	-0.74	-0.73	-0.76
-1.00	-1.26	-1.34	-1.47	-1.65

$J=10\text{kN/m}$ $\sigma_y=500\text{MPa}$	n			
	3	5	10	20
T	Q			
0.50	0.29	0.04	-0.14	-0.23
0.25	0.18	-0.04	-0.19	-0.27
0	0.05	-0.17	-0.29	-0.36
-0.25	-0.12	-0.35	-0.46	-0.53
-0.50	-0.31	-0.58	-0.73	-0.81
-1.00	-0.74	-1.11	-1.40	-1.63

J=10kN/m $\sigma_v=1000\text{MPa}$	<i>n</i>			
	3	5	10	20
<i>T</i>	<i>Q</i>			
0.50	0.46	0.1	-0.17	-0.30
0.25	0.39	0.04	-0.19	-0.31
0	0.30	-0.04	-0.25	-0.34
-0.25	0.19	-0.16	-0.36	-0.43
-0.50	0.05	-0.33	-0.54	-0.63
-1.00	-0.29	-0.78	-1.16	-1.39
J=10kN/m $\sigma_v=1500\text{MPa}$	<i>n</i>			
	3	5	10	20
<i>T</i>	<i>Q</i>			
0.50	0.4	0.12	-0.07	-0.17
0.25	0.36	0.07	-0.11	-0.20
0	0.29	-0.01	-0.18	-0.26
-0.25	0.2	-0.13	-0.3	-0.36
-0.50	0.08	-0.28	-0.48	-0.56
-1.00	-0.21	-0.70	-1.07	-1.28

Tab. A.2. Results for MBLA models, characterized by J=25kN/m

J=25kN/m $\sigma_v=315\text{MPa}$	<i>n</i>			
	3	5	10	20
<i>T</i>	<i>Q</i>			
0.50	-0.02	0.007	0.04	0.04
0.25	-0.14	-0.10	-0.03	-0.01
0	-0.28	-0.25	-0.17	-0.15
-0.25	-0.46	-0.44	-0.38	-0.35
-0.50	-0.65	-0.69	-0.69	-0.70
-1.00	-1.10	-1.26	-1.43	-1.60
J=25kN/m $\sigma_v=500\text{MPa}$	<i>n</i>			
	3	5	10	20
<i>T</i>	<i>Q</i>			
0.50	-0.14	-0.09	-0.03	0.008
0.25	-0.25	-0.2	-0.13	-0.09
0	-0.39	-0.34	-0.27	-0.24
-0.25	-0.55	-0.53	-0.49	-0.48
-0.50	-0.75	-0.77	-0.78	-0.83
-1.00	-1.21	-1.36	-1.50	-1.66
J=25kN/m $\sigma_v=1000\text{MPa}$	<i>n</i>			
	3	5	10	20
<i>T</i>	<i>Q</i>			
0.50	0.06	0.03	-0.02	-0.07
0.25	-0.04	-0.07	-0.08	-0.11
0	-0.18	-0.21	-0.21	-0.23
-0.25	-0.36	-0.42	-0.44	-0.46
-0.50	-0.57	-0.69	-0.75	-0.80
-1.00	-1.08	-1.35	-1.59	-1.78
J=25kN/m $\sigma_v=1500\text{MPa}$	<i>n</i>			
	3	5	10	20
<i>T</i>	<i>Q</i>			
0.50	0.29	0.04	-0.16	-0.27
0.25	0.20	-0.03	-0.20	-0.29
0	0.09	-0.14	-0.29	-0.37

-0.25	-0.07	-0.31	-0.46	-0.53
-0.50	-0.26	-0.54	-0.72	-0.80
-1.00	-0.73	-1.13	-1.48	-1.7

Tab. A.3. Results for MBLA models, characterized by J=50kN/m

J=50kN/m $\sigma_v=315\text{MPa}$	<i>n</i>			
	3	5	10	20
<i>T</i>	<i>Q</i>			
0.50	-0.08	-0.04	0.009	0.02
0.25	-0.20	-0.14	-0.07	-0.04
0	-0.34	-0.29	-0.20	-0.12
-0.25	-0.50	-0.48	-0.41	-0.33
-0.50	-0.70	-0.72	-0.70	-0.69
-1.00	-1.16	-1.29	-1.44	-1.55
J=50kN/m $\sigma_v=500\text{MPa}$	<i>n</i>			
	3	5	10	20
<i>T</i>	<i>Q</i>			
0.50	-0.10	-0.04	0.01	0.02
0.25	-0.22	-0.15	-0.07	-0.12
0	-0.35	-0.29	-0.20	-0.23
-0.25	-0.52	-0.48	-0.41	-0.37
-0.50	-0.72	-0.73	-0.71	-0.72
-1.00	-1.19	-1.35	-1.50	-1.34
J=50kN/m $\sigma_v=1000\text{MPa}$	<i>n</i>			
	3	5	10	20
<i>T</i>	<i>Q</i>			
0.50	-0.16	-0.10	-0.05	-0.01
0.25	-0.25	-0.19	-0.13	-0.09
0	-0.38	-0.33	-0.28	-0.25
-0.25	-0.54	-0.52	-0.50	-0.49
-0.50	-0.74	-0.77	-0.79	-0.82
-1.00	-1.22	-1.40	-1.58	-1.73
J=50kN/m $\sigma_v=1500\text{MPa}$	<i>n</i>			
	3	5	10	20
<i>T</i>	<i>Q</i>			
0.50	-0.09	0.02	0.08	0.08
0.25	-0.19	-0.08	0.001	0.02
0	-0.32	-0.24	-0.16	-0.13
-0.25	-0.50	-0.46	-0.40	-0.39
-0.50	-0.72	-0.74	-0.75	-0.76
-1.00	-1.25	-1.45	-1.66	-1.82

Tab. A.4. Results for MBLA models, characterized by J=100kN/m

J=100kN/m $\sigma_v=315\text{MPa}$	<i>n</i>			
	3	5	10	20
<i>T</i>	<i>Q</i>			
0.50	-0.12	-0.06	-0.004	0.01
0.25	-0.24	-0.16	-0.08	-0.04
0	-0.38	-0.31	-0.22	-0.16
-0.25	-0.55	-0.50	-0.42	-0.36
-0.50	-0.75	-0.74	-0.72	-0.70
-1.00	-1.21	-1.32	-1.46	-1.61

$J=100\text{kN/m}$ $\sigma_v=500\text{MPa}$	n			
	3	5	10	20
T	Q			
0.50	-0.13	-0.06	-0.005	0.01
0.25	-0.24	-0.17	-0.084	-0.04
0	-0.38	-0.30	-0.21	-0.22
-0.25	-0.54	-0.50	-0.42	-0.36
-0.50	-0.74	-0.75	-0.72	-0.72
-1.00	-1.21	-1.37	-1.51	-1.67
$J=100\text{kN/m}$ $\sigma_v=1000\text{MPa}$	n			
	3	5	10	20
T	Q			
0.50	-0.15	-0.08	-0.03	-0.006
0.25	-0.23	-0.17	-0.10	-0.06
0	-0.36	-0.30	-0.23	-0.19
-0.25	-0.52	-0.50	-0.45	-0.42
-0.50	-0.72	-0.75	-0.74	-0.75
-1.00	-1.20	-1.40	-1.57	-1.74
$J=100\text{kN/m}$ $\sigma_v=1500\text{MPa}$	n			
	3	5	10	20
T	Q			
0.50	-0.13	-0.08	-0.04	-0.02
0.25	-0.20	-0.16	-0.11	-0.09
0	-0.32	-0.30	-0.26	-0.23
-0.25	-0.48	-0.50	-0.47	-0.46
-0.50	-0.67	-0.74	-0.76	-0.78
-1.00	-1.15	-1.38	-1.60	-1.76

Tab. A.5. Results for MBLA models, characterized by $J=250\text{kN/m}$

$J=250\text{kN/m}$ $\sigma_v=315\text{MPa}$	n			
	3	5	10	20
T	Q			
0.50	-0.14	-0.07	-0.01	0.008
0.25	-0.26	-0.17	-0.08	-0.05
0	-0.40	-0.32	-0.22	-0.15
-0.25	-0.57	-0.51	-0.43	-0.38
-0.50	-0.77	-0.75	-0.72	-0.72
-1.00	-1.26	-1.35	-1.47	-1.62
$J=250\text{kN/m}$ $\sigma_v=500\text{MPa}$	n			
	3	5	10	20
T	Q			
0.50	-0.16	-0.08	-0.01	0.004
0.25	-0.27	-0.18	-0.09	-0.05
0	-0.40	-0.32	-0.22	-0.17
-0.25	-0.57	-0.51	-0.43	-0.38
-0.50	-0.77	-0.76	-0.73	-0.71
-1.00	-1.26	-1.39	-1.52	-1.68
$J=250\text{kN/m}$ $\sigma_v=1000\text{MPa}$	n			
	3	5	10	20
T	Q			
0.50	-0.17	-0.1	-0.04	-0.02
0.25	-0.26	-0.19	-0.12	-0.08
0	-0.38	-0.33	-0.25	-0.22

-0.25	-0.55	-0.52	-0.46	-0.44
-0.50	-0.74	-0.72	-0.75	-0.76
-1.00	-1.22	-1.41	-1.58	-1.74
$J=250\text{kN/m}$ $\sigma_v=1500\text{MPa}$	n			
	3	5	10	20
T	Q			
0.50	-0.19	-0.14	-0.08	-0.06
0.25	-0.27	-0.22	-0.16	-0.13
0	-0.38	-0.35	-0.30	-0.27
-0.25	-0.54	-0.54	-0.50	-0.49
-0.50	-0.73	-0.78	-0.79	-0.80
-1.00	-1.20	-1.40	-1.61	-1.77

Tab. A.6. Results for MBLA models, characterized by $J=500\text{kN/m}$

$J=500\text{kN/m}$ $\sigma_v=315\text{MPa}$	n			
	3	5	10	20
T	Q			
0.50	-0.15	-0.08	-0.01	0.005
0.25	-0.27	-0.18	-0.09	-0.05
0	-0.41	-0.33	-0.23	-0.17
-0.25	-0.58	-0.52	-0.43	-0.38
-0.50	-0.78	-0.76	-0.73	-0.73
-1.00	-1.30	-1.38	-1.47	-1.50
$J=500\text{kN/m}$ $\sigma_v=500\text{MPa}$	n			
	3	5	10	20
T	Q			
0.50	-0.17	-0.09	-0.02	0.002
0.25	-0.28	-0.19	-0.10	-0.05
0	-0.41	-0.33	-0.23	-0.17
-0.25	-0.58	-0.52	-0.43	-0.38
-0.50	-0.78	-0.77	-0.73	-0.72
-1.00	-1.29	-1.42	-1.53	-1.62
$J=500\text{kN/m}$ $\sigma_v=1000\text{MPa}$	n			
	3	5	10	20
T	Q			
0.50	-0.19	-0.12	-0.05	-0.03
0.25	-0.28	-0.21	-0.13	-0.09
0	-0.40	-0.34	-0.26	-0.22
-0.25	-0.56	-0.53	-0.47	-0.45
-0.50	-0.76	-0.78	-0.76	-0.77
-1.00	-1.25	-1.43	-1.59	-1.75
$J=500\text{kN/m}$ $\sigma_v=1500\text{MPa}$	n			
	3	5	10	20
T	Q			
0.50	-0.23	-0.16	-0.1	-0.08
0.25	-0.30	-0.24	-0.18	-0.14
0	-0.42	-0.38	-0.32	-0.28
-0.25	-0.57	-0.56	-0.53	-0.50
-0.50	-0.76	-0.80	-0.80	-0.82
-1.00	-1.23	-1.43	-1.62	-1.78

A RIG FOR TESTING THE LEG OF A WHEEL-LEGGED ROBOT

Antoni GRONOWICZ*, Jarosław SZREK*, Sławomir WUDARCZYK*

*Institute of Machines Design and Operation, Faculty of Mechanical Engineering, Wrocław University of Technology,
 ul. Łukasiewicza 7/9, 50-371 Wrocław, Poland

antoni.gronowicz@pwr.wroc.pl, jaroslaw.szrek@pwr.wroc.pl, slawomir.wudarczyk@pwr.wroc.pl

Abstract: The paper describes a rig specially constructed for testing a single leg of the wheel-legged robot being designed and presents exemplary test results. The aim of the tests was to verify the mechanical structure and control system operation in laboratory conditions. The operation of the control, communication and data transmission modules was verified. Also tests aimed at selecting proper parameters for the drive controllers were carried out on the test rig.

Key words: Mobile Robot, Suspension, Control System

1. INTRODUCTION

Mobile robots on a wheeled chassis are capable of considerable speeds, but only on level ground. Walking robots are capable of negotiating obstacles, but their speed on flat ground is very low. Wheel-legged robots combine the advantages of both the above designs. In favourable conditions they can travel on wheels at a high speed and when they encounter an obstacle they negotiate it by walking (Guccione, 2003; Grand, 2002; Halme, 2000). This means that walking is used only in cases when the obstacle cannot be negotiated by driving or when it cannot be avoided. The suspension system of such wheel-legged systems has a special kinematic structure (Gronowicz, 2009a; Szrek, 2009) whereby it is more universal and suitable for performing complicated tasks, such as climbing stairs (Gonzales, 2009).

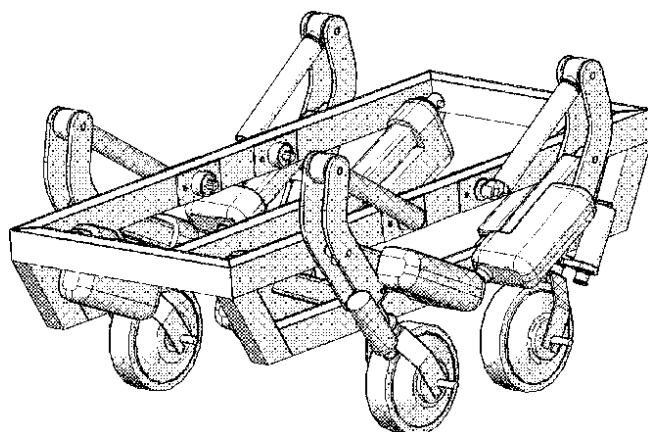


Fig. 1. 3D model of wheel-legged robot being designed

The peculiar feature of the wheel-legged robot considered here (Fig. 1) is the behaviour of its horizontal platform during travel on bumpy terrain. When the robot encounters an obstacle it surmounts it by walking. The kinematic structure of the leg was so designed as to effect the lifting of the platform by means of only

one drive (a servomotor). The walking motion is effected by the simultaneous operation of two linear drives. In addition, the leg incorporates a road wheel and a turn executing drive.

Before a prototype of the robot was built, a rig for testing a single robot leg had been constructed whereby a series of preliminary tests could be carried out.

2. DESIGN OF TEST RIG

The basic dimensions of the wheel-legged robot leg were determined through a geometric synthesis based on created numerical models. A kinematic scheme of a single robot leg is shown in Fig. 2.

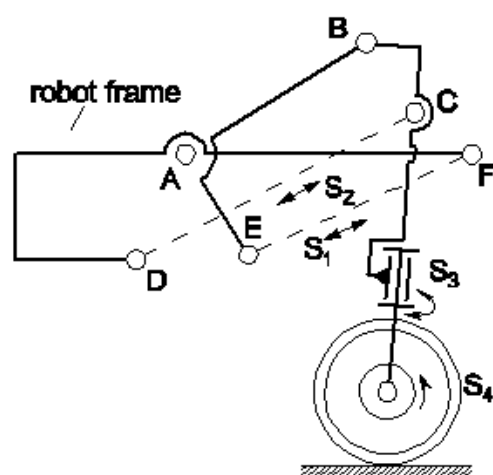


Fig. 2. Kinematic scheme of robot leg (in scale)

Concurrently the test rig was being constructed. This required close integration of simulation studies with construction work. For the preliminary design the kinematic and dynamic parameters of the system and the driving forces for different robot leg motion

variants were determined through repeated simulations. Any alterations (e.g. introduction of drive units) to the design required additional simulation studies. As a result, the dimensions of the particular components and their mass parameters were specified more precisely, proper drive units and construction materials were selected, the mechanism's nodes were designed and an algorithm for controlling the drives was developed. The whole construction process was carried out interactively.

In order to determine the actual mechanical properties of the robot's leg and to test the control system it was decided to build a rig for testing a single robot leg. First of all it was necessary to build a stationary structure replacing the function of the other three legs and mimicking the motion and loads of the leg attached to the robot frame. A kinematic scheme of the rig for testing the robot leg is shown in Fig. 3.

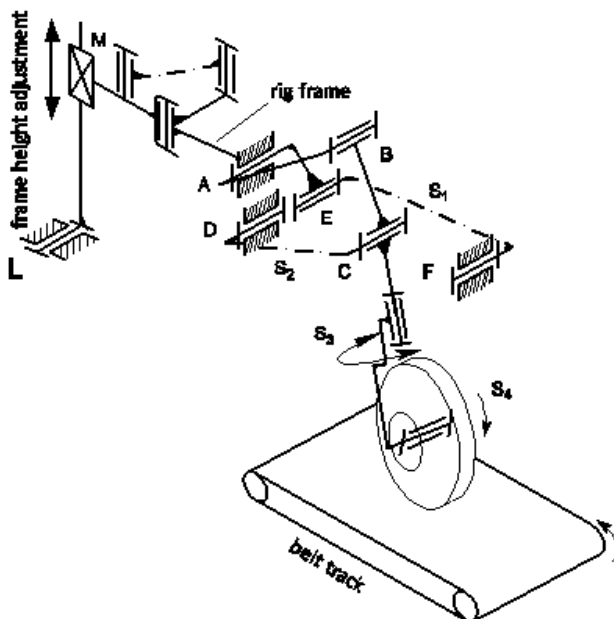


Fig. 3. Kinematic scheme of rig for testing wheel-legged leg

It was assumed that the robot vehicle's frame would always remain horizontal. This is effected through proper changes in the extension of each leg's levelling servomotors (S1). This means that the frame performs vertical motion while maintaining a constant orientation. For technical reasons (possible locking of sliding pair M) on the test rig the motion of the robot frame was replaced by the rotational motion of the rig's frame around point L. As a result, the motion of the levelling servomotor forces the rotation of the frame whereby the axle of the road wheel moves horizontally (rotates or slides relative to the base). Such coordinates of pair L were selected as to make it possible to exclude this motion from the tests. This means that the maximum change of the frame angle during levelling results in a wheel axis displacement not larger than 7 mm. The rig also makes possible stepwise adjustment of frame elevation (H) from the ground. Robot travelling motion in the rig is executed by means of a belt track. Thanks to this solution the robot's travelling properties, such as travelling speed under different working loads, possible accelerations, etc., can be tested. The wheel load (on the track) as a function of time is measured using tensometric scales. Crank AE is a tensometric beam correlating the servomotor force with the wheel load via the control system.

During obstacle negotiation each of the legs is raised in turn (losing contact with the ground) and executes the walking motion while the robot frame remains supported by the other three legs. In order to study the walking mode, the rotary motion of the frame is locked by means of an additional support. Then the leg can move freely in the air. The test rig makes it possible to test the wheel-legged robot leg in its two main operating modes and to integrate the mechanical system with the control system.

3. RIG FOR TESTING ROBOT LEG

A photograph of the rig for testing a single robot leg is shown in Fig. 4. The rig comprises: a frame made from hollow sections, a set of servomotors with controllers, a supervising computer with communication interfaces, and a measuring system.



Fig. 4. Rig for testing robot leg

3.1. Robot leg drive units

The choice of drive units is largely determined by the input system operation assumptions. The electric drive system comprises two electric servomotors LA36 made by LINAK (leg lifting and walking), a HUB-24M drive wheel and an ARE4568 drive effecting its turn. Each of the drives effects the movement of a different motion unit of the leg gear. The selected robot leg drives are characterized by:

- high reliability,
- operability in difficult conditions,
- overload protection,
- high operating speed,
- an ability to work with different speeds at the maximum torque,
- an ability of being frequently start/stop switched,
- ease of assembly,
- an ability to operate in any position.

The adopted servomotors are shown in Fig. 5 and their specifications are given in Tab. 1.

Typical drives and generally available components were considered during the design stage. All the motors are mass-produced, but some of the components had to be slightly modified. A position sensor had to be mounted on the drive wheel motor. Since the motor has no axle extending outside its housing

it was necessary to make alterations inside: an additional rack was introduced and a sensor with a resolution of 512 pulse/rev. was mounted on it. A schematic showing the place where the position sensor was installed is shown in Fig. 6. Originally there was a brake in the drive, introducing axial clearance which translated into a protrusion clearance of 8 mm. Since this is not allowable in the robot leg structure the brake was removed and replaced with a flexible coupling. The original servomotors have encoders inside and the latter were used to determine the size of protrusion.

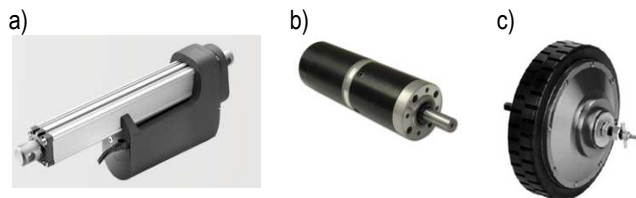


Fig. 5. Robot leg drives: a) servomotor LINAK - LA-36 (levelling and walking), b) wheel turn motor ARE4568, c) drive wheel HUB-24M

Tab. 1. Specifications of drives

Levelling and walking servomotor Linak - LA-36			
stroke	150 mm	power	140W
initial length	350mm	supply voltage	24V
push force	1700N		
Turn effecting drive ARE-24V-4568-3000-R14-EN			
transmission ratio	1:14	supply voltage	24V
rpm	171 rpm	torque	0.81 Nm
belt-toothed gear ratio	1:3		
Road wheel drive			
wheel radius	105 mm	supply voltage	24V
rpm	125 rpm	torque	13.5 Nm
current	10 A	speed	4.9 km/h

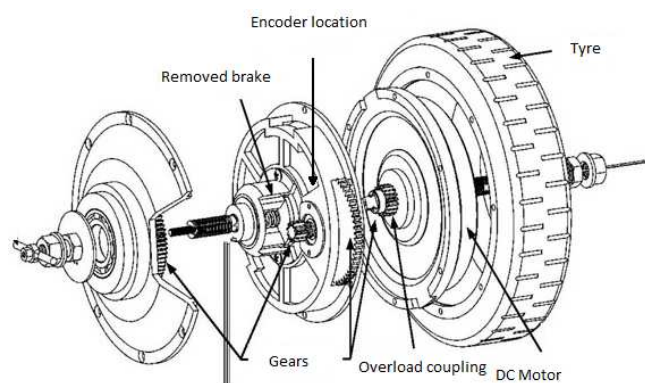


Fig. 6. Place where position sensor was installed

4. CONTROL SYSTEM WITH MEASURING SYSTEM

Before it could be installed in the robot, the control measuring system had to be tested. Controller modules, motor executing

system modules, data processing system modules and measuring system modules were designed and made.

The individual modules were integrated into the overall control system and subjected to testing. The measuring and control system structure is shown in Fig. 7. The design of the controller is such that it can be used in mobile objects with many degrees of freedom. Special care was taken to ensure small dimensions, easy expandability and universal communication.

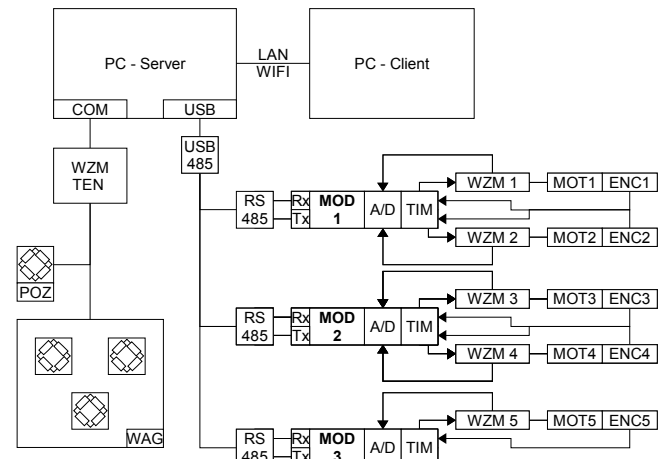


Fig. 7. Structure of control system

The particular components of the measuring and control system are described below:

The local drive controller modules (MOD) are based on the STM32F103RbT6 microcontroller with the ARM Cortex core. The system is in a 64-pin enclosure and it has all the resources and peripherals necessary to control the motors. The control system incorporates a timer block (TIM), an a/d converter block (A/D) and a serial communication block.

Position and speed are measured by incremental encoders mounted on the axle of each of the drives. The position and rotational speed of the motor can be determined on the basis of pulse counts. Moreover, having a leg kinematics model one can easily determine the leg's configuration and kinematic parameters. The (quadrature) signal from the encoder is supplied to the timer inputs where it is counted.



Fig. 8. Lifting drive with measuring beam

A tensometric beam was employed to measure wheel load (Fig. 8). The beam also serves as a crank transforming servomo-

tor protrusion into the rotational motion of the leg for the lifting function. Owing to the fact that the sensor is part of the leg and is located on the crank it is possible to read the force directly connected with the degree of pressure exerted by the leg on the ground and the force is not disturbed by any other components.

Furthermore, thanks to this solution no additional measuring system needs to be introduced into the system and the sensor is not exposed to damage (from torsion, lateral forces, etc.). Besides measuring the pressure exerted by the wheel on the ground (monitoring ensuring robot stability), the tensometric beam supplies information about wheel/ground contact loss instants. This information is useful for negotiating obstacles by walking.

The signal from the strain gauge (operating in the Wheatstone bridge circuit) is amplified and read by the robot's central computer. The ADT4U sensor made by Wobit was used as the amplifier and processing circuit. Communication with the module is via a serial interface using the Modbus protocol.

The pressure exerted on the ground was additionally registered by the tensometric scales shown in Fig. 9.

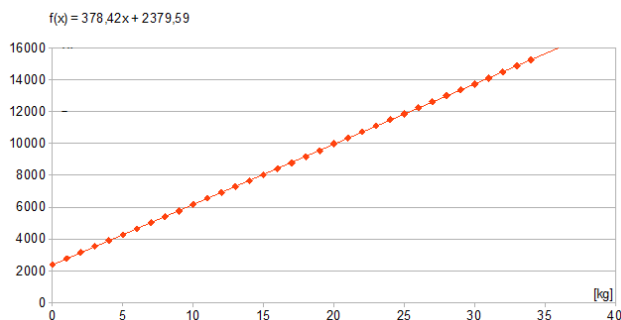
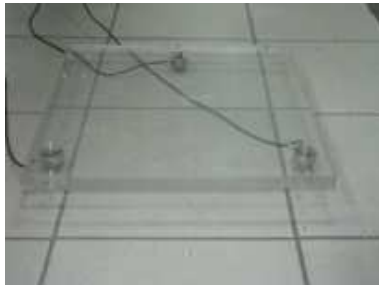


Fig. 9. Tensometric scales and their characteristics with regression function

The driving motors are controlled by the PWM signal generated in the timer block (MOD). The PWM signal is appropriately amplified by power amplification systems (WZM). Additional digital signals are used to change direction. The WZM modules also incorporate a circuit measuring the current which is read by the analog-to-digital converters.

5. TESTS ON RIG

In order to verify the leg's mechanical part and its measuring, control and communication systems tests were carried out on the test rig. During the tests the motions of the leg drives were executed for different speeds and all the measuring data were recorded. Among other things, the following were checked:

- the general functionality – to verify whether all the modules performed the functions for which they were designed;

- the communication functionality – to verify whether the particular units supplied information about the particular modules and drives in the leg (the control instructions, their implementations and performance were tested);
- the control parameters – the drive controllers perform control using the PID algorithm; the task value is sent from the supervising computer level and a local module carries out the request; the control parameters were matched experimentally by carrying out a series of tests for different settings in order to check the system dynamics and the accuracy of the control;
- the measuring path and data interpretation – to verify the whole flow of data in the leg control system being a part of the global robot control system.

Exemplary data (Fig. 10) supplied by the measuring system are: servomotor position (protrusion), speed, motor current, and wheel load (POZ sensor). The data are parameterized with time (ms). The tests showed the data readings to be correct and provided a basis for developing robot control algorithms. The tests were carried out for several cycles at different motions speeds. Conditions very similar to the ones characteristic of obstacle negotiation (the wheel is in contact with the ground and then is lifted) were reproduced in the test rig.

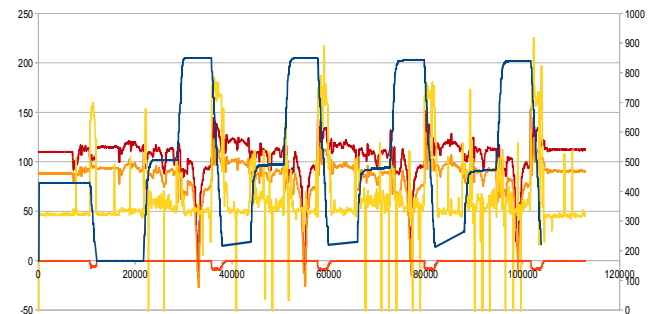


Fig. 10. Exemplary measurement data obtained from leg test rig

The diagram in Fig. 11 shows the servomotor protrusion and the force measured by the tensometric beam. A change in the sign of the force value represents an instant when the wheel loses contact with the ground. It appears from the data that the measuring system works correctly and the data can be used for the autonomous determination of the robot parameters. However, the data are not ideal. For example, at 25s (25000 ms) a considerable drop in the force level was registered, which was caused by the coming to a sudden stop when the limit switched was reached.

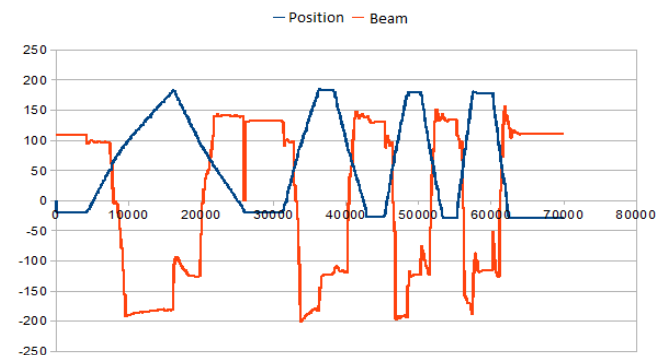


Fig. 11. The servomotor protrusion and the force measured by the tensometric beam

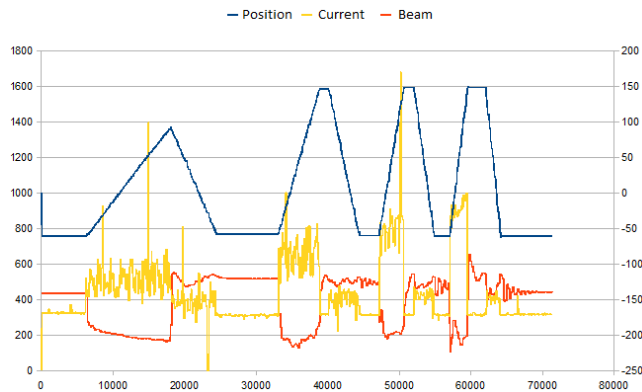


Fig. 12. Current, force, position

Moreover, the drive current referred to the force in the beam and the servomotor protrusion was measured (Fig. 12). Also in this case the obtained data agree with the intuition – the current is higher during leg raising than during leg lowering.

6. CONCLUSION

The tests on the leg testing rig were the first experimental verification in the whole wheel-legged robot design process. The operation of the leg was tested and the perceived shortcomings were eliminated. The control and measuring system of the leg (and so that of the robot) was thoroughly tested. The control, communication and data transmission modules were found to operate properly. Also tests aimed at selecting proper parameters for the drive controllers were carried out on the test rig.

Moreover, the results of the robot leg tests were used to preliminarily verify the control software whereby the design process significantly accelerated. Guidelines for developing robot control algorithms, which will ensure the autonomous operation of the robot, were formulated on the basis of the test data.

REFERENCES

1. **Gonzalez A., Ottaviano E., Ceccarelli M.** (2009), On the kinematic functionality of a four-bar based mechanism for guiding wheels in climbing steps and obstacles, *Mechanism and Machine Theory*, Vol. 44, 1507–1523.
2. **Grand Ch., BenAmar F., Plumet F., Bidaud Ph.** (2002), Stability control of a wheel-legged mini-rover, *Proceedings of the CLAWAR Conference*.
3. **Gronowicz A., Szrek J.** (2009a), Idea of a quadruped wheel-legged robot, *Archive of Mechanical Engineering*, Vol. 56, nr 3, 263-278.
4. **Gronowicz A., Szrek J.** (2009b), Design of LegVan wheel-legged robot's mechanical and control system, in: *SYROM 2009: proceedings of the 10th IFToMM International Symposium on Science of Mechanisms and Machines*, held in Brasov, Romania, October 12-15, Springer.
5. **Guccione S., Muscato S.** (2003), The wheeleg robot, *IEEE Robotics & Automation Magazine*, December.
6. **Halme, A., Leppänen I., Salmi S., Ylönen S.** (2000), Hybrid locomotion of wheel-legged machine, *Proceedings of the CLAWAR Conference*.
7. **Szrek J.** (2009), *Synthesis of the kinematic and control system of a quadruped wheel-legged robot (Synteza układu kinematycznego i sterowania czworonożnego robota kołowo-kroczącego)*, PhD Thesis, Wrocław (in Polish).

This research, under project no. N502 271037, was funded from the resources for science in the years 2009-2012 in Poland.

LIMITATION OF CAUCHY FUNCTION METHOD IN ANALYSIS OF ESTIMATORS OF FREQUENCY AND FORM OF NATURAL VIBRATIONS OF CIRCULAR PLATE WITH VARIABLE THICKNESS AND CLAMPED EDGES

Jerzy JAROSZEWICZ*, Krzysztof K. ŻUR**

*Faculty of Management, Białystok University of Technology, ul. Ojca Tarasiuka 2, 16-001 Kleosin, Poland

**Faculty of Mechanical Engineering, Białystok University of Technology, ul. Wiejska 45C, 15-351 Białystok, Poland

j.jaroszewicz@pb.edu.pl, krzysztof.zur@gmail.com

Abstract: In this paper the Bernstein-Kieropian double estimators of basic natural frequency of circular plate with power variable thickness along the radius and clamped edges in diaphragm form were analyzed in a theoretical approach. The approximate solution of boundary problem of transversal vibration by means of Cauchy function and characteristic series method has been applied for chosen values of power indicator of variable thickness m and material Poisson's ratio ν has been chosen which led to exact form solutions. Particular attention has been given to a singularity arising from the uncertainty of estimates of Bernstein-Kieropian. Improving this method has been obtained the general form of Cauchy function for arbitrary values of m and ν , which are physically justified. Therefore, the aim of the paper was to explore the reason why for a plate above a certain value $m = 3.97$ exact solution, which Conway couldn't receive (Conway, 1958a, b).

Key words: Vibration, Circular Plate, Boundary Value Problem, Cauchy Function, Bernstein-Kieropian's Estimators

1. INTRODUCTION

In a previous paper (Jaroszewicz, 2008) authors analyzed the use of simplest lower estimator to calculate the basic frequency of axi-symmetrical vibration of plates with variable thickness circular diaphragm type. The existence of the simplest estimator of the actual value of the parameter depending on the frequency rate of change characterized by thick plate ($m = 3.25$ to 5.999) was analyzed. The accuracy of the method differed from the FEM and in order to improve the accuracy of the estimators it was decided to use a higher order, in this case double. Using the bilateral estimators the similar problem arose in the calculation of exact solution in a paper by Conway (Conway 1958a, 1958b). It seems that the problem lies in the fact that diaphragms for meters which is close to 4 in the center of symmetry have a very low rigidity and on a boundary value it creates a hole in the middle with a radius of 1mm to 23mm. As a common known plate with a hole required 2 additional boundary conditions on the edge of the hole, the hole is a singularity which requires detailed analysis. It is widely known that clarification of the model leads to the complexity of solutions. The compromise between the possibilities of addressing coastal vibrations and stability of mechanical systems and simplifying gives the total allowable use of methods of the influence functions, and partial discretization characteristic series. Good results achieved in previous publication (Jaroszewicz et al., 2008), which included linear modeling of mechanical systems with discrete-continuous parameters encouraged authors to use the above-mentioned methods for studying vibration plates diaphragm type of ring. In this case, the influence of the function, which is the product of the Cauchy and Heaviside unit functions were applied. This function features the influence of derivatives, which are fundamental solutions of linear differential equations and can build their base of the integrated general solutions

with various types of δ ratios in the Dirac. For the vibration test plate with varying parameters method of partial discretization has been used. It is based on the method of influence and has been previously proposed by Zoryj and Jaroszewicz to analyze vibration plates fixed and variable thickness with an additional mass focused (Jaroszewicz and Zoryj, 2005, 2006). The record for continuous or continuous-discrete mass distribution systems discrete can be replaced with one, two and n -degrees of freedom, which are characterized by the same function of stiffness. The plate's mass focuses on the rings with a certain radius. Total weight of the replacement is equal to its own weight plates. This procedure uses a universal characteristic of the equation.

2. FORMULATION OF THE PROBLEM

R – radius circular plate having a clamped edge whose cross section presented in Fig.1 has been considered. Its thickness h and flexural rigidity D change in the following way (Tab. 1).

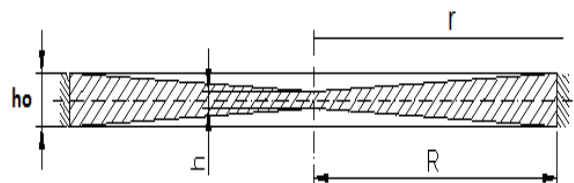
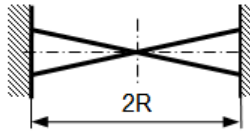
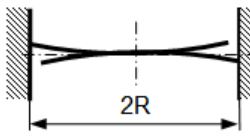


Fig. 1. Cross section of the plate of diaphragm type

$$h = h_0 \left(\frac{r}{R}\right)^m, D = D_0 \left(\frac{r}{R}\right)^m, 0 < r \leq R, D_0 = \frac{E h_0^3}{12(1-\nu^2)} \quad (1)$$

where: $D_0, h_0, m \geq 0$ are the constants, r – denotes the radial coordinate, E – Young's modulus, ν – denotes Poisson's ratio.

Tab.1. Variable thickness plates

Diaphragm	Thickness	Schema
Linear variable thickness	$h = h_0 \left(\frac{r}{R}\right)^{\frac{m}{3}},$ $2 < m < 6$	
Power variable thickness	$h = h_0 \left(\frac{r}{R}\right)^m$	

Investigation of free, axi-symmetrical vibrations of such a plate is reduced to an analysis of the boundary problem (Conway, 1958a, 1958b; Jaroszewicz and Zoryj, 2005):

$$L_0[u] - pr^{-\frac{2}{3}m}u = 0 \quad (2)$$

$$u(R) = 0, u'(R) = 0, \quad (3)$$

where:

$$L_0[u] = u^{IV} + \frac{2}{r}(m+1)u^{III} + \frac{1}{r^2}(m^2 + m + vm - 1) + \frac{1}{r^3}(m-1)(vm-1)u, \quad (4)$$

$$p = \frac{\rho h_0}{D_0} R^{\frac{2}{3}m} \omega^2,$$

$u = u(r)$ – denotes the amplitude of line of bending, ρ – density of the material of the plate, ω – the parameter of frequency (angular velocity). Boundary value conditions corresponding to a clamped edge (3) have been defined as zero values of deflection and zero values of the angle of deflection for $r = R$. Additional conditions pertaining to the center of symmetry of a plate ($r = 0$) have limited values of deflection $u(0) < \infty$ and zero values of the angle of deflection $u'(0) = 0$. The value $m = 0$ refers to the plate with constant thickness; $m > 0$ to plates of the diaphragm type with thickness decreasing toward the axial center; $m < 0$ to disc type plates with thickness increasing toward the axial center (Woźniak, 2005; Jaroszewicz and Zoryj, 2005). The border of variation of the power index $m \geq 0$ has been determined, for which the most simple estimators of the basic frequency ω_1 exist and therefore can be calculated, i.e. it has been searched for the lowest proper value of the border problem (2.÷3). In the problem (2.÷3), a limitation of solution for r going to zero and their first up to the third derivatives, with respect to the independent variable r is required (Conway, 1958b).

General form of Cauchy function was proposed by Zoryj and Jaroszewicz by mean following expression:

$$K_0(r, \alpha) = \frac{1}{(1-v)m} \left[\frac{1}{2\sqrt{D}} (r^{S_3} \alpha^{S_4+m+1} - r^{S_4} \alpha^{S_3+m+1}) - \frac{1}{2-m} (r^{2-m} \alpha^{m+1} - \alpha^3) \right], \quad (5)$$

where: S_1, S_2, S_3, S_4 – roots of characteristic equation, D – determinant of square equation:

$$s^2 - (2-m)s - m(1-v), \quad (6)$$

$$D = (1 - \frac{m}{2})^2 + m(1-v). \quad (7)$$

Equation (6) received from characteristic equation:

$$s\{s^3 + 2(m-2)s^2 + [4 - 5m + m^2 + vm]s + m(2-m)(1-v)\}, \quad (8)$$

which roots present in next form:

$$s_1 = 0, s_2 = 2 - m, s_{3,4} = -\frac{m}{2} + 1 \mp \sqrt{D}. \quad (9)$$

So, for $L_0[u] = 0$ the fundamental system of solutions, in those cases is (according to Euler's theory of equations) as follows:

$$m = 0, 1, \ln r, r^2, r^2 \ln r, \\ m = 2, 1, \ln r, r^{\sqrt{2-2v}}, r^{-\sqrt{2-2v}}. \quad (10)$$

Based on those calculations, the following remarks can be formulated:

- all roots of the cubic equation (8), as well as those of the quadratic equation (6) are real numbers for any given physically justified values of m – power indexes and values of Poisson's ratio ν ($\nu \in (0, 0.5)$);
- the equation (6) has no other multiple (repetitive) roots for $m \in (-\infty, +\infty)$ and $\nu \in (0, 0.5)$;
- the fundamental systems of solutions for Euler's differential equations $L_0[u] = 0$ possess logarithmic peculiarities only in cases $m = 0, m = 2$ and are determined by the formula (10); in all of the rest cases they have power character peculiarities.

3. THE BILATERAL ESTIMATORS FOR BASIC FREQUENCY IN PARTICULAR CASE $\nu = 1/m$

Take into account the series known Bernstein-Kieropian's estimators (Bernstein and Kieropian, 1960) with the following form can be applied:

$$(a_1^2 - 2a_2)^{-\frac{1}{2}} < \gamma_0 < \sqrt{2}(a_1 + \sqrt{a_1^2 - 4a_2})^{-\frac{1}{2}} \quad (11)$$

where: γ_0 – mean value of Bernstein-Kieropian estimators, $\gamma_- = (a_1^2 - 2a_2)^{-\frac{1}{2}}$ – lower estimator, $\gamma_+ = \sqrt{2}(a_1 + \sqrt{a_1^2 - 4a_2})^{-\frac{1}{2}}$ – upper estimator.

Coefficient a_1 scrutinized in previous work (Jaroszewicz 2008), where exact formula has been constructed:

$$a_1 = \frac{3^4}{(6-m)(6+m)(9+m)(12+m)}. \quad (12)$$

To develop formula for a_2 in a similar form formula in following form should be present:

$$A_1 B_1 + A_2(1 - 2a) \equiv A_1 \cdot \frac{1}{a} \cdot F(m), \quad (13)$$

where:

$$F(m) = [(a+1)(b+1)(b+2)]^{-1} - 0.5[c(c+1)]^{-1} \quad (14)$$

Second addition in expression can be present in form:

$$B_2(1 + 2a) = \frac{1}{2} B_1 \cdot f(m) \quad (15)$$

where:

$$f(m) = [a(c+1)(c+2)]^{-1}. \quad (16)$$

Now exploit determination (14)÷(16) also formulas (Jaroszewicz 2008):

$$A_2 = \frac{1}{2}A_1[a(2a-1)c(c+1)]^{-1}, \quad (17)$$

$$B_2 = \frac{1}{2}B_1[a(2a+1)(c+1)(c+2)]^{-1} \quad (18)$$

we constructed coefficient a_2 record in form expression:

$$a_2 = \frac{1}{a^2(b+1)} \left[\frac{F(m)}{(a-1)b} + \frac{1}{2(a+1)(b+2)(c+1)(c+2)} \right]. \quad (19)$$

Take into account identity $m = 4.5 = 1.5(1-a)$ the first component sum (19) in form has been found:

$$\frac{F(m)}{(a-1)b} = -\frac{81(m-3)(m+24)}{2(15-2m)(9+m)(6+m)(12+m)(18-m)(21-m)}. \quad (20)$$

Considering also identity:

$$\frac{1}{2(a+1)(b+2)(c+1)(c+2)} = \frac{81}{2(12+m)(15-2m)(21-m)(24-m)}. \quad (21)$$

Finally from (19) general form second coefficients of characteristic series a_2 has been received:

$$a_2 = \frac{3^{9.5}}{2(12+m)(6+m)(18-m)(21-m)(24-m)(6-m)^2(9+m)^2}. \quad (22)$$

Example results of calculation for changed cases $2 < m < 6$ and $\nu = 1/m$ obtain on the basis of formulas (11), (12) and (22) present in the Tab. 1, 2 and Fig. 2.

4. DISCUSSES OF RESULTS OF CALCULATIONS OF BASE FREQUENCY

Results of calculation where compared with previous paper (Jaroszewicz 2008) in Tab. 1 and Fig. 2 which were calculated by means Cauchy function and characteristic series method using simplest estimator and exact solution received on base Bessel special function by Conway, Hondkiewicz and Kovalenko (Kovalenko, 1959; Hondkiewicz, 1959).

Boundary values, for which the upper estimator does not exist can be settled on the basis of the investigation of under roots expression form change (23) $a_1^2 - 4a_2$ with $m = 3.97$ change sign from positive to negative with $m = 3.98$ so calculating accurate values a_1 and a_2 on the base of (19) we have respectively:

$$\begin{aligned} a_1^2 - 4a_2|_{m=3.97} &= 7 \cdot 10^{-7} > 0, \\ a_1^2 - 4a_2|_{m=3.98} &= -6 \cdot 10^{-7} < 0. \end{aligned} \quad (23)$$

Under estimated values there for it cannot be even used in approximate application however the simplest lower estimator can be applied to preliminary engineering calculations for constant and for variable thickness plates when $0 \leq m \leq 4$.

It should be noticed that in the case of a constant thickness plate ($m = 0$), the multiplier $\gamma = \gamma_0 = 10.2122$ is independent from ν (Kovalenko, 1959; Vasylenko and Oleksiejčuk, 2004). So the ratio of coefficients:

$$\frac{\gamma}{\gamma_0} = 1.1678. \quad (24)$$

It does agree with results of calculations obtained by Conway in (Conway, 1958a). Continuing in analogical fashion the basic frequency for other combinations of m and ν has been calculated.

The results of calculations are presented in Tab. 3.

In Tab. 3 are presented values received by Jaroszewicz J. and Zoryj L. cases for which Conway derive characteristic function on base special Bessel function. Ratio γ/γ_0 of natural frequency plate constants thickness and plate of variable thickness for Conway values m, ν . This Tab. contain model value of solution with we compare approximate results.

In Tab. 3 Conway couldn't apply the exact method (Conway, 1958a), because the condition $\nu = \frac{2m-3}{9}$ was not fulfilled.

5. ESTIMATE OF RESULTS CALCULATION OF BASE FORM

As an example the current assumption was given $m = 3$, $\nu = 1/3$ which considers linear thickness of plate $h = h_0 \frac{r}{R}$.

The way of calculation has been illustrated on example of equation (2), which will have following form:

$$L_0[u] - pr^{-2}u = 0.$$

$$L_0[u] \equiv u^{IV} + \frac{8}{r}u^{III} + \frac{12}{r^2}u^{II} \quad (25)$$

with boundary conditions (3).

On the base of (5) and (8) Cauchy function has been received in form:

$$K_0(r, \alpha) = \frac{1}{6}(r\alpha^2 - r^{-2}\alpha^5) + \frac{1}{2}(r^{-1}\alpha^4 - \alpha^3) \quad (26)$$

and limited for $r = 0$ solutions of equation (2):

$$u = C_1U_1(r) + C_2U_2(r), \quad (27)$$

where:

$$U_i(r) = a_{0i} + pa_{1i} + p^2a_{2i} + \dots \quad (i = 1, 2), \quad (28)$$

$$a_{ij} = \int_0^r K_0(r, \alpha) \alpha^{-2} \alpha_{j-1,i}(\alpha) d\alpha, \quad (29)$$

$$a_{01} = 1, \quad a_{02} = r, \quad a_{11} = \frac{r^2}{24}, \quad a_{21} = \frac{r^4}{24 \cdot 360},$$

$$a_{12} = \frac{r^3}{120}, \quad a_{22} = \frac{r^5}{120 \cdot 840}. \quad (30)$$

Appropriate forms of natural vibration can be derived similarly as for constant thickness plate (Kovalenko, 1959; Hondkiewicz, 1959). On the base of formulas (26-30) we are able to find for parameter of base frequency ($\gamma_0 = 8.75$) following values:

$$\frac{\gamma_0^2}{24} = 3.19, \quad \frac{\gamma_0^2}{120} = 0.64,$$

$$U_1(\chi) = 1 + 3.19\chi^2 + \dots, \quad U_2(\chi) = \gamma(1 + 0.64\chi^2 + \dots) \quad (31)$$

where: $\chi = (\frac{r}{R})^2$.

Then form (27) by using boundary condition $U(R) = 0$ we find:

$$\alpha = \frac{C_2}{C_1} = -\frac{U_1(R)}{U_2(R)} = -2.55. \quad (32)$$

Moreover basic form in first approximate can be describe by means of the following function:

$$-U(R) = U_1 + \alpha U_2 = 1.64\chi^3 - 3.19\chi^2 + 2.55\chi - 1 \quad (33)$$

Tab. 2. Results of calculation of base frequency

No.		1.	2.	3.	4.	5.	6.	7.	8.	9.
Coefficient m		2	2.5	3	3.7	3.975	4.49	5	5.5	5.999
Two first terms of characteristic series	a_1	1/61	1/61	1/60	1/55	1/52	1/43	3/97	1/18	250
	a_2	2/58941	3/75050	1/2016	6/7956	1/10684	8/5017	19/559	13/100	31250.2
Simplest lower estimator	$\gamma(m) = (a_1)^{-1/2}$	7.80	7.83	7.75	7.41	7.19	6.58	5.69	4.24	0.06
The double sides estimator	γ_-	8.38	8.56	8.65	8.62	8.55	8.27	7.75	6.73	0.83
	γ_+	8.45	8.66	8.84	9.19	10.16	-	-	-	-
	γ_0	8.42	8.61	8.75	8.91	9.36	-	-	-	-
Value of exact solution	γ_{exact}	8.46	8.60	8.75	-	-	-	-	-	-

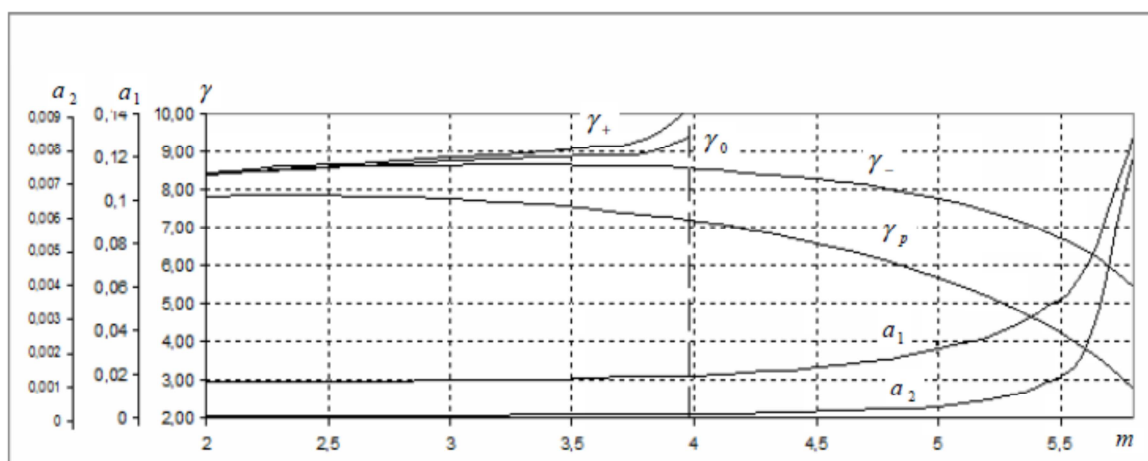


Fig. 2. The curve showing influence of the plate thickness index on the bilateral estimators of the frequency coefficients

Tab. 3. Results of calculations (Jaroszewicz and Zoryj, 2005)

L.p.	m	ν	$\frac{\gamma_0}{\gamma}$	$\frac{T}{T_0}$
1	2	$\frac{1}{9}$	$\frac{10.2144}{9.4562} = 1.0802$	1.0824
2	$\frac{18}{7}$	$\frac{5}{21}$	$\frac{10.2144}{9.0777} = 1.1252$	1.1261
3	$\frac{18}{7}$	$\frac{7}{18}$	$\frac{10.2144}{8.6376} = 1.1825$	Conway does not applying exact solution

From condition $U(R) = 0$ by extracting the solution $\chi = 1$ we have received square equation:

$$1.64\chi^2 - 1.56\chi + 1 = 0 \quad (34)$$

which does not possess real roots. On this base we can conclude, that in case $m = 3, \nu = \frac{1}{3}$ basic form corresponds to the anodal form similar as for plates with constant thickness.

Obviously anodal forms do not exist in this specific case and wave parameter equals zero.

6. SUMMARY

On the basis of Fig. 2 it can be seen that the simplest estimator underestimates results of the value with the increase of the coefficient m . In contrast to double estimate γ_-, γ_+ gives accurate results, this follows from the analysis of the value of the denominator of the estimator γ_0 the value calculation is consistent with the exact solution for $m = 3$, is 8.75 the same is true for $m = 2$ (8.40) and $m = 2.5$ (8.60). Deriving of the above mentioned formulas for the Cauchy function (5), as well as fundamental systems of function operator $L_0[u]$ allows to study of the convergence problem (velocity of convergence) of solutions of equation (4) in form of power series in respect to parameters of frequencies, depending on values of parameters m and ν .

Having the influence functions of operator $L_0[u]$ corresponding solutions and use them for any given physically justified values of parameters m and ν ($m \in (-\infty, +\infty)$; $\nu \in (0, 0.5)$) can be consequently determined, when the exact solutions are unknown on base general form of Cauchy function (5). On the basis

of quoted solutions, simple engineering formulas for frequencies estimators of circular plates, which are characterized by variable parameters distribution, can be derived and limits of their application can be identified. The bilateral estimators calculated using four first elements of the series, allows to credibly observe an influence material's constants: Young modulus – E , Poisson ratio – ν , density – ρ , on the frequencies on axi-symmetrical vibrations of circular plates, which thickness or rigidity changes along the radius according to the power function. The bilateral estimator underrate values, application of bilateral estimator significantly improves the accuracy of calculations terms of exacts solutions.

REFERENCES

1. **Bernstein S.A., Kieropian K.K.** (1960), *Opredelenije častot kolebanij steržnevych system metodom spektralnoi funkcii*, Gosstroizdat, Moskva.
2. **Chandrika P., Raj K.J., Som R.S.** (1972), Axisymmetric Vibrations of Circular Plater of Linearmy Varying Thickness, *Journal of Applied Mathematics and Physics*, Vol. 23, 941-948.
3. **Conway H.D.** (1958a), Some special solutions for the flexural vibrations of discs of varying thickness, *Ing. Arch.*, 26, 6, 408-410.
4. **Conway H.D.** (1958b), An analogy between the flexural vibrations of a cone and a disc of linearly varying thickness, *Z. Angew. Math. Mech.*, 37, 9/10, 406-407.
5. **Hondkiewiç W.S.** (1964), *Sobstviennyje kolebanija plastin i obolochek*, Nukowa Dumka, Kiev.
6. **Jaroszewicz J., Zoryj L., Katunin A.** (2004), Double estimators of natural frequencies of axial symmetrical vibrations of circular plates of varying thickness, *International Conference Energy in Sciences and Technics*, Suwalki, 45-56.
7. **Jaroszewicz J., Misiukiewicz M., Puchalski W.** (2008), Limitations in application of basic frequency simplest lower estimators in investigation of natural vibrations circular plates with variable thickness and clamped edges, *Journal of Theoretical and Applied Mechanics*, Vol. 46, nr 1, 109-121.
8. **Jaroszewicz J., Zoryj L.** (2000), Investigation of the effect of axial loads on the transverse vibrations of a vertical cantilever with variables parameters, *International Applied Mechanics*, Volume 36, Number 9, 1242-1251.
9. **Jaroszewicz J., Zoryj L.** (2005), *Methods of analysis natural vibration of axi-symmetrical plates using Cauchy function*, Białystok.
10. **Jaroszewicz J., Zoryj L.** (2006), The method of partial discretization in free vibration problems of circular plates with variable distribution of parameters, *International Applied Mechanics*, 42, 3, 364-373.
11. **Jaroszewicz J., Zoryj L., Katunin A.** (2006), Influence of additional mass rings on frequencies of axi-symmetrical vibrations of linear variable thickness clamped circular plates, *Journal of Theoretical and Applied Mechanics*, 44, 4, 867-880.
12. **Kovalenko A.D.** (1959), *Kruglyje plastiny peremennoj tolschchiny*, Gosudarstvennoje Izdanie Fiziko-Matematicheskoy Literatury, Moskva.
13. **Vasylenko N.V., Oleksiejčuk O.M.** (2004), *Teoriya kolyvań i stijkosti ruchu*, Vyscha Shkola, Kiev.
14. **Woźniak C.** (2001), *Mechanics of elasticity plates and shells*, Polish Academy of Sciences, PWN, Warsaw.

POSITIVE REALIZATIONS FOR DESCRIPTOR DISCRETE-TIME LINEAR SYSTEMS

Tadeusz KACZOREK*

*Faculty of Electrical Engineering, Białystok University of Technology, ul. Wiejska 45D, 15-351 Białystok, Poland

kaczorek@isep.pw.edu.pl

Abstract: Conditions for the existence of positive realizations for descriptor discrete-time linear systems are established. A procedure for computation of positive realizations for improper transfer matrices is proposed. The effectiveness of the method is demonstrated on numerical example.

Key words: Positive, Realization, Procedure, Descriptor, Linear Systems

1. INTRODUCTION

A dynamical system is called positive if its trajectory starting from any nonnegative initial state remains forever in the positive orthant for all nonnegative inputs. An overview of state of the art in positive theory is given in the monographs (Farina and Rinaldi, 2000; Kaczorek, 2002). Variety of models having positive behavior can be found in engineering, economics, social sciences, biology and medicine, etc. The positive fractional linear systems have been addressed in Kaczorek (2008a, 2009a, 2011d).

An overview on the positive realization problem is given in Benvenuti and Farina (2004), Farina and Rinaldi (2000), Kaczorek (2002, 2009b). The realization problem for positive continuous-time and discrete-time linear systems has been considered in Kaczorek (2004, 2006a, c, 2011a, c) and the positive minimal realization problem for singular discrete-time systems with delays in Kaczorek (2005). The realization problem for fractional linear systems has been analyzed in Kaczorek (2008b, 2011b, d) and for positive 2D hybrid systems in Kaczorek (2008c). A method based on the similarity transformation of the standard realizations to the desired form has been proposed in Kaczorek (2011c).

Positive stable realizations problem for continuous-time standard and fractional linear systems has been addressed in Kaczorek (2011a, b) and computation of realizations of discrete-time cone systems in Kaczorek (2006b).

In this paper a method for computation of positive realizations of descriptor discrete-time linear systems will be proposed.

The paper is organized as follows. In section 2 the positive realization problem for standard discrete-time linear systems is recalled. The positive realization problem for descriptor discrete-time linear systems is formulated and solved in section 3. The proposed procedure for computation of positive realizations of a given improper transfer matrix is illustrated by numerical example in section 4. Concluding remarks are given in section 5.

The following notation will be used: \mathfrak{R} – the set of real numbers, $\mathfrak{R}^{n \times m}$ – the set of $n \times m$ real matrices, $\mathfrak{R}_+^{n \times m}$ – the set of $n \times m$ matrices with nonnegative entries and $\mathfrak{R}_+^n = \mathfrak{R}_+^{n \times 1}$, $\mathfrak{R}^{p \times m}(z)$ – the set of $p \times m$ rational matrices in z with real coefficients, $\mathfrak{R}^{p \times m}[z]$ – the set of $p \times m$ polynomial matrices in z with real coefficients, I_n – the $n \times n$ identity matrix.

2. PRELIMINARIES AND POSITIVE REALIZATION PROBLEM FOR STANDARD SYSTEMS

Consider the standard discrete-time linear system:

$$x_{i+1} = Ax_i + Bu_i, \quad i \in Z_+ = \{0, 1, \dots\} \quad (2.1a)$$

$$y_i = Cx_i + Du_i \quad (2.1b)$$

where: $x_i \in \mathfrak{R}^n$, $u_i \in \mathfrak{R}^m$, $y_i \in \mathfrak{R}^p$ are the state, input and output vectors and $A \in \mathfrak{R}^{n \times n}$, $B \in \mathfrak{R}^{n \times m}$, $C \in \mathfrak{R}^{p \times n}$, $D \in \mathfrak{R}^{p \times m}$.

Definition 2.1. The system (2.1) is called (internally) positive if $x_i \in \mathfrak{R}_+^n$, $y_i \in \mathfrak{R}_+^p$, $i \in Z_+$ for any initial conditions $x_0 \in \mathfrak{R}_+^n$ and all inputs $u_i \in \mathfrak{R}_+^m$, $i \in Z_+$.

Theorem 2.1. The system (2.1) is positive if and only if (Farina and Rinaldi, 2000; Kaczorek, 2002):

$$A \in \mathfrak{R}_+^{n \times n}, \quad B \in \mathfrak{R}_+^{n \times m}, \quad C \in \mathfrak{R}_+^{p \times n}, \quad D \in \mathfrak{R}_+^{p \times m}. \quad (2.2)$$

The transfer matrix of the system (2.1) is given by:

$$T(z) = C[I_n z - A]^{-1} B + D. \quad (2.3)$$

The transfer matrix $T(z) \in \mathfrak{R}^{p \times m}(z)$ is called proper if and only if:

$$\lim_{z \rightarrow \infty} T(z) = K \in \mathfrak{R}^{p \times m} \quad (2.4)$$

and it is called strictly proper if $K = 0$. Otherwise the transfer matrix is called improper.

Definition 2.2. Matrices (2.2) are called a positive realization of transfer matrix $T(z)$ if they satisfy the equality (2.3).

Different methods for computation of a positive realization (2.2) for a given proper transfer matrix $T(z)$ have been proposed in Kaczorek (2002, 2011a, b, d).

3. POSITIVE REALIZATION PROBLEM FOR DESCRIPTOR SYSTEMS

Consider the descriptor discrete-time linear system:

$$Ex_{i+1} = Ax_i + Bu_i, \quad i \in Z_+ = \{0, 1, \dots\} \quad (3.1a)$$

$$y_i = Cx_i \quad (3.1b)$$

where: $x_i \in \mathfrak{R}^n$, $u_i \in \mathfrak{R}^m$, $y_i \in \mathfrak{R}^p$ are the state, input and output vectors and $E, A \in \mathfrak{R}^{n \times n}$, $B \in \mathfrak{R}^{n \times m}$, $C \in \mathfrak{R}^{p \times n}$.

It is assumed that $\det E = 0$ and the pencil of (E, A) is regular, i.e.:

$$\det[Ez - A] \neq 0 \quad \text{for some } z \in \mathbb{C} \quad (3.2)$$

where: \mathbb{C} is the field of complex numbers.

Definition 3.1. The descriptor system (3.1) is called (internally) positive if $x_i \in \mathfrak{R}_+^n$, $y_i \in \mathfrak{R}_+^p$, $i \in Z_+$ for any initial conditions $x_0 \in \mathfrak{R}_+^n$ and all inputs $u_i \in \mathfrak{R}_+^m$, $i \in Z_+$.

If the nilpotency index μ of the matrix E is greater or equal to 1 (Kaczorek, 1992) then the transfer matrix of (3.1) is improper and given by:

$$T(z) = C[Ez - A]^{-1}B \in \mathfrak{R}^{p \times m}(z). \quad (3.3)$$

The improper matrix (3.3) can be always written as the sum of strictly proper part $T_{sp}(z)$ and the polynomial part $P(z)$, i.e.

$$T(z) = T_{sp}(z) + P(z) \quad (3.4a)$$

where:

$$P(z) = D_0 + D_1 z + \dots + D_q z^q \in \mathfrak{R}^{p \times m}[z], \quad q \in N = \{1, 2, \dots\} \quad (3.4b)$$

and $q = \mu - 1$.

Theorem 3.1. Let the matrices:

$$A \in \mathfrak{R}_+^{n \times n}, \quad B \in \mathfrak{R}_+^{n \times m}, \quad C \in \mathfrak{R}_+^{p \times n} \quad (3.5)$$

be a positive realization of the strictly proper transfer matrix $T_{sp}(z)$. Then there exists a positive realization of $T(z) \in \mathfrak{R}^{p \times m}(z)$ of the form:

$$\begin{aligned} \bar{E} &= \begin{bmatrix} I_n & 0 & 0 & \dots & 0 & 0 \\ 0 & 0 & 0 & \dots & 0 & 0 \\ 0 & I_m & 0 & \dots & 0 & 0 \\ \vdots & \vdots & \vdots & \dots & \vdots & \vdots \\ 0 & 0 & 0 & \dots & I_m & 0 \end{bmatrix} \in \mathfrak{R}_+^{\bar{n} \times \bar{n}}, \\ \bar{A} &= \begin{bmatrix} A & B & 0 & \dots & 0 & 0 \\ 0 & I_m & 0 & \dots & 0 & 0 \\ 0 & 0 & I_m & \dots & 0 & 0 \\ \vdots & \vdots & \vdots & \dots & \vdots & \vdots \\ 0 & 0 & 0 & \dots & 0 & I_m \end{bmatrix} \in \mathfrak{R}_+^{\bar{n} \times \bar{n}}, \quad \bar{B} = \begin{bmatrix} 0 \\ I_m \\ 0 \\ \vdots \\ 0 \end{bmatrix} \in \mathfrak{R}_+^{\bar{n} \times m}, \\ \bar{C} &= [C \quad D_0 \quad D_1 \quad \dots \quad D_q] \in \mathfrak{R}_+^{p \times \bar{n}}, \quad \bar{n} = n + (q+1)m \end{aligned} \quad (3.6)$$

if and only if:

$$D_k \in \mathfrak{R}_+^{p \times m} \quad \text{for } k = 0, 1, \dots, q. \quad (3.7)$$

Proof. If the matrices (3.5) are a positive realization of $T_{sp}(z)$ then the standard system:

$$x_{i+1} = Ax_i + Bu_i \quad (3.8a)$$

$$y_i = Cx_i \quad (3.8b)$$

is positive and $x_i \in \mathfrak{R}_+^n$, $i \in Z_+$ for any initial conditions $x_0 \in \mathfrak{R}_+^n$ and all inputs $u_i \in \mathfrak{R}_+^m$, $i \in Z_+$. Defining the new state vector:

$$\bar{x}_i = \begin{bmatrix} x_i \\ u_i \\ u_{i+1} \\ \vdots \\ u_{i+q} \end{bmatrix} \in \mathfrak{R}^{\bar{n}} \quad (3.9)$$

and using (3.6) we obtain:

$$\bar{E}\bar{x}_{i+1} = \bar{A}\bar{x}_i + \bar{B}u_i \quad (3.10a)$$

$$\bar{y}_i = \bar{C}\bar{x}_i \quad (3.10b)$$

From (3.10) it follows that $\bar{x}_i \in \mathfrak{R}_+^{\bar{n}}$ and $\bar{y}_i \in \mathfrak{R}_+^p$ for $i \in Z_+$ if and only if (3.7) holds since $x_i \in \mathfrak{R}_+^n$ and $u_i \in \mathfrak{R}_+^m$ for $i \in Z_+$. Using (3.6), (3.3) and (3.4) it is easy to verify that:

$$\begin{aligned} \bar{C}[\bar{E}z - \bar{A}]^{-1}\bar{B} &= [C \quad D_0 \quad D_1 \quad \dots \quad D_q] \\ &\times \begin{bmatrix} I_n z - A & -B & 0 & \dots & 0 & 0 \\ 0 & -I_m & 0 & \dots & 0 & 0 \\ 0 & I_m z & -I_m & \dots & 0 & 0 \\ \vdots & \vdots & \vdots & \dots & \vdots & \vdots \\ 0 & 0 & 0 & \dots & I_m z & -I_m \end{bmatrix}^{-1} \begin{bmatrix} 0 \\ -I_m \\ 0 \\ \vdots \\ 0 \end{bmatrix} \\ &= [C \quad D_0 \quad D_1 \quad \dots \quad D_q] \begin{bmatrix} [I_n z - A]^{-1}B \\ I_m \\ I_m z \\ \vdots \\ I_m z^q \end{bmatrix} \\ &= C[Ez - A]^{-1}B + D_0 + D_1 z + \dots + D_q z^q \\ &= T_{sp}(z) + P(z) = T(z). \end{aligned} \quad (3.11)$$

The positive realization problem for the descriptor system can be stated as follows. Given an improper rational matrix $T(z) \in \mathfrak{R}^{p \times m}(z)$, find its positive realization (3.6).

If the conditions of Theorem 3.1 are satisfied then the desired positive realization (3.6) of $T(z)$ can be computed by the use of the following procedure.

Procedure 3.1.

- Step 1. Decompose the given matrix $T(z)$ into the strictly proper part $T_{sp}(z)$ and the polynomial part $P(z)$ satisfying (3.4).
- Step 2. Using one of the well-known methods (Kaczorek, 2002, 2011 a, b) find the positive realization (3.5) of $T_{sp}(z)$.
- Step 3. Knowing the realization (3.5) and the matrices $D_k \in \mathfrak{R}_+^{p \times m}$, $k = 0, 1, \dots, q$ of (3.4b) find the desired realization (3.6).

4. EXAMPLE

Find a positive realization (3.6) of the transfer matrix:

$$T(z) = \begin{bmatrix} \frac{z^4 - 3z^3 + 3z^2 - 2z + 0.5}{z^2 - 3z + 2} & \frac{z^3 - 2z^2 - 4z + 4}{z^2 - 4z + 3} \\ \frac{3z^3 - 11z^2 + 6z + 0.5}{z^2 - 4z + 3} & \frac{2z^4 - 9z^3 + 8z^2 + 2z + 3.2}{z^2 - 5z + 6} \end{bmatrix}. \quad (4.1)$$

Using Procedure 3.1 we obtain the following.

Step 1. The transfer matrix (4.1) has the strictly proper part:

$$T_{sp}(z) = \begin{bmatrix} \frac{z-1.5}{z^2-3z+2} & \frac{z-2}{z^2-4z+3} \\ \frac{z-2.5}{z^2-4z+3} & \frac{z-2.8}{z^2-5z+6} \end{bmatrix} \quad (4.2)$$

and the polynomial part:

$$P(z) = \begin{bmatrix} z^2+1 & z+2 \\ 3z+1 & 2z^2+z+1 \end{bmatrix} = D_0 + D_1 z + D_2 z^2, \quad (q=2) \quad (4.3a)$$

where:

$$D_0 = \begin{bmatrix} 1 & 2 \\ 1 & 1 \end{bmatrix}, \quad D_1 = \begin{bmatrix} 0 & 1 \\ 3 & 1 \end{bmatrix}, \quad D_2 = \begin{bmatrix} 1 & 0 \\ 0 & 2 \end{bmatrix}. \quad (4.3b)$$

Step 2. The strictly proper transfer matrix (4.2) can be rewritten in the form:

$$T_{sp}(z) = \frac{1}{(z-1)(z-2)(z-3)} \times \begin{bmatrix} (z-1.5)(z-3) & (z-2)^2 \\ (z-2.5)(z-2) & (z-2.8)(z-1) \end{bmatrix} \quad (4.4)$$

and the well-known Gilbert method can be applied to find its positive realization (Kaczorek, 2002, 2011a; Shaker and Dixon, 1977). Following Gilbert method we compute the matrices:

$$T_1 = \lim_{z \rightarrow z_1=1} (z-z_1)T_{sp}(z) = \begin{bmatrix} \frac{z-1.5}{z-2} & \frac{z-2}{z-3} \\ \frac{z-2.5}{z-3} & \frac{(z-1)(z-2.8)}{(z-2)(z-3)} \end{bmatrix}_{z=1} = \begin{bmatrix} 0.5 & 0.5 \\ 0.75 & 0 \end{bmatrix}, \quad (4.5a)$$

$$r_1 = \text{rank } T_1 = 2,$$

$$T_2 = \lim_{z \rightarrow z_2=2} (z-z_2)T_{sp}(z) = \begin{bmatrix} \frac{z-1.5}{z-1} & \frac{(z-2)^2}{(z-1)(z-3)} \\ \frac{(z-2)(z-2.5)}{(z-1)(z-3)} & \frac{z-2.8}{z-3} \end{bmatrix}_{z=2} = \begin{bmatrix} 0.5 & 0 \\ 0 & 0.8 \end{bmatrix}, \quad (4.5b)$$

$$r_2 = \text{rank } T_2 = 2,$$

$$T_3 = \lim_{z \rightarrow z_3=3} (z-z_3)T_{sp}(z) = \begin{bmatrix} \frac{(z-1.5)(z-3)}{(z-1)(z-2)} & \frac{z-2}{z-1} \\ \frac{z-2.5}{z-1} & \frac{z-2.8}{z-2} \end{bmatrix}_{z=3} = \begin{bmatrix} 0 & 0.5 \\ 0.25 & 0.2 \end{bmatrix}, \quad (4.5c)$$

$$r_3 = \text{rank } T_3 = 2$$

$$\begin{aligned} T_1 &= C_1 B_1, \quad C_1 = \begin{bmatrix} 0.5 & 0.5 \\ 0.75 & 0 \end{bmatrix}, \quad B_1 = \begin{bmatrix} 1 & 0 \\ 0 & 1 \end{bmatrix}, \\ T_2 &= C_2 B_2, \quad C_2 = \begin{bmatrix} 0.5 & 0 \\ 0 & 0.8 \end{bmatrix}, \quad B_2 = \begin{bmatrix} 1 & 0 \\ 0 & 1 \end{bmatrix}, \\ T_3 &= C_3 B_3, \quad C_3 = \begin{bmatrix} 0 & 0.5 \\ 0.25 & 0.2 \end{bmatrix}, \quad B_3 = \begin{bmatrix} 1 & 0 \\ 0 & 1 \end{bmatrix} \end{aligned} \quad (4.6)$$

and:

$$A = \text{blockdiag}[I_{r_1} z_1, I_{r_2} z_2, I_{r_3} z_3] = \text{diag}[1, 1, 2, 2, 3, 3],$$

$$B = \begin{bmatrix} B_1 \\ B_2 \\ B_3 \end{bmatrix} = \begin{bmatrix} 1 & 0 \\ 0 & 1 \\ 1 & 0 \\ 0 & 1 \\ 1 & 0 \\ 0 & 1 \end{bmatrix}, \quad (4.7)$$

$$C = [C_1 \quad C_2 \quad C_3] = \begin{bmatrix} 0.5 & 0.5 & 0.5 & 0 & 0 & 0.5 \\ 0.75 & 0 & 0 & 0.8 & 0.25 & 0.2 \end{bmatrix}.$$

Step 3. The desired positive realization of (4.1) has the form:

$$\begin{aligned} \bar{E} &= \begin{bmatrix} I_6 & 0 & 0 & 0 \\ 0 & 0 & 0 & 0 \\ 0 & I_2 & 0 & 0 \\ 0 & 0 & I_2 & 0 \end{bmatrix} \in \mathfrak{R}_+^{\bar{n} \times \bar{n}}, \\ \bar{A} &= \begin{bmatrix} A & B & 0 & 0 \\ 0 & I_2 & 0 & 0 \\ 0 & 0 & I_2 & 0 \\ 0 & 0 & 0 & I_2 \end{bmatrix} \in \mathfrak{R}_+^{\bar{n} \times \bar{n}}, \quad \bar{B} = \begin{bmatrix} 0 \\ -I_2 \\ 0 \\ 0 \end{bmatrix} \in \mathfrak{R}_+^{\bar{n} \times 2}, \end{aligned} \quad (4.8)$$

$$\bar{C} = [C \quad D_0 \quad D_1 \quad D_2] \in \mathfrak{R}_+^{2 \times \bar{n}},$$

$$\bar{n} = n + (q+1)m = 6 + 3 \cdot 2 = 12$$

and the matrices A , B , C , D_0 , D_1 , D_2 are given by (4.7) and (4.3b).

5. CONCLUDING REMARKS

A method for computation of positive realizations for descriptor discrete-time linear systems has been proposed. Conditions for the existence of positive realizations for given improper transfer matrices have been established. A procedure for computation of positive realizations has been proposed and illustrated by a numerical example. The proposed method can be easily extended to descriptor continuous-time linear systems and asymptotically stable descriptor discrete-time linear systems. An open problem is an extension of this method for fractional descriptor linear systems.

REFERENCES

1. Benvenuti L., Farina L. (2004), A tutorial on the positive realization problem, *IEEE Trans. Autom. Control*, Vol. 49, No. 5, 651-664.

2. **Farina L. Rinaldi S.** (2000), *Positive Linear Systems, Theory and Applications*, J. Wiley, New York.
3. **Kaczorek T.** (1992), *Linear Control Systems*, Vol.1, Research Studies Press, J. Wiley, New York.
4. **Kaczorek T.** (2002), *Positive 1D and 2D Systems*, Springer-Verlag, London.
5. **Kaczorek T.** (2004), Realization problem for positive discrete-time systems with delay, *System Science*, Vol. 30, No. 4, 117-130.
6. **Kaczorek T.** (2005), Positive minimal realizations for singular discrete-time systems with delays in state and delays in control, *Bull. Pol. Acad. Sci. Techn.*, Vol 53, No. 3, 293-298.
7. **Kaczorek T.** (2006a), A realization problem for positive continuous-time linear systems with reduced numbers of delays, *Int. J. Appl. Math. Comp. Sci.*, Vol. 16, No. 3, 325-331.
8. **Kaczorek T.** (2006b), Computation of realizations of discrete-time cone systems, *Bull. Pol. Acad. Sci. Techn.*, Vol. 54, No. 3, 347-350.
9. **Kaczorek T.** (2006c), Realization problem for positive multivariable discrete-time linear systems with delays in the state vector and inputs, *Int. J. Appl. Math. Comp. Sci.*, Vol. 16, No. 2, 101-106.
10. **Kaczorek T.** (2008a), Fractional positive continuous-time linear systems and their reachability, *Int. J. Appl. Math. Comp. Sci.*, Vol. 18, No. 2, 223-228.
11. **Kaczorek T.** (2008b), Realization problem for fractional continuous-time systems, *Archives of Control Sciences*, Vol. 18, No. 1, 43-58.
12. **Kaczorek T.** (2008c), Realization problem for positive 2D hybrid systems, *COMPEL*, Vol. 27, No. 3, 613-623.
13. **Kaczorek T.** (2009a), Fractional positive linear systems, *Kybernetes: The International Journal of Systems and Cybernetics*, Vol. 38, No. 7/8, 1059-1078.
14. **Kaczorek T.** (2009b), *Polynomial and Rational Matrices*, Springer-Verlag, London.
15. **Kaczorek T.** (2011a), Computation of positive stable realization for linear continuous-time systems, *Bull. Pol. Acad. Sci. Techn.*, Vol. 59, No. 3, 273-281.
16. **Kaczorek T.** (2011b), Positive stable realizations of fractional continuous-time linear systems, *Int. J. Appl. Math. Comp. Sci.*, Vol. 21, No. 4, 697-703.
17. **Kaczorek T.** (2011c), Positive stable realizations with system Metzler matrices, *Proc. MMAR Conf.*, 22-25 Sept. 2011, Międzyzdroje, Poland.
18. **Kaczorek T.** (2011d), *Selected Problems in Fractional Systems Theory*, Springer-Verlag.
19. **Shaker U. Dixon M.** (1977), Generalized minimal realization of transfer-function matrices, *Int. J. Contr.*, Vol. 25, No. 5, 785-803.

This work was supported by National Science Centre in Poland under work no. N N514 6389 40.

STIFFNESS MATRIX ANALYSIS OF SIX-REVOLUTE SERIAL MANIPULATOR

Józef KNAPCZYK*, Mateusz RYSKA*

*Cracow University of Technology, Al. Jana Pawła II 37 b, 31-864 Kraków, Poland

j_kn@mech.edu.pl, mateusz.ryska@o2.pl

Abstract: This paper presents a simple procedure that can be used to determine the stiffness matrix of 6R serial manipulator in selected points of the work space with joint stiffness coefficients taking into account. Elastokinematical model for the robot manipulator FANUC S-420F was considered as spatial and serial kinematical chain composed of six rigid links, connected by ideal revolute joint (without clearances and deformable elements), with torsion elasticity of the joint drive system (relative torsion deformations are proportional to acted torques) taking into account. Assumed model is used for displacement analysis of the end-effector for a given applied force in quasi-static condition. The analysis results are presented as Cartesian stiffness matrix of studied manipulator.

Key words: Serial Manipulator, Jacobian Matrix, Cartesian Stiffness Matrix

1. INTRODUCTION

Serial robots are mainly used in industry for the tasks required good repeatability but not necessarily high accuracy of the end-effector pose in workspace (position and orientation according to ISO9283). For example, these robots are used for pick-and-place, painting and welding operations. Nevertheless, many serial robots are now used for machining operations that require high precision and stiffness.

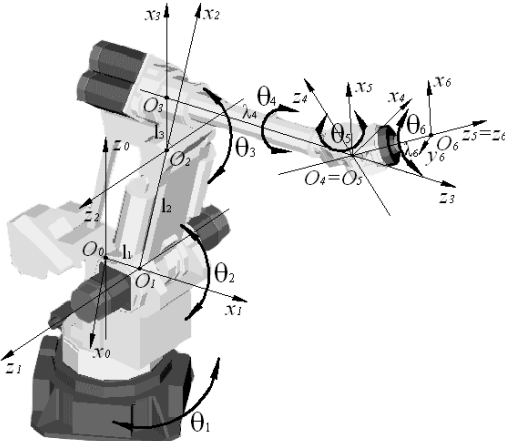


Fig. 1. Industrial Robot FANUC S-420F (Kim and Treit, 1995)

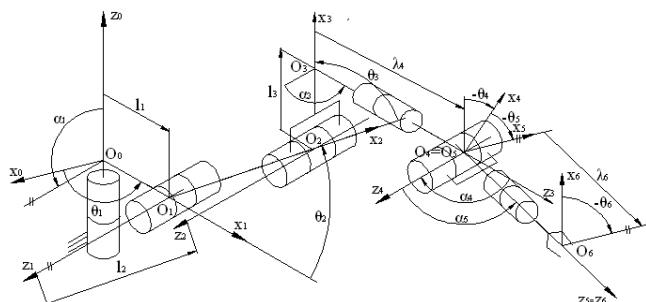


Fig. 2. Kinematical model of manipulator 6R FANUC S-420F

Elastokinematical models of serial manipulators are used for stiffness analysis and presented in: Dumas et al. (2011), Góra and Trela (2011a, b), Kim and Treit (1995) and Morecki et al. (1995); however, the identification of stiffness parameters has yet to be determined. Two methods were used to obtain the Cartesian stiffness matrix of serial manipulator. The first method consists of clamping all of the joints except one to measure its elastic deflection under applied load. The joint stiffness matrix of manipulator is obtained by repeating the procedure for each revolute joint. Therefore, only six experiments are required with this method to evaluate stiffness matrix of the 6R manipulator throughout its workspace. The second method measures the displacements of the end-effector due to certain applied loads and evaluates the stiffness matrix throughout its workspace with some interpolations. This method gives better results than the first when many tests are performed under different manipulator configurations.

This paper presents the Cartesian stiffness matrix analysis of the 6R robot FANUC S-420F (see Figs. 1 i 2).

2. STIFFNESS MATRIX FORMULATION

Kinematical model of 6R robot manipulator (FANUC S-420F) is considered as serial kinematical chain with six revolute joints (Fig.2). Denavit-Hartenberg (D-H) parameters are given in Tab. 1.

The (6×6) Jacobian matrix of the manipulator is:

$$\mathbf{J} = \begin{bmatrix} \frac{\partial p_x}{\partial \theta_1} & \frac{\partial p_y}{\partial \theta_1} & \frac{\partial p_{xz}}{\partial \theta_1} & \frac{\partial \varphi_x}{\partial \theta_1} & \frac{\partial \varphi_y}{\partial \theta_1} & \frac{\partial \varphi_z}{\partial \theta_1} \end{bmatrix}^T \quad (1)$$

where: p_x, p_y, p_z – point coordinates of the end-effector; $\varphi_x, \varphi_y, \varphi_z$ – angular coordinates of the end-effector with respect to the base frame axes, θ_i – angular coordinate of the revolute joint i ($i = 1, 2, \dots, 6$).

The links of the robot are assumed as rigid bodies, and the joint stiffness (with control loop stiffness and actuators mechanical stiffness taking into account) is represented with linear torsion spring. In the case of small elastic deformation the following relation can be written (Dumas et al., 2011; Kim and Treit, 1995; Tsai, 1999):

$$m_i = k_i \Delta \theta_i \quad (2)$$

where: m_i – torque applied on the joint i , $\Delta \theta_i$ – torsion deformation, k_i – i -th joint stiffness value.

Assuming that frictional forces at the joints are negligible and neglecting the gravitational effect we can apply the principle of virtual work to derive a transformation between the joint torques and end-effector forces:

$$\mathbf{m} = \mathbf{J}^T \mathbf{f} \quad (3)$$

where: $\mathbf{m} = [m_1 \dots m_6]^T$, $\mathbf{f} = [F_x F_y F_z M_x M_y M_z]^T$,

\mathbf{f} – vector of the end-effector output force and moment (the components are described with respect to the base frame); $\Delta \mathbf{d}$ – displacement of the end-effector (in Cartesian coordinates) as proportional to the quasi-static output load:

$$\Delta \mathbf{d} = \mathbf{C} \mathbf{f} = \mathbf{K}^{-1} \mathbf{f} \quad (4)$$

where: $\Delta \mathbf{d} = [\Delta p_x \Delta p_y \Delta p_z \Delta \varphi_x \Delta \varphi_y \Delta \varphi_z]^T$

$$\mathbf{K} = \mathbf{J}^{-T} (\mathbf{K}_\theta - \mathbf{K}_C) \mathbf{J}^{-1} \quad (5)$$

$$\mathbf{K}_\theta = \text{diag}[k_1 k_2 \dots k_6] \quad (6)$$

$$\mathbf{K}_C = \left[\frac{\partial \mathbf{J}^T}{\partial \theta_i} \right] \mathbf{m} \quad (i = 1, 2, \dots, 6)$$

\mathbf{C} (6x6) – compliance matrix, \mathbf{K} (6x6) – stiffness matrix of manipulator, \mathbf{K}_θ – diagonal joint stiffness matrix, \mathbf{J} – kinematical Jacobian matrix, \mathbf{K}_C – complementary stiffness matrix. According to (5) stiffness matrix of manipulator depends on both constant matrix \mathbf{K}_θ and variable matrix \mathbf{K}_C , depended on position. It make sense that joint stiffness identification is easier when \mathbf{K}_C is negligible with respect to \mathbf{K}_θ . From equations (4) and (5) it can be derived:

$$\Delta \mathbf{d} \cong \mathbf{J} \mathbf{K}_\theta^{-1} \mathbf{J}^T \mathbf{f} \quad (7)$$

Let the joint compliances be the components of the six-dimensional vector:

$$\boldsymbol{\kappa} = [\kappa_i]^T = [1/k_i]^T \quad (i = 1, 2, \dots, 6) \quad (8)$$

The 6-dimensional vector (7) describing small displacement of the end-effector can be expressed as:

$$\Delta \mathbf{d} = \mathbf{F} \boldsymbol{\kappa} \quad (9)$$

where:

$$\mathbf{F} = \begin{bmatrix} J_{11} \sum_{i=1}^6 J_{i1} f_i & \dots & J_{16} \sum_{i=1}^6 J_{i6} f_i \\ \dots & \dots & \dots \\ J_{61} \sum_{i=1}^6 J_{i1} f_i & \dots & J_{66} \sum_{i=1}^6 J_{i6} f_i \end{bmatrix} \quad (10)$$

Therefore, \mathbf{f} – vector of load, $\Delta \mathbf{d}$ – vector of displacement and matrix \mathbf{F} are associated with each test in determined position and load case. When only one test is considered, then matrix \mathbf{F} is (6x6). If it is nonsingular, then equation (9) has a unique solution (Dumas et al., 2011):

$$\boldsymbol{\kappa} = \mathbf{F}^{-1} \Delta \mathbf{d} \quad (11)$$

When several tests are considered, the equation system (9) becomes over-determined. Assuming that n tests are taken into account, matrix \mathbf{F} becomes (6nx6), no longer square matrix, and the joint compliance vector $\boldsymbol{\kappa}$ cannot be calculated using (11), because the number of equations is higher than the number of unknowns. In this case it is possible to find a vector $\boldsymbol{\kappa}$ that minimizes the Euclidean norm of the approximation error of the

system. From equation system (9) it is apparent that the higher the number of tests gives the higher the degree of constraint of the equation system, and the more accurate solution, i.e., the more accurate evaluation of the joint stiffness values. Obviously, the higher number of tests is connected with the more expensive identification procedure. Therefore, it is suggested to find compromise between identification accuracy and cost, for example five tests are a good compromise.

It is possible to identify the stiffness values of the first three joints of a six-revolute manipulator by measuring only the translational displacements of its end-effector loaded by force.

2.1. Numerical example

Problem is to determine the stiffness matrix of manipulator Fanuc S-420F, with only torsion flexibility in the first three joints taking into account. For a given vertical force applied on the end-effector its linear displacements are measured. The robot with the end-effector loaded by gravity force is shown in Fig. 3. The measurement results are presented as compliance characteristics on Fig. 4.

The D-H parameters of the considered manipulator are given in Tab. 1. The first three elements of the compliance matrix, that influenced on the linear displacement of the end-effector, are presented in Appendix A.

Tab. 1. D-H parameters of manipulator Fanuc S-420F

l	$\alpha_i [^\circ]$	$l_i [\text{mm}]$	$\lambda_i [\text{mm}]$	$\theta_i [^\circ]$
1	90	270	0	± 150
2	0	900	0	$\pm 57,5$
3	90	270	0	$\pm 72,5$
4	-90	0	1300	± 360
5	90	0	0	± 125
6	0	0	260	± 360

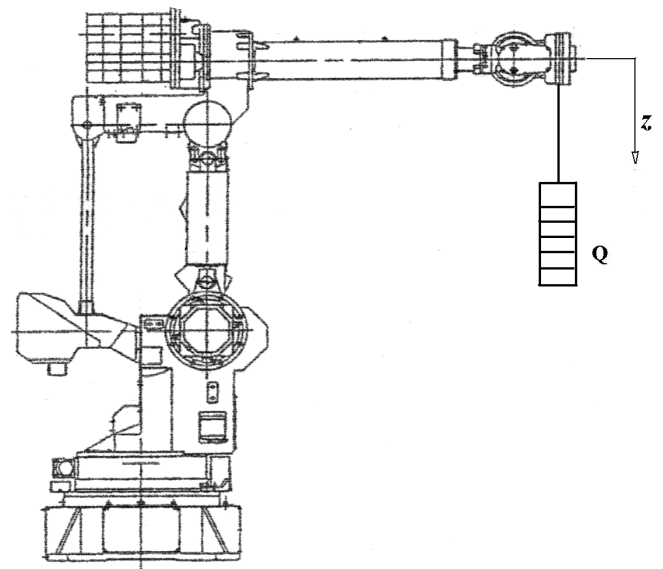


Fig. 3. Robot manipulator Fanuc S-420F with the end-effector loaded by vertical force Q

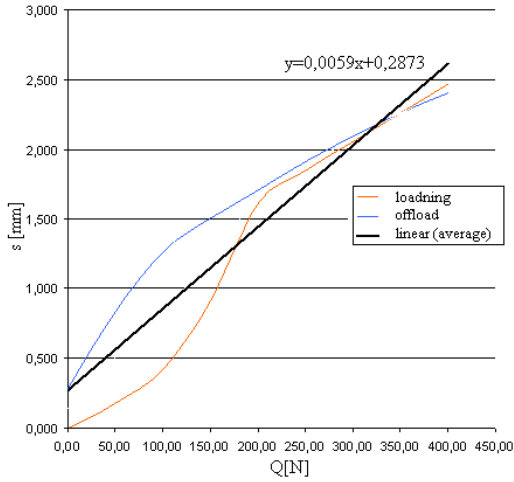


Fig. 4. Compliance characteristics (s – vertical displacement of the end-effector of robot Fanuc S-420F with respect to Q – vertical force), determined on the basis of stand measurement results

A comparison between joint stiffness data as given in Kim and Treit (2011) for robot PUMA 560: $k_1=66.230$; $k_2=66.50$; $k_3=11.610$; $k_4=0.202$; $k_5=0.101$; $k_6=0.144$ [kNm/rad]; given in Dumas et al. (2011) for robot Kuka KR240-2: $k_1=1.410$; $k_2=0.401$; $k_3=0.935$; $k_4=0.360$; $k_5=0.370$; $k_6=0.380$ [kNm/rad].

Measurements of Cartesian coordinates of the end-effector loaded by vertical force are as follows:

$$p_x = 279.85; p_y = 2751.95; p_z = 145.14 \text{ [mm];}$$

$$\varphi_x = 89.34; \varphi_y = 46.57; \varphi_z = 0.73 \text{ [°].}$$

By solving the inverse kinematical problem the respective joint coordinates are obtained:

$$\theta_i = -84.91^\circ; 65.00^\circ; -12.31^\circ; 0.00^\circ; 9.64^\circ; 0.00^\circ$$

Assuming that joint stiffness coefficients of the considered manipulator Fanuc S-420F are the same as given values for manipulator PUMA 560 and using formulae (A3) for the (3x3) element of the stiffness and compliance matrix were calculated $c_{33} = 0.00183$ [mm/N]; $k_{33} = 546.6$ [mm/N]. Respective values of this element determined on the basis of measurements made for manipulator Fanuc S-420F are: $c_{33} = 0.0059$ [mm/

N]; $k_{33} = 169.5$ [mm/N].

Suggestions for explaining this difference include variations between assumed and real values of joint stiffness coefficients. It can be concluded that stiffness coefficients of the first three joints of manipulator Fanuc S-420F are about three times greater than the respective given for manipulator PUMA 560.

3. CONCLUSION

The subject of this paper was to describe a method for stiffness analysis of serial manipulator. Elastokinematical model of the considered manipulator was assumed with the links as rigid bodies, and with the linear torsion springs in revolute joints (with control loop stiffness and actuators mechanical stiffness taking into account). Numerical example for the stiffness matrix of manipulator Fanuc S-420F is given. Cartesian stiffness matrix obtained by using presented method can be applied for planning the Cartesian trajectory of the end-effector with its load taken into account, for example tool path planning considering robot performance indices.

REFERENCES

1. Dumas C. et al. (2011), Joint stiffness identification of six-revolute industrial serial robots. *Robotics and Computer-Integrated Manufacturing* 27, 881-888.
2. Góra M., Trella R. (2011a), Determination of stiffness characteristics of serial type manipulator by using wire sensors. *Technical Transactions, Czasopismo Techniczne*, Wyd. PK, Kraków, 1M/2011, 41-48.
3. Góra M., Trella R. (2011b), Experimental determination of stiffness matrix elements of serial type manipulator, *Pomiary Automatyka Robotyka*, 2/2011, 687-696.
4. Kim H.Y., Treit D.A. (1995), Configuration dependent stiffness of the PUMA 560 manipulator: Analytical and experimental results. *Mechanism and Machine Theory*, Vol.30, No 8, 1269-1277.
5. Morecki A., Knapczyk J., Kędzior K. (2002), *Theory of mechanisms and manipulators*, WNT Warszawa.
6. Tsai L.W., (1999), *Robot Analysis. The Mechanics of Serial and Parallel Manipulators*, A Wiley & Sons, Inc. New York.

APPENDIX: DIAGONAL ELEMENTS OF COMPLIANCE MATRIX C (4) FOR MANIPULATOR FANUC S-420F (D-H parameters are given in Tab.1)

$$\begin{aligned}
 c_{11} = & \frac{1}{\kappa_1} \left[(-s_1(l_1 + l_2c_2 + l_3c_{23} + s_{23}\lambda_4) - \lambda_6((s_1c_{23}c_4 - c_1s_4)s_5 + s_1s_{23}c_5))^2 \right] + \\
 & + \frac{1}{\kappa_2} \left[c_1^2(l_2s_2 + l_3c_{23} - c_{23}\lambda_4 + (s_{23}c_4s_5 - c_{23}c_5)\lambda_6)^2 \right] + \\
 & + \frac{1}{\kappa_3} \left[c_1^2(l_3s_{23} - c_{23}\lambda_4 + (s_{23}c_4s_5 - c_{23}c_5)\lambda_6)^2 \right] + \\
 & + \frac{1}{\kappa_4} \left[\lambda_6^2 \left(s_1s_{23}(-c_{23}\lambda_4 + s_{23}c_4s_5 - c_{23}c_5) + \right. \right. \\
 & \left. \left. + c_{23}(s_1s_{23}\lambda_4 + (s_1c_{23}c_4 - c_1s_4)s_5 + s_1s_{23}c_5) \right)^2 \right] + \\
 & + \frac{1}{\kappa_5} \left[\lambda_6^2 ((-s_1c_{23}s_4 - c_1c_4)(s_{23}c_4s_5 - c_{23}c_5) + s_{23}s_4((s_1c_{23}c_4 - c_1s_4)s_5 + s_1s_{23}c_5))^2 \right]
 \end{aligned} \tag{A.1}$$

$$\begin{aligned}
c_{22} = & \frac{1}{\kappa_1} \left[c_1 (l_1 + l_2 c_2 + l_3 c_{23} + s_{23} \lambda_4) + \lambda_6 ((c_1 c_{23} c_4 + c_1 s_4) s_5 + s_1 s_{23} c_5)^2 \right] + \\
& + \frac{1}{\kappa_2} \left[s_1^2 (l_2 s_2 + l_3 s_{23} - c_{23} \lambda_4 + (s_{23} c_4 s_5 - c_{23} c_5) \lambda_6)^2 \right] + \\
& + \frac{1}{\kappa_3} \left[s_1^2 (l_3 s_{23} - c_{23} \lambda_4 + (s_{23} c_4 s_5 - c_{23} c_5) \lambda_6)^2 \right] + \\
& + \frac{1}{\kappa_4} \left[\lambda_6^2 \left(-c_{23} (c_1 s_{23} \lambda_4 + (c_1 c_{23} c_4 + s_1 s_4) s_5 + c_1 s_{23} c_5) - \right. \right. \\
& \left. \left. - c_1 s_{23} (-c_{23} \lambda_4 + s_{23} c_4 s_5 - c_{23} c_5) \right)^2 \right] + \\
& + \frac{1}{\kappa_5} \left[\lambda_6^2 (-s_{23} s_4 ((c_1 c_{23} c_4 + s_1 s_4) s_5 + c_1 s_{23} c_5) + (c_1 c_{23} s_4 - s_1 c_4) (s_{23} c_4 s_5 - c_{23} c_5))^2 \right]
\end{aligned} \tag{A.2}$$

$$\begin{aligned}
c_{33} = & \frac{1}{\kappa_2} \left[(s_1 (s_1 (l_1 + l_2 c_2 + l_3 c_{23} + s_{23} \lambda_4) + \lambda_6 ((s_1 c_{23} c_4 - c_1 s_4) s_5 + s_1 s_{23} c_5))) + \right. \\
& + c_1 (c_1 (l_2 s_2 + l_3 c_{23} + s_{23} \lambda_4) + ((c_1 c_{23} c_4 + s_1 s_4) s_5 + c_1 s_{23} c_5) \lambda_6) \left. \right)^2 + \\
& + (s_{23} c_4 s_5 - c_{23} c_5) \lambda_6 \left. \right] + \\
& + \frac{1}{\kappa_3} \left[(s_1 (s_1 (l_3 c_{23} + s_{23} \lambda_4) + \lambda_6 ((s_1 c_{23} c_4 - c_1 s_4) s_5 + s_1 s_{23} c_5))) + \right. \\
& + c_1 (c_1 (l_3 c_{23} + s_{23} \lambda_4) + ((c_1 c_{23} c_4 - c_1 s_4) s_5 + c_1 s_{23} c_5) \lambda_6) \left. \right)^2 \right] + \\
& + \frac{1}{\kappa_4} \left[(c_1 s_{23} (s_1 s_{23} \lambda_4 + \lambda_6 ((s_1 c_{23} c_4 - c_1 s_4) s_5 + s_1 s_{23} c_5) - \right. \\
& - s_1 s_{23} (c_1 s_{23} \lambda_4 + ((c_1 c_{23} c_4 + s_1 s_4) s_5 + s_1 s_{23} c_5) \lambda_6)) \left. \right)^2 \right] + \\
& + \frac{1}{\kappa_5} \left[\lambda_6^2 ((-c_1 c_{23} s_4 + s_1 c_4) (s_1 c_{23} c_4 - c_1 s_4) s_5 + s_1 s_{23} c_5) + \right. \\
& + (s_1 c_{23} s_4 + c_1 c_4) (c_1 c_{23} c_4 + s_1 s_4) s_5 + c_1 s_{23} c_5 \left. \right)^2 \right]
\end{aligned} \tag{A.3}$$

where $c_i = \cos \theta_i$, $s_i = \sin \theta_i$, $c_{ij} = \cos(\theta_i + \theta_j)$, $s_{ij} = \sin(\theta_i + \theta_j)$

LOAD-DEPENDENT CONTROLLER OF THE ACTIVE SEAT SUSPENSION WITH ADAPTIVE MASS RECOGNIZING

Igor MACIEJEWSKI*

*Division of Mechatronics and Applied Mechanics, Institute of Mechatronics, Nanotechnology and Vacuum Technique,
Koszalin University of Technology, ul. Śniadeckich 2, 75-453 Koszalin, Poland

igor.maciejewski@tu.koszalin.pl

Abstract: The paper deals with the load dependent control system of active seat suspension. This system based on the primary controller which evaluates the desired active force, the reverse model which calculates the input signal of force actuator and the adaptation mechanism which recognizes the actual mass loading. An optimisation procedure additionally presented in this paper allows to find the primary controller settings that minimizes the vibration of cabin's floor transmitted to operator's seat at the pre-defined value of the maximum relative displacement of suspension system.

Key words: Vibration Isolator, Active System, Adaptive Control

1. INTRODUCTION

In the case of typical working machines without flexible wheel suspension, a seat suspension is the only one system, which can protect the operator against vibration. Most often, the passive seat suspension amplifies the vibration amplitudes at resonance frequency. Natural frequency of the conventional seats with an air-spring and hydraulic shock-absorber is between 1-2 Hz (Maciejewski et al., 2009). Low effectiveness of passive seats for a low frequencies and high amplitudes of excitation signal endanger driver's health and finally causes cutting down the working time.

The main aim of the paper is to present an effective way for minimization the vibration risk, acting on the operators of earth-moving machines during their work. In particular the new control algorithm evaluation and the solving multi-criteria optimisation problem are discussed in this paper. The investigation concentrates on the currently manufactured seat, to obtain concurrent improvement at low frequency vibration (active systems) and also at higher frequency vibration (passive systems). The optimal seat should isolate the amplitudes of whole range of excitation frequency and has to show the high system robustness in response to varying mass loading.

2. MODEL OF THE ACTIVE SEAT SUSPENSION

In Fig. 1 a model of the active seat suspension system containing an air-spring and a hydraulic shock-absorber is shown. This system uses the active air-flow to the air-spring (inflating and exhausting) which is regulated by the control system and the proportional directional control valves. The proportional valves have an unlimited number of stable states that are proportional to the analogue input signal obtained from the controller (Beater, 2007). The proportional flow control valves are used in the active seat suspension system and therefore the mass flow rates \dot{m}_I and \dot{m}_E are proportional to the voltage input signal u_I and u_E , respectively. Inflating the air-spring is carried out by an external

air compressor and the exhaust of the air-spring is released directly to the atmosphere. The air-flow changes the air pressure inside the air-spring and the variation of pressure creates an active force for the suspension system.

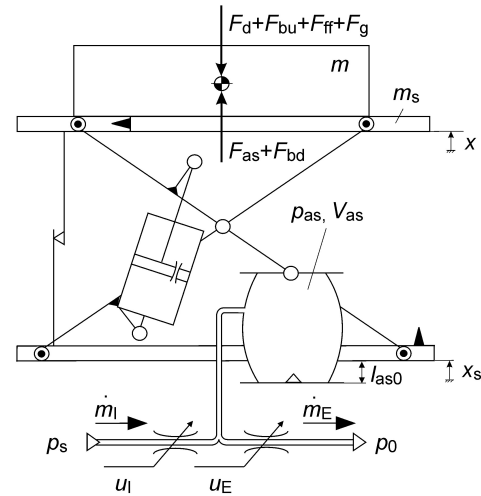


Fig. 1. Model of the active seat suspension

The equation of motion of this seat suspension has been shown in the author's previous papers (Maciejewski et al., 2009, 2010). The mathematical models of reduced forces acting on the suspended mass: the air-spring force F_{as} , the hydraulic shock-absorber force F_d , the forces of end-stop buffers: bottom F_{bd} and top F_{bu} , the overall friction force of suspension system F_{ff} and the gravity force F_g have been presented in those papers as well.

3. CONTROL SYSTEM DESIGN

Conventional seat suspension systems are sensitive to changes in their working conditions. The static and dynamic

behaviour of the system depends on the mass m loading the suspension, because the suspension system spring force F_{as} is a function of the pressure inside the air-spring (Maciejewski et al., 2010). This results in differing vibro-isolating properties of the conventional seat suspension system for different weights of machine operator. The active seat should ensure the same vibration isolating properties of the suspension system for each operator. This effect can be obtained using a load-dependent controller for the active seat suspension system that is shown in Fig. 2.

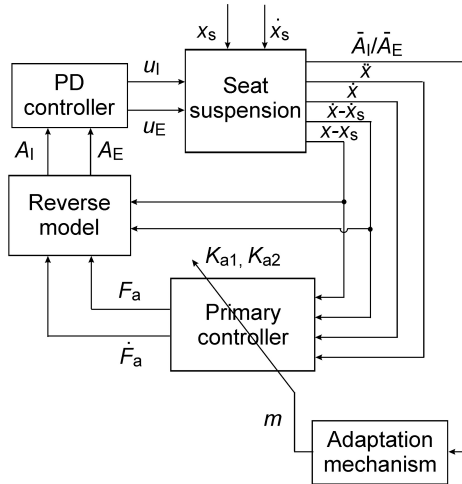


Fig. 2. Control system of the active seat suspension with adaptive mass recognizing

In this control system (Fig. 2), the desired active force (F_a, \dot{F}_a) is calculated using the primary controller. If the desired force is evaluated, then such force should be approximately reproduced by the active element applied in seat suspension. Therefore the actual effective areas (A_I, A_E) of proportional control valves are calculated using reverse model of the air spring. The actuating time of the force actuator is eliminated because the PD controller speed up the control signals (u_I, u_E). In addition, an adaptation mechanism evaluates the controller settings (K_{a1}, K_{a2}) as a function of the suspended mass (m). The suspended mass is recognized based on the mean values over time of the effective cross section areas of inlet and outlet valves (\bar{A}_I, \bar{A}_E). A detailed description of the each control system components are presented in the next subsections.

3.1. Simplified model of the air-spring

A simplified model of the air-spring relies on isothermal behaviour of air. According to this model, the actual value of air pressure p_{as} inside the chamber is defined as [3]:

$$p_{as} = \frac{1}{V_{as}} (RT(\dot{m}_I - \dot{m}_E) - p_{as} \dot{V}_{as}) \quad (1)$$

where: V_{as} is the variable volume of the air-spring, R is the gas constant, T is the air temperature. Defining pressure-force relation of the air-spring $p_{as} = \frac{\delta_{as}}{A_{ef}} F_{as} + p_{as0}$ and its variable volume $V_{as} = A_{ef} \left(\frac{x - x_s}{\delta_{as}} + l_{as0} \right)$ the force of the air-spring can be calculated as follows:

$$\dot{F}_{as} = \frac{1}{x - x_s + \delta_{as} l_{as0}} \cdot \left(RT(\dot{m}_I - \dot{m}_E) - \left(F_{as} + \frac{A_{ef}}{\delta_{as}} p_{as0} \right) (\dot{x} - \dot{x}_s) \right) \quad (2)$$

where: δ_{as} is the reduction ratio of the air-spring, l_{as0} is the initial length of the air-spring, A_{ef} is the effective area of air-spring, p_{as0} is the initial pressure of the air-spring. The reduction ratio δ_{as} is defined as a proportion of the motion of the suspension system relative to the air-spring.

The mass flow rates \dot{m}_I and \dot{m}_E are calculated using the Mietluk-Awtuszko function (Kiczowski, 2005), that assumes the adiabatic air-flow, as follows:

– for inflating of the air-spring:

$$\dot{m}_I = 0.5787 A_I p_s \sqrt{\kappa} \sqrt{\frac{1}{RT}} \alpha \frac{1 - \left(\frac{\delta_{as} F_{as} + p_{as0}}{A_{ef} p_s} \right)^{\frac{1}{\alpha}}}{\alpha - \left(\frac{\delta_{as} F_{as} + p_{as0}}{A_{ef} p_s} \right)^{\frac{1}{\alpha}}} \quad (3)$$

– for exhausting of the air-spring:

$$\dot{m}_E = 0.5787 A_E \left(\frac{\delta_{as} F_{as} + p_{as0}}{A_{ef}} \right) \sqrt{\kappa} \sqrt{\frac{1}{RT}} \alpha \frac{1 - p_0 / \left(\frac{\delta_{as} F_{as} + p_{as0}}{A_{ef}} \right)^{\frac{1}{\alpha}}}{\alpha - p_0 / \left(\frac{\delta_{as} F_{as} + p_{as0}}{A_{ef}} \right)^{\frac{1}{\alpha}}} \quad (4)$$

where: A_I is the effective cross section area of inlet valve, A_E is the effective cross section area of outlet valve, p_s is the air pressure of power supply, p_0 is the atmospheric pressure, κ is the adiabatic coefficient, α is the parameter of the Mietluk-Awtuszko function.

3.2. Reverse model of the air-spring

The description of the air-spring force relating to the mass flow rate (Eq. (2)) can be rearranged in the following form:

$$\dot{m}_I - \dot{m}_E = \frac{1}{RT} \left(\dot{F}_{as} (x - x_s + \delta_{as} l_{as0}) + \left(F_{as} + \frac{A_{ef}}{\delta_{as}} p_{as0} \right) (\dot{x} - \dot{x}_s) \right) \quad (5)$$

where: $\dot{m}_I - \dot{m}_E$ is the mass flow rate to achieve the desired air-spring force F_{as} at variable deflection $x - x_s$ and velocity $\dot{x} - \dot{x}_s$ of the air-spring. In order to obtain such mass flow rate, the effective cross section area of proportional valve should be calculated as follows:

– for inlet valve:

$$A_I = \frac{\dot{m}_I}{0.5787 A_I p_s \sqrt{\kappa} \sqrt{\frac{1}{RT}} \alpha \frac{1 - \left(\frac{\delta_{as} F_{as} + p_{as0}}{A_{ef} p_s} \right)^{\frac{1}{\alpha}}}{\alpha - \left(\frac{\delta_{as} F_{as} + p_{as0}}{A_{ef} p_s} \right)^{\frac{1}{\alpha}}}} \quad (6)$$

– for outlet valve:

$$A_E = \frac{\dot{m}_E}{0.5787 A_E \left(\frac{\delta_{as} F_{as} + p_{as0}}{A_{ef}} \right) \sqrt{\kappa} \sqrt{\frac{1}{RT}} \alpha \frac{1 - p_0 / \left(\frac{\delta_{as} F_{as} + p_{as0}}{A_{ef}} \right)^{\frac{1}{\alpha}}}{\alpha - p_0 / \left(\frac{\delta_{as} F_{as} + p_{as0}}{A_{ef}} \right)^{\frac{1}{\alpha}}}} \quad (7)$$

Assuming that the proportional directional control valves are utilized then the effective cross section areas: A_I and A_E are proportional to the electric input signals: u_{Iv} and u_{Ev} . In order to take into account the actuating times: t_I and t_E of the proportional control valves (for inlet and outlet valves, respectively), the

electric input signals are subsequently formed by proportional-derivative (PD) controller as follows:

$$u_{Iv} = \frac{1}{k_I}(t_I \dot{A}_I + A_I), \quad u_{Ev} = \frac{1}{k_E}(t_E \dot{A}_E + A_E) \quad (8)$$

where: k_I is the static gain of inlet valve and k_E is the static gain of inlet valve. The electric input signals for inlet and outlet control valves are finally limited in the operating ranges as:

$$u_I = \begin{cases} 0 & \text{for } u_{Iv} < 0 \\ u_{Iv} & \text{for } 0 < u_{Iv} \leq u_{max} \\ u_{max} & \text{for } u_{Iv} > u_{max} \end{cases} \quad (9)$$

$$u_E = \begin{cases} 0 & \text{for } u_{Ev} < 0 \\ u_{Ev} & \text{for } 0 < u_{Ev} \leq u_{max} \\ u_{max} & \text{for } u_{Ev} > u_{max} \end{cases} \quad (10)$$

where: u_{max} is the maximum input voltage that is responsible for the complete opening of proportional control valves.

3.3. Formulation of the primary controller

The full active system is used to determine desired force F_a that should be introduced into the suspension system actively (Fig. 3a). Subsequently, this desired force should be reproduced by the air-spring force F_{as} in hybrid suspension system (Fig. 3b).

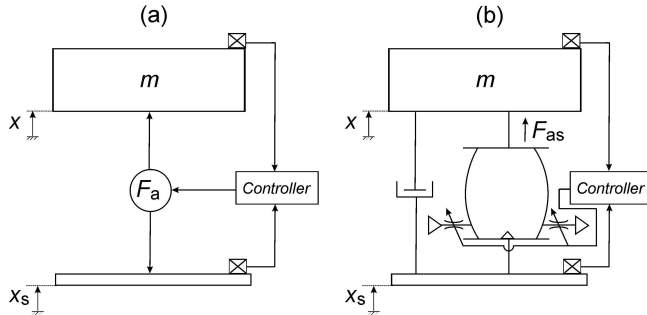


Fig. 3. Simplified seat suspension models: active (a), hybrid (b)

The relationships for the desired active force and its time derivative can be formulated in the following form (Maciejewski, 2012):

$$F_a = K_{a1}(x - x_s) + K_{a2}\dot{x} \quad (11)$$

$$\dot{F}_a = K_{a1}(\dot{x} - \dot{x}_s) + K_{a2}\ddot{x} \quad (12)$$

where: $x - x_s$ is the relative displacement of suspension system, \dot{x} is the suspended mass velocity, $\dot{x} - \dot{x}_s$ is the relative velocity of suspension system, \ddot{x} is the suspended mass acceleration, K_{a1} and K_{a2} are the primary controller settings to be designed.

3.4. Optimisation of the primary controller settings

In order to improve operator comfort the effective suspended mass acceleration \ddot{x}_{RMS} should be small. At the same time it is necessary to ensure that the maximum relative displacement of suspension system $(x - x_s)_{max}$ is small enough to ensure that even very rough road profiles do not cause the deflection limits to be reached [2]. The trade-off between operator comfort

and suspension deflection can be selected by the primary controller settings: K_{a1} and K_{a2} that are optimised for different requirements defined by the machine operators.

In this case the minimization of the effective suspended mass acceleration is proposed as:

$$\min_{K_{a1}, K_{a2}} \ddot{x}_{RMS}(K_{a1}, K_{a2}) \quad (13)$$

using a constraint imposed on the maximum relative displacement of suspension system in the following form:

$$(x - x_s)_{max}(K_{a1}, K_{a2}) \leq (x - x_s)_c \quad (14)$$

where: $(x - x_s)_c$ defines the constraint value. An appropriate selection of such value allows to choose the vibro-isolation properties of the suspension system.

The set of Pareto-optimal solutions, that are obtained for different mass loading: 50 kg, 75 kg, 100 kg, 125 kg, 150 kg, are presented in Fig. 4.

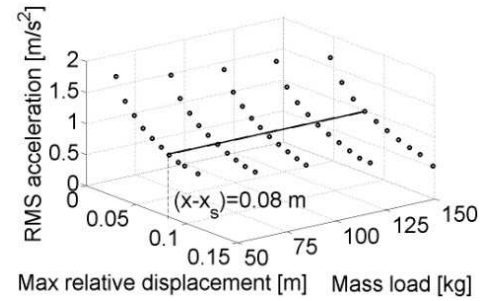


Fig. 4. Pareto-optimal point distribution for the active seat suspension obtained for different mass loading

The optimisation results (Fig. 4) show, that is possible to achieve nearly the same dynamic behaviour of active seat suspension for the same value $(x - x_s)_c = 0.08$ m of the maximum relative displacement of suspension system. In order to achieve such a system performance, the controller settings K_{a1}, K_{a2} have to be described as a function of suspended mass m . They are approximated using the exponential functions as follows:

$$K_{a1} = a_{a1} \exp(b_{a1} m) \quad (15)$$

$$K_{a2} = a_{a2} \exp(b_{a2} m) \quad (16)$$

where: a_{a1}, b_{a1} and a_{a2}, b_{a2} are the coefficients of the exponential functions to be evaluated by the least square approximation. The approximation results, that show the dependency of the controller settings: K_{a1} and K_{a2} for different m , are shown in Fig. 5.

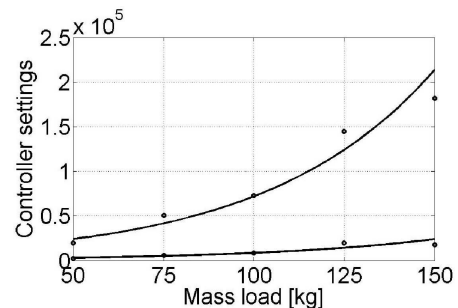


Fig. 5. Optimal controller settings

3.5. Adaptation mechanism

The load-dependent controller is proposed to control the active suspension system more efficient. The controller settings: K_{a1} and K_{a2} depend on the information of the suspended body mass and such value has to be known. This causes that an additional sensor could be employed in order to recognize the suspended mass m . However, the online available information of the air-spring inflation/deflation are helpful to recognize the mass load of the active pneumatic seat suspension. Using a principle that the mean values of inflated and exhausted air are equal ($\bar{m}_I = \bar{m}_E$), the corresponding Mietluk-Awtuszko functions (Eqs. (3) and (4)) can be compared in the following form:

$$\bar{A}_I p_s \frac{1-\bar{p}_{as}/p_s}{\alpha-\bar{p}_{as}/p_s} = \bar{A}_E \bar{p}_{as} \frac{1-p_0/\bar{p}_{as}}{\alpha-p_0/\bar{p}_{as}} \quad (17)$$

where: \bar{p}_{as} are the mean value over time of the air-spring pressure. Determining the quotient \bar{A}_I/\bar{A}_E of the effective cross section areas of inlet and outlet valves, the Eq. (17) can be rearranged as follows:

$$\frac{\bar{A}_I}{\bar{A}_E} = \frac{((\bar{p}_{as})^2 - p_0 \bar{p}_{as})(\alpha p_s - \bar{p}_{as})}{(\alpha \bar{p}_{as} - p_0)((p_s)^2 - p_s \bar{p}_{as})} \quad (18)$$

Setting $f(\bar{p}_{as}) = 0$ produces the cubic equation in the following form:

$$a(\bar{p}_{as})^3 + b(\bar{p}_{as})^2 + c\bar{p}_{as} + d = 0 \quad (19)$$

with the coefficients: a, b, c, d of the cubic equation described as follows:

$$a = 1 \quad (20)$$

$$b = -\frac{\bar{A}_I}{\bar{A}_E} \alpha p_s - \alpha p_s - p_0 \quad (21)$$

$$c = -\frac{\bar{A}_I}{\bar{A}_E} \alpha (p_s)^2 + \frac{\bar{A}_I}{\bar{A}_E} p_s p_0 + \alpha p_s p_0 \quad (22)$$

$$d = -\frac{\bar{A}_I}{\bar{A}_E} (p_s)^2 p_0 \quad (23)$$

Solving the cubic equation (Eq. (19)) amounts to finding the roots of a cubic function. Defining a discriminant of the cubic equation as follows:

$$\Delta = \left(\frac{p}{3}\right)^3 + \left(\frac{q}{2}\right)^2 \quad (24)$$

where:

$$p = \frac{c}{a} - \frac{b^2}{3a^2}, \quad q = \frac{2b^3}{27a^3} + \frac{d}{a} - \frac{bc}{3a^2} \quad (25)$$

Then for $\Delta < 0$ is possible to find each real roots of the cubic function (Eq. (19)) in the following form:

$$(\bar{p}_{as})_k = 2\sqrt{\frac{-p}{3}} \cos\left(\frac{\varphi + 2(k-1)\pi}{3}\right) - \frac{b}{3a} \quad (26)$$

where:

$$\varphi = \arccos\left(\frac{\frac{q}{2}}{\sqrt{\frac{-p^3}{27}}}\right) \quad (27)$$

and $k = 1, \dots, 3$ is the number of root found. The body mass should be calculated for given root number of the cubic equation (Eq. (19)) as follows:

$$m = \frac{(\bar{p}_{as} - p_0) \bar{A}_{ef}}{\delta_{as} g} \quad (28)$$

Using Eqs. (24)-(28) online calculation of the body mass based on the effective cross section areas of inlet and outlet valves: \bar{A}_I and \bar{A}_E is enabled. However, information of the actual cross section areas of inlet and outlet valves is not easily accessible. Therefore an adaptive load recognizing of the active suspension system is performed based on the control signals of inlet and outlet valves: \bar{u}_I and \bar{u}_E . In this paper, a quotient of the effective cross section areas of inlet and outlet valves \bar{A}_I/\bar{A}_E is assumed for the high performance pneumatic valves to be approximately equal to a quotient of their control signals multiplied by the corresponding static gains $k_I \bar{u}_I/k_E \bar{u}_E$ (i.e. $\bar{A}_I/\bar{A}_E \approx k_I \bar{u}_I/k_E \bar{u}_E$). The simulation results of recognized suspended mass as a function of the actual suspended mass, that are obtained for the root number $k = 3$ and for the simulation time of 300 s, are presented in Fig. 6a. Corresponding relative errors of the recognized mass are shown in Fig. 6b.

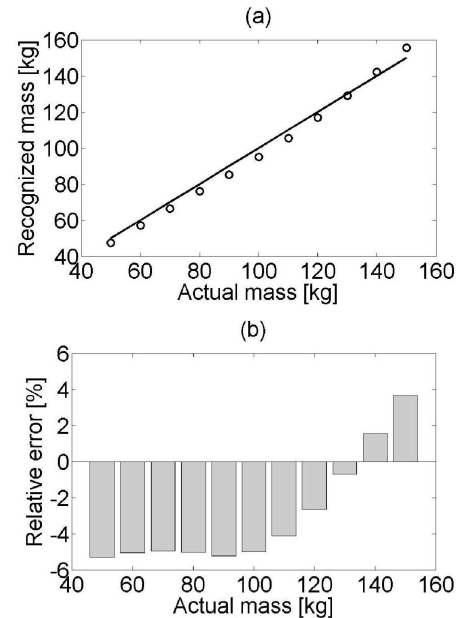


Fig. 6. Recognized suspended mass in function of the actual suspended mass (circles) and its linear dependency (solid line) (a), corresponding relative error of the recognized mass (b)

4. SIMULATION RESULTS

The transmissibility curves of the simulated conventional passive suspension system for variations of the mass loading $\pm 50\%$ are presented in Fig. 7a. As shown in this figure, the change of mass influences the dynamic behaviour of passive seat suspension. The suspension system loaded with a high mass (150 kg) causes amplification of vibration at the resonance frequency, but for higher frequencies the best vibro-isolating properties are obtained. The system loaded with a low mass (50 kg) has much lower amplification of vibration at resonance, but its vibration isolating properties at higher frequency range are poor. The dynamic behaviour of the active seat suspension (Fig. 7b) loaded by a high mass (150 kg) and low mass (50 kg) are much closer to each other than the corresponding behaviour of the passive seat suspension. The main improvement of the system robustness is observed in the frequency range 0.5-4

Hz. In that frequency range the air-flow effectively controls the air-spring force.

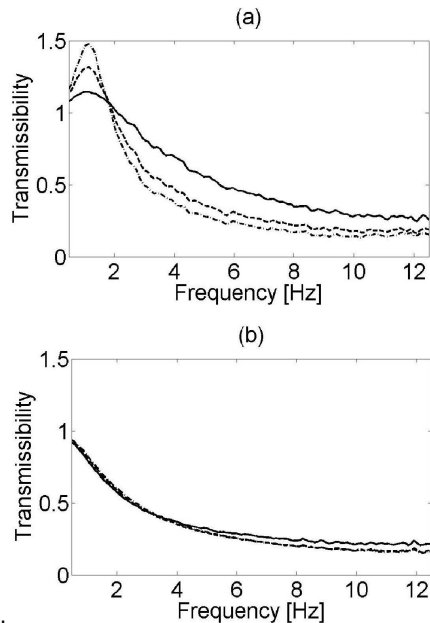


Fig. 7. Transmissibility curves of the passive (a) and active (b) seat suspension obtained for the suspended masses: 50 kg (solid line), 100kg (dashed line), 150 kg (dashed-dotted line)

5. CONCLUSIONS

The air-spring control system applied to the active seat suspension significantly improves the performance of machine operators' seat. The calculated reverse model of air-spring together with designed primary controller efficiently controls the active seat suspension dynamic behaviour. Moreover, the elaborated controller with adaptive mass recognizing ensures the desired system robustness to varying mass loading. In order to achieve the desired vibro-isolation properties of active seat suspension, an appropriate selection of the constraint value imposed on the maximum relative displacement of suspension system is required. Based on the chosen value, the controller settings are evaluated and their values define the vibration damping effectiveness of active seat.

REFERENCES

1. **Beater P.** (2007), *Pneumatic Drives, System Design, Modelling and Control*, Springer-Verlag, Berlin Heidelberg.
2. **Fialho I., Balas G.J.** (2002), Road Adaptive Active Suspension Design Using Linear Parameter-Varying Gain-Scheduling, *IEEE Transactions on Control Systems Technology*, Vol. 10 No 1, 43-54.
3. **Gerc E. W.** (1973), *Pneumatic drives. Theory and calculation*, (in Polish), WNT, Warsaw.
4. **Kiczowski T.** (2005), *Algorithms and models applied in the design of pneumatic driving systems* (in Polish), Publishing House of Koszalin University of Technology, Koszalin.
5. **Maciejewski I.** (2012), Control system design of active seat suspensions, *Journal of Sound and Vibration*, Vol. 331, 1291-1309.
6. **Maciejewski I., Meyer L., Krzyzynski T.** (2009), Modelling and multi-criteria optimisation of passive seat suspension vibro-isolating properties, *Journal of Sound and Vibration*, Vol. 324, 520-538.
7. **Maciejewski I., Meyer L., Krzyzynski T.** (2010), The vibration damping effectiveness of an active seat suspension system and its robustness to varying mass loading, *Journal of Sound and Vibration*, Vol. 329, 3898-3914.

MEAN STRESS VALUE IN SPECTRAL METHOD FOR THE DETERMINATION OF FATIGUE LIFE

Adam NIEŚLONY*, Michał BÖHM*

*Faculty of Mechanical Engineering, Department of Mechanics and Machine Design, Opole University of Technology,
ul. Mikołajczyka 5, 45-271 Opole, Poland

a.nieslony@po.opole.pl, m.bohm@doktorant.po.opole.pl

Abstract: The paper presents a proposal of account of mean stress value in the process of the determination of the fatigue life, using the spectral method. The existing approaches have been described and some chosen stress models used to take into account the influence of the mean value in the process of the determination of fatigue life have been introduced. Those models, referring to their linear character, have been used to determine the power spectral density function (PSD) of the transformed stress taking into account the mean value. The method introduced by the authors allows a wide usage of many formulas used to predict the fatigue life by means of the spectral method.

Key words: Mean Stress, Fatigue Life, Spectral Method

1. INTRODUCTION

Structures and machine components being subjected to variable loads require constant monitoring during operation due to the emerging phenomenon of material fatigue. Also, when designing new constructions or modification of nodes of machine elements, it is required to check their load capacity and fatigue life before finally being put into operation. The verifications of this type are performed in laboratories carrying out the strength of materials fatigue tests, or if it is not possible because of e.g. the size and cost, then calculations are made only with a view to the best possible estimate of fatigue life. The way of calculations depends of the character of the load. In the case of load-amplitude with no mean value, the expected number of cycles to fatigue crack initiation can be read directly from graphs of fatigue, for example, Wöhler curve. If there are evident mean values in the course, then their effect must be taken into account on fatigue. For this purpose you can use the charts to take account of the influence of the mean load, for example, Smith chart or Wöhler graphs drawn up for various cycle asymmetry coefficients $R = \sigma_{min}/\sigma_{max}$.

2. MEAN VALUE OF RANDOM LOADING

The assignation of fatigue under variable amplitude or random load is generally done in the time domain using an algorithm determining the course of the cycles of variable amplitude, using a chosen model to circumscribe the impact of the mean load and the hypothesis of summation of fatigue damage. The papers by Łagoda et al., (1998, 2001) present the results of fatigue tests under uniaxial random tension-compression with the mean value of samples made of steel 10HNAP. They proposed an algorithm for calculating the fatigue life using the rain flow cycle counting method and the hypothesis of summation of fatigue damage by Palmgren-Miner. The authors of this work have analyzed three paths to take into account the influence of the mean value, that are:

- I – not taking into calculations the mean value,
- II – taking into calculations the influence of the mean value by transforming each of the cycle amplitude on the basis of their local mean value determined while cycle counting,
- III – taking into calculations the influence of the mean value by transforming the whole load course on the basis of its global mean value.

Fig. 1 shows an diagram of the algorithm of the calculation of fatigue life taking into calculations the mean stress value. In this work the K coefficient has been introduced, which allows you to calculate the transformed amplitude according to the method II:

$$\sigma_{aTi} = \sigma_{ai} \cdot K_i(\sigma_{mi}), \quad (1)$$

for the i -th cycle emphasised by the rain flow algorithm from a random course with amplitude σ_{ai} and the mean value σ_{mi} . Method III is based on the principle of the transformation of the entire random stress course using the global mean value:

$$\sigma_T(t) = [\sigma(t) - \sigma_m] \cdot K(\sigma_m). \quad (2)$$

Amplitude of the transformed cycle σ_{aTi} for this case is obtained directly by counting cycles of the course $\sigma_T(t)$ using the cycle counting algorithm. Summation of fatigue damage is done according to the formula:

$$D = \sum_{i=1}^n \frac{n_i}{N(\sigma_{aTi})} \quad (3)$$

where: D – fatigue damage parameter, n_i – the number of cycles of amplitude σ_{aTi} , $N(\sigma_{aTi})$ – the number of cycles determined from the Wöhler diagram for the transformed amplitude σ_{aTi} . Fatigue life N_{cal} expressed in cycles is determined from the formula:

$$N_{cal} = \frac{N_{blok}}{D} \quad (4)$$

where N_{blok} is the number of distinguished cycles of the analyzed section of the stress course.

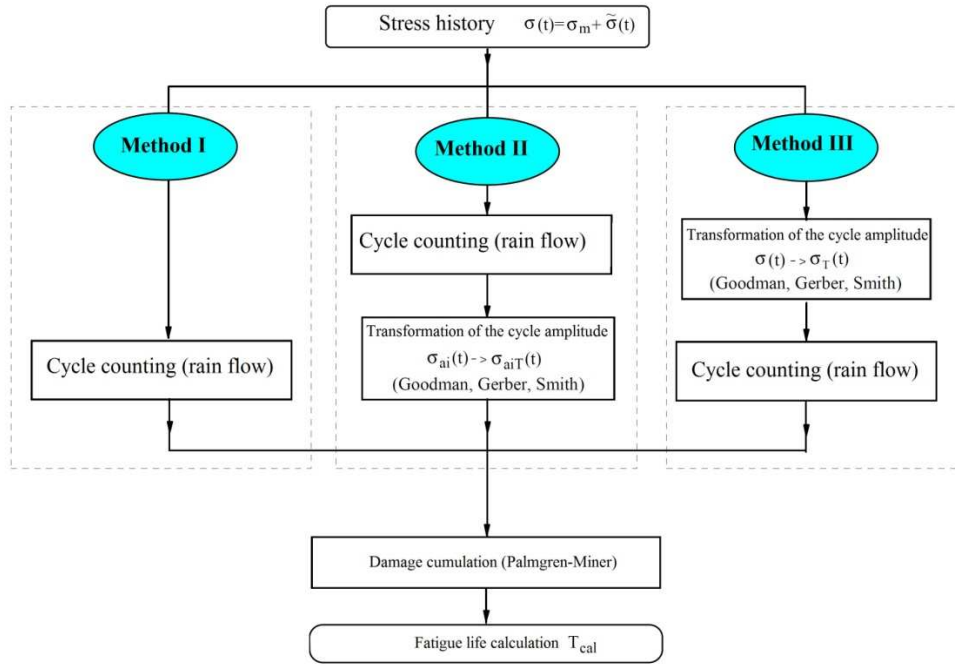


Fig. 1. Three paths to calculate the fatigue life T_{cal} (Łagoda et al., 2001)

The study showed that the course of a stationary random and symmetrical distribution of values of the instantaneous probability methods II and III are equivalent and can be used interchangeably in the calculations. In special cases, the K coefficient is determined from the formulas derived on the basis of the adopted model to take account of the mean stress. In literature you will find a significant number of models of this type (Łagoda et al., 2001; Pawliczek, 2000; Böhm, 2010) for which the K coefficient takes the form:

$$K_S = \frac{1}{1 - \frac{\sigma_m}{R_e}} \quad (5)$$

$$K_{Go} = \frac{1}{1 - \frac{\sigma_m}{R_m}} \quad (6)$$

$$K_M = \frac{1}{1 - \frac{\sigma_m}{\sigma'_f}} \quad (7)$$

$$K_{Ge} = \frac{1}{1 - \left(\frac{\sigma_m}{R_m}\right)^2} \quad (8)$$

$$K_K = \frac{1}{\exp\left(-\alpha \cdot \frac{\sigma_m}{R_m}\right)} \quad (9)$$

where: K_S , K_{Go} , K_M , K_{Ge} , K_K – coefficients determined on the basis of appropriate models of Soderberg, Goodman, Morrow, Gerber and Kwofie, σ_m – mean cycle value of the stress course, R_e – plasticity limit, R_m – tensile strength, σ'_f – fatigue strength coefficient, α – mean stress sensitivity of the material.

Fatigue life can be assigned also in the frequency domain using a stochastic analysis of random processes, the so-called

spectral method. Taking into account the mean stress in this case is hard because the stress in the course of this method is represented by a power spectral density function, which contains information about the occurring locally and globally mean value in a way that is difficult to use in practice. In literature, however, we can find only a few suggestions on this issue. Kihl and Sarkani (1999) show the effect of the mean value on fatigue life of welded steel joints. The tests were set to be run under both cyclic and random loadings with non-zero and zero mean stress value. The authors derived a formula to find the expected number of cycles to initiation of fatigue cracks in the case of random loads with extremes of Rayleigh distribution with a nonzero mean value of stress:

$$N_{cal} = \left(1 - \frac{\sigma_m}{R_m}\right)^{-B} \frac{2^{\frac{B}{A}} \sigma_x^B A}{\Gamma\left(1 - \frac{B}{2}\right)} \quad (10)$$

where: N_{cal} – number of cycles to fatigue crack initiation, A and B – life axis and slope of the constant amplitude Wöhler curve, σ_x – is the RMS stress of the narrowband random loading, $\Gamma(\cdot)$ – is the gamma function, σ_m – global mean stress value of the random stress history, R_m – tensile strength. It is easy to notice that in the formula (10), the part being responsible for taking into account the mean value is $(1 - \sigma_m/R_m)^{-B}$, which modifies the cycle number till the initiation of the fatigue crack determined by the Miles formula (Nieslony and Macha, 2007).

3. PSD OF A RANDOM FUNCTION WITH THE MEAN VALUE

Let us analyse an example of one-dimensional stationary random process $x(t)$ showing the characteristics of ergodicity. The assumption that $x(t)$ represents the physical signal is often convenient to present as the sum of the static x_m and dynamic $x_d(t)$ or fluctuant component:

$$x(t) = x_m + x_d(t). \quad (11)$$

Static component can be described by the mean value given by the formula:

$$x_m = \lim_{T \rightarrow \infty} \frac{1}{T} \int_0^T x(t) dt, \quad (12)$$

and the dynamic component by the signals variance:

$$\mu_x = \lim_{T \rightarrow \infty} \frac{1}{T} \int_0^T [x(t) - x_m]^2 dt. \quad (13)$$

The variance, however, does not describe the spectral structure of a random process, and this information is essential for the proper estimation of the number of cycles and the amplitude distribution of the load during the fatigue calculations. Therefore for this purpose the power spectral density (PSD) function is being used. Power spectral density of the signal describes the overall structure of a random process using the frequency spectral density of mean values of the physical signal in question. This value can be determined for the interval from f to $f + \Delta f$ using a central-pass filter with a narrow band and averaging the square on the output of the filter (Bendat and Piersol, 1976):

$$\Psi_x(f, \Delta f) = \lim_{T \rightarrow \infty} \frac{1}{T} \int_0^T x^2(t, f, \Delta f) dt, \quad (14)$$

where: Ψ_x – the mean square value of the process $x(t)$, T – time of observation, $x(t, f, \Delta f)$ – component of $x(t)$ in the frequency range from f to $f + \Delta f$. For small values of Δf the formula (14) shows the one-sided PSD function.

$$G_x(f) = \lim_{\Delta f \rightarrow 0} \frac{\Psi_x(f, \Delta f)}{\Delta f} = \lim_{\Delta f \rightarrow 0} \frac{1}{\Delta f} \left[\lim_{T \rightarrow \infty} \frac{1}{T} \int_0^T x^2(t, f, \Delta f) dt \right]. \quad (15)$$

A characteristic property of the $G_x(f)$ function is the relation to the autocorrelation function. In particular, for stationary signals, these functions are closely related by the Fourier transformation:

$$G_x(f) = 2 \int_{-\infty}^{\infty} R_x(\tau) e^{-j2\pi f\tau} d\tau, \quad (16)$$

where:

$$R_x(\tau) = \lim_{T \rightarrow \infty} \frac{1}{T} \int_0^T x(t)x(t+\tau)dt, \quad (17)$$

is the autocorrelation function of the signal $x(t)$. Mean value x_m of the random process can be determined from the autocorrelation function:

$$x_m = \sqrt{R_x(\infty)}, \quad (18)$$

and the mean value of $x(t)$ is a function of the PSD presented as a Dirac function at zero frequency

$$x_m = \sqrt{\int_{0^-}^{0^+} \delta(0) G_x(f) df}. \quad (19)$$

The formula (19) shows that the mean value is equal to the positive square root of the "surface" underlying the Dirac function.

This is an abstract space, as Dirac function takes the value $+\infty$ for an infinite small interval. For this reason, the direct use of formula (19) to determine the mean value on the basis of a PSD function of a random function is virtually impossible. Numerical algorithms to estimate the PSD functions are limited to the basic frequency resolution and the value of the function $R_x(0)$ results from the mean value $x(t)$ and from the mean square value of a random process from the interval $(0, \Delta f)$. Proper separation of these two values is impossible without additional information such as of the static value. Therefore, in practice, we analyze those two values separately, the dynamic and static component of the random process according to equation (11).

4. PSD FUNCTION OF A TRANSFORMED STRESS COURSE

The crossing of the signal $x(t)$ by a linear system with constant parameters determined by the impulse response $h(\tau)$ and the transfer function $H(f)$ describes the following relationships (Bendat and Piersol, 1976, 1980; Kirsten, 2002):

$$y(t) = \int_0^{\infty} h(\tau) x(t - \tau) d\tau, \quad (20)$$

$$G_y(f) = |H(f)|^2 G_x(f), \quad (21)$$

where: $y(t)$ – output signal of the system, $G_x(f)$ and $G_y(f)$ – respectively PSD input and output. From the equation (21) we can notice that the power spectral density of the output signal can be calculated knowing the gain factor $|H(f)|$ of the system. Fig. 2(a) shows schematically the signal pass through a linear system. The spectral method of determining the fatigue life using the PSD function is used to describe the course of stress directly in the frequency domain. If the stress course includes a static and a fluctuant component then the transformed course should be designated according to equation (2). Treating the fluctuant component of the course $[\sigma(t) - \sigma_m]$ as an input signal of a linear system with constant coefficient of strengthening $|H(f)| = K(\sigma_m)$ we can determine the PSD of a transformed strain course:

$$G_{\sigma T}(f) = K(\sigma_m)^2 G_{\sigma}(f), \quad (22)$$

where $G_{\sigma}(f)$ are the power spectral density of a centered stress course. Fig. 2(b) presents the interpretation of the linear process of strain transformation due to the mean value, which can be compared to the transition signal by a linear system, Fig. 2(a). Formula (22) allows the use of different forms of $K(\sigma_m)$ -factor, for example, described by equations (5)-(9), in the process of determining the fatigue life by means of spectral method taking into account the static stress component. The main advantage of the proposed solution is that the transformation is subjected to power spectral density function before using the models to determine the fatigue life. This gives the possibility of applying fatigue formulas in the spectral method for the waveforms developed for narrow-band frequency and the more universal solutions correctly describing most of the random waveforms used in the calculation of fatigue (Nieslony and Macha, 2007; Nieslony, 2003, 2008).

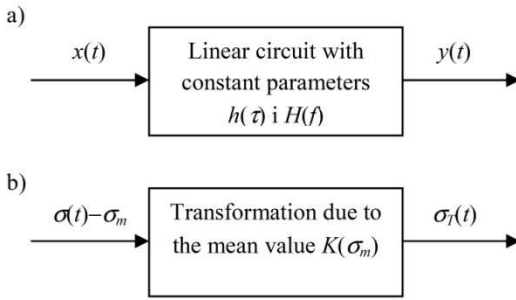


Fig. 2. Single entry linear system (a) and interpretation of the linear process of transformation strain due to the average value (b)

Such a method is proposed by Dirlik (1985) which is developed by using the empirical formula describing the probability distribution of amplitudes ranges.

$$p(\Delta\sigma) = \frac{1}{2\sqrt{m_0}} \left[\frac{K_1}{K_4} e^{\frac{-Z}{K_4}} + \frac{K_2 Z}{R^2} e^{\frac{-Z^2}{2R^2}} + K_3 Z e^{\frac{-Z^2}{2}} \right], \quad (23)$$

where: Z , K_1 , K_2 , K_3 , K_4 , R – factors which are functions of the first five moments m_k ($k = 0, \dots, 4$) of the transformed PSD stress function:

$$m_k = \int_0^\infty G_{\sigma T}(f) f^k df. \quad (24)$$

Fatigue life is calculated using the selected hypotheses of fatigue damage accumulation, e.g. for a linear Palmgren-Miner hypothesis with the amplitude below the fatigue limit we obtain:

$$N_{cal} = \frac{1}{\int_0^\infty \frac{p(\Delta\sigma)}{N(\Delta\sigma)} d\Delta\sigma}, \quad (25)$$

where the number of cycles for a range of amplitudes is calculated on the basis of the characteristics of the material fatigue:

$$N(\Delta\sigma) = \sigma_{af}^m N_0 \left(\frac{\Delta\sigma}{2} \right)^{-m}. \quad (26)$$

5. CALCULATION ALGORITHM

In order to calculate the fatigue life using the spectral method and taking into account the impact of the mean stress on fatigue life you should follow these steps:

- Assign or define the PSD of the fluctuant component of the stress course $G_\sigma(f)$ and its static part σ_m ,
- Calculate the coefficient $K(\sigma_m)$ according to the right model, formulas (5)-(9), and the choice of model depends of the mean stress value sensitivity of material,
- Calculate PSD of then transformed stress $G_{\sigma T}(f)$ according to the equation (22),
- Calculate the fatigue life using spectral method formulas i.e. (23) and (25) (Nieslony A. and Macha E., 2007).

6. CONCLUSIONS AND OBSERVATIONS

Based on the literature research it can be noticed, that there are no papers that would propose the transformation of the power spectral density function of the stress, to take into account the influence of the mean value on the fatigue life. The proposed formula (21) allows the calculation of the PSD of the transformed stress, using models that are well known and widely verified in experimental researches. The proposal of Kihl and Sarkani (1999) uses a Rayleigh amplitude distribution approximation, which reduces the area of application of the formula (9) only to narrowband processes. The method introduced by the authors doesn't have this limitation and therefore allows a wide usage of many formulas used to predict the fatigue life by means of the spectral method. Compared with the time domain fatigue life prediction methods, the spectral method shows greater efficiency and it can be used there, where a multiplicand fatigue calculation is required (constructions optimization, fatigue damage maps etc.). The experimental verification should be performed to verify the correctness of the fatigue calculations evaluated according to the proposed method, nevertheless the transformation of the PSD function in the spectral method is equivalent to the formula (2) in the time domain.

REFERENCES

- Bendat J.S., Piersol A.G. (1976), *Methods of analysis and measurement of random signals* (in Polish), PWN, Warszawa.
- Bendat J.S., Piersol A.G. (1980), *Engineering Applications of Correlation and Spectral Analysis*, John Wiley & Sons, New York.
- Böhm M. (2010), *Influence of static stresses on fatigue life of cast iron under variable-amplitude loading* (in Polish), MSc Thesis, Opole, 65.
- Dirlik T. (1985), *Application of Computers in Fatigue Analysis*, PhD Thesis, UK: University of Warwick.
- Kihl D., Sarkani S. (1999), Mean stress effects in fatigue of welded joint, *Probabilistic Engineering Mechanics*, 97-104.
- Kirsten K. (2002), *Spectral methods in mathematics and physics*, Chapman & Hall/CRC, London New York.
- Łagoda T., Macha E., Pawliczek R. (1998), *Influence of the expected random stress history on fatigue life of 10HNAP steel under uniaxial tension* (in Polish), *PMR*, Warszawa, Z. 11/1998, 121-138.
- Łagoda T., Macha E., Pawliczek R. (2001), The influence of the mean stress on fatigue life of 10HNAP steel under random loading, *International Journal of Fatigue*, 23, 283-291.
- Nieslony A. (2003), *Generalization of the spectral method of fatigue life determination to the extend of multiaxial loads* (in Polish), PhD Thesis, Opole, 109.
- Nieslony A. (2008), *Determination of fatigue damage layers by means of the spectral method* (in Polish), Publishing house of Opole University of Technology, Opole.
- Nieslony A. (2010), Comparison of some selected multiaxial fatigue failure criteria dedicated for spectral method, *Journal of Theoretical and Applied Mechanics*, Warsaw, Nr 48, 233-254.
- Nieslony A., Macha E. (2007), *Spectral method in multiaxial random fatigue*, Springer-Verlag, Berlin Heidelberg.
- Pawliczek R. (2000), Predictment of the fatigue life under cyclic bending and torsion with the mean stress value (in Polish), *Scientific Issue of the Opole University of Technology*, Opole, Issue 62, 83-104.

INTEGRATION OF THE EQUATIONS OF MOTION OF MULTIBODY SYSTEMS USING ABSOLUTE NODAL COORDINATE FORMULATION

Grzegorz ORZECZOWSKI*, Janusz FRĄCZEK*

*The Institute of Aeronautics and Applied Mechanics, The Faculty of Power and Aeronautical Engineering,
Warsaw University of Technology, ul. Nowowiejska 24, 00-665 Warsaw, Poland

gorzech@meil.pw.edu.pl, jfraczek@meil.pw.edu.pl

Abstract: Recently, a finite element formulation, called the absolute nodal coordinate formulation (ANCF), was proposed for the large rotation and deformation analysis of flexible bodies. In this formulation, absolute position and slope coordinates are used to define the finite element configuration. Infinitesimal or finite rotations are not used as nodal coordinates. The ANCF finite elements have many unique features that distinguish them from other existing finite element methods used in the dynamic analysis of the flexible multibody systems. In such systems, there appears the necessity of solving systems of differential-algebraic equations (DAEs) of index 3. Accurate solving of the DAEs is a non-trivial problem. However, in the literature about the ANCF one can hardly find any detailed information about the procedures that are used to solve the DAEs. Therefore, the current paper is devoted to the analysis of selected DAE solvers, which are applied to simulations of simple mechanisms.

Key words: Flexible Bodies, Multibody Systems, Absolute Nodal Coordinate Formulation, ANCF, Differential-Algebraic Equations, DAE Solvers

1. INTRODUCTION

In flexible multibody systems (FMS), rigid, flexible and very flexible bodies are interconnected by mechanical joints that allow for large relative reference translations and rotations between bodies (Frączek, 2002). In recent years, a particular interest of many research centres concentrated on the problems of effective analysis of multibody systems, whose bodies undergo large deformations and displacements. One of such methods is the Absolute Nodal Coordinate Formulation (ANCF) (Shabana, 1997). The characteristic feature of this formulation is lack of rotational degrees of freedom. Instead, to define rotation, one uses three independent slope coordinate vectors. The result is that ANCF elements usually have more nodal coordinates than the standard elements used in the FEM analysis. However, a single ANCF element is capable to obtain some complex deformed shapes (Shabana and Yakoub, 2001). Moreover, beam and shell ANCF elements may be treated as isoparametric elements, so that an arbitrary rigid body displacements, including rigid body rotations, produces zero strains (Shabana, 2003). On top of that, in the case of fully parameterised elements (i.e. those, which have all first-order slope vectors in each node), elastic forces may be calculated not only from classical beam, plate or shell theories, but also by using general continuum mechanics approach based on linear or nonlinear strain-displacement relationships.

Additionally, in the ANCF method, mass matrix of system is a constant one, even in the case of three-dimensional analysis. This fact has an essential influence on effectiveness of methods used for solving equations of motion. Moreover, the formulae expressing external forces assume concise and simple forms. Because the mass matrix of the finite element is a constant matrix, centrifugal and Coriolis forces do not appear in the equations of motion. Instead, elastic forces and their Jacobian matrix de-

pend strongly nonlinearly on nodal coordinates, even in the cases of simple systems consisting of two-dimensional elements.

From the point of view of numerical analysis, the equations of motion used to describe a flexible multibody system constitute a system of differential-algebraic equations (DAE), whose structure is similar to that of equations describing rigid multibody systems (Frączek, 2002). Such a system has a differentiation index equal to 3, and consists of differential equations and algebraic constraints equations (usually nonlinear) (Haug, 1989). Solving differential-algebraic equations is a much more complicated and less recognized task than solving ordinary differential equations (ODE) (Brenan et al., 1996). This is because the DAEs have some features of weakly conditioned ordinary differential equations. Furthermore, in the case of thin or stiff structures, the ANCF coupled deformation modes can be associated with very high frequencies that can be source of numerical problems. Because of that, effectiveness of some integration algorithms is low (Hussein et al., 2008). The mentioned characteristics of DAEs and ANCF cause that the choice of an adequate algorithm for integrating equations of motion is not a trivial task, and needs a thorough analysis (Frączek and Malczyk (in print)). In this work, we present an approach to the analysis of selection of DAE solvers in application to simple analyses of dynamics of flexible mechanisms.

Special, dedicated methods have been used for solving the differential-algebraic equations. In total, five different algorithms were tested. The algorithms *DASSL* (Brenan et al., 1996), *GAMD* (Iavernaro and Mazzia, 1998), as well as *Radau* and *Radau5* (Haier and Wanner, 1996) were provided for free by their authors. However, the algorithm *HHT-13* (Hussein et al., 2008) is an original method, specially implemented for the needs of the ANCF. It is a generalization of the Hilbert-Hughes-Taylor (HHT) method (Bathe, 1996) applied to DAEs. All the algorithms, besides of the *DASSL*, are capable of directly solving DAEs

of index 3. In the case of the *DASSL*, it is necessary to convert the DAE system to the form of equations of index reduced to 1.

The presented algorithms, applied for solving the DAEs, have been tested with the use of three long-term analyses of multibody systems. The analysed model was a simple mechanism of a single physical pendulum moving in a gravitational field. In the first case, the pendulum was modelled as a rigid body, in the second case – as a flexible body of high stiffness (high value of Young's modulus), and the third model was a flexible pendulum of high flexibility. In each model, one analysed selected parameters, such as changes of period and amplitude of oscillations, as well as changes in total energy of the system. Because dissipation forces did not appear in the models, the total energy of the system should be preserved, so its value should not change in time. Moreover, for rigid pendulum, and for flexible pendulum of high stiffness, also period and amplitude of oscillations should keep their values unchanged. Then, the change in these values observed in a numerical solution may signify lack of accuracy of the applied method.

The presented work is organised in the following way. In section 2, we present the essentials of the absolute nodal coordinate formulation. Expressions defining basic quantities that appear in equations of motion are given there, as well as notation of differential-algebraic equations of the analysed motion. In section 3, the analysed methods of solving of differential-algebraic equations of motion are briefly characterised. The results of performed simulation of example tests are enclosed in section 4. The last section presents summary of results of the carried-out tests, and final conclusions.

2. BACKGROUND

A single node of fully-parameterised, three-dimensional ANCF element may be characterised by at least twelve parameters [13]:

$$\mathbf{e}^i = \begin{bmatrix} \mathbf{r}^i & \frac{\partial \mathbf{r}^i}{\partial x} & \frac{\partial \mathbf{r}^i}{\partial y} & \frac{\partial \mathbf{r}^i}{\partial z} \end{bmatrix} \quad (1)$$

where i is node number, \mathbf{r}^i is the vector defining global position of the node, and vectors $\partial \mathbf{r}^i / \partial \alpha$ are, for $\alpha = x, y, z$, the global slope vectors of the element nodes. Here x, y, z are the coordinates of an arbitrary point on the element in the undeformed configuration.

A standard ANCF beam element contains two fully-parameterised nodes [16]:

$$\mathbf{e}^T = [\mathbf{e}^1 \quad \mathbf{e}^2] \quad (2)$$

Using the definition of element nodal coordinates, given by equation (2), we can write position vector of an arbitrary point P in the form:

$$\mathbf{r}^P = \mathbf{S}(x, y, z) \mathbf{e} \quad (3)$$

where \mathbf{S} is the matrix containing the element's shape functions, which is independent of nodal coordinates. For the beam element, this matrix takes the form:

$$\mathbf{S} = [s_1 \mathbf{I} \quad s_2 \mathbf{I} \quad \cdots \quad s_8 \mathbf{I}] \quad (4)$$

where s_1, s_2, \dots, s_8 are the element's shape functions, and \mathbf{I} is a 3×3 identity matrix. For the two-node ANCF beam element of twenty-four parameters, these functions can be represented

as follows [16]:

$$\begin{cases} s_1 = 1 - 3\xi^2 + 2\xi^3, & s_2 = l(\xi - 2\xi^2 + \xi^3), \\ s_3 = l(\eta - \xi\eta), & s_4 = l(\zeta - \xi\zeta), \\ s_5 = 3\xi^2 - 2\xi^3, & s_6 = l(-\xi^2 + \xi^3), \\ s_7 = l\xi\eta, & s_8 = l\xi\zeta. \end{cases} \quad (5)$$

where l is length of the element, while $\xi = x/l$, $\eta = y/l$ and $\zeta = z/l$ are the element natural coordinates.

The mass matrix of ANCF element can be calculated based on kinetic energy relationships. The global velocity vector may be found by differentiating the position vector (3) with respect to time:

$$\mathbf{v}^P = \dot{\mathbf{r}}^P = \mathbf{S} \dot{\mathbf{e}} \quad (6)$$

Kinetic energy of the element can be defined as:

$$E_k = \frac{1}{2} \int_V \rho \mathbf{v}^T \mathbf{v} dV \quad (7)$$

where ρ and V are, respectively, mass density and volume of a finite element. It is worth noting that the density and the volume pertain to the initial configuration of an undeformed element.

Substituting velocity equation (6) into equation (7) we obtain:

$$E_k = \frac{1}{2} \dot{\mathbf{e}}^T \int_V \rho \mathbf{S}^T \mathbf{S} dV \dot{\mathbf{e}} = \frac{1}{2} \dot{\mathbf{e}}^T \mathbf{M} \dot{\mathbf{e}} \quad (8)$$

where \mathbf{M} is the symmetric mass matrix of the finite element:

$$\mathbf{M} = \int_V \rho \mathbf{S}^T \mathbf{S} dV \quad (9)$$

It is worthy to note that the above matrix is a constant one.

In the ANCF the Coriolis forces, tangent and centrifugal forces, and other forces resulting from differentiation of kinetic energy are equal to zero. Therefore, non-zero force values in equations of motion can only originate from external forces, from reactions in nodes, and from elastic forces. The vector of elastic forces can be written as:

$$\mathbf{Q}_s^T = \frac{\partial E_s}{\partial \mathbf{e}} \quad (10)$$

where E_s is the elastic energy. This energy can be expressed as a function of the Green-Lagrange strain vector $\boldsymbol{\varepsilon}$, and the second Piola-Kirchhoff stress vector $\boldsymbol{\sigma}$ in the following form:

$$E_s = \frac{1}{2} \int_V \boldsymbol{\varepsilon}^T \boldsymbol{\sigma} dV \quad (11)$$

For the linear elastic model of material, which is actually taken into consideration, we may formulate the following relationship between vectors of stress and strain:

$$\boldsymbol{\sigma} = \mathbf{D} \boldsymbol{\varepsilon} \quad (12)$$

where \mathbf{D} is the matrix of elastic coefficients. Substituting equation (12) into (11) we obtain:

$$E_s = \frac{1}{2} \int_V \boldsymbol{\varepsilon}^T \mathbf{D} \boldsymbol{\varepsilon} dV \quad (13)$$

Then, for calculating the value of elastic energy, it is enough to determine the strain vector. The latter is associated with the Green-Lagrange strain tensor, which can be found using the following relationship:

$$\boldsymbol{\varepsilon}_m = \frac{1}{2}(\mathbf{J}^T \mathbf{J} - \mathbf{I}) \quad (14)$$

where \mathbf{J} is the deformation gradient matrix:

$$\mathbf{J} = \frac{\partial \mathbf{r}}{\partial \mathbf{x}} \quad (15)$$

Differentiating the function given by equation (13) with respect to the element nodal coordinates we obtain:

$$\mathbf{Q}_s^T = \int_V \left(\frac{\partial \boldsymbol{\varepsilon}}{\partial \mathbf{e}} \right)^T \mathbf{D} \boldsymbol{\varepsilon} dV \quad (16)$$

Making use of equation (16), one can directly determine elastic force values for a given element. It is known, however, that when this relationship is used in the case of a classic ANCF beam element, there may appear volume locking [7]. To avoid this effect, one can apply selective reduced integration [6]. In order to do so, the matrix of elastic coefficients \mathbf{D} should be divided into two parts:

$$\mathbf{D} = \mathbf{D}^0 + \mathbf{D}^\nu \quad (17)$$

where Poisson effect is taken into account only in the matrix \mathbf{D}^ν . Then, \mathbf{D}^0 is a diagonal matrix having the following form:

$$\mathbf{D}^0 = \begin{bmatrix} E & 0 & 0 & 0 & 0 & 0 \\ 0 & E & 0 & 0 & 0 & 0 \\ 0 & 0 & E & 0 & 0 & 0 \\ 0 & 0 & 0 & G & 0 & 0 \\ 0 & 0 & 0 & 0 & Gk_2 & 0 \\ 0 & 0 & 0 & 0 & 0 & Gk_3 \end{bmatrix} \quad (18)$$

where E is the Young's modulus, G is the Kirchhoff's modulus, while k_2 and k_3 are shear correction factors that are used for correction of transverse shear stiffness. As one can see, the values in matrix \mathbf{D}^0 do not depend on the value of Poisson's ratio ν .

The following equation shows how Poisson effect is taken into account in matrix \mathbf{D}^ν :

$$\mathbf{D}^\nu = \frac{E\nu}{(1+\nu)(1-2\nu)} \begin{bmatrix} 2\nu & 1 & 1 & 0 & 0 & 0 \\ 1 & 2\nu & 1 & 0 & 0 & 0 \\ 1 & 1 & 2\nu & 0 & 0 & 0 \\ 0 & 0 & 0 & 0 & 0 & 0 \\ 0 & 0 & 0 & 0 & 0 & 0 \\ 0 & 0 & 0 & 0 & 0 & 0 \end{bmatrix} \quad (19)$$

We substitute the formula of elastic coefficients (17) into elastic energy equation (13) and obtain:

$$E_s = \frac{1}{2} \int_V \boldsymbol{\varepsilon}^T \mathbf{D}^0 \boldsymbol{\varepsilon} dV + \frac{1}{2} \int_V^{\text{RED}} \boldsymbol{\varepsilon}^T \mathbf{D}^\nu \boldsymbol{\varepsilon} dV \quad (20)$$

where the component containing matrix \mathbf{D}^0 is computed using full integration, while the component with matrix \mathbf{D}^ν is integrated in a reduced way. In the case of the considered beam element, the reduced integration means that the function is integrated only along the beam's axis.

The only relationship to be determined is that of the generalised external force \mathbf{Q}_e associated with the gravity forces whose acceleration equals \mathbf{g} :

$$\mathbf{Q}_e = \int_V \mathbf{S}^T \rho \mathbf{g} dV \quad (21)$$

Using the following expressions the dynamic equations of the

flexible multibody system can be obtained in a matrix form as (Haug, 1989):

$$\begin{cases} \mathbf{M} \ddot{\mathbf{e}} + \mathbf{Q}_s + \boldsymbol{\Phi}_e^T \boldsymbol{\lambda} = \mathbf{Q}_e \\ \boldsymbol{\Phi} = \mathbf{0} \end{cases} \quad (22)$$

where $\boldsymbol{\lambda}$ is vector of the Lagrange multipliers, vector $\boldsymbol{\Phi}$ contains nonlinear constraints equations, while $\boldsymbol{\Phi}_e = \partial \boldsymbol{\Phi} / \partial \mathbf{e}$ is Jacobian matrix of the vector of constraints relative to system parameters.

Because constraints equations and their Jacobian matrix take a standard form, well known from rigid multibody systems Haug, 1989; Nikravesh, 1988), they will not be described here in detail.

Equations (22) can be solved by means of typical integration algorithms used for ordinary differential equations. It can be done after decreasing their differentiation index to one, i.e. by double differentiation of constraints equations. However, solving equations of such a type may lead to computational problems, so it is necessary to apply measures stabilizing equations of constraints (i.e. Baumgarte stabilization (Nikravesh, 1988)). For that reason, a more effective way might be the application of algorithms dedicated for solving differential-algebraic equations.

3. ALGORITHMS FOR SOLVING DIFFERENTIAL-ALGEBRAIC EQUATIONS

Four algorithms applicable for solving equation (22) will be analysed in this section: the algorithm *DASSL* based on the backward differentiation formulae, the algorithms *Radau* and *Radau5* based on implicit Runge-Kutta method, the algorithm *GAMD* based on generalised Adams method, and the algorithm *HHT-13* based on generalised HHT method. These algorithms represent different groups of numerical methods applicable for solving DAE systems. Therefore, the obtained results may contain valuable hints on applicability of various numerical schemes in solution of DAEs in the proposed initial formulation.

In most of these algorithms, it is necessary to modify the solved equations, so that they take the forms adequate for the applied algorithm. Appropriate transformations will be presented in further part of this section.

3.1. Method of backward differentiation – algorithm *DASSL*

The software of *DASSL* is an implementation of the method of backward differentiation (*Backward Differentiation Formulae*, BDF) [2], with variable order of the method changing from one to five. This was one of the first numerical methods developed for integrating DAE systems. It allows solving differential-algebraic equations of index not greater than one.

The differential scheme implemented in the *DASSL* procedure makes it possible to solve an equation system given in the following, implicit form:

$$\mathbf{G}(t, \mathbf{y}_d, \dot{\mathbf{y}}_d) = \mathbf{0} \quad (23)$$

where \mathbf{y}_d is the system state vector, and \mathbf{G} is a vector of state equations. The program *DASSL* requires differential-algebraic equations expressed as a first-order system of equations. In order to reduce the order of equation (22), one can use the new set of variables:

$$\mathbf{u} = \dot{\mathbf{e}} \quad (24)$$

However, to decrease the integration index, one can perform

one differentiation of the constrains vector with respect to time:

$$\dot{\Phi} = \Phi_e \dot{e} + \Phi_t = 0 \quad (25)$$

Substituting equations (24) and (25) into (22), we obtain:

$$\begin{cases} M\ddot{u} + Q_s + \Phi_e^T \lambda = Q_e \\ u - \dot{e} = 0 \\ \Phi_e u + \Phi_t = 0 \end{cases} \quad (26)$$

Exclusion of equations of constrains from the above system of equations causes that the constrains may be violated (Haug, 1989). In order to prevent it, a new set of variables should be introduced, which leads to a formulation with index stabilization (the Gear-Gupta-Leimkuhler method (Gear et al., 1985)):

$$\begin{cases} M\ddot{u} + Q_s + \Phi_e^T \lambda = Q_e \\ u - \dot{e} + \Phi_e^T \mu = 0 \\ \Phi_e u + \Phi_t = 0 \\ \Phi = 0 \end{cases} \quad (27)$$

where μ is the vector of the new variables, which have the character of Lagrange multipliers. One considers solution to the above equation system as a correct one if the vector μ is permanently equal to zero. Numerical solution to equation (27) guarantees that the equations of position and velocity constrains are fully satisfied. The index of the above equation is equal to two. It can be further decreased to the value of one by substituting the multipliers λ and μ with the new variables, $\eta = \lambda$ and $\zeta = \mu$. The obtained equation has a differentiation index equal to one. The method has many advantages, first of all one does not need to perform the double differentiation of constrains equations, thus avoiding high computational costs. After introducing the new variables, we obtain:

$$\begin{cases} M\ddot{u} + Q_s + \Phi_e^T \eta = Q_e \\ u - \dot{e} + \Phi_e^T \zeta = 0 \\ \Phi_e u + \Phi_t = 0 \\ \Phi = 0 \end{cases} \quad (28)$$

The state vector and the vector of state equations, used in the DASSL program, have the forms:

$$y_d = [u^T \quad e^T \quad \eta^T \quad \zeta^T]^T \quad (29)$$

$$G = \begin{bmatrix} M\ddot{u} + Q_s + \Phi_e^T \eta - Q_e \\ u - \dot{e} + \Phi_e^T \zeta \\ \Phi_e u + \Phi_t \\ \Phi \end{bmatrix} \quad (30)$$

It is noticeable that the vector G depends both on the state vector, and its derivative. In order to effectively carry out the simulation, one not only needs to calculate the value of vector G , but also calculate the Jacobian matrix for this vector with respect to the state vector, as well as its derivative.

Making use of the relationships presented above, we can prepare appropriate procedures needed by the DASSL program for the analysis of a multibody system. The advantage of the presented method, called the *Stabilized Index 1* (SI1) formulation, is that it takes into account the influence of constrains on positions and velocities in the system. Owing to that fact, the obtained results are often more accurate in comparison to those which don't take advantage of stabilization. A disadvantage of the SI1 formulation is high computational cost associated with calculation of the vector G and its Jacobian matrix.

3.2. Implicit Runge-Kutta methods – algorithms *Radau* and *Radau5*

The programs *Radau* and *Radau5* are based on implicit Runge-Kutta methods (*Radau IIA* method) [8] with an automatic control of integration step. In the *Radau* method, the order is variable, equal to 5, 9 or 13, while the *Radau5* method has a constant order, equal to 5.

Both algorithms are used for solving weekly-conditioned ordinary differential equations, as well as differential-algebraic equations of index not greater than 3. The algorithms are capable of solving first-order equations of the explicit form:

$$M_r \dot{y}_r = F_r(t, y_r) \quad (31)$$

where M_r is a constant matrix of masses, y_r is the state vector, and F_r is a vector function of the right sides. In the case of solving DAEs M_r is a singular matrix. This matrix must not be confused with the mass matrix M of a multibody system, i.e. that appearing in equation (22).

Similarly as in the case of DASSL program, it is necessary to lower the order of equation to one, which can be done by substitution defined by equation (24). One obtains the equation of motion in the form:

$$\begin{bmatrix} M & 0 & \Phi_e^T \\ 0 & I & 0 \\ 0 & 0 & 0 \end{bmatrix} \begin{bmatrix} \dot{u} \\ \dot{e} \\ \lambda \end{bmatrix} = \begin{bmatrix} Q_e - Q_s \\ u \\ \Phi \end{bmatrix} \quad (32)$$

The structure of the above equation reflects the structure of equation (31). However, it must be noted that the matrix corresponding to the matrix M_r is not a constant one. Due to this fact, the above equation should be re-written in a different form. In order to do so, one introduces new variables $w = \dot{u}$, which represent accelerations of the vector e . Then, the differential equations may be written as additional constrains equations:

$$\begin{bmatrix} 0 & 0 & 0 & 0 \\ 0 & I & 0 & 0 \\ 0 & 0 & I & 0 \\ 0 & 0 & 0 & 0 \end{bmatrix} \begin{bmatrix} \dot{w} \\ \dot{u} \\ \dot{e} \\ \dot{\lambda} \end{bmatrix} = \begin{bmatrix} Mw + \Phi_e^T \lambda + Q_s - Q_e \\ w \\ u \\ \Phi \end{bmatrix} \quad (33)$$

On the basis of the above equations, one can easily write, in an explicit form, the matrix of masses and the vector of right sides for the *Radau* programs. It is clear that now the mass matrix is a constant (and singular) one. The state vector can be written as:

$$y_r = [w^T \quad u^T \quad e^T \quad \lambda^T]^T \quad (34)$$

To use the programs *Radau* and *Radau5* effectively, one needs to calculate the Jacobian matrix for vector F_r with respect to the state vector y_r . This matrix takes a more simple form than the Jacobian matrix for the program DASSL (although computational cost is still high).

3.3. Generalized Adams method – algorithm *GAMD*

The *GAMD* software is an implementation of the generalized Adams method (GAM – acronym of *Generalized Adams Method*) (Iavernaro and Mazzia, 1998). This is a method of variable order (3, 5, 7 or 9), with automatic control of integration step. By using this algorithm, one can solve differential-algebraic equations of index not greater than 3. In this algorithm, the authors used

a part of the code from the procedure *Radau5*.

The *GAMD* algorithm can solve equations having identical form as those solved by *Radau5*, i.e. given by equation (31). The algorithm solves equations in an explicit form, such as equation (33), with the state vector from equation (34). In practice, both *Radau* programs and the *GAMD* program use the same procedures for calculating the mass matrix, the vector of right sides, and the Jacobian matrix of this vector.

3.4. Generalized HHT method – algorithm *HHT-I3*

The implicit algorithm *HHT-I3* serves for directly solving differential-algebraic equations of index equal to 3, having the form represented by equation (22) (Hussein et al., 2008). The algorithm is based on classic Hilbert-Hughes-Taylor method (Bathe, 1996) adapted for solving DAEs of index equal to 3. This algorithm has the possibility of selecting the magnitude of numerical damping, and was tested in application to flexible bodies modelled with the use of the ANCF method. The algorithm offers the possibility of automatic selection of integration step. In contrast to previously described methods used for solving DAEs, any widely available implementation of this algorithm has not been known to the authors. Because of that, the algorithm was originally implemented by the authors for the needs of this paper.

The HHT method is often used for solving second-order ordinary differential equations. It is based on the Newmark method (Bathe, 1996). Numerical damping, introduced into this method, facilitates eliminating undesirable, high-frequency oscillations. The Newmark method is unconditionally stable, but is characterised by first-order convergence. The HHT method also introduces numerical damping, is unconditionally stable, and guarantees second-order (quadratic) convergence.

When using the *HHT-I3* method, we write equation (22) in the form:

$$\begin{cases} \mathbf{M}\ddot{\mathbf{e}} = \mathbf{H} \\ \Phi = \mathbf{0} \end{cases} \quad (35)$$

where the vector $\mathbf{H}(t, \mathbf{e}, \dot{\mathbf{e}}) = \mathbf{Q}_e - \mathbf{Q}_s - \Phi_e^T \lambda$.

The algorithm *HHT-I3* solves equation (35) in a direct way, so that there is no simple division into the vector of right sides and the state vector, unlike to what was needed in the case of previously described general-purpose algorithms. It is necessary, however, to assume initial conditions for positions and velocities, and prepare appropriate procedures for computation of the Jacobian matrix. It is worth emphasizing that computational cost of determining Jacobian matrix in the procedure *HHT-I3* is comparable to that encountered in the programs *Radau* and *GAMD*. A detailed description of the *HHT-I3* algorithm can be found in literature (Hussein et al., 2008).

It should be emphasized that, in the program *HHT-I3*, there is no implemented procedure for assessing the necessity of recalculating the Jacobian matrix in a consecutive steps of integration. In consequence, this matrix is calculated in each integration step. This characteristic of the procedure causes that its effectiveness might be much lower than effectiveness of other algorithms, in which a method for assessing Jacobian matrix is implemented.

4. TEST EXAMPLE

Simple numerical tests are proposed for the programs presented in section 3. The tests are concerned with computations

of dynamics of three-dimensional mechanisms, both rigid and flexible ones. The purpose of the tests is an initial assessment of effectiveness of the integrating algorithms through evaluation of their computational accuracy, numerical stability and time of computations.

The computations were performed with the use of Fortran program on a computer equipped with a four-core, eight-thread processor with 3.4 GHz nominal frequency and 8 MB cache memory (Intel Core i7-2600K).

As a test example, we have chosen a problem of dynamic analysis of a single physical pendulum fixed at one of its ends to a base by the revolute joint. The pendulum moves under the influence of gravitation forces. The element has a cuboidal shape of 40cm length, 4cm height and 2cm depth. In all models, the element's material has a density of 7801kg/m³ and the Poisson ratio equal to 0.3. At the initial moment, the pendulum is in a horizontal position.

It is known that rigid physical pendulum should move with constant frequency of oscillations and constant amplitude, irrespective of duration of stimulation time. In such a system, there are no dissipation forces, so that total energy of the system must be preserved. Of course, because of errors arising in the process of integration (including the integration and numerical errors) the value of the mentioned quantities might change in time. One can assess the range of this variability for individual algorithms.

In the case of analysis of dynamics of a rigid physical pendulum it is possible to calculate the theoretical period of oscillations. For an infinitesimal angle of oscillation, the theoretical period of oscillation can be expressed by the formula:

$$T_0 = 2\pi \sqrt{\frac{I_0}{mgr}} \quad (36)$$

where I_0 is moment of inertia of the body with respect to the point of rotation, m is mass of the body, g is acceleration of gravity, and r is the distance between the centre of mass and the point of rotation. For the presented data, this period equals $T_0 = 1.04s$.

In order to calculate the period of oscillation of a rigid physical pendulum moving in a finite range of oscillation angles, one should determine the value of the following integral:

$$T_t = \frac{2T_0}{\pi} \int_0^{\pi/2} \frac{d\varphi}{\sqrt{1 - k^2 \sin^2 \varphi}} \quad (37)$$

where φ is the independent variable, and $k = \sin \frac{1}{2} \alpha_{\max}$, in which α_{\max} is the maximum angle of pendulum, measured with respect to the equilibrium position (in the considered case, this angle equals 90°). The integral was calculated numerically, and the period of oscillations was found equal to $T_t = 1.22s$.

In the simulations described in this section, one assumed the ending time equal to $t_k = 600s$. During the simulations, we calculated the parameters such as total energy value, amplitude decay, and elongation of oscillation period. The value of total energy was calculated directly. The percentage amplitude decay was calculated from the formula:

$$A_z = \frac{A_0 - A}{A_0} \times 100\% \quad (38)$$

where A_0 is the theoretical value of amplitude, and A is its current value. Positive values of this parameter mean that oscillations are damped (the maximal value of 100% indicates complete decay of oscillations), while negative values of A_z denote oscillations

of increasing amplitude.

The period elongation of oscillations can be calculated in a similar way:

$$T_w = \frac{T - T_t}{T_t} \times 100\% \quad (39)$$

where T is the current value of oscillation period, and T_t is its theoretical value calculated from equation (37). For a rigid pendulum, T_w should be always equal to zero. Its negative value means shortening of the period.

The results presented in Tab. 1, 2 and 3 are extreme values of the analysed quantities calculated for the whole duration of simulation. All the analyses were carried out for default values of majority of the parameters in solving procedures. The variable values were absolute errors (denoted as A_{tol}) and relative errors (R_{tol}). When analysing the procedure *HHT-I3*, it was only possible to determine the value of relative error – the A_{tol} value was ignored in this procedure.

4.1. Rigid physical pendulum

In this case, position of the body is described with a vector of seven independent coordinates (three of them describing position of the centre of mass, and four others are Euler parameters defining orientation of the body), and there are six equations of constraints (one equation for Euler parameters, and five equations for the revolute joint). Therefore, the analysed system has one degree of freedom.

For a rigid body, total energy is a sum of element's kinetic energy and its potential energy in gravitation field. In Tab. 1, there are presented results of performed simulations. In the cases of procedures *Radau* and *Radau5*, some of the simulations ended ahead of time, because the selected integration step was too small. In such a situation, there are no results in Table 1, and the value in the column of computational time means the time of simulation termination due to the procedure error.

Tab. 1 presents results for three selected tolerance values.

For the greatest tolerance value (test I), we managed to obtain acceptable results only in the case of the algorithm *HHT-I3*. For the remaining programs, simulation failed, or oscillations of pendulum were strongly damped. The results obtained in test II showed that the algorithms *DASSL*, *GAMD* and *HHT-I3* solved the problem without difficulties, and the simulation results could be considered as acceptable. In the cases of algorithms *GAMD* and *HHT-I3*, the oscillations were mildly damped; however, the algorithm *DASSL* produced oscillations of increasing amplitude. This was an undesirable effect which, for a longer duration of simulation, might indicate lack of convergence of the solution.

When the lowest values of tolerances (test III) were applied, all the algorithms gave satisfactory results. In this case, the algorithm *DASSL* proved the most effective, and gave very good overall results. It might result from the fact that the applied S11 formulation takes into account not only the equations of constraints (which are considered in all remaining algorithms), but also their velocities.

The algorithm *DASSL* proved the best one as far as time of computations was concerned. The calculation step, selected by the program, was relatively big, and computation of the Jacobian matrix was performed not very frequently. Slower than this one were the algorithms from the *Radau* group. At the same time it should be noted that the results obtained with different algorithms of this group, and the times of computations for the constant-order algorithm (*Radau5*) and the variable-order algorithm (*Radau*) were comparable.

The *GAMD* algorithm turned out to be twice slower than the *Radau* algorithms, however, it could solve the problem in which tolerance values were much higher. The *HHT-I3* algorithm turned out to be the slowest one. It was due to the fact that, in this algorithm, the Jacobian matrix was computed in each iteration step. Moreover, this method was designed especially for the needs of the ANCF method, therefore the algorithm might not optimally select integration step in the case of analysis of rigid bodies (where mass matrix is not a constant one). Nevertheless, by using this algorithm, we could obtain correct solution even for the greatest tolerance values.

Tab. 1. Results of simulation of rigid physical pendulum

Tolerance	Algorithm	Total energy [J]	Amplitude decay [%]	Period elongation [%]	Computation time [s]
Test I: A_{tol} 10^{-6} R_{tol} 10^{-3}	<i>DASSL</i>	-2.40	48.8	-8.99	0.82
	<i>Radau5</i>	-	-	-	sim. to 1.3
	<i>Radau</i>	-	-	-	sim. to 3.3
	<i>GAMD</i>	-1.73	35.4	-6.85	9.67
	<i>HHT-I3</i>	-0.11	0.99	-0.22	9.87
Test II: A_{tol} 10^{-7} R_{tol} 10^{-5}	<i>DASSL</i>	0.27	-5.50	1.29	1.5
	<i>Radau5</i>	-	-	-	sim. to 37.6
	<i>Radau</i>	-	-	-	sim. to 130
	<i>GAMD</i>	-0.59	12.0	-2.58	12.8
	<i>HHT-I3</i>	-0.39	7.9	-1.73	8.6
Test III: A_{tol} 10^{-9} R_{tol} 10^{-7}	<i>DASSL</i>	0.004	-0.08	0.02	2.9
	<i>Radau5</i>	0.05	0.32	-0.07	8.5
	<i>Radau</i>	0.05	0.28	-0.06	8.6
	<i>GAMD</i>	0.05	-0.07	0.01	20.3
	<i>HHT-I3</i>	-0.03	0.6	-0.13	35.3

4.2. Flexible physical pendulum

The pendulum was constructed with the use of standard, fully parameterised, ANCF beam elements. Elastic forces were computed by applying selective, reduced integration, in order to avoid the influence of volume locking on the results. The pendulum, shown in Fig. 1, was divided into six finite elements, so that the system was described by eighty-four differential equations. Additionally, one must take into account six algebraic equations of constraints describing the revolute joint. In comparison to the rigid pendulum, this system of equation of motion consisted of the same number of algebraic equations, and twelve times greater number of differential equations. We also carried out simulations with the use of a pendulum consisting of ten finite elements. However, the differences between the results of simulation of this pendulum, and those obtained for the six-element pendulum were insignificant, so that only the latter would be presented here.

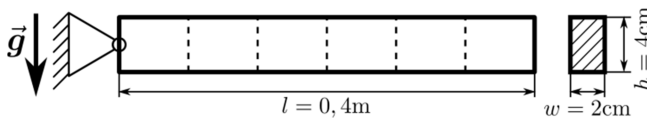


Fig. 1. Flexible physical pendulum

The simulations were carried out for two flexible models differing from one another by the values of Young's modulus. In the first case, Young's modulus was equal to $E = 2 \times 10^{11}$ Pa. Such a stiff pendulum should deform only insignificantly when moving in the field of gravitational forces. Because of that, the courses obtained in simulation should be similar to those of determined for rigid pendulum. It means that the values of amplitude and period of oscillation are comparable to respective values of oscillation amplitude and period of the rigid pendulum.

The difficulty of solving a system of high stiffness is associated with the fact that the equations of a standard ANCF beam element with high value of Young's modulus contain high-frequency components, which causes numerical difficulties. The following example will illustrate how the above-described algorithms could cope with solving a very stiff system of equations.

In the second model, the value of Young's modulus was decreased to $E = 2 \times 10^7$ Pa. The ANCF formulation is exceptionally effective in the case of models of low stiffness (Gerstmayr and Shabana, 2006), so that the described algorithms should solve this problem with relatively low computational cost. Low stiffness of the pendulum means that there might appear significant deformations of various frequencies, so that making comparisons between amplitudes and oscillation periods is useless. Therefore, only total energy value was calculated for this model. The results shown in Tab. 1 and 2 indicate that the information about total energy value is sufficient for assessment of accuracy of the analysed algorithms. For the systems with flexible bodies, total energy value was calculated as a sum of kinetic energy, potential energy of gravity forces and elastic energy (according to formula (20)).

Tab. 2 summarises simulation results obtained for the first, stiffer pendulum model. The tests carried out with the use of the *Radau* algorithms ended ahead of time in each case, because of too small integration step applied by the procedure. The results obtained by using the *DASSL* algorithm are printed in italics, because duration of all simulations performed with this algorithm exceeded the maximum allowable computation time equal to 10 hours. In such cases, the value in the "computation time" column means the time of calculation end reached after 10 hours of computations. We managed to obtain correct results only when using the algorithms *GAMD* and *HHT-I3*.

None of the algorithms gave satisfactory results for the highest tolerance values (test I). The results obtained with the use of the *GAMD* algorithm indicated that the oscillations were completely damped, while those produced by the *HHT-I3* were at variance with the physical sense of the problem. Simulation results obtained for lower tolerance values were fully acceptable, and their accuracy increased with decreasing tolerance values. The algorithm *HHT-I3* proved much more effective than the *GAMD* (despite the fact that its implementation was not optimal) for medium and low tolerance values. In the case of the highest tolerances (test I), the computations performed with the use of this algorithm took a much longer time, which was due to the fact that the computed results were erroneous (oscillations of increasing amplitude).

Tab. 2. Results of simulation of flexible physical pendulum ($E = 2 \times 10^{11}$ Pa)

Tolerance	Algorithm	Total energy [J]	Amplitude decay [%]	Period elongation [%]	Computation time
Test I: <i>Atol</i> 10^{-6} <i>Rtol</i> 10^{-3}	<i>DASSL</i>	0.01	0.32	0.18	<i>sim. to 30.3s</i>
	<i>Rasau5</i>	-	-	-	sim. to 0.6s
	<i>Radau</i>	-	-	-	sim. to 1s
	<i>GAMD</i>	-4.90	100	-15.5	18m 19s
	<i>HHT-I3</i>	138.4	-102	98.9	1h 16m 28s
	<i>DASSL</i>	-0.001	0.06	0.09	<i>sim. to 75s</i>
Test II: <i>Atol</i> 10^{-7} <i>Rtol</i> 10^{-5}	<i>Rasau5</i>	-	-	-	sim. to 8.7s
	<i>Radau</i>	-	-	-	sim. to 2.3s
	<i>GAMD</i>	0.07	-1.36	0.32	1h 25m 57s
	<i>HHT-I3</i>	-0.02	0.44	-0.09	17m 38s
	<i>DASSL</i>	5×10^{-6}	-0.02	0.12	<i>sim. to 83.3s</i>
	<i>Rasau5</i>	-	-	-	sim. to 16.0s
Test III: <i>Atol</i> 10^{-9} <i>Rtol</i> 10^{-7}	<i>Radau</i>	-	-	-	sim. to 16.4s
	<i>GAMD</i>	0.07	0.02	-0.008	2h 47m 20s
	<i>HHT-I3</i>	-0.002	0.04	-0.02	1h 03m 44s
	<i>DASSL</i>	-	-	-	<i>sim. to 30.3s</i>

Tab. 3. Results of simulation of flexible physical pendulum
($E = 2 \times 10^7 \text{ Pa}$)

Tolerance	Algorithm	Total energy [J]	Computation time
Test I:	DASSL	0.007	2h 57m 04s
A_{tol}	Rasau5	1.27	17m 02s
10^{-6}	Radau	3.67	27m 45s
R_{tol}	GAMD	0.07	11m 31s
10^{-3}	HHT-I3	2.46	3m 54s
Test II:	DASSL	0.007	42m 48s
A_{tol}	Rasau5	0.07	13m 38s
10^{-7}	Radau	0.09	28m 51s
R_{tol}	GAMD	0.07	14m 50s
10^{-5}	HHT-I3	-0.25	11m 36s
Test III:	DASSL	0.007	43m 08s
A_{tol}	Rasau5	0.07	28m 34s
10^{-9}	Radau	0.08	28m 44s
R_{tol}	GAMD	0.07	1h 00m 48s
10^{-7}	HHT-I3	0.007	1h 14m 44s

In Tab. 3, there are shown results of simulation of the pendulum which can be subject to significant deformations because of low value of Young's modulus. In the case of this model, it was possible to obtain some results for all algorithms and all tolerance values. In the case of test I, acceptable results were obtained only when using the algorithms *DASSL* and *GAMD*. The results obtained with the use of the remaining methods significantly differ from the nominal values. However, for lower tolerance values, all the results can be treated as acceptable. With the exception of the algorithm *HHT-I3*, all other algorithms gave results which did not differ much from one another when one assumed medium or low tolerance values.

Calculation time in the carried-out simulations proved strongly dependent on the tolerance values. The lowest impact of tolerances on computation time was observed in the algorithms *Radau* and *Radau5*. The algorithms *GAMD* and *HHT-I3* exhibited significant increase in computation time with decreasing tolerance value. In the case of algorithm *DASSL*, all the simulations lasted relatively long, and computations time needed in test I was much longer than that in tests II and III.

For this model, application of the algorithms *GAMD* and *HHT-I3* gave correct results in a shortest time (for all tolerance values). However, for the lowest tolerance values, the algorithms *Radau* and *Radau5* proved much more effective.

5. SUMMARY AND CONCLUSION

The results presented in this paper have shown significant differences in effectiveness of algorithms used for solving differential-algebraic equations in application to multibody systems. Correct results were obtained for all analysed models only when applying the algorithms *GAMD* and *HHT-I3*. The algorithms *Radau* and *Radau5* were not able to solve the system of a flexible pendulum of high stiffness, and the calculations performed for this system with the use of the *DASSL* algorithm lasted unacceptably long.

Considering the time of computation, one could conclude that the algorithm *HHT-I3* was the most effective one in the cases of simulations where tolerance values were medium or high.

In this respect, the characteristics of algorithm *GAMD* were similar. The algorithm *DASSL* proved very effective in the analysis of pendulum modelled with the use of a rigid body, while in the analysis of the flexible pendulum this algorithm turned out to be the slowest one. Nevertheless, the results obtained with the use of this algorithm were often the most accurate ones. The algorithms *Radau* and *Radau5* did not differ much, neither in accuracy of computations, nor in effectiveness (in some simulations, however, the algorithm *Radau5* was much faster). These algorithm proved to be effective in cases of low tolerance values.

On the basis of the presented results we can state that, for solving a multibody system, one should apply, in the first place, the algorithms *GAMD* or *HHT-I3*. If it turns out that these algorithms have too low effectiveness, one can try to apply the algorithm *Radau5*, which in some cases may give a higher effectiveness. The algorithm *Radau* is based on the same method of solving DAEs as the algorithm *Radau5*. However, we have not notice any substantial advantages of using this algorithm in comparison to the algorithm *Radau5*. Unlike the previous ones, the algorithm *DASSL* turns out to be a good one only in the cases of systems with low number of degrees of freedom, for example when analysing a rigid body. In the analysis of flexible systems, this algorithm was usually the slowest one.

It should be emphasised that this publication does not fully exhaust the presented topic. The works are carried out, aimed at complementing the results with the analyses of more complex examples. The algorithms have been tested, so far, only on relatively simple models; neither have we taken into account such properties of integrating procedures as, e.g., the ability of solving equations with inconsistent initial conditions. The mentioned problems are beyond the scope of this publication and need further analyses.

REFERENCES

1. Bathe K. J. (1996), *Finite Element Procedures*, Prentice Hall, New Jersey.
2. Brenan K. E., Campbell S. L., Petzold L. R. (1996), *Numerical Solution of Initial-Value Problems in Differential-Algebraic Equations*, SIAM, Philadelphia.
3. Frączek J. (2002), *Modelowanie mechanizmów przestrzennych metodą układów wieloczłonowych*, Oficyna Wydawnicza Politechniki Warszawskiej, Warszawa.
4. Frączek J., Malczyk P., Parallel Divide and Conquer Algorithm for Constrained Multibody System Dynamics based on Augmented Lagrangian Method with Projections-based Error Correction, *Nonlinear Dynamics*, DOI: 10.1007/s11071-012-0503-22012, to be printed.
5. Gear C. W., Leimkuhler B., Gupta G. K. (1985), Automatic integration of Euler-Lagrange equations with constraints, *Journal of Computational and Applied Mathematics*, Vol. 12-13, No. 0, 77-90.
6. Gerstmayr J., Matikainen M., Mikkola A. (2008), A geometrically exact beam element based on the absolute nodal coordinate formulation, *Multibody System Dynamics*, Vol. 20, No. 4, 359-384.
7. Gerstmayr J., Shabana A. A. (2006), Analysis of Thin Beams and Cables Using the Absolute Nodal Co-ordinate Formulation, *Nonlinear Dynamics*, Vol. 45, No. 1, 109-130.
8. Hairer E., Wanner G. (1996), *Solving ordinary differential equations II. Stiff and differential-algebraic problems*, Springer-Verlag, Berlin.
9. Haug E. J. (1989), *Computer-Aided Kinematics and Dynamics of Mechanical Systems, Volume I: Basic Methods*, Allyn and Bacon, Massachusetts.

10. **Hussein B., Negrut D., Shabana A. A.** (2008), Implicit and explicit integration in the solution of the absolute nodal coordinate differential/algebraic equations, *Nonlinear Dynamics*, Vol. 54, No. 4, 283-296.
11. **Iavernaro F., Mazzia F.** (1998), Solving ordinary differential equations by generalized Adams methods: properties and implementation techniques, *Applied Numerical Mathematics*, Vol. 28, No. 2-4, 107-126.
12. **Nikravesh P. E.** (1988), *Computer-Aided Analysis of Mechanical Systems*, Prentice Hall, New Jersey.
13. **Shabana A. A.** (1997), Definition of the Slopes and the Finite Element Absolute Nodal Coordinate Formulation, *Multibody System Dynamics*, Vol. 1, No. 3, 339-348.
14. **Shabana A. A.** (2003), *Dynamics of Multibody Systems*, Cambridge University Press, Cambridge.
15. **Shabana A. A.** (2008), *Computational Continuum Mechanics*, Cambridge University Press, Cambridge.
16. **Shabana A. A., Yakoub R. Y.** (2001), Three Dimensional Absolute Nodal Coordinate Formulation for Beam Elements: Part I and II, *Journal of Mechanical Design*, Vol. 123, No. 4, 606-621.

Acknowledgements: This work was realised as a part of research project No. N N514 673340 financed by the National Science Centre.

LOADS OF LOWER LIMB JOINTS DURING BICYCLE RIDE

Andrzej A. STĘPNIEWSKI*

*Department of Technical Sciences, Faculty of Production Engineering,
University of Live Sciences in Lublin, ul. Doświadczalna 50 A, 20-280 Lublin, Poland

andrzej.stepniewski@up.lublin.pl

Abstract: This work features a geometric and static analysis of the lower limb during bicycle ride. Basic dimensions are indicated, which are necessary for the description of movement geometry. The simplified flat model was adopted for the analysis. Using the transformation of Denavit-Hartenberg frames, vectors were developed for the position of the rotation axis of the joints in immovable frame. The inverse kinematics problem was solved. The course of displacement changes in the ankle joint was adopted as an angle function for crankset position, based on experimental research results, published in professional literature. The course was approximated with fifth grade polynomial. Joint displacements and loads were established. A sample calculation is presented, illustrating the subject computational algorithm.

Key words: Bicycle, Lower Limb, Movement Geometry, Matrix Method, Static Analysis, Jacobian

1. INTRODUCTION

Bicycle riding is currently becoming more and more recognised and accessible form of recreation, physical well-being improvement and muscle building (Szczerek, 2012).

The course of displacement and joint and muscle loads depends on the assumed riding position, frame geometry, saddle and handlebars position, and the length of cranksets (Wanich et al., 2007). Another key factor is the crankset load, which depends on the gear ratio, configuration and type of the ground, air resistance and pedalling technique. Other important factors are bicycle weight, resistance of bicycle drivetrain systems (chain, bearing) and resistance of tyre rolling on the ground.

The correct selection of parameters influencing travel comfort and safety has been subject to many studies, with the literature dominated by the results of experimental studies. The studies concern the influence of bicycle element dimensions on selected values, e.g. the influence of the dimensions of steering system on stability during fast ride (Prince and Al-Jumaily, 2011), the influence of the dimensions of pedal crank on the knee joint load (Boyd et al., 1997), the influence of different geometry of the frame on the crank load (Gregor et al., 2002) and muscle load (Ricard et al., 2006).

The research also covered the kinematics and dynamics of the cyclist, e.g. the vector of angle (Cockcroft, 2011) and load (Park S.-Y. et al., 2012), (Li Li and Caldwell, 1998) change, in the hip, knee and ankle joints for the constant pedalling power using EMG measurement method. The study (Diefenthaler et al., 2008) also investigated trunk movement using a camera. Another elements subject to measurements are generated power, pulse and the level of lactic acid under isokinetic conditions (Koninckx et al., 2010), oxygen demand, blood pressure (Shimomura et al., 2009) and strength adaptation of muscles for changing speed (Neptune and Herzog, 2000).

The referred studies provide data for calculations as well as results of multi-faceted research inspiring the direction for theoretical works, furthermore they allow for verification of these works. In the context of theoretical publications, which utilise commercial software, the work (Apkarian et al., 1989) can be regarded

as trailblazing. The authors give mathematical formulas, using the matrix method of kinematics and estimate the load of lower limb joints on the basis of Newton-Euler equations.

The aim of this work is establishing the geometry of lower limb movement and indicating displacement and balancing torque in joints during bicycle ride. A preliminary analysis was introduced, in which a solution to the inverse kinematics problem was provided and the load of joints was estimated. The research used Jacobian matrix transforming the vector of loading force acting on pedal bearing into balancing torques in the joints. The work also provided an algorithm simplifying the estimation of Jacobian matrix. The estimations did not account for the issue of inertia. The analysis assumed that the torque applied to the crankset is of constant value during round full angle cycle. A simulation of movement was performed using own software.

2. ANALYSIS OF LIMB MOVEMENT DURING PEDALLING

Analysis of limb movement during pedalling comes down to indicating:

- the coordinates of the position of knee and ankle joint rotation axes in the frame $\{x_0, y_0\}$ adopted as immovable,
- inverse problem solution, i.e. indicating the value of angular positions in joints as coordinate functions for the pedal axis position.

Fig. 1a presents kinematic chain of lower limb during bicycle riding scaled in Denavit-Hartenberg frame. We have adopted the flat model of lower limb (Siemieniako et al., 2010) simplified as compared to that suggested in Zielińska and Trojnacki (2009). Together with the crankset, it creates an articulated pentagon, which constitutes a problematic issue in indicating a uniform inverse problem solution.

It is necessary to introduce dependencies between the two selected angles. The most preferable angle indicated as the function of the second angle is the position angle in the ankle joint β_p – Fig. 1b. The course of value changes for the angle $\beta_p = f(\alpha_k)$ depends on anatomical structure, individual riding style and there even occurs a differentiation between the course for left and right leg, which was confirmed by the Authors of the paper (Kusiak

and Winiarski, 2009) in their experimental research. In order to describe the course $\beta_p = f(\alpha_k)$ an equation of adopting fifth grade polynomial to a set of n points of the coordinates $(\alpha_{k,i}, \beta_{p,i})$.

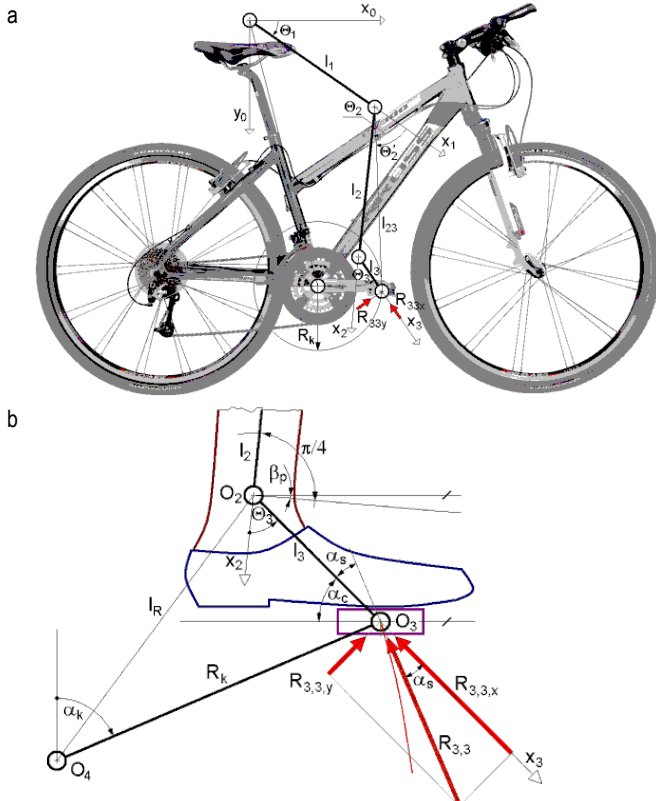


Fig. 1. Kinematic chain geometry; a – lower limb during bicycle ride, b – crankset system

A movement analysis of lower limb was performed for the simplified flat model. Movement trajectory of point O_3 was described using the parametric equations of the circle, thus the coordinates of the position of the pedal axis $(x_{O3,0}, y_{O3,0})$ in relation to the immovable frame $\{x_0, y_0\}$, according to Fig. 1a and 1b may be described as:

$$\begin{aligned} x_{O3,0} &= x_{O4,0} + R_K \sin \alpha_k, \\ y_{O3,0} &= y_{O4,0} + R_K \cos \alpha_k. \end{aligned} \quad (1)$$

The kinematics matrix method using the Denavit-Hartenberg frame transformation was used in order to transform the vectors of positions $r_{O_i,i}$ of the points marked "O*i*", determined in frames "i" into vectors of coordinates $(x_{O_i,0}, y_{O_i,0})$ determined in relation to the immovable frame $\{x_0, y_0\}$.

The matrices transforming coordinate frames from zero into first, from first into second and from second into third will have the form:

$$\mathbf{A}_i = \begin{bmatrix} c_i & -s_i & 0 & l_i c_i \\ s_i & c_i & 0 & l_i s_i \\ 0 & 0 & 1 & 0 \\ 0 & 0 & 0 & 1 \end{bmatrix}, \text{ where } i = 1, 2, 3, \quad (2)$$

whereas $s_i = \sin \theta_i$, $c_i = \cos \theta_i$, l_i – distance between the axes of the turning pairs of the unit i , θ_i – rotation angle between the units $i-1$ and i .

Coordinates of the vectors for the kinematic pair centres

O_1 , O_2 and O_3 in immovable frame, which will be used for further calculations and in the programme of movement animation, may be defined as follows:

$$\begin{bmatrix} x_{O1,0} \\ y_{O1,0} \\ z_{O1,0} \\ 1 \end{bmatrix} = \mathbf{A}_1 \mathbf{r}_{O1,1} = \begin{bmatrix} l_1 c_1 \\ l_1 s_1 \\ 0 \\ 1 \end{bmatrix}, \quad (3)$$

$$\begin{bmatrix} x_{O2,0} \\ y_{O2,0} \\ z_{O2,0} \\ 1 \end{bmatrix} = \mathbf{A}_1 \mathbf{A}_2 \mathbf{r}_{O2,2} = \begin{bmatrix} l_1 c_1 + l_2 c_{12} \\ l_1 s_1 + l_2 s_{12} \\ 0 \\ 1 \end{bmatrix}, \quad (4)$$

$$\begin{bmatrix} x_{O3,0} \\ y_{O3,0} \\ z_{O3,0} \\ 1 \end{bmatrix} = \mathbf{A}_1 \mathbf{A}_2 \mathbf{A}_3 \mathbf{r}_{O3,3} = \begin{bmatrix} l_1 c_1 + l_2 c_{12} + l_3 c_{123} \\ l_1 s_1 + l_2 s_{12} + l_3 s_{123} \\ 0 \\ 1 \end{bmatrix}. \quad (5)$$

Treating the variable distance $O_1 O_3 = l_{23}$ as known, the coordinates of the vector for the position of turning pair O_3 in relation to the frame $\{x_0, y_0\}$ may be also determined as:

$$\begin{bmatrix} x_{O3,0} \\ y_{O3,0} \\ z_{O3,0} \\ 1 \end{bmatrix} = \mathbf{A}_1 \mathbf{A}_{23} \mathbf{r}_{O3,3} = \begin{bmatrix} l_1 c_1 + l_{23} c_{123} \\ l_1 s_1 + l_{23} s_{123} \\ 0 \\ 1 \end{bmatrix}, \quad (6)$$

where: \mathbf{A}_{23} – matrix transforming the frame $\{x_1, y_1\}$ into frame $\{x_3, y_3\}$, $s_{12} = \sin(\theta_1 + \theta_2)$, $c_{12} = \cos(\theta_1 + \theta_2)$, $s_{123} = \sin(\theta_1 + \theta_2')$, $c_{123} = \cos(\theta_1 + \theta_2')$.

Inverse problem solution implies determining the angles θ_1 , θ_2' , θ_2 and angle θ_3 (Fig. 1a). For the purposes of inverse problem solution we must determine the following:

– the value of the angle θ_3 based on Fig. 1b according to dependency:

$$\Theta_3(\beta_p) = 0.5\pi + \beta_p - \alpha_c, \quad (7)$$

– the variable distance $O_1 O_3 = l_{23}$, which may be calculated according to dependency:

$$l_{23}(\Theta_3) = \sqrt{l_2^2 + l_3^2 + 2l_2 l_3 \cos \Theta_3}, \quad (8)$$

– the value of the angle θ_1 and θ_2' as dimension function $l_{23}(\Theta_3)$, by using the dependency (6) and solving the simultaneous equations:

$$x_{O3,0} = l_1 c_1 + l_{23} c_{123}, \quad y_{O3,0} = l_1 s_1 + l_{23} s_{123}, \quad (9)$$

we obtain the value of angle θ_1 as the function $l_{23}(\Theta_3)$:

$$\Theta_1 = 2 \operatorname{atan2} \left(B_1 + \sqrt{A_1^2 + B_1^2 - D_1^2}, A_1 + D_1 \right), \quad (10)$$

where: $A_1 = 2x_{O3,0}l_1$, $B_1 = 2y_{O3,0}l_1$, $D_1 = x_{O3,0}^2 + y_{O3,0}^2 + l_1^2 - l_{23}^2(\Theta_3)$;

– the value of the angle θ_2' as the dimension function $l_{23}(\Theta_3)$:

$$\Theta_2' = \operatorname{atan2} \left(\sqrt{1 - A_2^2}, A_2 \right), \quad (11)$$

where: $A_2 = \frac{x_{O3,0}^2 + y_{O3,0}^2 + l_1^2 - l_{23}^2(\Theta_3)}{2l_1 l_{23}(\Theta_3)}$.

From the triangle $O_1 O_2 O_3$, based on Fig. 1b, we can derive

the value of angle Θ_2 :

$$\Theta_2 = \text{atan2}\left(\sqrt{1-A_3^2}, A_3\right) + \Theta_2', \quad (12)$$

where: $A_2 = \frac{l_2^2 - l_3^2 + l_{23}^2(\Theta_3)}{2l_2l_{23}(\Theta_3)}$;

– the value of the angle α_s , may be determined based on the dependency:

$$\alpha_s = \text{atan2}\left(\sqrt{1-A_4^2}, A_4\right), \quad (13)$$

where: $A_4 = \frac{R_K^2 + l_3^2 - (x_{O4,0} - x_{O2,0})^2 - (y_{O4,0} - y_{O2,0})^2}{2l_3R_K}$,

whilst the coordinates $(x_{O2,0}, y_{O2,0})$ are determined based on the dependency (4).

3. LIMB STATIC ANALYSIS

Static analysis serves to determine the load of joints for imparted motion along the trajectory, which comprises mainly values of the torque for balancing the load of the foot during pedalling.

The load $R_{3,3}$ of the pedal determines the dependency:

$$R_{3,3} = \frac{M_K}{R_K}, \quad (14)$$

where: M_K is the imparted torque for loading the turning pair of the crankset during the ride.

The values of the coordinates of the loading force vector, determined within a frame of coordinates with the starting point O_3 determine the dependencies:

$$R_{3,3,x} = R_{3,3} \sin \alpha_s, \quad R_{3,3,y} = R_{3,3} \cos \alpha_s. \quad (15)$$

The vector of the loading force acting on the foot transforms into vectors of torques for driving forces in joints, according to the dependency:

$$\mathbf{M}_R = \mathbf{J}_{3,3}^T \mathbf{R}_{3,3}, \quad (16)$$

where: \mathbf{M}_R – the vector of driving torques in the joints, $\mathbf{R}_{3,3}$ – the vector of loading force acting on pedal bearing, determined in the frame $\{x_3, y_3\}$, $\mathbf{J}_{3,3}^T$ – transposed Jacobian matrix transforming the vector of loading force acting on pedal bearing into balancing torques in the joints.

Transposed Jacobian matrix $3 \times n$ is specified as follows:

$$\mathbf{J}_{3,3}^T = \begin{bmatrix} \beta_{1,3,x} & \beta_{1,3,y} & \beta_{1,3,z} \\ \beta_{2,3,x} & \beta_{2,3,y} & \beta_{2,3,z} \\ \beta_{3,3,x} & \beta_{3,3,y} & \beta_{3,3,z} \end{bmatrix}, \quad (17)$$

whose elements may be determined according to an algorithm simplifying the method of their derivation, presented in Stępniewski (2008):

$$\begin{bmatrix} \beta_{i,3,x} \\ \beta_{i,3,y} \\ \beta_{i,3,z} \end{bmatrix} = \begin{bmatrix} \beta_{i+1,3,x} \\ \beta_{i+1,3,y} \\ \beta_{i+1,3,z} \end{bmatrix} + l_i \begin{bmatrix} l_{i+1,3,y} \\ m_{i+1,3,y} \\ n_{i+1,3,y} \end{bmatrix}, \quad (18)$$

whereas:

$$\begin{bmatrix} \beta_{3,3,x} \\ \beta_{3,3,y} \\ \beta_{3,3,z} \end{bmatrix} = \begin{bmatrix} 0 \\ l_3 \\ 0 \end{bmatrix}, \quad (19)$$

where: $[l_{i+1,3,y} \ m_{i+1,3,y} \ n_{i+1,3,y}]^T$ the matrix composed of elements from the first, second and third column of the second line of the matrix \mathbf{A}_3 ($i = 2$) and $\mathbf{A}_2\mathbf{A}_3$ ($i = 1$), thus for ($i = 2$):

$$\begin{bmatrix} \beta_{2,3,x} \\ \beta_{2,3,y} \\ \beta_{2,3,z} \end{bmatrix} = \begin{bmatrix} 0 \\ l_3 \\ 0 \end{bmatrix} + l_2 \begin{bmatrix} s_3 \\ c_3 \\ 0 \end{bmatrix} = \begin{bmatrix} l_2 s_3 \\ l_2 c_3 + l_3 \\ 0 \end{bmatrix}. \quad (20)$$

Based on the second line of the matrix $\mathbf{A}_2\mathbf{A}_3$:

$$\begin{bmatrix} \beta_{1,3,x} \\ \beta_{1,3,y} \\ \beta_{1,3,z} \end{bmatrix} = \begin{bmatrix} l_2 s_3 \\ l_3 + l_2 c_3 \\ 0 \end{bmatrix} + l_1 \begin{bmatrix} s_{23} \\ c_{23} \\ 0 \end{bmatrix} = \begin{bmatrix} l_1 s_{23} + l_2 s_3 \\ l_1 c_{23} + l_2 c_3 + l_3 \\ 0 \end{bmatrix}. \quad (21)$$

The value of torques in joints, balancing the load acting on foot, according to the dependency (16) is determined as follows:

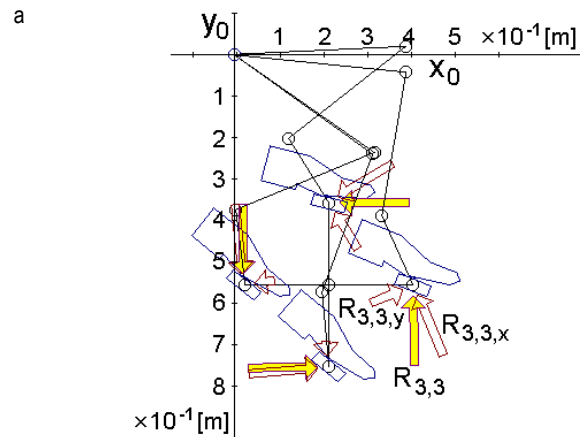
$$\begin{bmatrix} M_{R1} \\ M_{R2} \\ M_{R3} \end{bmatrix} = \mathbf{J}_{3,3}^T \mathbf{R}_{3,3} = \begin{bmatrix} l_1 s_{23} + l_2 s_3 & l_1 c_{23} + l_2 c_3 + l_3 & 0 \\ l_2 s_3 & l_2 c_3 + l_3 & 0 \\ 0 & l_3 & 0 \end{bmatrix} \begin{bmatrix} R_{3,3,x} \\ R_{3,3,y} \\ 0 \end{bmatrix},$$

$$\begin{bmatrix} M_{R1} \\ M_{R2} \\ M_{R3} \end{bmatrix} = \begin{bmatrix} (l_1 s_{23} + l_2 s_3) R_{3,3,x} + (l_1 c_{23} + l_2 c_3 + l_3) R_{3,3,y} \\ l_2 s_3 R_{3,3,x} + (l_2 c_3 + l_3) R_{3,3,y} \\ l_3 R_{3,3,y} \end{bmatrix}. \quad (22)$$

4. NUMERICAL EXAMPLE

The calculation involved the following data: length: $l_1 = 0.40\text{m}$, $l_2 = 0.35\text{m}$, $l_3 = 0.18\text{m}$, $R_K = 0.195\text{m}$, coordinates of the position of crankset turning pair in the hip joint frame: $(x_{O4,0}, y_{O4,0}) = (0.22, -0.55)$, constant angle $\alpha_c = 45^\circ$, nine coordinates $(\alpha_{k,i}, \beta_{p,i})$: $(0, 40^\circ)$, $(45^\circ, 5^\circ)$, $(90^\circ, 0)$, $(135^\circ, -15^\circ)$, $(180^\circ, -55^\circ)$, $(225^\circ, 25^\circ)$, $(270^\circ, 30^\circ)$, $(315^\circ, 35^\circ)$, $(360^\circ, 40^\circ)$. The calculation adopts constant torque for loading the crankset $M_K = 10\text{ N}\cdot\text{m}$ and constant force of a foot of one leg on the pedal during the full cycle (pedal with gear).

The results of the above calculations are presented in Fig. 2.



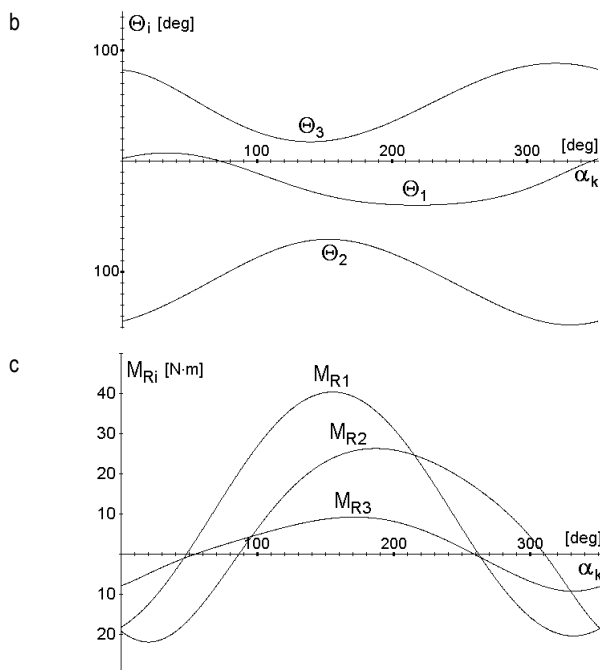


Fig. 2. Calculation results; a – simulation of limb movement during bicycle ride, b – courses of displacements in joints, c – courses of balancing torques in joints

5. CONCLUSIONS

On the basis of the performed geometrical and static analyses, the following conclusions are to be made:

- Lower limb together with flat version crankset creates an articulated pentagon with three drives.
- Movement in the ankle joint is not strictly determined, realisation of movement is possible for several different courses of the joint angle changes.

Based on the acquired results it can be stated that:

- The ranges of relative angular displacements in the joints are: hip 55° , knee 75° and ankle 65° .
- The extreme values of relative angular displacements in the joints are: hip 10° with $\alpha_k = 35^\circ$ and -45° with $\alpha_k = 220^\circ$, knee -70° with $\alpha_k = 150^\circ$ and -145° with $\alpha_k = 330^\circ$, ankle 20° with $\alpha_k = 140^\circ$ and 85° with $\alpha_k = 320^\circ$.
- The torques are of similar character and reach the maximum values in the joints: hip 40 N-m with $\alpha_k = 155^\circ$, knee 25 N-m with $\alpha_k = 190^\circ$ and ankle 10 N-m with $\alpha_k = 170^\circ$.
- During the full cycle there occur two positions, where torques in the joints change their sense: in hip and ankle joint with $\alpha_k = 50^\circ$ and $\alpha_k = 260^\circ$, in knee joint with $\alpha_k = 85^\circ$ and $\alpha_k = 310^\circ$.

The above values were obtained by means of adopted geometrical measurements of the limb and bicycle, assuming constant torque for loading the crankset. Further analysis involves: changeability of the load torque, inertia interaction and optimisation of the geometrical measurements. It seems preferable to develop a comprehensive limb model, including the anatomical structure of the joints, which would allow for estimating the contact load of bones and ligaments. Obtained results of the estimation would give ground for clarification of practical guidelines concerning the use of a bike, e.g. for knee arthroscopy rehabilitation, where "movement therapy" is advisable.

REFERENCES

1. **Apkarian J., Naumann S., Cairns B.** (1989), A three-dimensional kinematic and dynamic model of the lower limb, *J. Biomechanics*, Vol. 22, No. 2, pp. 143-155.
2. **Boyd T. F., Neptune R. R., Hull M. L.** (1997), Pedal and knee loads using a multi-degree-of-freedom pedal platform in cycling, *J. Biomechanics*, Vol. 30, No. 5, 505-511.
3. **Cockcroft S. J.** (2011), *An evaluation of inertial motion capture technology for use in the analysis and optimization of road cycling kinematics*, Stellenbosch University.
4. **Diefenthaler F., Carpes F. P., Bini R. R., Mota C. B., Guimarães A. C. S.** (2008), Methodological proposal to evaluate sagittal trunk and spine angle cyclists: Preliminary study, *Brazilian Journal of Biomechanics*, Vol. 2, No. 4, 284-293.
5. **Gregor S. M., Perell K. L., Rushatakov S., Miyamoto E., Muffoletto R., Gregor R. J.** (2002), Lower extremity general muscle moment patterns in healthy individuals during recumbent cycling, *Clinical Biomechanics*, Vol. 17, Issue 2, 123-129.
6. **Koninckx E., Van Leemputte M., Hespel P.** (2010), Effect of isokinetic cycling versus weight training on maximal power output and endurance performance in cycling, *European Journal of Applied Physiology*, Vol. 109, Issue 4, 699-708.
7. **Kusiak M., Winiarski S.** (2009), *The impact of cyclist's position on the miographic image of the main muscle groups of lower limb used during cycling* (in Polish), Katedra Biomechaniki AWF, Wrocław.
8. **Li Li, Caldwell G. E.** (1998), Muscle coordination in cycling: effect of surface incline and posture, *J Appl Physiol* 85, 927-934.
9. **Neptune R. R., Herzog W.** (2000), Adaptation of muscle coordination to altered task mechanics during steady-state cycling, *Journal of Biomechanics* 33, 165-172.
10. **Park S.-Y., Lee S.-Y., Kang H. C., Kim S.-M.** (2012), EMG analysis of lower limb muscle activation pattern during pedaling experiments and computer simulations, *International Journal of Precision Engineering and Manufacturing*, Vol. 13, No. 4, 601-608.
11. **Prince P. J., Al-Jumaily A.** (2011), Bicycle steering and roll responses, *Science* 15, Vol. 332, No. 6027, 339-342.
12. **Ricard M. D., Hills-Meyer P., Miller M. G. Michael T. J.** (2006), The effects of bicycle frame geometry on muscle activation and power during a wingate anaerobic test, *Journal of Sports Science and Medicine* 5, 25-32.
13. **Shimomura K., Murase N., Osada T., Kime R., Anjo M., Esaki K., Shiroishi K., Hamaoka T., Katsumura T.** (2009), A study of passive weight-bearing lower limb exercise effects on local muscles and whole body oxidative metabolism: a comparison with simulated horse riding, bicycle, and walking exercise, *Dynamic Medicine*, 8:4 doi: 10.1186/1476-5918-8-4.
14. **Siemieniako F., Ostaszewski M., Kuźmierowski T.** (2010), Analysis of requirements for exoskeleton construction, *Int. J. of Applied Mechanics and Engineering*, Vol. 15, No. 3, 841-846.
15. **Stępniewski A. A.** (2008), *Simplified algorithm for estimating jacobians and angle speed vectors of manipulator's elements* (in Polish), rozdz. do pracy pod red.: J. Wojnarowski i I. Adamiec-Wójcik: Teoria maszyn i mechanizmów, WAT-H. Bielsko-Biała, 311-320.
16. **Szczerek A.** (2012), *Obesity treatment, slimming diet and other diets HLMZ* (in Polish), <http://www.asmed.hg.pl/rower.htm> 5.03.2012.
17. **Wanich T., Hodgkins Ch., Columbiere J.-A., Muraski E., Kennedy J. G.** (2007), Cycling Injuries of the Lower Extremity, *J Am Acad Orthop Surg* 15, 748-756.
18. **Zielińska T., Trojnecki M.** (2009), Analysis of the distribution of surface reaction power during dynamically constant walk of a two-legged robot (in Polish), *Pomiary Automatyka Robotyka*, No. 7-8, 6-10.
19. http://www.winiarski.awf.wroc.pl/omnie_pliki/konf_skn_20

IMPACT PROCESS IDENTIFICATION FOR IMPACT CYLINDER PISTON

Andrzej ZBROWSKI*, Wojciech JÓŹWIK*

*Institute for Sustainable Technologies, National Research Institute, ul. Pułaskiego 6/10, 26-600 Radom, Poland

andrzej.zbrowski@itee.radom.pl, wojciech.jozwik@itee.radom.pl

Abstract: The phenomenon of the tool rebound from the object processed, that can be noticed particularly in the case of impact marking, has a negative influence on the quality of the processing of moving objects, which is a result of the blur effect caused by the shift of the object processed at the time of its retraction. The objective of the study was to determine the influence of both the capacity of the chamber of the accumulator and the working pressure on the characteristics of the phenomenon of the piston rebound from the obstacle that can be noticed after it hits a hard fender for the very first time. The article presents the results of research consisting in the analysis of the rebound phenomenon for impact cylinder pistons. The tests were carried out for cylinders whose structure allowed for the change in the capacity of the accumulator chamber. Cylinders with the pistons of 40 and 100 mm in diameter and supplied by 4 and 6 bar pressure were subject to tests that were undertaken at the test stand equipped with Phantom V310 high speed digital camera

Key words: Impact Cylinder, High Speed Camera, Marking, Bounce, Kinetic Energy

1. INTRODUCTION

Impact cylinders are a kind of pneumatic actuators characterised by the speed of the movement of the piston several times higher than the one of typical actuators, which depending on the structure, can even reach the speed greater than 10 m/s. Sudden acceleration is caused by the differential surface system, as a result of which the entire surface of the piston is subject to the influence of the pressure of the air stored in the container, known as an accumulator, located at the back of the cylinder.

High working velocities of the piston allow for the application of impact cylinders as a drive system ensuring high level of kinetic energy. A relation between the energy and the mass as well as the dimensions of the drive constitutes a significant advantage of the device. The application of the pneumatic drive system greatly increases the resistance of the kinematic system to overload taking place at the time of the impact. These features allow for the application of high speed actuators in situations when the piston's force is of percussive character. The main areas of technological application include marking, perforation and the production of light pressed products (Lenczewski and Łunarski, 1999; 2000, 2011; Mikulczyński and Kiczowski, 1999).

Because of the application of the gaseous working medium, the collision of the piston with the obstacle is characterized by a high restitution coefficient. As a result of the collision, uncontrolled rebound of the piston from the object and its pneumatically enforced return to the object's surface take place. These are caused by the influence of the pressure of the air stored in the chamber of the cylinder (Liu and Jiang, 2007). The second time the piston hits the object ends with a dynamic finisher.

This phenomenon badly influences the quality of edges created at the time of marking or pressing. The intensity of disturbances increases in the case of operations performed on a fast moving object. As a result of a constant movement of the object, the area of the second impact of the piston does not agree with

the first one and thus the edges of the initially created cavity are damaged and blurred. In order to estimate the parameters of the technological process of quick marking, it is necessary to determine the real time of the impact of the head with the processed surface.

Current studies concerning the determination of energy parameters of cylinders allowed the characteristics of the piston stroke to be recorded with the use of laser triangulation method (Czajka and Giesko, 2008). The resolution of the method, however, did not allow for the recording of the brief collision of the tool with the obstacle. Simulation tests for high speed cylinders were predominantly directed at the development of a mathematical model enabling the optimization of process parameters and the selection of a proper tool (Kiczowski and Grymek, 2000). The application of high speed digital cameras enabled the movement of the piston to be recorded with high resolution which allowed for exact identification and analysis of the collision process (Zbrowski and Jóźwik, 2012a, b). The application of high speed vision techniques resulted in the increase in sampling frequency up to 6 kHz.

2. PRESENTATION OF THE PROBLEM

Tests carried out with view of determining the movement characteristics for impact cylinders indicated that after the collision of the piston with the obstacle a rebound of the piston connected with a dynamic finisher and a stop could be noticed.

In the case of some applications, the rebound of the piston is pretty disadvantageous as repeated uncontrolled strikes of the piston may worsen the quality of the geometry or the structure of the processed surface. A blur effect caused by the shift of the processed object can be observed for the processing of fast moving objects (Fig. 1).

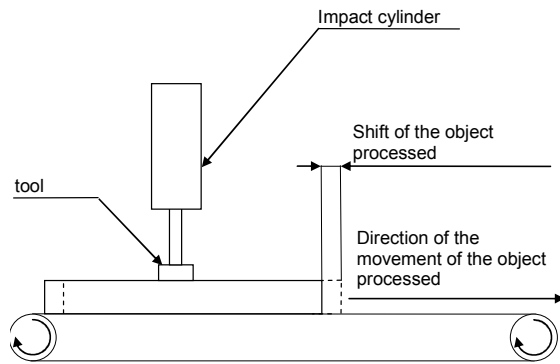


Fig. 1. Blur effect caused by the rebound

The characteristics of the movement of the piston (Fig. 2) depict the rebound effect in which after the collision of the piston with the fender, an oscillatory change in the direction of the movement can be noticed.

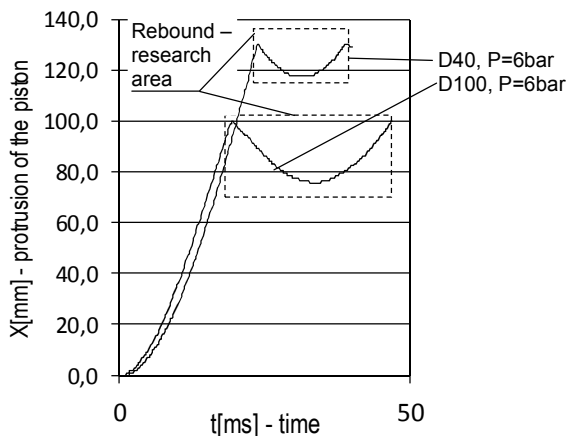


Fig. 2. Characteristics of the moment of the piston in the time function

The objective of the tests conducted was to determine the influence of the capacity of the chamber of the accumulator and the working pressure on the characteristics of the rebound of the piston from the processed surface after the first strike.

3. RESEARCH METHOD AND TEST STAND

The measurements were carried out on the test stand intended particularly for impact cylinder tests (Giesko et al., 2007; Czajka et al., 2008; Giesko and Zbrowski, 2008) that was modified in a way enabling the observation of the phenomenon (Fig. 3). The movement of the cylinder was impeded by a 25 mm thick steel plate that was used as a hard fender, which was located 130 mm away from the head of the piston of the D40 cylinder and 100 mm from the head of the piston of the D100 cylinder.

A high speed Phantom V 310 camera by Vision Research and halogen lighting were used (Fig. 3). The tests were carried out for actuators equipped with a regulation screw enabling the regulation of the volume of the chamber of the accumulator. The cylinders that were under investigation had piston of 40 and 100 mm in diameter and they were supplied by the air of 4 and 6 bars.

The measurement system was calibrated with the use of the pattern length located behind the piston, parallel to the direction

of its movement. The parameters of the camera and the lighting system used allowed the phenomenon to be recorded at the speed of 6000 fps, resolution of 800x600 pixels and the exposure time of 0.1 ms.

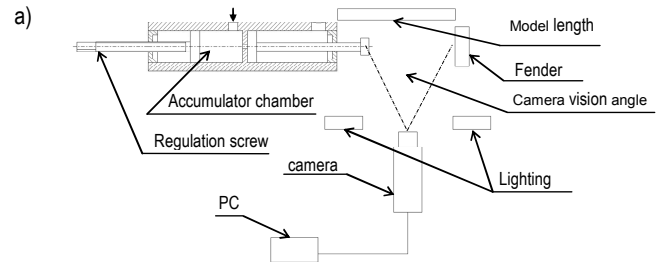


Fig. 3. Measurement stand: a) draft, b) view

4. TESTS RESULTS

Characteristics of the movement of the piston were determined with the use of TEMA MOTION commercial software intended for image analysis. High resolution of the method revealed that after its collision with the fender, the piston rebounds of its surface and then hits the obstacle again and stops. The speed of the first impact is presented in Fig. 4.

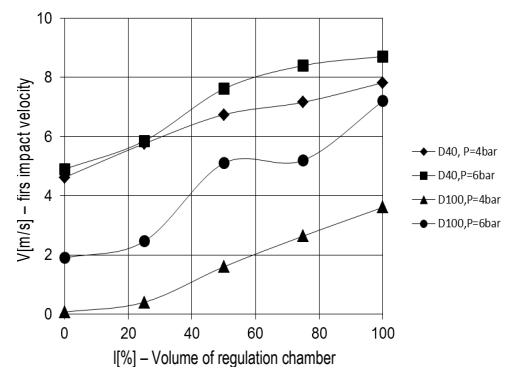


Fig. 4. Impact speed

The rebound phenomenon was not observed for the D100 actuator with the minimum capacity of the chamber of the accumulator.

From the characteristics of the movement path of the piston recorded in the function of time (Fig. 5) it appears that for D40 and D100 cylinders supplied by the pressure of 0.4 MPa, the distance of the rebound increases together with the volume of the regulatory chamber, whereas for the D100 actuator fed by the pressure of 0.6 MPa, the rebound time is visibly shorter, with no significant differences in the distance.

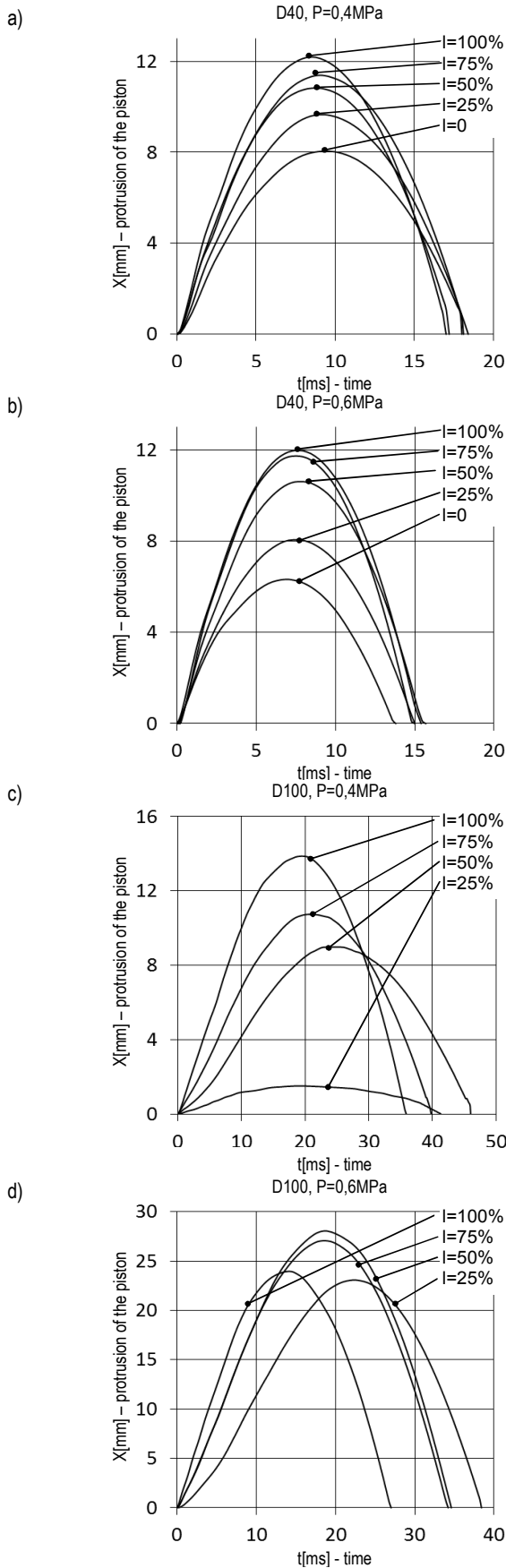


Fig. 5. Characteristics of the movement path of the piston in the function of time: a) D40 actuator with pressure of 0.4 MPa, b) D40 actuator with pressure of 0.6 MPa, c) D100 actuator with pressure of 0.4 MPa, d) D100 actuator with pressure of 0.6 MPa. (The „l” values stand for the volume of the regulation chamber)

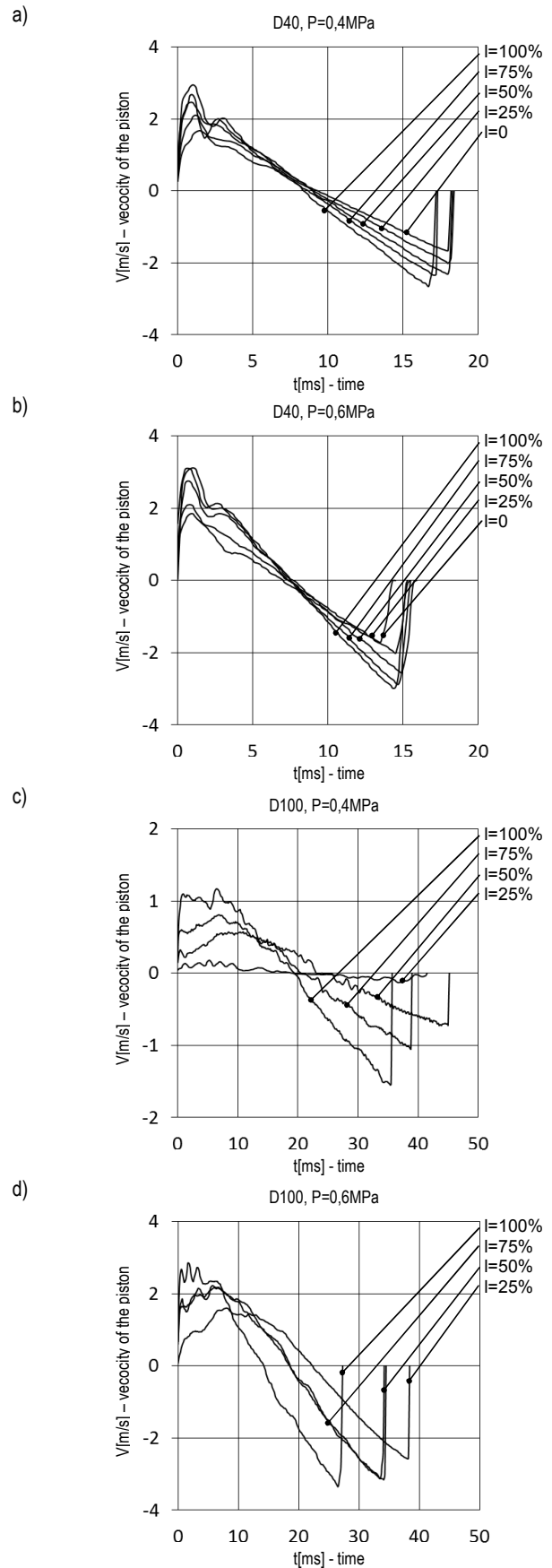


Fig. 6. Characteristics of the speed of the piston in the function of time: a) D40 actuator with pressure of 0.4 MPa, b) D40 actuator with pressure of 0.6 MPa, c) D100 actuator with pressure of 0.4 MPa, d) D100 actuator with pressure of 0.6 MPa. (The „l” values stand for the volume of the regulation chamber)

The characteristics of the speed of the piston movement in the function of time (Fig. 6) indicate that the speed of the rebound is proportional to the volume of the chamber of the accumulator and the supply pressure.

The increase in the volume of the chamber of the accumulator leads to the growth in the distance the piston moves at after the rebound (Fig. 7) and accelerates the speed of the rebound (Fig. 8).

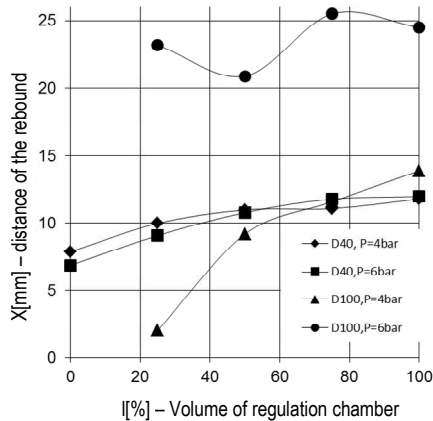


Fig. 7. Characteristics of the distance of the rebound in relation to the volume of the chamber of the accumulator

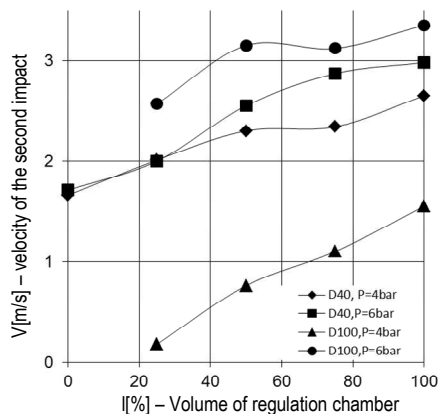


Fig. 8. Characteristics of the speed of the finisher in relation to the volume of the chamber of the accumulator

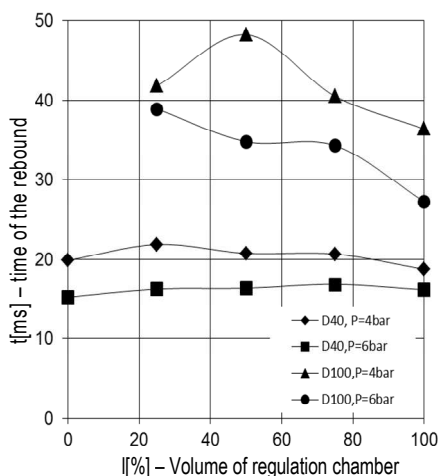


Fig. 9. Characteristics of the rebound time in relation to the volume of the chamber of the accumulator

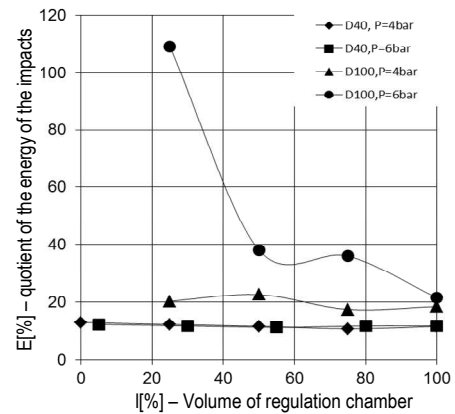


Fig. 10. Energy characteristics for the finisher in relation to the volume of the chamber of the accumulator

At the time of the first collision, there was vacuum in the chamber of the D100x200 actuator (speed of the piston decreased) (Lenczewski and Łunarski, 2001). The increase in the speed of the backward movement of the piston could be noticed for ca. 8 ms after the rebound (Fig. 7). High value of the rebound for the feed pressure of 6 bars is a result of the increased speed of the first impact in comparison to the feed pressure of 4 bars.

The rebound time for the D40 cylinder does not change much, while for the D100 actuator it decreases together with the level to which the regulatory chamber is filled up (Fig. 9). For the D40 actuator the energy of the finisher amounted to ca. 12% of the energy of the first impact. For the D100 actuator the energy quotient for the first and the second impact is dependent on the feed pressure and the volume of the chamber of the accumulator (Fig. 10).

5. CONCLUSIONS

Application of high speed vision techniques enables precise recording of the collision of the piston of the impact cylinder with the obstacle.

The characteristics of the movement of the piston obtained can be used for the designing of technological stands in which the object processed moves at a great speed in relation to the tool mounted on the piston of the impact cylinder. The determination of the rebound time allows the permissible speed of the shift of the object processed to be established.

On the basis of the tests conducted a following remark can be made: D100 actuators supplied by the standard pressure of 6 bars are characterized by a longer rebound time than D40 ones. This is connected with the piston stroke; the speed of the repeated rebound is, however, greater than in the case of the D40 actuator.

The reduction of the feed pressure for both the actuators tested results in a prolonged time of rebound and badly influences the efficiency of the technological process.

REFERENCES

1. Czajka P., Giesko T. (2008), Characteristic calculation of impact cylinders with an adjusting chamber (in Polish), *Problemy Eksploatacji*, 3, 123-131.
2. Czajka P., Giesko T., Zbrowski A. (2008), Method and apparatus for the determination and optimization of work parameters of the

- pneumatic impact cylinders (in Polish), *Przegląd Mechaniczny*, 12, 24-28.
3. **Giesko T., Zbrowski A.** (2008), Method and apparatus for the determination and optimization of work parameters of the pneumatic impact cylinders (in Polish), VI International Scientific-Technical Conference Technika i Technologia Montażu Maszyn, Kalnica, 28-30 May 2008, *Zeszyty Naukowe Politechniki Rzeszowskiej, Mechanika*, 72, 237-244.
 4. **Giesko T., Zbrowski A., Czajka P.** (2007), Method and device for testing the impact cylinders (in Polish), *Pneumatyka Przemysłowe Systemy Sprężonego Powietrza*, 2, 34-37.
 5. **Kiczowski T., Grymek, S.** (2000), The computer program to support calculation of high-speed pneumatic cylinders with built-in chamber (in Polish), Krajowa Konferencja Pneuma 2000, 25-27.10.2000; Kielce, *Zeszyty Naukowe Politechniki Świętokrzyskiej, seria: Elektryka*, nr: 39, 147-154.
 6. **Lenczewski J., Łunarski J.** (1999), The pneumatic impact cylinder (in Polish), *Technologia i Automatyzacja Montażu*, 1, 30-32.
 7. **Lenczewski J., Łunarski J.** (2000), Pneumatic impact presses (in Polish), *Technologia i Automatyzacja Montażu*, 1, 36-37.
 8. **Lenczewski J., Łunarski J.** (2001), The pneumatic impact punching in pre mounting operations (in Polish), *Technologia i Automatyzacja Montażu*, 1, 30-32.
 9. **Liu Y.; Jiang Ch.** (2007), Pneumatic actuating device with nanopositioning ability utilizing PZT impact force coupled with differential pressure, *Precision Engineering*, Vol: 31, Issue: 3, 293-303
 10. **Mikulczyński T., Kiczowski T.** (1999), Application of high-speed pneumatic drive for dynamic squeezing of moulding sands (in Polish), *Przegląd Odlewnictwa*, Vol. 13, Z. 4, 141 -143.
 11. **Zbrowski A., Jóźwik W.** (2012), Determination of energy parameters of impact cylinder, *The 8th International Conference Mechatronic Systems And Materials 2012*. 8-13 July, 2012 Białystok. Abstract book, 70.
 12. **Zbrowski A., Jóźwik W.** (2012), Determination of the characteristics of the impact cylinders with use of fast camera (in Polish), *Problemy Eksploatacji*, 3/2012 (in press).

ABSTRACTS

Adam Adamowicz, Piotr Grześ

Convective Cooling of a Disc Brake During Single Braking

This study is primarily focused on the investigation of an impact of heat transfer coefficient on heat dissipation from the solid disc using the finite element method (FEM). The analysis was carried out within four individual cases of braking of the passenger vehicle simulating mountain descent with different velocities and the following release periods, where the convective terms of cooling were dependent on the angular velocity of the disc. For the purpose of confronting contrasting conditions of the braking action, apart from heating region, the whole surface of the disc was insulated. The process was performed under the operation conditions of a real front disc brake, whose dimensions and thermophysical properties of materials were adopted and applied to the FE model. It was concluded that the influence of cooling of the exposed surfaces of the disc during relatively short braking is insignificant. However the period after brake release results in considerable decrease in temperature of the disc.

Jacek Bałchanowski, Antoni Gronowicz

Design and Simulations of Wheel-Legged Mobile Robot

The problems of determining dynamic and kinematic parameters of wheel-legged mobile robot were considered in the paper. The numerical computer model of robot was worked out and simulation researches of suspension were completed. The motion of wheel on road with obstacles and walking motion of wheel were analyzed for determining kinematic and dynamic parameters.

Paweł Baranowski, Paweł Bogusz, Paweł Gotowicki, Jerzy Małachowski

Assessment of Mechanical Properties of Offroad Vehicle Tire: Coupons Testing and FE Model Development

In this paper the subsequent stages of tire rubber coupons mechanical properties experimental assessment are presented. Experimental uniaxial tension and compression tests were carried out on the strength testing machine with the assistance of high-speed camera and special software for strain measurements. Obtained stress-strain curves were applied into the chosen Mooney-Rivlin constitutive rubber material model in order to estimate necessary material constants. Simultaneously, the numerical off-road vehicle tire model was developed. Geometry of the tire and rim was achieved using a 3D scanning method. Moreover, with the assistance of microscope and X-ray device the tire cords pattern was verified, which in the next stages was implemented into the FE model. Consequently, tire radial deflection test was simulated in order to validate evaluated material constants and proposed concept of the numerical tire modelling. Obtained results were compared with the actual deflection test data included in technical documentation of the tire.

Leszek Cedro

Identification of an Electrically Driven Manipulator Using the Differential Filters – Input Error Method

The paper presents an example of solving the parameter identification problem in case of robot with three degrees of freedom has been presented. The identification has been performed with the use of elaborated differential filters. The applied identification method does not require differential equations solving but only determining the appropriate derivatives. Identification method and its generalizations using the object inverse model require information on time derivatives of the input and output signals. The required derivative order depends on the order of differential equations describing the object.

Adam Czaplicki, Krzysztof Dziewiecki, Tomasz Sacewicz

Identification of Internal Loads at the Selected Joints and Validation of a Biomechanical Model During Performance of the Handspring Front Somersault

The handspring front somersault in pike position is analyzed in this paper. The computations have been based on a three-dimensional model of the human body defined in natural coordinates. The time histories of net muscle torques and internal reactions at the ankle, knee, hip and upper trunk-neck joints have been obtained after the solution of the inverse dynamics problem. The sagittal, frontal and transverse plane components of selected net muscle torques and internal reactions are presented and discussed in the paper. It has also been demonstrated that natural coordinates provide a useful framework for modelling spatial biomechanical structures.

Marek Dźwiarek

Practical Examples of Determination of Frequency of Periodical Inspection of Machinery Safety Systems

The paper deals with the problem of choosing an appropriate inspection interval for monitoring of safety related control systems in machinery. According to international standards the safety related systems are categorized according to their Safety Integrity Levels or Performance Levels, depending on their reliability parameters. Extremely simple, approximate models have been proposed in order to provide practitioners without reliability training with useful tools for the determination of inspection policies. The method(s) based on the required availability of the system. The paper presents some practical examples of systems of categories B, 1 and 3, respectively. The frequencies of periodical inspection are calculated for: system monitoring closure of the door, behind which a dangerous element moves slowly, system of monitoring the access door on the automated production line and system, in which a light curtain is employed to monitor the access to the dangerous zone of an automatic assembly machine.

Marcin Graba

Numerical Verification of the Relationship Between The "In-Plane Geometric Con-Straints" used in Fracture Mechanics Problems

In the paper, numerical verification and catalogue of the numerical solutions based on Modify Boundary Layer Approach to determine the relationship between Q-stress and T-stress are presented. Based on the method proposed by Larsson and Carlsson, the Q-stress value are calculated for some elastic-plastic materials for different value of T-stress and external load expressed by J-integral. The influence of the external load, T-stress value and material properties on Q-stress value were tested. Such catalogue may be useful during solving the engineering problems, especially while is needed to determine real fracture toughness with including the geometric constraints, what was proposed in FITNET procedures.

Antoni Gronowicz, Jarosław Szrek, Sławomir Wudarczyk

A Rig for Testing the Leg of a Wheel-Legged Robot

The paper describes a rig specially constructed for testing a single leg of the wheel-legged robot being designed and presents exemplary test results. The aim of the tests was to verify the mechanical structure and control system operation in laboratory conditions. The operation of the control, communication and data transmission modules was verified. Also tests aimed at selecting proper parameters for the drive controllers were carried out on the test rig.

Jerzy Jaroszewicz , Krzysztof K. Żur

Limitation of Cauchy Function Method in Analysis of Estimators of Frequency and Form of Natural Vibrations of Circular Plate with Variable Thickness and Clamped Edges

In this paper the Bernstein-Kieropian double estimators of basic natural frequency of circular plate with power variable thickness along the radius and clamped edges in diaphragm form were analyzed in a theoretical approach. The approximate solution of boundary problem of transversal vibration by means of Cauchy function and characteristic series method has been applied for chosen values of power indicator of variable thickness m and material Poisson's ratio ν has been chosen which led to exact form solutions. Particular attention has been given to a singularity arising from the uncertainty of estimates of Bernstein-Kieropian. Improving this method has been obtained the general form of Cauchy function for arbitrary values of m and ν , which are physically justified. Therefore, the aim of the paper was to explore the reason why for a plate above a certain value $m=3.97$ exact solution, which Conway couldn't receive (Conway, 1958a, b).

Tadeusz Kaczorek

Positive Realizations for Descriptor Discrete-Time Linear Systems

Conditions for the existence of positive realizations for descriptor discrete-time linear systems are established. A procedure for computation of positive realizations for improper transfer matrices is proposed. The effectiveness of the method is demonstrated on numerical example.

Józef Knapczyk , Mateusz Ryska

Stiffness Matrix Analysis of Six-Revolute Serial Manipulator

This paper presents a simple procedure that can be used to determine the stiffness matrix of 6R serial manipulator in selected points of the work space with joint stiffness coefficients taking into account. Elastokinematical model for the robot manipulator FANUC S-420F was considered as spatial and serial kinematical chain composed of six rigid links, connected by ideal revolute joint (without clearances and deformable elements), with torsion elasticity of the joint drive system (relative torsion deformations are proportional to acted torques) taking into account. Assumed model is used for displacement analysis of the end-effector for a given applied force in quasi-static condition. The analysis results are presented as Cartesian stiffness matrix of studied manipulator.

Igor Maciejewski

Load-Dependent Controller of the Active Seat Suspension with Adaptive Mass Recognizing

The paper deals with the load dependent control system of active seat suspension. This system based on the primary controller which evaluates the desired active force, the reverse model which calculates the input signal of force actuator and the adaptation mechanism which recognizes the actual mass loading. An optimisation procedure additionally presented in this paper allows to find the primary controller settings that minimizes the vibration of cabin's floor transmitted to operator's seat at the pre-defined value of the maximum relative displacement of suspension system.

Adam Niesłony, Michał Böhm

Mean Stress Value in Spectral Method for the Determination of Fatigue Life

The paper presents a proposal of account of mean stress value in the process of the determination of the fatigue life, using the spectral method. The existing approaches have been described and some chosen stress models used to take into account the influence of the mean value in the process of the determination of fatigue life have been introduced. Those models, referring to their linear character, have been used to determine the power spectral density function (PSD) of the transformed stress taking into account the mean value. The method introduced by the authors allows a wide usage of many formulas used to predict the fatigue life by means of the spectral method.

Grzegorz Orzechowski, Janusz Frączek

Integration of the Equations of Motion of Multibody Systems Using Absolute Nodal Coordinate Formulation

Recently, a finite element formulation, called the absolute nodal coordinate formulation (ANCF), was proposed for the large rotation and deformation analysis of flexible bodies. In this formulation, absolute position and slope coordinates are used to define the finite element configuration. Infinitesimal or finite rotations are not used as nodal coordinates. The ANCF finite elements have many unique features that distinguish them from other existing finite element methods used in the dynamic analysis of the flexible multibody systems. In such systems, there appears the necessity of solving systems of differential-algebraic equations (DAEs) of index 3. Accurate solving of the DAEs is a non-trivial problem. However, in the literature about the ANCF one can hardly find any detailed information about the procedures that are used to solve the DAEs. Therefore, the current paper is devoted to the analysis of selected DAE solvers, which are applied to simulations of simple mechanisms.

Andrzej A. Stępniewski

Loads of Lower Limb Joints During Bicycle Ride

This work features a geometric and static analysis of the lower limb during bicycle ride. Basic dimensions are indicated, which are necessary for the description of movement geometry. The simplified flat model was adopted for the analysis. Using the transformation of Denavit-Hartenberg frames, vectors were developed for the position of the rotation axis of the joints in immovable frame. The inverse kinematics problem was solved. The course of displacement changes in the ankle joint was adopted as an angle function for crankset position, based on experimental research results, published in professional literature. The course was approximated with fifth grade polynomial. Joint displacements and loads were established. A sample calculation is presented, illustrating the subject computational algorithm.

Andrzej Zbrowski, Wojciech Jóźwik

Impact Process Identification for Impact Cylinder Piston

The phenomenon of the tool rebound from the object processed, that can be noticed particularly in the case of impact marking, has a negative influence on the quality of the processing of moving objects, which is a result of the blur effect caused by the shift of the object processed at the time of its retraction. The objective of the study was to determine the influence of both the capacity of the chamber of the accumulator and the working pressure on the characteristics of the phenomenon of the piston rebound from the obstacle that can be noticed after it hits a hard fender for the very first time. The article presents the results of research consisting in the analysis of the rebound phenomenon for impact cylinder pistons. The tests were carried out for cylinders whose structure allowed for the change in the capacity of the accumulator chamber. Cylinders with the pistons of 40 and 100 mm in diameter and supplied by 4 and 6 bar pressure were subject to tests that were undertaken at the test stand equipped with Phantom V310 high speed digital camera